USING FDM AND FEM TO SIMULATE THE DECARBURIZATION IN AISI 1074 DURING HEAT PROCESSING AND ITS IMPACT

A Thesis
Presented to
The Academic Faculty

by

In Partial Fulfillment
of the Requirements for the Degree
Doctor of Philosophy in the
School of Materials Science and Engineering

Georgia Institute of Technology
August 2011

USING FDM AND FEM TO SIMULATE THE DECARBURIZATION IN AISI 1074 DURING HEAT PROCESSING AND ITS IMPACT

Approved by:

Dr. Thomas H. Sanders, Jr., Advisor
School of Materials Science and Engineering
Georgia Institute of Technology

Dr. Arun Gokhale
School of Materials Science and Engineering
Georgia Institute of Technology

Dr. Naresh Thadhani
School of Materials Science and Engineering
Georgia Institute of Technology

Dr. Sheldon Jeter
School of Mechanical Engineering
Georgia Institute of Technology

Dr. Joe K. Cochran
School of Materials Science and Engineering
Georgia Institute of Technology

Date Approved: [May, 11th, 2011]

Dedicated to my parents

ACKNOWLEDGEMENTS

First of all, please allow me to take this opportunity to express my gratitude for the great assistance, guidance and support I have received over the course of my study at Georgia Tech. Without them, the completion of this work would not have been possible. I would like to thank Dr. Thomas Sanders Jr. for providing instrumental and patient guidance and support as well as for giving me the freedom to pursue my own ideas. I would also like to thank Dr. Arun Gokhale, Dr. Naresh Thadhani, Dr. Joe Cochran and Dr. Sheldon Jeter for taking the time to serve on my thesis committee and for making many constructive suggestions which improved my work vastly.

I also want to extend my gratitude to all the faculty and staff with whom I have worked with, especially Mrs. Susan Bowman, who makes our study and life a lot easier by taking care of all the administrative matters. Mr. Tim Banks and Mr. James Cagle have provided valuable technical assistance in many aspects of my work. I am indebted to Dr. Laura Cerully and Dr. Garritt Tucker for the enlightening discussions we had. I also want to acknowledge the help I received from fellow graduate students in and beyond the Sanders and Cochran groups.

This work has been funded by an NIST ATP grant with Deep Springs Technology (Toledo, OH) and I would like to take this opportunity to thank everyone from Deep Springs who has collaborated on this project. A special note needs to be made to acknowledge the professional guidance I received during my internship with Western Digital Corporation (San Jose, CA) in the fall of 2010, where I gained the experience and

confidence that make me more prepared to rise to the occasion in the face of future challenges.

Last but not least, I need to thank my parents for their immense and selfless support, love and sacrifice for me, without which I could not be where I am now. My father passed away earlier in 2010 and my mother shouldered the tremendous grief all by herself. My parents managed to teach me the one single most important lesson I could ever learn: no matter how bad things may seem, wallowing in self-pity does not make anything better, what I need to do is to brace myself, to focus on positive things in life, and to prove that their sacrifice is not futile, that I am the son they deserve.

TABLE OF CONTENTS

LIST OF TABLES

LIST OF FIGURES

LIST OF SYMBOLS AND ABBREVIATIONS

X	ferrite decarburization depth
C_b	solid solubility of carbon in ferrite
C_I	initial carbon concentration in the alloy
D	diffusion coefficient of carbon in ferrite
t	time
D_0	pre-exponential factor
Q	activation energy
R	gas constant
T	temperature in Kelvin
α	ferrite phase in Fe-C phase diagram
γ	austenite phase in Fe-C phase diagram
$p(d)$	probability density function
d	average particle diameter
M	mean value of the diameter distribution
S	stand deviation of the diameter distribution
ϕ	concentration function
i, j	numbering in row and column
$\Delta x, \Delta y$	grid step length in the -x and -y directions
N	outward carbon flux density
A	sample space area
K	stiffness matrix
u	displacement vector
F	force vector

a, b, p and q	stoichiometric coefficients of a chemical reaction
A and B	reactants of a chemical reaction
P and Q	products of a chemical reaction
ν	reaction rate
J_1, J_2, J_3	first, second and third deviatoric stress invariant
λ	hydrostatic tensor
σ_{ij}	stress tensor
$\sigma_1, \sigma_2, \sigma_3$	principal stress tensors
U_{SE}	potential energy
U_S	surface energy
a	half crack length
E	Young's modulus
γ	surface energy coefficient
σ	applied stress
U	elastic energy of the system
a_c	critical half crack length
σ_f	critical applied stress
G	energy release rate
G_c	critical energy release rate
J	J-integral
W	loading work per unit volume or for elastic bodies, strain energy density
γ	path of the integral which encloses or contains the crack tip
ds	increment of the contour path
T	outward traction vector on ds
μ	displacement vector at ds

σ_x	stress level close to the tip of the opening
K_I	stress intensity factor
r	distance from the opening tip
θ	directional angle
m	sphere's mass
d_{avg}	average sphere diameter
ϱ_s	sphere density
f_v	relative density
t_w	wall thickness
R_t^i	external load
R_{Vt}^i	volume force
R_{St}^i	surface force
R_{Ct}^i	concentrated force
μ	friction coefficient
v_1, v_2	friction coefficient
$H(x)$	shape function matrix
D	operator matrix
L	truss element length
B	strain-displacement matrix
W	internal strain energy
V	unit of volume
A	integration area

AISI	American Iron and Steel Institute

FEM	finite element method
FDM	finite difference method
psi	pound per square inch
ULF	updated Lagrange formulation

SUMMARY

The metallurgical processes and the products developed from these processes have been the cornerstone on which our civilizations have developed and flourished. Many of the new materials that have been developed over centuries were often the result of serendipitous occurrences. Because of the importance of new materials to the improvement of society, it is necessary to accelerate the way in which new alloys and processes are designed, developed and implemented.

Over the last two decades the computational side of materials science has thrived as a result of bigger and faster computers. However, the application of new computational methods to the development of new materials and structures is still in the early stages primarily because of the complexity of most metallurgical processes. One such process is the decarburization of steel. Because of the importance of the microstructure on the mechanical properties, changes in the near surface properties are affected by the loss of carbon in the alloy. The topics investigated in this thesis include a variety of alloys and microstructures that are considered to be important in the development of a unique structure necessary for a more efficient method of recovering natural gas and oil from underground reserves as well as structures for energy absorbing systems. Since both the material application and the structure are new, this research represents an ideal opportunity to combine processing, properties, microstructure and computations to accelerate the development of these new structures.

Compared to other commercially available proppants which tend to fail in demanding environments, the thin-walled hollow metal proppants are regarded more promising due to the low density and high mechanical strength. The energy-absorbing composite material manufactured by embedding said spheres in the Mg/Al matrix material is optimized by improving sphere and matrix properties at each step in the

process. Ultimately the mechanical strength, fracture toughness, and energy absorption are expected to achieve a factor of 2-5 higher than previously reported.

Modeling makes it economically practical to assess the targeted materials' overall properties, behaviors and the mechanical responses in conjunction with stress environment, material properties, material dimensions among other variables, before a structure is built. Additionally, more advanced modeling can enable the quantitative descriptions of more complex metallurgical phenomena such as the effects of impurity elements and deformation under complex loading conditions.

CHAPTER I

INTRODUCTION

A new kind of proppants (small-sized spheres used in oil wells to prop fissures open and provide an efficient conduit for oil and natural gas flow through the openings and significantly increase extraction) need to be developed to compensate for the inadequacies of glass made of proppants, ceramic, and polymer, which tend to collapse prematurely in a high-temperature, high-pressure environment [1-3]. Proppants made from thin-walled maraging steel hollow spheres are considered a promising replacement thanks to their high degree of spheroidicity, high mechanical strength and ductility, and presumably low production cost. In order to obtain higher strength and minimize the residual stress, the steel for proppants is heated up to 700 ºC to allow for recrystallization, precipitation hardening and carburization [4-7]. At the same time, decarburization, a phenomenon basically described as loss of carbon content to the environment due to its reaction with certain components in the atmosphere, will occur and debilitate the product by depriving it of the carbon element, rendering the parts made of such steels unreliable [8-9]. Understandably, the weakening effects become more pronounced when factoring in the thin-walled hollow sphere structure, considering the wall thickness measures somewhere between 60 and 200 μm and the decarburization depth can reach as far as 75% of the wall thickness after 100 minutes decarburization, depending on the specific microstructure.

Apart from the hollow sphere structure, the microstructure of the material itself is another aspect that makes this work special. Spheroidite is one of the lesser known steels characterized by its very unique microstructures. In spheroidite, the second-phase

cementite (Fe_3C) particles embedded in the ferrite (Fe-0.02%C) matrix assume the spherical shape, instead of the commonly observed thin-stripped, lenticular or acicular shape [10]. Decarburization basically is a two-step process, namely the diffusion of carbon through the matrix, and the transfer of carbon from the sample to the atmosphere. There have been many reports on the study of decarburization, both experimentally and theoretically [11-15]. According to the research conducted by Wagner and Buckle [16], an existing model can effectively predict the decarburization depth in a ferrite sample held at a certain temperature up to 912 ºC. However, as the decarburization that occurs during the heat treatment of AISI 1074 steel featuring spheroidite microstructure cannot be well described by the existing model, a microstructure-specific, time-dependent diffusion model needs to be constructed to better characterize the decarburization behavior that transpires under these particular circumstances.

In order to avoid any potential danger caused by the decarburization-related strength loss, just knowing the progression pattern of decarburization is not nearly enough. The mechanical property variations must be determined accordingly. In particular, the mechanical properties need to be associated with the microstructural variations over the course of decarburization. In order to obtain the material properties of the spheroidite being heat treated, an FEM model is constructed using the FEM software Abaqus.

Once the impact of decarburization is determined, it is important to find out how hollow maraging steel spheres with different geometric traits behave under stress. Experimentally, the maraging steel spheres are deformed between two parallel-positioned alumina plates. The process is simulated using FEM to properly estimate the stress-resistance of the said spheres. The next step would be to embed those hollow spheres into Mg/Al alloy matrix to manufacture a light-weight, energy-absorbing, impact-resistant composite material. Statistically accurate geometry for the composite materials is generated to provide theoretical guidance for the optimization process of the target

material's properties in conjunction with a series of geometric characteristics such as the sphere size distribution, sphere wall thickness, volumetric fraction of the hollow spheres among others.

Background and literature review are included in Chapter II. The simulation methods will be explained in detail in Chapter III. Chapters IV and V will lay out the simulation results both in terms of the decarburization phenomenon and the related mechanics analysis. Then the conclusion and future work will be discussed in the following chapters.

CHAPTER II

BACKGROUND

Because of the weakening effects decarburization has on steel products, it is crucial for the evolving microstructure to be investigated both experimentally and theoretically, as the carbon-depleted zones expand into the sample being heat treated. The existing Wagner's model has been found not to coincide with our experimental observations well [17]. The experiment results were obtained using samples featuring a unique microstructure under certain heat processing conditions. In this work, finite difference method (FDM) is used to model the decarburization zones that form at the surfaces of AISI 1074 steel samples with spheroidite microstructure during certain heat treatments. In order to reach that goal, the sample space is discretized into a fine grid in which spherical second-phase cementite particles are interspersed. The evolution of the carbon concentration pattern in the sample space is calculated using the finite difference equations derived based on Fick's diffusion laws, approximation of partial differential equations by finite difference equations, and conservation of mass at the boundaries. The simulation results are well upheld by experimental observations and yield in-depth analyses for the decarburization phenomenon in spheroidite. The effects of each parameter are to be further studied and the model is expected to ultimately expand to include other Fe-C alloy microstructures and heat treatments as well.

2.1 Proppant Manufacturing

The proppants are structurally strong, millimeter-sized and lightweight spheres often used to enhance the oil extraction efficiency by holding the crevasses open when the oil and natural gas reserve is being extracted from underground reservoirs. As the

necessity of reducing foreign energy dependence has been propelled to a new height in the wake of the recession and the Gulf oil spill disaster, a new kind of low-cost, more manufacturing-favored and structurally stronger proppants that can provide higher extraction efficiency are in need of development. Proppants currently available in the market are limited by a variety of defects: glass proppants are costly to produce while unable to withstand the demanding extraction environment; ceramic proppants can only tolerate the pressure up to 15,000 psi, whereas the closing pressure over 20,000 psi is often detected in the opened fissures [18]; polymer proppants, ductile and lightweight as they are, can only tolerate a maximum pressure up to 6,000 psi and start melting at 75 ºC, which is lower than the ambient temperature in operation [19-20]. Using those proppants allow for a maximum efficiency of 33% for the available reserve to be effectively extracted [3], whereas using the proposed thin-walled steel hollow spheres as proppants could provide many advantages: theoretically, the hollow metal spheres require less expensive raw materials, the production procedures need much less complicated reduction techniques which have been tested and proved to work with extruded thin metal strips, and the new proppants are expected to last longer in a much more demanding environment as a result greatly reducing the production cost. Even after they ultimately crumple under pressure, the gas held inside the hollow proppants will be released and form bubbles that would still act as conductive agent for the extraction process. Due to the listed advantages brought about by using the hollow steel spheres, this project was initiated in hopes not only to produce proppants of better quality, but to introduce revolutionary changes to the current proppant production paradigm as well.

Figure 1 shows a simple sketch for the production process for the thin-walled hollow metal spheres. Firstly, some metal oxide slurry (mostly Fe_3O_4) is sprayed on the organic sacrificial polystyrene cores, which later are incinerated at higher temperatures. Then, as the temperature continues to rise, the hydrogen atmosphere is applied to reduce the remaining metal oxide shells to elemental metal. In the following step, the

intermediates enter the sintering stage where the fissures and pores in the loosely connected as-reduced metal shells are eliminated via sintering. Up to this point in the process, no carbon has been added to the shell structure, so the gas carburization that follows aims to add to the shell a certain amount of carbon to enhance the strength. Then the gas-carburized products move on to the cooling stage, where decarburization is likely to occur.

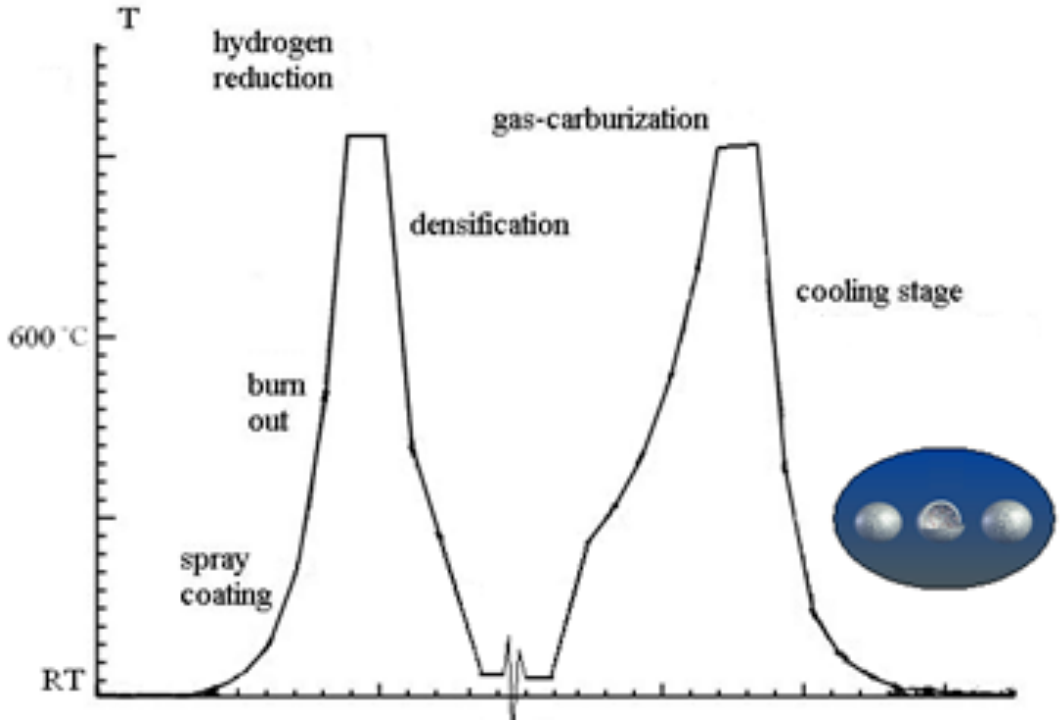

Figure 1. Production process of proppants

As to the question why the study of decarburization is so important, the answer is that low alloy steels' strength and ductility are closely dependent upon the carbon content. In such steels, the carbon content is typically lower than 1% wt., whereas decarburization can consume up to almost all the carbon in the material, therefore leading to some undesirable fluctuations in the mechanical properties, which can be much more pronounced, as stated previously, when the changes takes place in thin-sheet structures instead of bulky materials. When such decarburized steels are used to manufacture components such as gears, springs and in this case proppants, on which many daily activities and production operations heavily rely. The weakening of such components

could disrupt or even cripple the whole working system by exposing it to the danger of unexpected failures below yielding limits and the disastrous consequences, which makes it necessary to understand the mechanism of decarburization and accurately assess its impact.

2.2 Carburization and Decarburization

Conventionally, the carburization procedure is employed to increase the carbon content in the near-surface region in steels. In this study, the technique is enlisted to homogenize the carbon content, to certain extent, through the cross section of the thin wall of the hollow spheres, in doing so to improve hardness and wearability while retaining corrosion resistance. One method by which steel is carburized is to heat it to a high temperature in a CO/CO_2 atmosphere [21-22]. The heat treatment involves heating the sample to the austenite phase field. However, when the system cools from the austenite phase temperature, the chemical potential of carbon in the atmosphere drops below that in the steel being heat treated and the carbon is removed from the steel. This process generally is defined as "decarburization", which weakens the strength of the steelworks in most cases.

In previous research [22], three different gas atmospheres have been tested as the cooling atmosphere after reduction, including CO/CO_2, H_2/Ar and air flow. In the case with CO/CO_2, excess carbon causes metal dusting on the sample's surface [23]. In order to avoid metal dusting, the ratio of CO/CO_2 has to be controlled in exact accordance with the process of the reaction, which is not practical given the means available [23-25]. Meanwhile, both air and H_2/Ar gas flow result in decarburization as the carbon tends to migrate from inside the matrix towards the surface due to the consumption of carbon by the reactions with certain atmospheric components at the surface. This research focuses on the decarburization in air atmosphere.

2.3 Existing Models

When decarburization occurs within a two-phase field (ferrite and austenite in this case), a discontinuous concentration profile of carbon is observed, as in Figure 2.

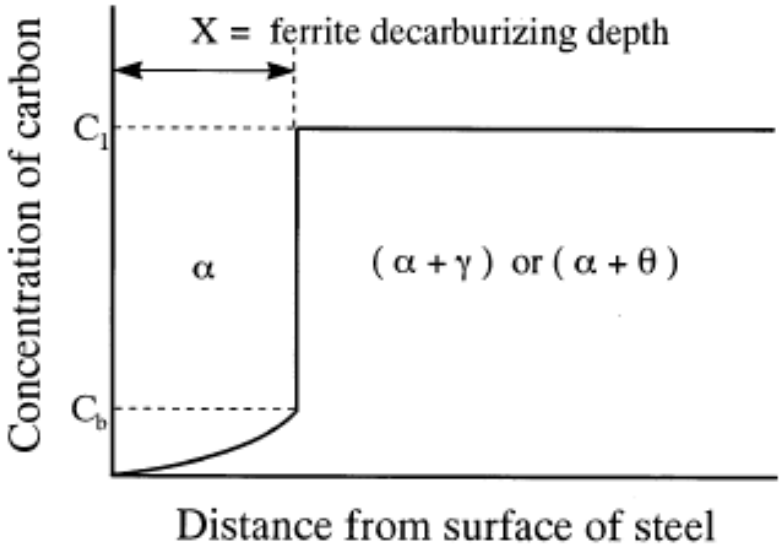

Figure 2. A schematic carbon concentration profile under the condition in which phase transformation occurs. The microstructure as a function of distance from the surface is presented using symbols α, γ and θ which represent ferrite, austenite and cementite, respectively [26]

The concentration profile in Figure 2 is an outcome of the different local equilibrium compositions on two sides of the phase interface, as well as different carbon diffusion coefficients in one phase from the other. Wagner [16], assuming that decarburization is governed by the diffusion of carbon over the concentration gradient between the two phases, works out an estimate for the diffusion depth through Equation 1.

$$X = \sqrt{\frac{6C_b \times D \times t}{3C_I - 2C_b}} \qquad (1)$$

Where X is the ferrite decarburization depth in millimeter, C_b and C_I (mol/mm^3) are the solid solubility of carbon in ferrite and the initial carbon concentration in the alloy, respectively; D is the diffusion coefficient of carbon in ferrite (mm^2/s) and t is time in

second. With Equation 1, decarburization depth X can be obtained if C_b, C_I, D and t are known. The diffusion coefficient D is determined with the Arrhenius equation, as shown in Equation 2.

$$D = D_0 \exp\left(-\frac{Q}{RT}\right) \qquad (2)$$

Where the pre-exponential factor (D_0) and the activation energy (Q) are 0.394 mm^2/sec and 80.22 KJ/mol in ferrite, respectively [13], with R and T standing for the gas constant and the temperature in Kelvin. Good agreement has been reached between the modeling results and experiments with ferrite microstructure in the temperature ranges A and B, as indicated in Figure 3.

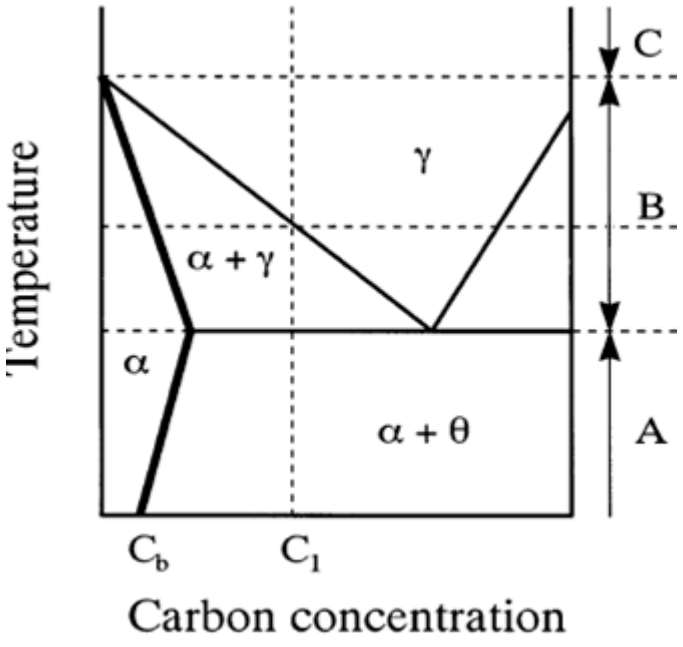

Figure 3. Schematic phase diagram in Fe-C binary system. at each temperature C_b is defined as the concentration value on the bold line, and C_I stands for the initial carbon concentration [13]

In region B, the ferrite decarburization depth is governed by the carbon diffusion in both ferrite (α) and austenite (γ) phases. As a result, ferrite grains grow into the

austenite region during decarburization, as illustrated in Figure 4. The elongated grains appear at the surface areas such that decarburization continues to happen in ferrite matrix, rendering Equation 1 not immediately applicable but it is assumed in Wagner's paper that the model could still apply in the entire temperature range B [13]. When the ambient temperature is higher than 912 ºC, which is the peak temperature of the ferrite/austenite two-phase field, namely region C in Figure 3, the solid solubility of ferrite drops to zero so it does not appear even when the carbon concentration reaches zero (the far left side of the Fe-C phase diagram), aforementioned model does not hold any more [27-29].

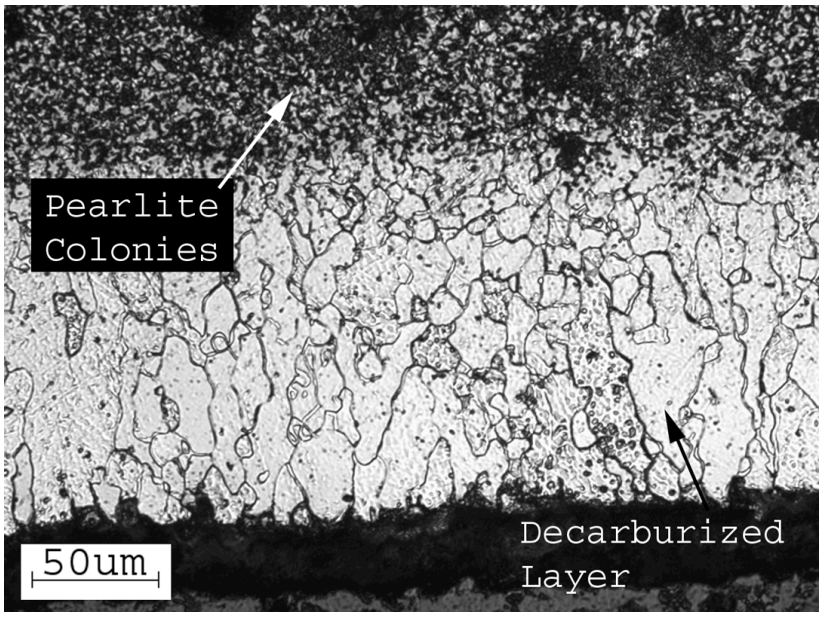

Figure 4. Edge of sample of AISI 1074 heat treated in air at 800 ºC for 100 minutes. A decarburized zone and elongated ferrite grains are evident along the edge of the sample [17]

When the decarburization takes place at 700 ºC, Wagner's model is supposed to be able to predict the decarburization depth. However, in the research conduct by L. Cerully et al. [22], in the AISI 1074 sample with spheroidite microstructure held in air at 700 ºC for 100 minutes, the decarburization depth observed in experiment can reach only as far as 80 μm, as opposed to approximately 300 μm predicted by Wagner's model. The discrepancy necessitates a new model specifically geared towards the samples that feature spheroidite microstructure.

2.4 Computing Software Tools

The FDM modeling for decarburization progress was done using Comsol Multiphysics 3.5.0.603. The FEM analyses for the mechanical properties of decarburized samples were conducted using the FEM software Abaqus 6.9-1. The two- and three-dimensional microstructures are generated using Matlab code that enables the control over the position distribution, size distribution, total volume fraction of the second phase particles, the thickness of decarburization zones, the type of the elements associated with the modeling, among other key parameters. In Section 5.2.2, Ansys 12.0.1 is used to depict the interactions between the contact surfaces when a hollow metal sphere is crushed between two parallel rigid alumina plates.

2.5 Microstructure Generation

In order to authentically recount the microstructural details of the material, the following observations are incorporated in the numerical modeling process. Figure 5 (b) is an optical micrograph of a spheroidite sample that has been heat treated under the aforementioned conditions and etched with 2% nital etchant, such that the decarburized areas formed in the cross section can be properly exposed, as opposed to a sample without treatment shown in Figure 5 (a). According to the industry definition [30-31], the carbon-depleted zones which consist of the remains of ferrite band and shrunk cementite particles are defined as the decarburization zone and its thickness the decarburization thickness.

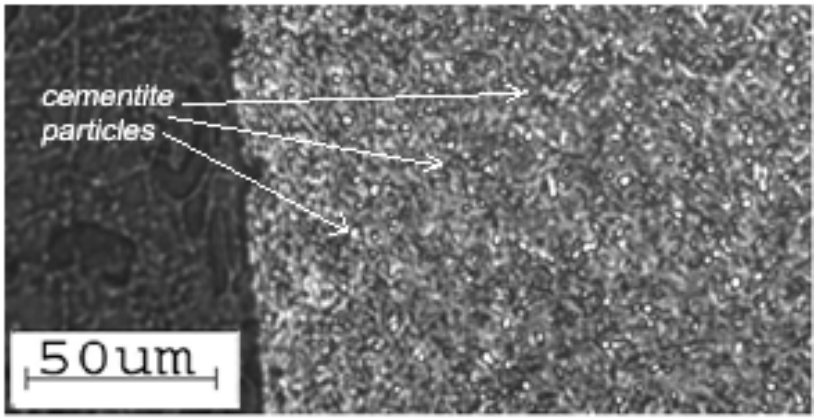

(a) a sample without treatment

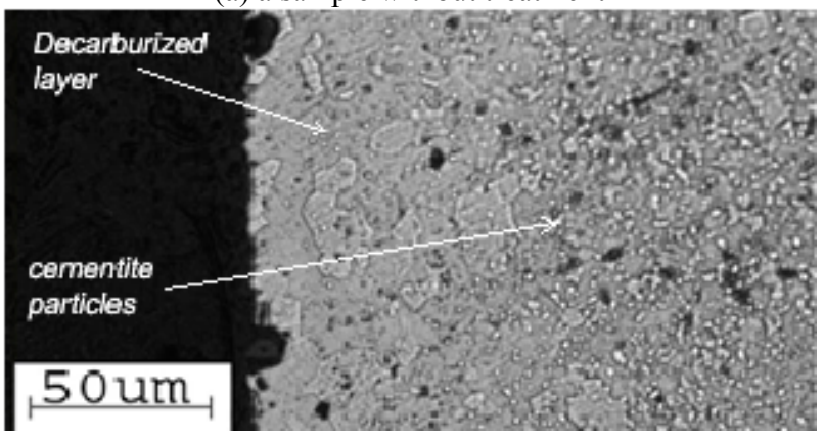

(b) a sample after being heat treated

Figure 5. Optical micrographs of the edge of an AISI 1074 (a) untreated sample and (b) a sample heat treated in air at 700 ºC for 80 minutes

The spherical cementite particles are unmistakable in Figure 5 (a) and (b), while Figure 5 (b) displays a decarburization layer formed during the heat treatment. The modeled sample space is created based on the micrographs in Figure 5, such that the characteristic microstructural features are rendered accurately. For the FDM modeling, two different views of the sample space used in the simulation are shown in Figure 6. The entire sample space is initially interspersed with certain number of particles and then discretized into a fine grid in which each unit is assigned either in the particles, in the matrix phase or at the boundary. Throughout discretization, the mesh is further refined in adaptive accordance with the decidedly non-uniform local geometrical traits, to increase the computational precision. For instance, the areas with more particles require more refined discretization. The discretization of the sample space with one particle is

illustrated in Figure 4(a) and part of the sample space with second-phase particles in Figure 6(b).

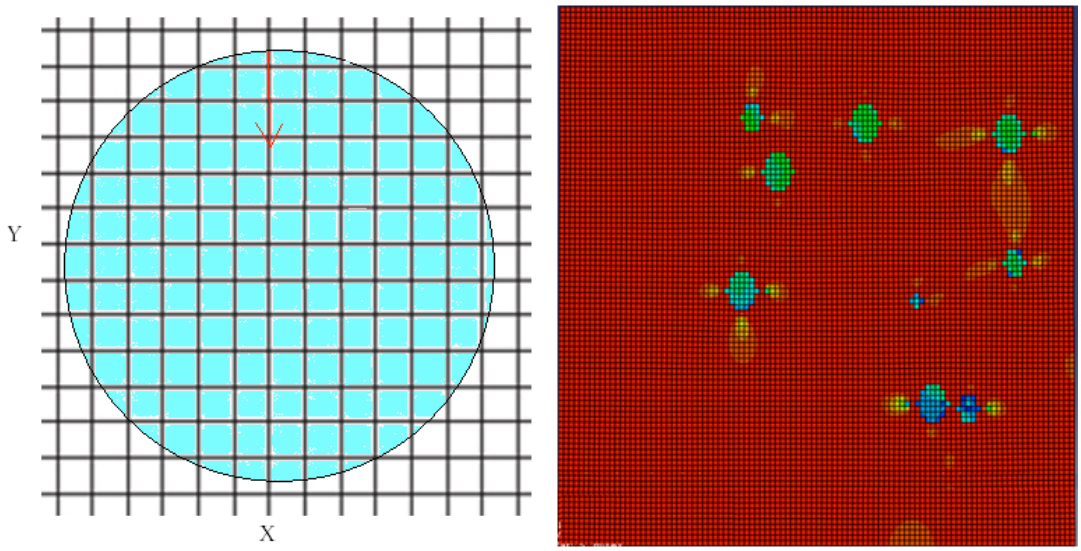

(a) (b)

Figure 6. Sample space discretization (a) with one particle (b) with sample space featuring spherical cementite particles using adaptive meshing method [32]

Parameters used for modeling need to be initialized, including the number of alloy compositions, diffusion coefficients, initial interface position, initial composition concentration and a variety of boundary conditions (periodic boundary conditions, free surface boundary conditions and boundaries with inward or outward carbon fluxes). As shown in Figure 6(b), the locations of the particles in the sample are assumed to be distributed following a uniform random distribution, whereas the particle size is determined by Gaussian normal distribution, as in Equation 3.

$$p(d) = \frac{1}{\sqrt{2\pi}dS} \exp\left[-\frac{(\ln d - M)^2}{2S^2}\right] \qquad (3)$$

The Gaussian normal distribution is considered the most "classic" continuous probability distribution, being one of the simplest and most convenient functions for particle distribution without rigorous justification, especially when it involves diffusion

of particles in substance [33-34]. In Equation 3, $p(d)$ is the probability density function and d is the particle diameter. The variables M and S represent the mean value and standard deviation of the distribution, respectively. Based on the observation of samples prepared by tracking and recontouring optical micrographs in transparent sheet, M was calculated as 2.14 μm and S as 0.5 μm.

In terms of FEM modeling, the assembling starts with defining a rectangular mesh (width and height, and thickness in three dimension) and adopting a proper mesh density (number of elements per unit length). Then the microstructure is created by randomly placing particles in the sample space, in the form of a circle in 2D or a sphere in 3D, while ensuring that their sizes are determined following Equation 3. The random seeding process is initiated by inserting in the sample place the origin of the first particle. The location of the origin is so determined that certain pad margins exist at the edges, in which way the particles generated later will not intersect with the boundaries. The radius of the particle determines which elements from the mesh will be included in the particles by comparing the inter-distance between the particles' origins to the preset radius length (if inter-distance < radius, the element will be included in the particle; vice versa). The same process is repeated and the total particle volume continues to accrue until the predetermined second-phase-particle volume fraction is reached. In common practice, as cavities and voids are often detected in steel, they are also included in the model in the same way the cementite particles are, with the volume fraction of the voids restricted to only 0.0000001% though. Microstructures generated following the previous method are shown in two- and three-dimension in Figure 7.

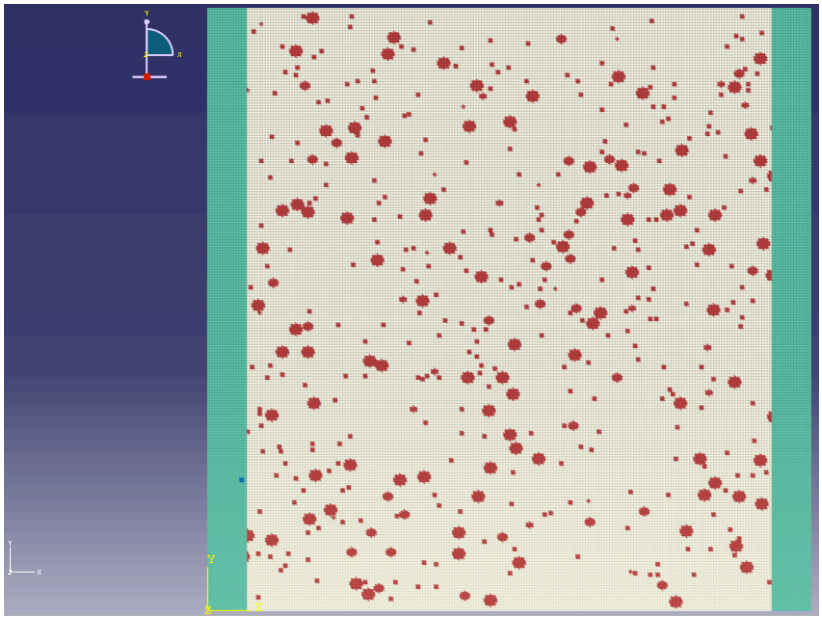

(a) 2D 600 µm × 600 µm

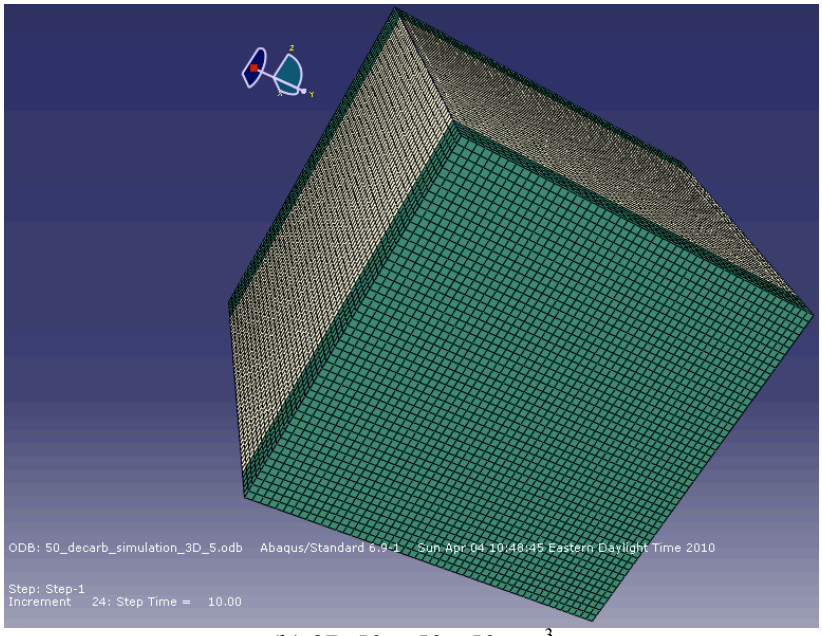

(b) 3D 50 × 50 ×50 µm^3

Figure 7. Generated models of the material microstructure (a) 2D 600 × 600 µm^2, (b) 3D 50 × 50 ×50 µm^3, and (c) 51º cross-section view

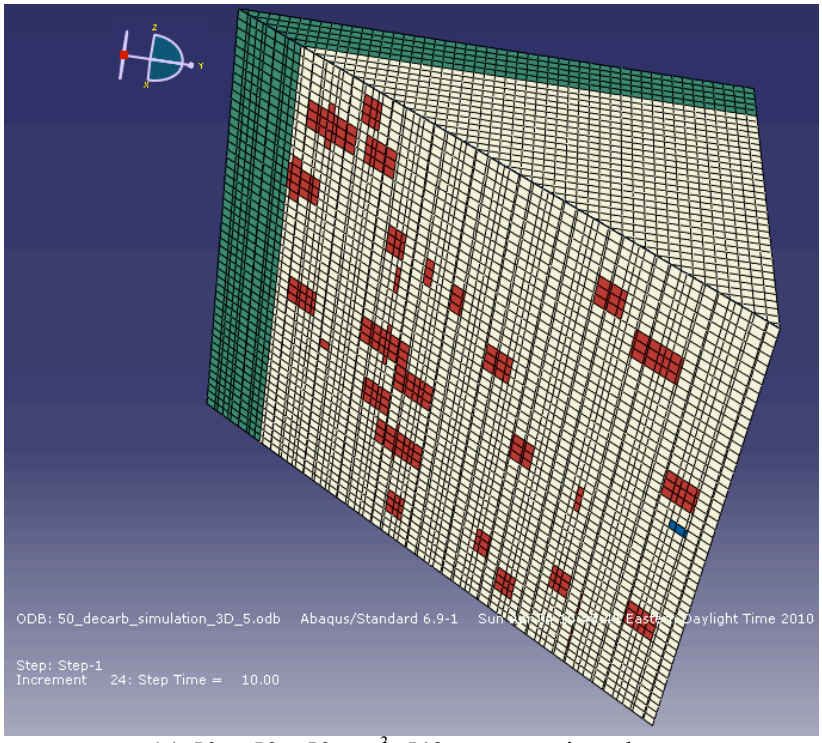

(c) 50 × 50 ×50 μm^3, 51° cross-section plane

Figure 7 continued

The grey-white part in Figure 7 represents the ferrite matrix phase while the cementite particles and voids are shown in red and blue, respectively. Decarburization zones are visible in green at the exterior of the sample. Cavities and voids, not dissolving as decarburization proceeds, remain in the decarburization zone whereas the cementite particles, which lose the carbon associated in Fe_3C and dissociate into pure iron and elemental carbon that subsequently reacts with oxygen and departs from the system in the form of CO, do not, hence no cementite particles in the decarburization zone.

As the average particle size is set as 2.14 μm and the characteristic dimension size of the model is 600 μm, at least a mesh density of 4 (4 pixels for one element) is needed to properly approximate the spherical shape of the particles. That also explains why the cementite particles appear more "square-ish" looking than strictly spherical in Figure 7(c), where there are only 1.25×10^5 elements in the 3D model (50 in each dimension). A mesh density too low cannot properly render the geometry for the spherical particles

while one too high would end up having the model diverge. This will be discussed extensively in the convergence section.

CHAPTER III

SIMULATION METHODS

3.1 Finite Difference Method

The finite difference method was first introduced by A. Thom in the 1920s under the title "the method of square" to solve nonlinear hydrodynamic equations [35]. The FDM techniques are based on the approximations that allow partial differential equations to be replaced by finite difference equations. These finite difference equations are algebraic in form and the solutions are correlated to the grid points.

Therefore, a solution to a finite difference problem generally involves three steps:

1. Divide the solution domain into grids of nodes

2. Approximate the given differential equations using finite difference equations that relates the solutions to grid points

3. Solve the finite difference equations subject to the prescribed boundary conditions and/or initial conditions.

Case in point, decarburization in its nature is the diffusion of carbon element from one phase to another, so Fick's second diffusion law, as in Equation 4, is used to predict how the diffusion process causes the carbon concentration field to evolve over time:

$$\frac{\partial \phi}{\partial t} = D \frac{\partial^2 \phi}{\partial x^2} \qquad (4)$$

or in the case where diffusion occurs in two or more dimensions, Fick's second law becomes Equation 5:

$$\frac{\partial \phi}{\partial t} = D\nabla^2 \phi \qquad (5)$$

Where ϕ is the concentration function in dimensions, in the unit of mol/m^2 or mol/m^3, t is time in second, D the diffusion coefficient. Considering that the characteristic geometry we are looking into is the cross section of the thin wall of a hollow sphere, with the thickness dimension much larger than the other two, a two-dimensional model should suffice in terms of determining the decarburization depth with respect to the wall thickness. The diffusion equation is accordingly altered to Equation 6:

$$\frac{\partial \phi}{\partial t} = D\left(\frac{\partial^2 \phi}{\partial x^2} + \frac{\partial^2 \phi}{\partial y^2}\right) \qquad (6)$$

Listed below in Equations 7, 8 and 9 are the commonly used finite difference formulas to approximate the first order derivative of a function *u(x)* using the function values only.

1. The first-order forward finite difference:

$$\left(\frac{\partial u}{\partial t}\right)_i = \frac{u_{i+1} - u_i}{\Delta x} - \frac{\Delta x}{2}\left(\frac{\partial^2 u}{\partial x^2}\right)_i - \frac{(\Delta x)^2}{6}\left(\frac{\partial^3 u}{\partial x^3}\right)_i + \cdots \qquad (7)$$

Forward difference truncated error $O(\Delta x)$

2. The first-order backward finite difference:

$$\left(\frac{\partial u}{\partial t}\right)_i = \frac{u_i - u_{i-1}}{\Delta x} - \frac{\Delta x}{2}\left(\frac{\partial^2 u}{\partial x^2}\right)_i - \frac{\left(\Delta x\right)^2}{6}\left(\frac{\partial^3 u}{\partial x^3}\right)_i + \cdots \qquad (8)$$

Backward difference truncated error $\mathrm{O}\left(\Delta x\right)$

3. The first-order central finite difference:

$$\left(\frac{\partial u}{\partial t}\right)_i = \frac{u_{i+1} - u_{i-1}}{2\Delta x} - \frac{\left(\Delta x\right)^2}{6}\left(\frac{\partial^3 u}{\partial x^3}\right)_i + \cdots \qquad (9)$$

Central difference truncated error $\mathrm{O}\left(\Delta x\right)$

The central finite difference formula approximates the actual partial differential equation with evidently smaller truncated error and is the formula that the rest of the derivations included in this work go with. Usually finite difference schemes for higher order derivatives can be deduced from the formulas for lower order derivatives. The central finite difference scheme for the second order derivative is shown in Equation 10:

$$\left(\frac{\partial^2 u}{\partial t^2}\right)_i = \frac{u_{i+1} - 2u_i + u_{i-1}}{\left(\Delta x\right)^2} + \mathrm{O}\left(\Delta x\right)^2 \qquad (10)$$

Central difference truncated error $\mathrm{O}\left(\Delta x\right)$

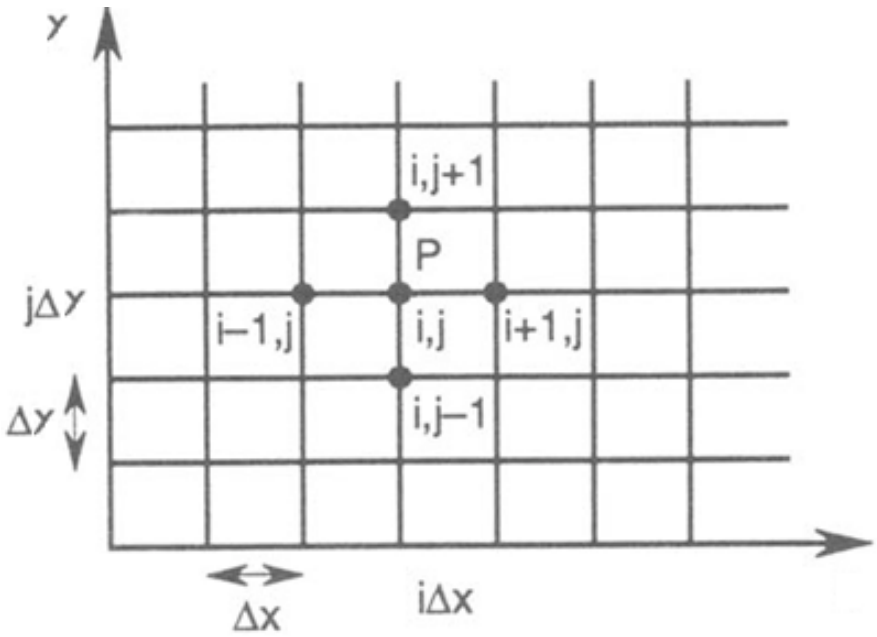

Figure 8. Finite difference mesh for two independent variables x and y

Figure 8 is part of the discretized sample space extending in -x and -y directions. Replacing $\left(\frac{\partial^2\phi}{\partial x^2}+\frac{\partial^2\phi}{\partial y^2}\right)$ in Equation 6 with the average of the central difference formulas on the i^{th} and $(i+1)^{th}$ rows and j^{th} and $(j+1)^{th}$ columns gives the formula in Equation 11 to calculate the concentration pattern variation.

$$\frac{\phi_{i,j}^{t+1}-\phi_{i,j}^{t}}{\Delta t}=\frac{D_{i,j}}{\Delta x^2}\left(\phi_{i-1,j}^{t}-2\times\phi_{i.j}^{t}+\phi_{i+1,j}^{t}\right)+\frac{D_{i,j}\Delta t}{\Delta y^2}\left(\phi_{i,j-1}^{t}-2\times\phi_{i.j}^{t}+\phi_{i,j+1}^{t}\right) \qquad (11)$$

Where the effective concentration $\left(\phi_{i,j}^{t+1}\right)$ at the time *(t+1)* of interest is obtained by iterating Equation 11, knowing the local diffusion coefficient, iteration time and the variation of local concentration with regards to the coordinates. Specifically, $D_{i,j}$ represents the diffusion coefficient at location *(i,j)* and Δx and Δy represent the grid step length in the -x and -y directions, respectively. The evolution of carbon concentration pattern in the sample space is tracked by iterating Equation 11 until all the cementite

particles have completely dissolved and the carbon concentration has reached homogeneity, or the pre-assigned iteration cycle number has been reached, whichever occurs first. The parametric values necessary for solving Equation 11 are listed in Table 1.

Table 1. Parameters used for decarburization simulation

Parameter table	Value	Meaning
C_l	0.000242 (wt%)	solid solubility of carbon in ferrite matrix
C_b	0.0667 (wt%)	carbon concentration in the cementite particles
dt	1×10^{-6} s	time step length
N	7.3003 mol/(m^2·s)	outward carbon flux density
D	1.9445E-11 mm^2/sec	diffusion coefficient for carbon in ferrite matrix
T	700 °C	temperature at which the decarburization takes place
R	8.314 J/(K·mol)	gas constant
Q	80,220 J/mol	activation energy of carbon diffusion in ferrite matrix
A	600 × 600 μm^2	sample space area

To validate the model, decarburization in sample spaces of two different sizes (6 × 6 μm^2 and 600 × 600 μm^2) has been simulated and compared in Chapter IV, Section 4.1. Additionally, the effects of boundary conditions, outward flux density and temperature are tested individually. In the tests done in Section 4.1, constants such as initial carbon concentration, iteration time step, activation energy and gas constant remain unchanged.

3.2 Finite Element Method

The term finite element was first coined by Clough in 1960 [36]. In the early 1960s, engineers used this method for approximating the solutions to complicated problems in stress analysis, fluid mechanics, heat transfer among other disciplines. The first book about the FEM was published by Zienkiewic and Cheung in 1967 [37]. In the late 1960s

and early 1970s, the FEM method was widely applied in a great variety of engineering disciplines. Most commercial FEM software packages were developed in the 1970s including Abaqus, Adina, Ansys, just to name a few.

Basically, FEM cuts a structure into "elements", and then connects those elements at "nodes" as if those nodes were pushing pins that hold elements into an entirety, as shown in Figure 9. Due to the complexity of today's machine parts and the fact that it is essentially impractical to establish a legitimate algebraic equation for the entire domain, dividing the domain into a number of small, easier-to-handle elements becomes a necessity and the field quantities are interpolated by a polynomial (shape function) over the elements, with adjacent elements sharing the connecting nodes of the same degree of freedom. By splicing the elements together, a set of simultaneous algebraic equations, termed stiffness matrix, are resulted and the field quantity becomes interpolated over the entire structure after being analyzed in a piecewise fashion.

More discussions about shape function are provided in Appendix A.

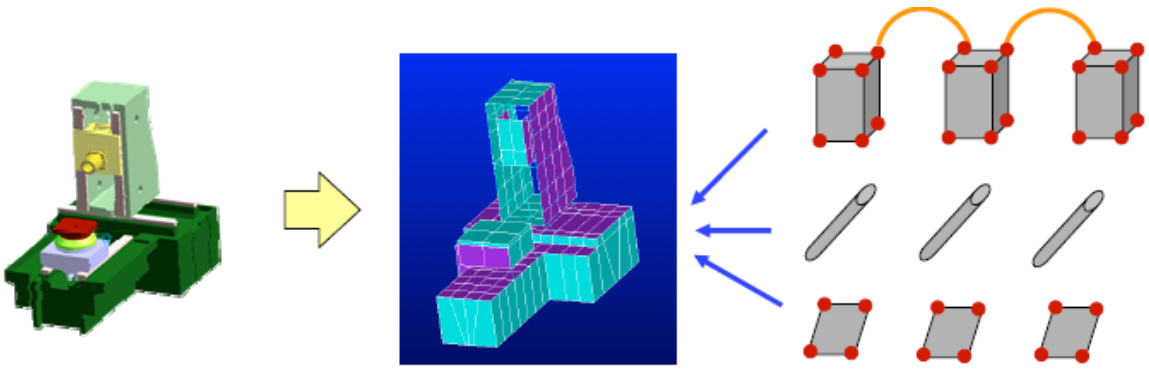

Figure 9. Typical elements and nodes in a machine component discretized using finite element method [38]

The simultaneous algebraic equations are organized in the form of $[K]\{u\} = \{F\}$, where K, u and F represent system property, response and the external impact that triggers the said response in different disciplines, as summarized in Table 2. In this work, only the mechanical properties of the materials are involved.

Table 2. Commonly used properties, behaviors and actions for different types of problems [39]

Problem type	Property [K]	Behavior {u}	Action {F}
Mechanical	stiffness	displacement	force
Thermal	conductivity	temperature	heat source
Fluid	viscosity	velocity	body force
Electrostatic	dielectric permittivity	electric potential	charge
Electromagnetic	Electric permittivity (E-P curve)/magnetic permeability (B-H curve)	resulted electric current/magnetic field	driving electric/magnetic field

The process of performing an FEM analysis is summarized as following:

1. Select analysis type (structural static analysis, modal analysis, transient dynamic analysis, buckling analysis, contact analysis, steady-state thermal analysis, transient thermal analysis, ...)

2. Select element type (2D or 3D; linear or quadratic; truss, beam, shell, plate, solid among other types)

3. Assign material properties (the Young's modulus, the tangent modulus, the Poisson's ratio, density, ...)

4. Create nodes

5. Build elements based on the connectivity between the nodes and the elements

6. Apply loads and boundary conditions

7. Solve the FEM problem

8. Post process (displacement, stress, strain, loading history, temperature distribution, time history, ...)

The FEM modeling can readily handle very complex geometries, restraints and loading, which constitutes the heart and power of this tool. It can also handle a vast

variety of engineering problems ranging from solid mechanics, dynamics, heat transfer problems, fluid mechanics, electromagnetics among others. The author has experience doing research using FEM knowledge in two of the aforementioned areas and it has been proved to be a very powerful approach in terms of solving engineering problems. Meanwhile, the disadvantages of the FEM modeling also need to be noted:

1. A general closed-form solution, which would permit one to examine system response to the changes of various parameters, is not produced

2. The FEM models can only obtain "approximate" solutions

3. The FEM models have inherent "cut-off" errors

3.3 Comparing the Two Methods

Both FDM and FEM are ways of approaching the solutions of partial differential equations. The major differences between the two methods are summarized as following:

1. The most attractive feature of FEM is its ability to approximate very complex geometries, boundaries and loading conditions with much ease, while FDM, in its basic form, is limited to handling no more complicated than rectangular shapes and simple derivative forms thereof

2. FDM is relatively easier to implement

3. To some extent, FDM could be considered as a simplified special case of FEM. In both approaches, the approximations are defined on the entire domain, but not necessarily continuous. The way in which FDM calculates the difference between neighboring nodes can be seen as one of the simplest correlation functions in FEM (linear).

Generally speaking, the quality of an FEM approximation is higher than its FDM equivalent, but this statement is extremely case-dependent and several examples to the contrary can be provided [40-43]. Also, FEM is the method of choice in all types of

analysis in structural mechanics (i.e. solving for deformation and stresses in solid bodies or dynamics of structures) while computational fluid dynamics (ie. fluid mechanics and diffusion/convection phenomena) tends to opt for FDM, a statement that echoes the choices of simulation methods in this work.

CHAPTER IV

DECARBURIZATION SIMULATION

As stated before, the presence of cementite particles, in which the carbon diffuses at a much lower rate than in the ferrite matrix, is the major reason why the decarburization zone progresses much more slowly into the sample space than predicted by Wagner's model. Results from Wagner's model are shown in Figure 2, to be compared with the plots of the evolution of the carbon concentration pattern over heat treatment obtained with finite difference modeling as introduced in Chapter III.

To test the soundness of the model, decarburization in two sample spaces of different size has been simulated. Additionally, the effects of periodic boundary conditions, outward carbon flux density, and temperature are tested individually. In all the analyses presented in Section 4.1, the initial carbon concentration, iteration time step length, activation energy and gas constant remain unchanged throughout, as in Table 1. Among the parameters and conditions to be tested, unless stated otherwise, the periodic boundary conditions are applied on the upper and lower boundaries of the sample space and the outward flux boundary conditions are applied on the left and right boundaries, resembling the situations in which the samples are processed.

4.1 Sample Space Size

Decarburization in a sample space of $6 \times 6\ \mu m^2$ containing three particles is simulated using this model. The sample space is so small that the simulation could be completed within approximately 120 seconds. The dissolution patterns observed at 20, 40, 60, 80, 100 and 120 seconds are shown in Figure 10.

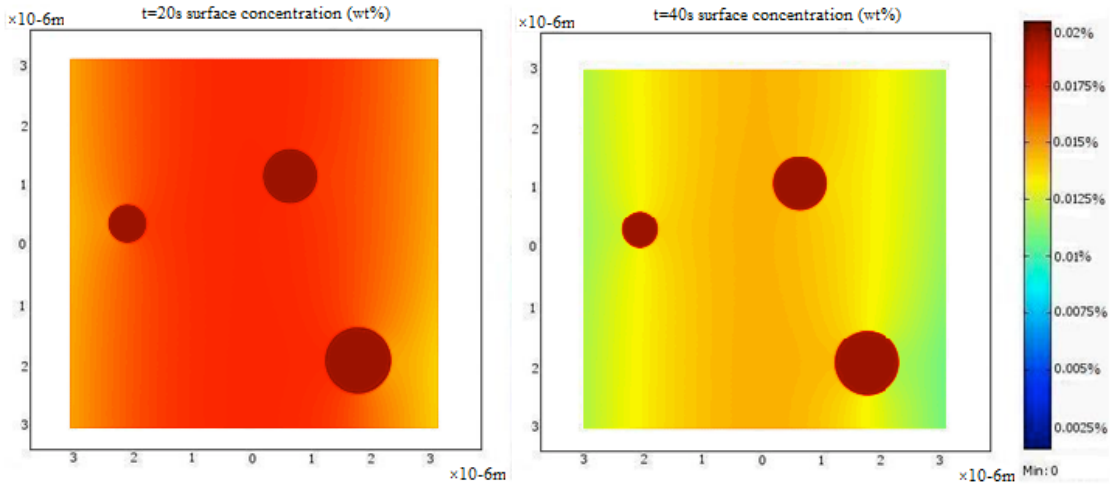

(a) 20s (b) 40s

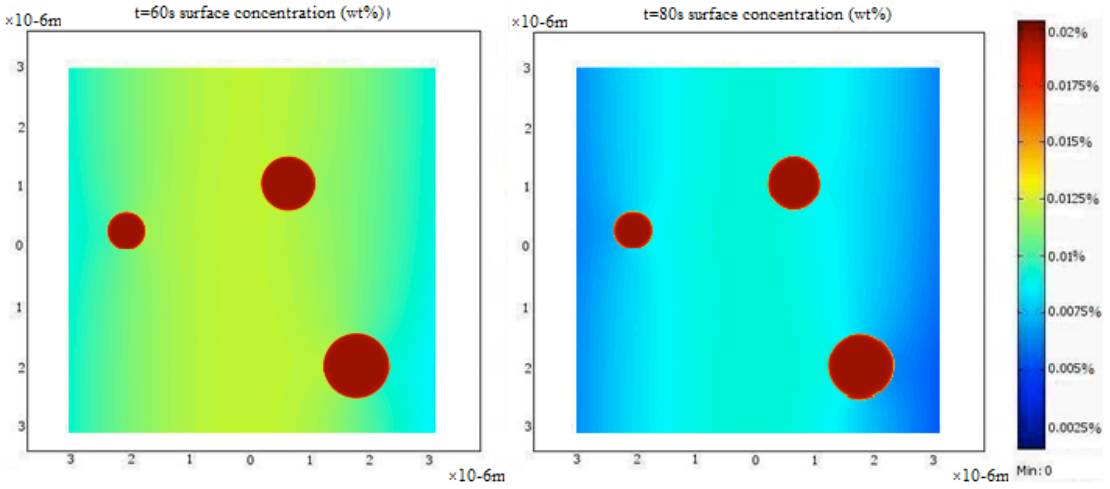

(c) 60s (d) 80s

Figure 10. Carbon concentration pattern in a sample space of 6 × 6 μm^2 after (a) 20 s (b) 40 s (c) 60 s (d) 80 s (e) 100 s (f) 120 s of heat processing in air at 700 ºC

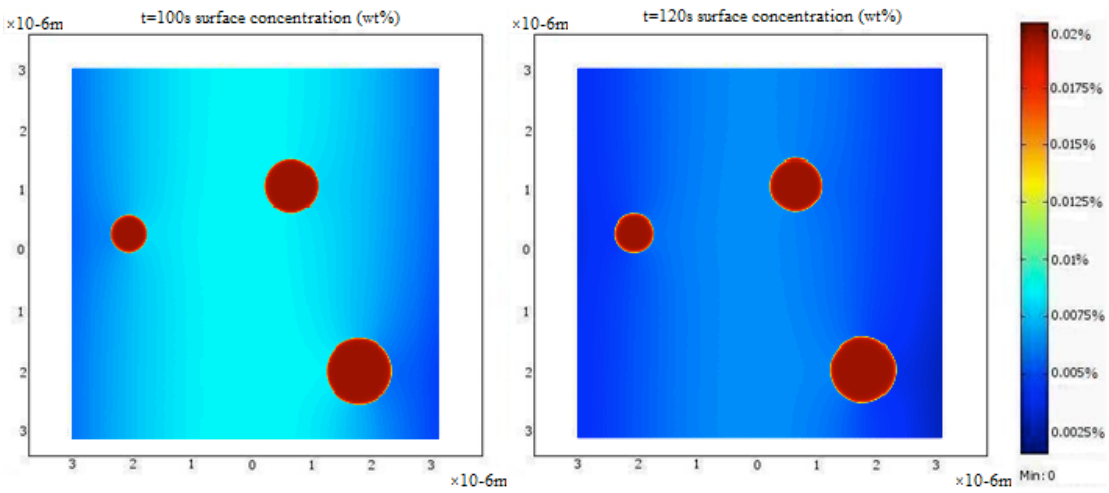

(e) 100s (f) 120s

Figure 10 continued

The shrinking of the cementite particles is unambiguous in Figure 10. The decarburization layer proceeds into the sample space starting from both left and right surfaces, where carbon reacts with oxygen and is consequently consumed. Limited by the low carbon diffusion coefficient, the dissolution of cementite particles is much slower than the carbon diffusion in the surrounding ferrite matrix, as the dissolution of a cementite particle starts at its circumference while the inner part retains the initial carbon concentration. In Figure 10(a), after 20 seconds, the carbon-depleted zone has reached the particles located closest to the surfaces. The interface between the ferrite matrix and the cementite particles remains discernible, as the particle has not begun to dissolve, due to the low carbon diffusion coefficient. In Figure 10(f) after 120 seconds, the particle located closest to the left surface (the one with the smallest initial diameter) is largely immersed in the decarburization layer and has partially dissolved, with the yellow annular ring surrounding the particle representing the concentration slope between the ferrite matrix and the cementite particle. The model is then tested with a sample space of $600 \times 600\ \mu m^2$, which matches the size of the samples heat treated experimentally. The results are shown in Figure 11.

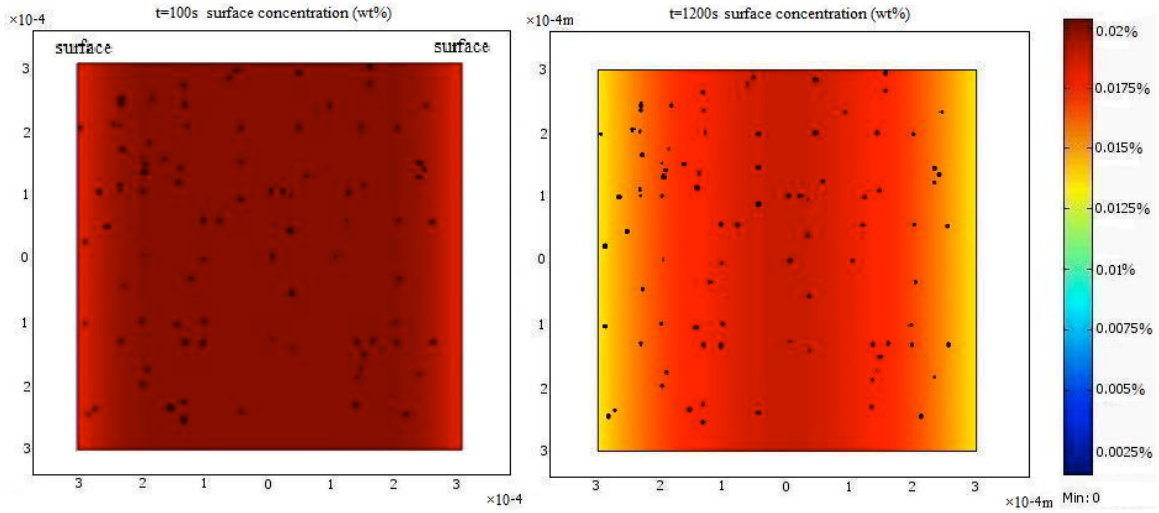

(a) 100 s (b) 1200 s

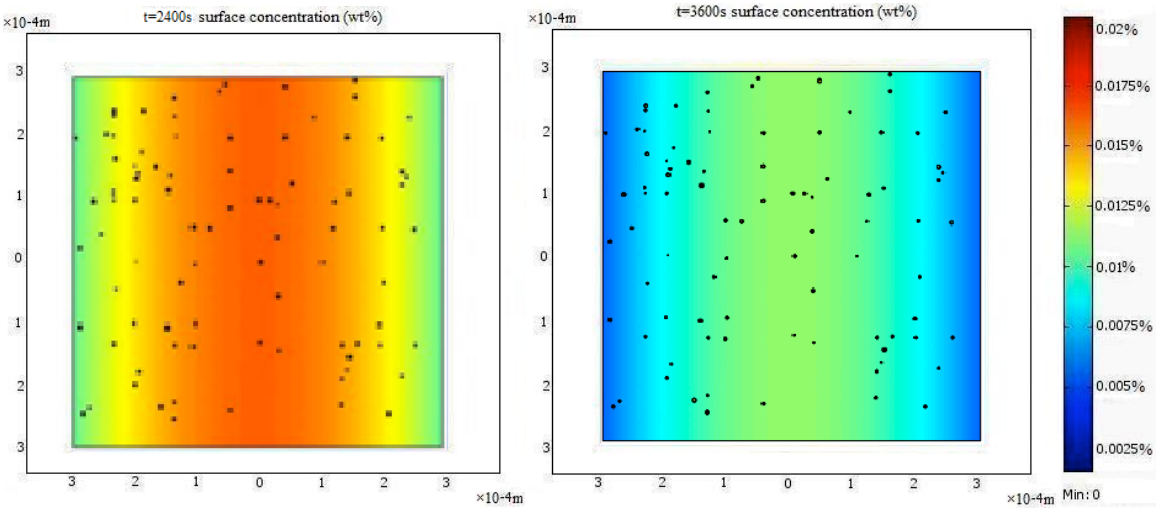

(c) 2400 s (d) 3600 s

Figure 11. Carbon concentration pattern in the sample space at (a)100 (b) 1200 (c) 2400 (d) 3600 (e) 4800 (f) 6000 seconds

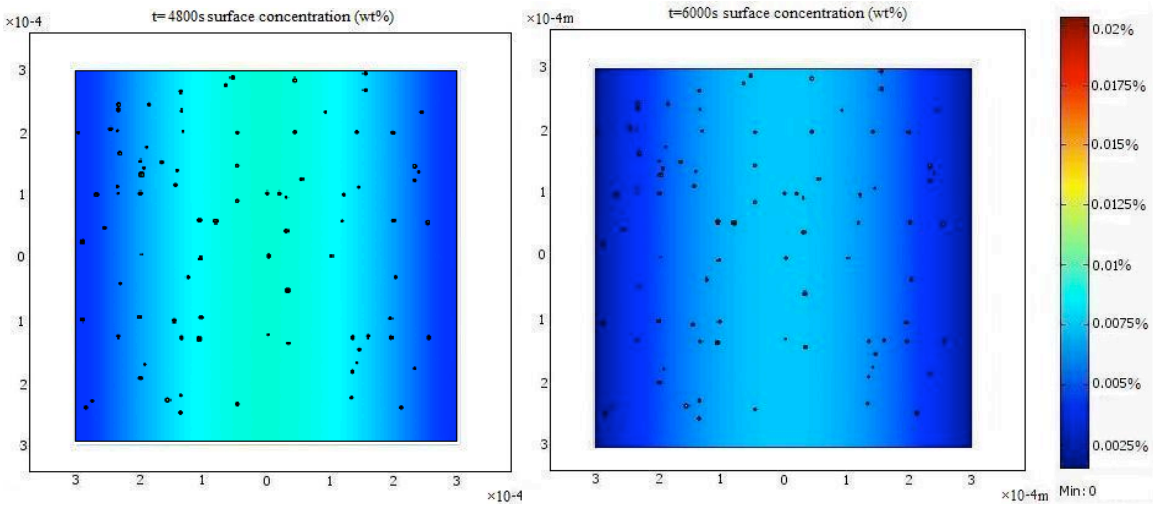

(e) 4800 s (f) 6000 s

Figure 11 continued

As the simulation proceeds, similar to what happens in the 6 × 6 μm^2 case, the spherical cementite particles shrink significantly, releasing carbon to the surrounding matrix. In Figure 11, the crimson red color in the majority of the sample space represents the inital carbon concentration in the ferrite matrix, while the dark blue color denotes the area in which carbon has been consumed. Figure 11(f) shows that the decarburization depth reaches as far as approximately 80 μm in 100 minutes at 700 ºC, closely matching the experimental results, which will be discussed in Chapter 4.3.

4.2 Outward Flux Density

According to Le Chatelier's principle, it is known that the reaction rate increases as the concentrations of the reactants increase and vice versa. The reaction rate is a function of the concentrations of all reactants, products and the ambient temperature, as described in Equations 12 and 13.

Consider a typical chemical reaction:

$$aA + bB = pP + qQ \qquad (12)$$

The lower case letters (a, b, p and q) represent the stoichiometric coefficients, while the capital letters denote the reactants (A and B) and the products (P and Q). According to Jerrica IUPAC's Gold Book definition [44], the reaction rate ν for a chemical reaction occurring in a closed system under constant conditions, without a built-up of reaction intermediates is defined in Equation 13.

$$v = \frac{1}{a}\frac{d[A]}{dt} = -\frac{1}{b}\frac{d[B]}{dt} = \frac{1}{p}\frac{d[P]}{dt} = \frac{1}{q}\frac{d[Q]}{dt} \qquad (13)$$

In this work, the reactions that occur at the surface and drains the carbon element from the steel sample are summarized as $2C + O_2 = 2CO$ / $C + O_2 = CO_2$. By using the formula provided in Equation 13 and the concentration parameters provided in Table 1, the reaction rate for carbon, a. k. a. the flux density is calculated to be 7.3 mol/($m^2 \cdot s$). However, with other parameters remaining constant, the decarburization depths are calculated using four flux densities (1.2 mol/($m^2 \cdot s$), 3.8 mol/($m^2 \cdot s$), 7.3 mol/($m^2 \cdot s$) and 10.2 mol/($m^2 \cdot s$)) for comparison, with the results plotted in Figure 12.

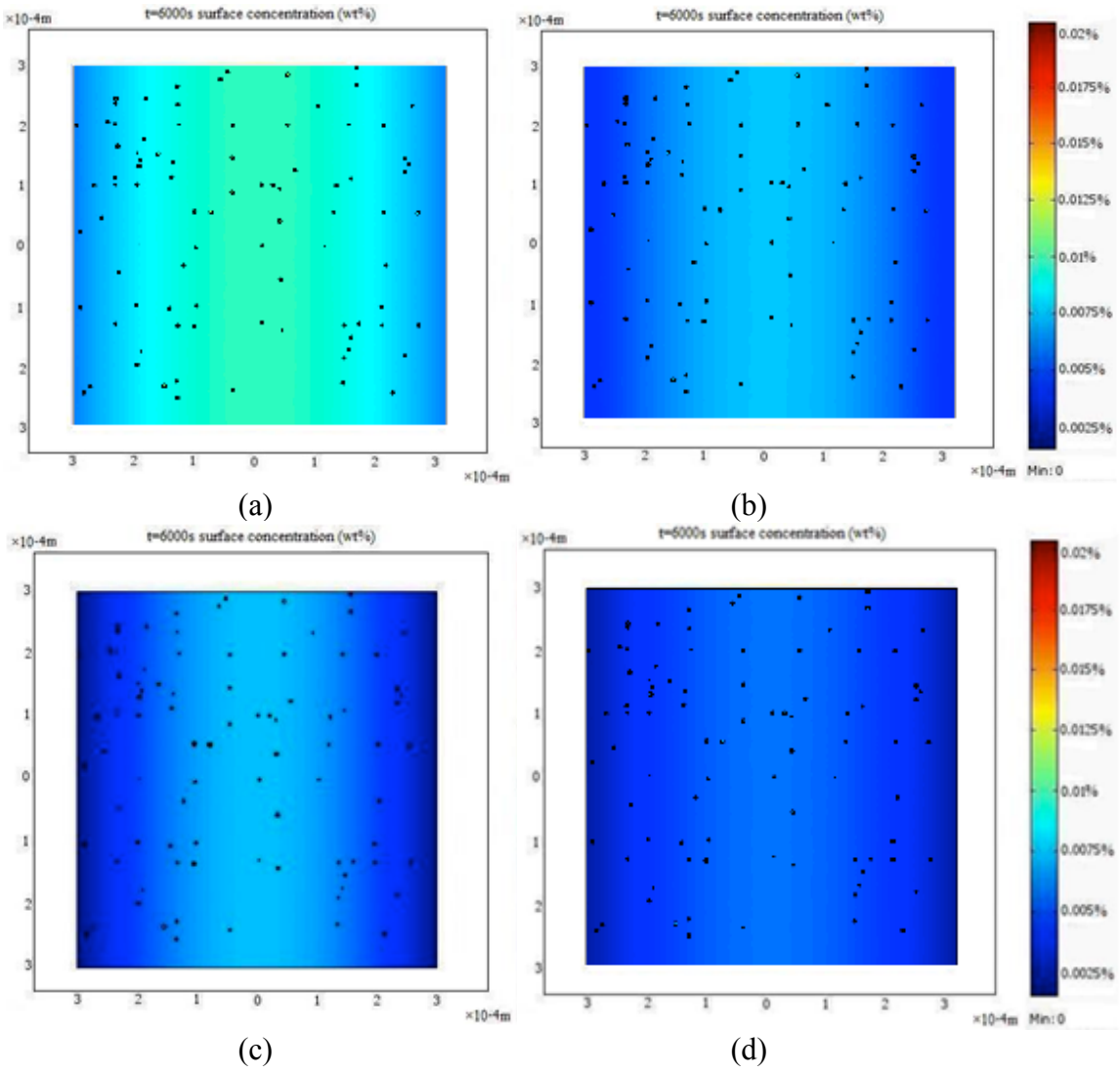

Figure 12. Simulated decarburization layers achieved with different outward flux densities after heat processing at 700 ºC after 100 minutes, with outward flux density at (a) 1.2 mol/($m^2 \cdot s$) (b) 3.8 mol/($m^2 \cdot s$) (c) 7.3 mol/($m^2 \cdot s$) (d) 10.2 mol/($m^2 \cdot s$)

As would be expected, the decarburization layer grows the fastest when the highest flux density is applied, approximately 110 μm after 100 minutes as illustrated in Figure 5(d), whereas the decarburization layer thickness reaches 80 μm, 40 μm and 10 μm with the flux density set at 7.3, 3.8 and 1.2 mol/($m^2 \cdot s$), respectively. Clearly, higher flux density imposes stronger driving force that dissipates the carbon from the ferrite matrix, ergo accelerating the decarburization process.

4.3 Boundary Conditions

In this section, the effects of three types of boundary conditions are investigated. The simulation results obtained under the same heat treatment conditions but with different boundary conditions are compared in Figure 13. The four cases essentially are different combinations of periodic boundary conditions, outward flux boundary conditions and concentration-fixing boundary conditions, as specified in the caption of Figure 13.

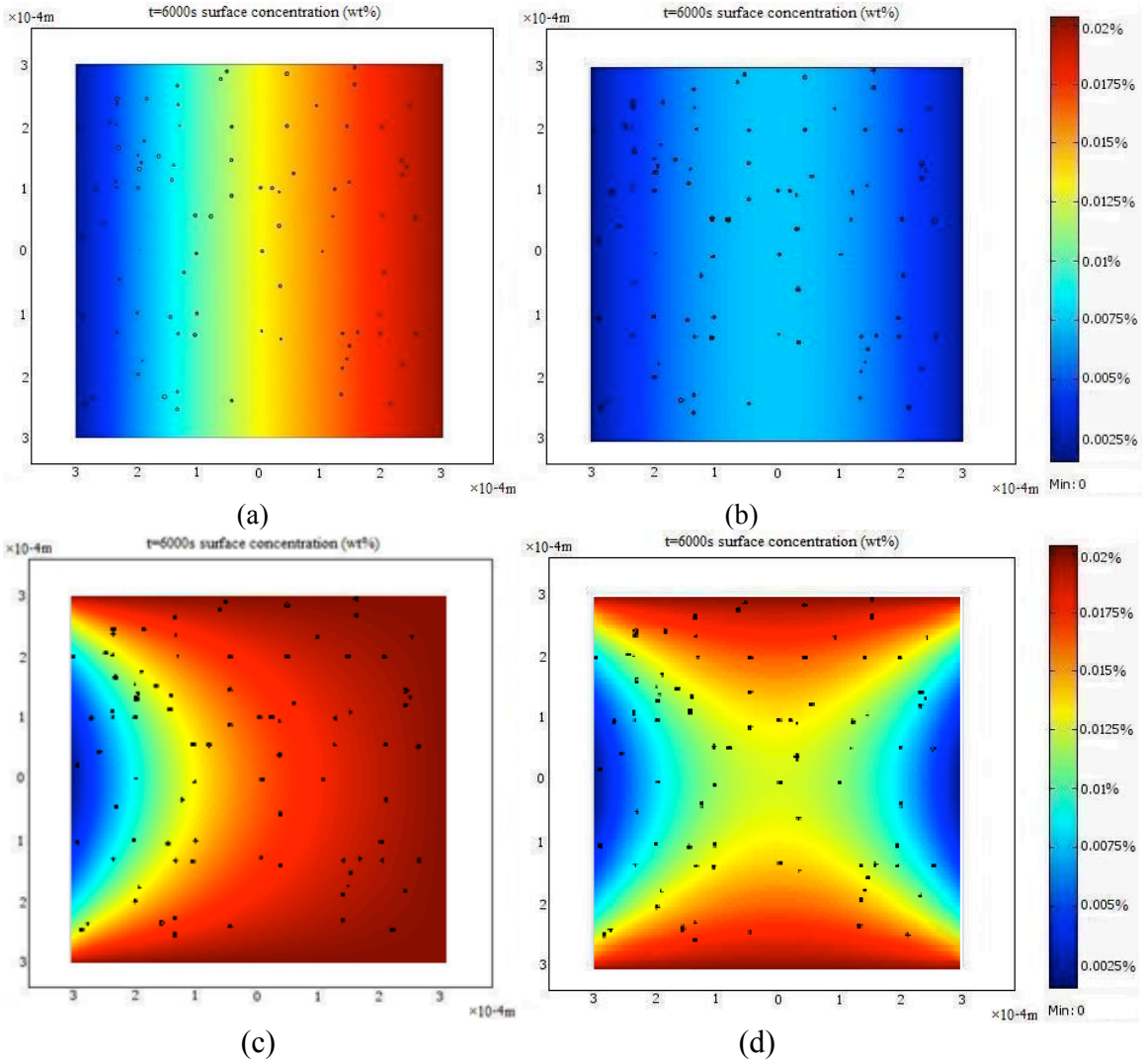

Figure 13. Simulated decarburization results achieved under different boundary conditions after heat processing: (a) upper and lower boundaries: periodic boundary conditions, left boundary: outward flux, right boundary: concentration-fixing (b) upper and lower boundaries: periodic boundary conditions, left and right boundaries: outward flux (c) upper, lower and right boundaries: concentration-fixing, left boundary: outward flux (d) upper and lower boundaries: concentration-fixing, left and right boundaries: outward flux

Without periodic boundary conditions (as in Figure 13 (c) and (d)), the decarburization layer encroaches into the sample space much more slowly and appears to be constrained between the upper and lower boundaries because the concentration-fixing boundaries prevent carbon from diffusing into or out of the sample space. The bottom line is, in the experiments conducted for model validation, both surfaces of the sample are exposed to the atmosphere during heat processing, so the two-sided outward flux boundary conditions are considered to approximate the reality better. As shown in Figure 13 (b), the decarburization layer grows into the material from the edges and eventually reaches about 80 μm after 100 minutes, a result better substantiated by the experimental observations than the simulation results obtained with outward flux boundary conditions only applied on one surface, as shown in Figure 13(a), where the decarburization depth is estimated to be 70 μm.

As an addendum to the discussion, it is occasionally argued that the outward flux at the boundaries should not be categorized as a boundary condition. For example, in heat transfer the inward/outward flux is more often termed the source and sink rather than boundary conditions. However, the newly added function tab in Comsol provides the option of inward/outward flux boundary condition. As soon as the simulation starts, the carbon concentration at the boundary is affected by the outward carbon flux term and functions as a carbon sink to the interior of the sample space. Therefore, from the software's point of view, the flux boundary is functionally equivalent to a concentration boundary condition where the concentration varies with time.

4.4 Temperature

Having determined the impact of other parameters, within the applicable range, the decarburizing temperature has been varied from 500 ºC, to 600 ºC, 700 ºC and 800 ºC, aiming to find out the impacts associated with temperature on the decarburization behavior, with result plots displayed in Figure 14.

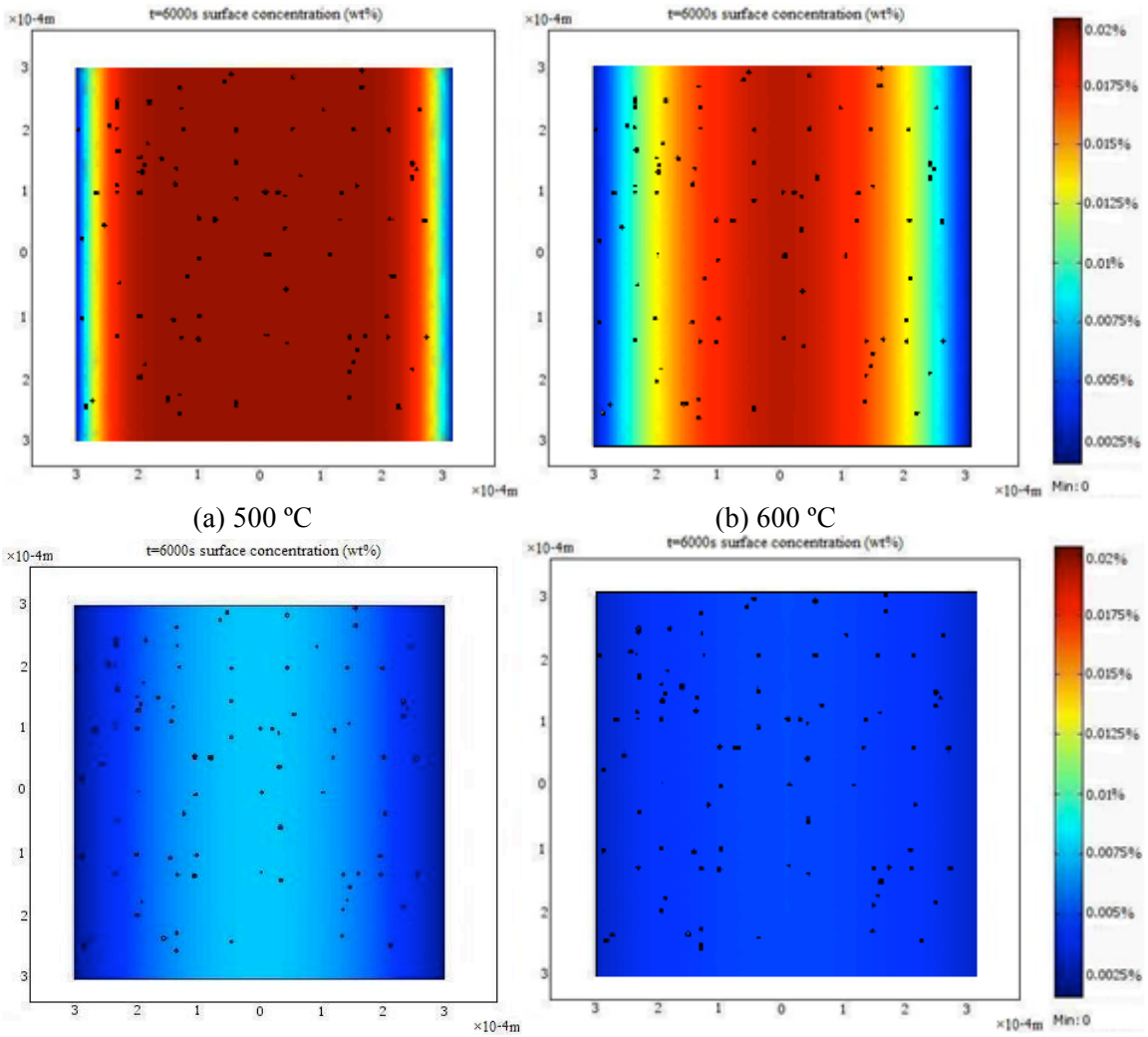

(a) 500 ºC (b) 600 ºC

(c) 700 ºC (d) 800 ºC

Figure 14. Simulated decarburization layers achieved after heat processing for 100 minutes at (a) 500 ºC (b) 600 ºC (c) 700 ºC and (d) 800 ºC

As shown in Figure 14, at 500 ºC, decarburization barely reaches beyond the surface layer after 100 minutes, whereas it can go well over 20 μm after the same time span at 600 ºC. The decarburization depth reaches around 80 μm at 700 ºC and 150 μm at 800 ºC. At higher temperatures, the carbon diffuses through the ferrite matrix to the surface much faster than it does at a lower temperature. As observed in Figure 14, variation of temperature affects the decarburization depth significantly because the diffusion coefficient is in an exponential relation with the ambient temperature, as manifested in the Arrhenius equation which relates the carbon diffusion coefficient to the pre-exponential constant, the activation energy and the temperature, as in Equation (2).

4.5 Experiment Validation

In order to validate the proposed decarburization model, experiments were carried out using AISI 1074 samples with a spheroidite microstructure heat treated at 700 ºC in air for different time spans. Samples were placed in a furnace and heated in air to 700 ºC for 20, 40, 60, 80 and 100 minutes respectively, and then were cooled to room temperature in air. The samples were prepared using standard metallographic techniques, so that the cross-sections could be properly exposed, as presented in Figure 15.

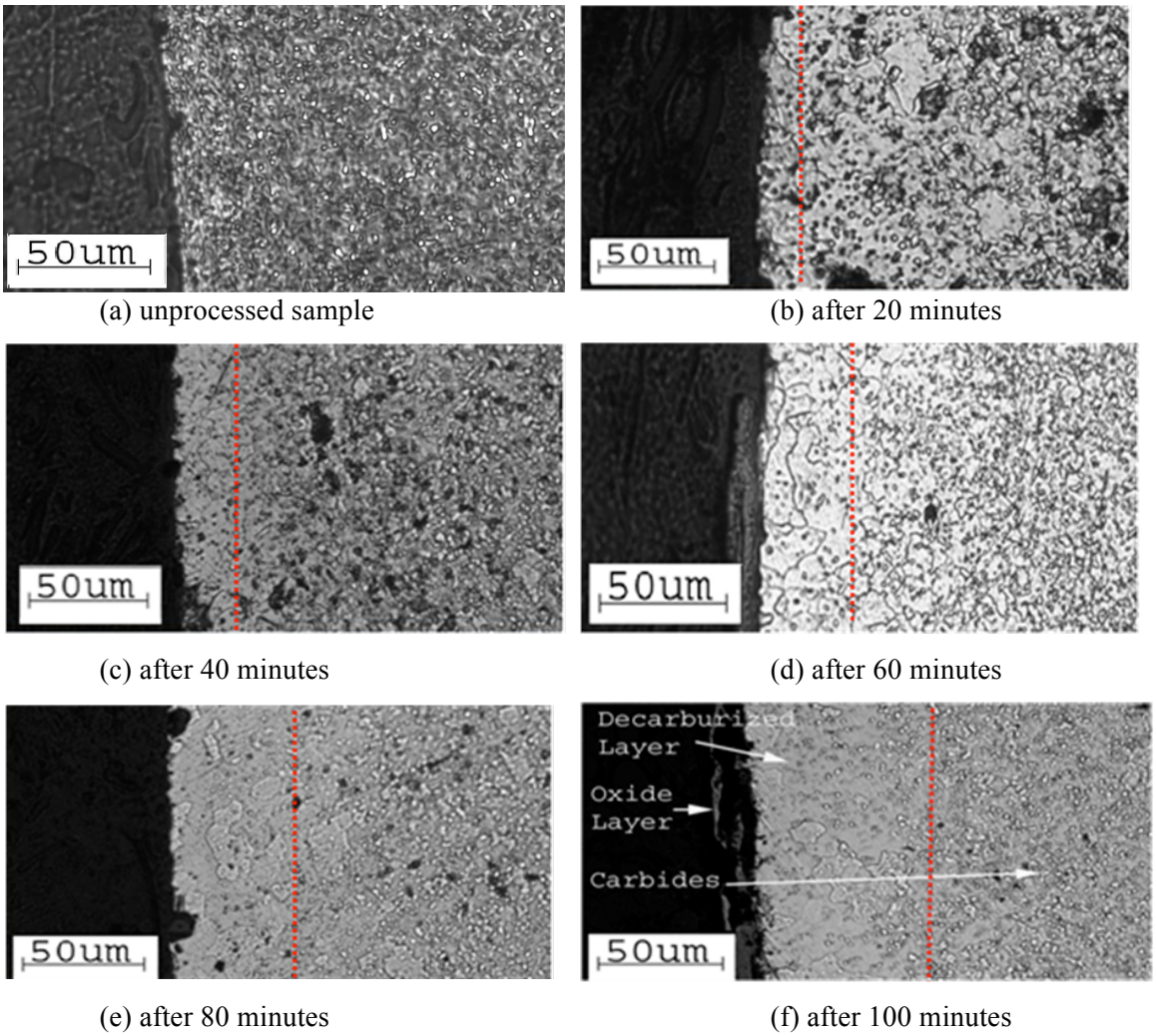

(a) unprocessed sample (b) after 20 minutes

(c) after 40 minutes (d) after 60 minutes

(e) after 80 minutes (f) after 100 minutes

Figure 15. Optical micrographs of the edge of AISI 1074 samples treated in air at 700 ºC for (a) 20 (b) 40 (c) 60 (d) 80 (e) 100 minutes

The thickness of the decarburization layer, as denoted by the red lines, increases appreciably with time from 0 prior to heat processing, to approximately 80 μm after the sample has been heat treated for 100 minutes. As compared in Table 3, the simulation results of decarburization layer thickness are well espoused by experiment observations.

Table 3. Evolution of decarburization depth with time in AISI 1074 samples heat treated at 700 ºC

Processing time (mins)	0	20	40	60	80	100
Simulated decarburization layer thickness (μm)	0	9.6	23.5	39.3	55.8	81.2
Estimated decarburization layer thickness from experiment (μm)	0	10	24	41	56	80

CHAPTER V

MECHANICAL PROPERTY SIMULATION

The decarburization growth model predicts the decarburization depth in Section 4.1 and the results are summarized in Table 4, the depth values were incorporated in the FEM model to determine the mechanical property variations of the decarburized steel samples. Validations are provided in Section 5.1.13.

Table 4. Acquired decarburization depth data to be used for simulation

Processing time (mins)	0	20	40	60	80	100
Simulated decarburization layer thickness (μm)	0	9.6	23.5	39.3	55.8	81.2
Estimated decarburization layer thickness from experiment (μm)	0	10	24	41	56	80

5.1 Mechanical Properties of Decarburized Steel Samples

5.1.1 Material Properties

Prior to the decarburization, the spheroidite microstructure consists of ferrite, cementite particles and voids. Ferrite is an iron-carbon solid solution with maximum 0.02% carbon dissolved in iron matrix as the major impurity. Cementite is a chemical compound with an orthorhombic crystal structure identified by the formula Fe_3C. Ferrite and cementite particles were both modeled with isotropically elastic-perfectly plastic behavior. Cementite is a hard brittle material, with a very low yield strength at 34.5 MPa, as opposed to that of ferrite at 285 MPa according to www.matweb.com [45]. After decarburization has started, the carbon at the surface reacts with oxygen and becomes completely consumed, forming decarburization zones in the process. For this model, pure iron is assumed to represent the material that remains in the decarburization zones. The values used for simulation are shown in Tables 5, 6 and 7.

Table 5. Material properties of ferrite (matrix phase) [45]

Density	7850 kg/m^3
Young's modulus	211 GPa
Poisson's ratio	0.29
Yield strength	285 MPa

Table 6. Material properties of cementite (particles) [45]

Density	7662 kg/m^3
Young's modulus	160 GPa
Poisson's ratio	0.26
Yield strength	34.5 MPa

Table 7. Material properties of pure iron (decarburization zones) [45]

Density	7874 kg/m^3
Young's modulus	211 GPa
Poisson's ratio	0.29
Yield strength	90 MPa

5.1.2 Boundary Conditions

In order to obtain equivalent elastic mechanical properties of the spheroidite, various boundary conditions have been used. In the two-dimensional case, axial tensile stress and shear stress are exerted on the sample (in some cases it is transverse tensile stress). As Figure 16 illustrates, axial tensile stress requires the center node of the bottom edge to be fixed in the -x and -y directions and the entire bottom edge fixed in the -y direction. The axial tensile stress is simulated by applying axial tension on the top edge in the -y direction with a maximum strain of 0.6%. Shear stress, on the other hand, is simulated by imposing a horizontal maximum strain of 0.6% on the top surface in the -x direction, while the top and bottom edges are fixed in the -y direction. The boundary conditions for transverse stress are similar to those for axial tensile stress: the center node of the left edge is clamped and the entire left edge fixed in the -x direction while the tensile stress is exerted on the right edge in the -x direction.

As illustrated in Figure 16(d), the boundary conditions used in a three-dimensional cases are much the same as those in two-dimensional cases, with the only

difference being that in three dimension, the boundary conditions need to be applied on the faces, edges and vertices of the sample space, instead of just the edges and vertices.

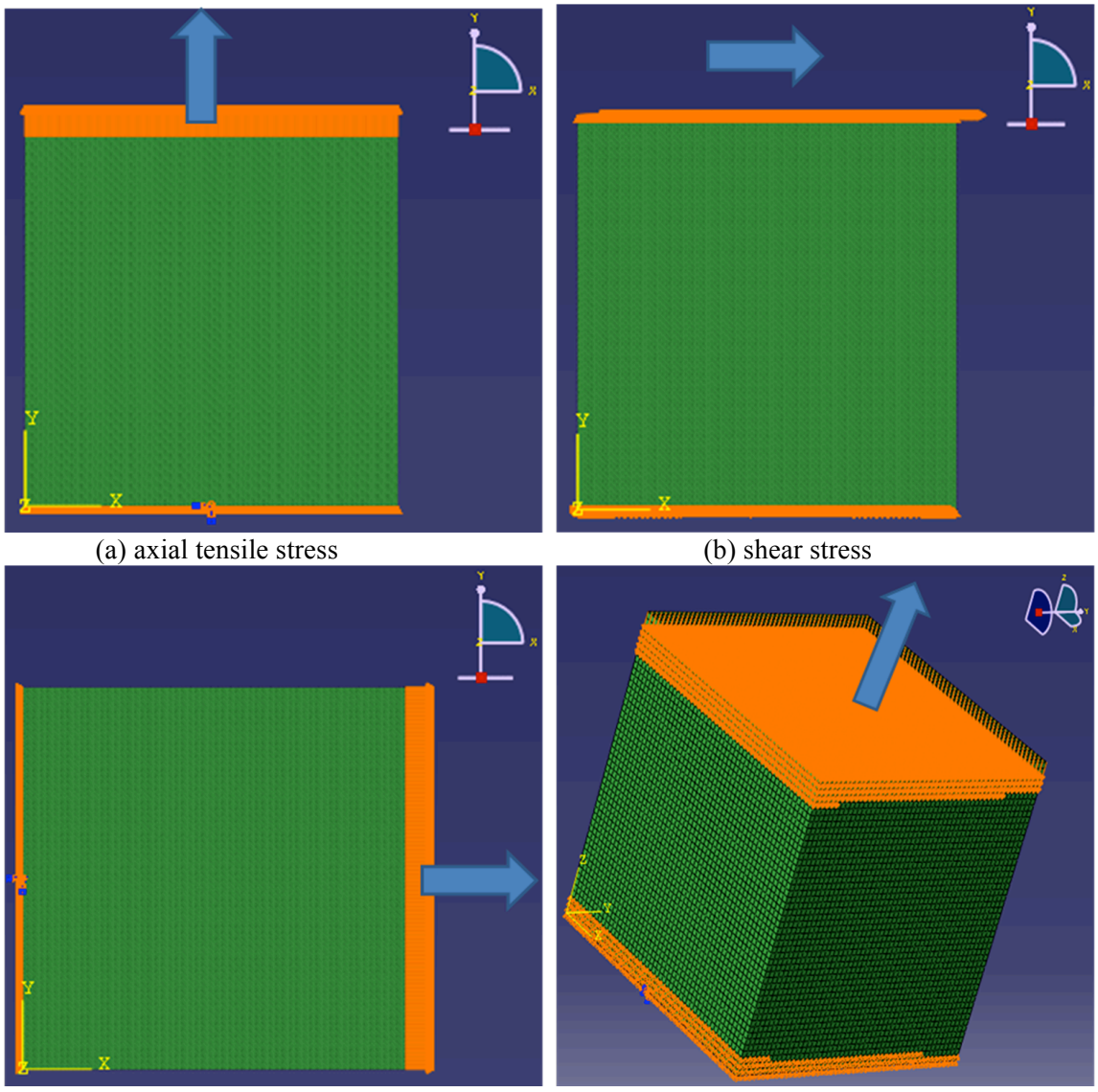

(a) axial tensile stress (b) shear stress

(c) transverse tensile stress (d) axial tensile stress in 3D

Figure 16. Boundary conditions used in the two- and three-dimensional cases

5.1.3 Optimal Mesh Density

Since our approximation of the spheroidite microstructure is based on a quadrilateral mesh, the only way to guarantee a Gaussian normal distribution for the size of spherical particles is to set the minimum mesh density above a certain number, in this case, 4. Using various mesh densities, the Matlab code is able to place pseudo-circular particles randomly in a $600 \times 600\ \mu m^2$ sample space. Although this approximation remains quite rough, as a trade-off, the 2D models can be handled with a standard personal computer with ease.

In order to verify the accuracy of the results with mesh density equal to 4, the same model was refined by increasing the mesh density up to 7. On a side note, regarding the extraction of mechanical property data, the stress values are determined by summing the directional component of the reaction forces along the edges (surfaces in 3D) and then dividing the summation with the length (area in 3D) over which the stress is applied. The strain is computed based on the displacement at each step interval. The Poisson's ratio is then figured out by dividing the average strain along the direction of the applied stress by that in the other directions perpendicular to the applied stress after each step interval. The simulation results imply that the stress-strain curves obtained using different densities (>4) are very similar as in Figure 17 and the resulted von Mises stress and logarithmic strain distributions within the model are almost identical in all the cases, as shown in Figure 18. The parameters and result data are provided in Tables 8 and 9.

For practical purposes, using a mesh density equal to 4 does not affect the accuracy of the analysis results, while costing significantly less time. Therefore, a mesh density of 4 will be assumed in all the following cases.

Table 8. Simulation parameters for mesh density comparison (axial tension)

Parameters	Sample size	Stress type	Volume fraction of cementite	Average particle diameter (μm)	Volume fraction of voids	Element type	Total strain
Mesh density of 4	600 × 600 μm^2	axial tension	6.67%	2.14	0.000001%	linear plane strain	0.006
Mesh density of 5	600 × 600 μm^2	axial tension	6.67%	2.14	0.000001%	linear plane stress	0.006
Mesh density of 6	600 × 600 μm^2	axial tension	6.67%	2.14	0.000001%	linear plane stress	0.006
Mesh density of 7	600 × 600 μm^2	axial tension	6.67%	2.14	0.000001%	linear plane stress	0.006

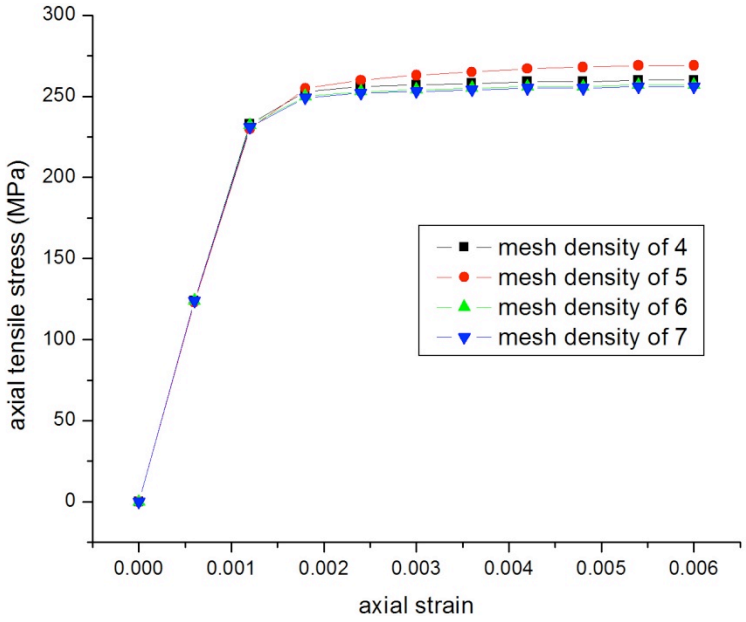

Figure 17. Comparison of the stress-strain curves obtained under axial tension using different mesh densities

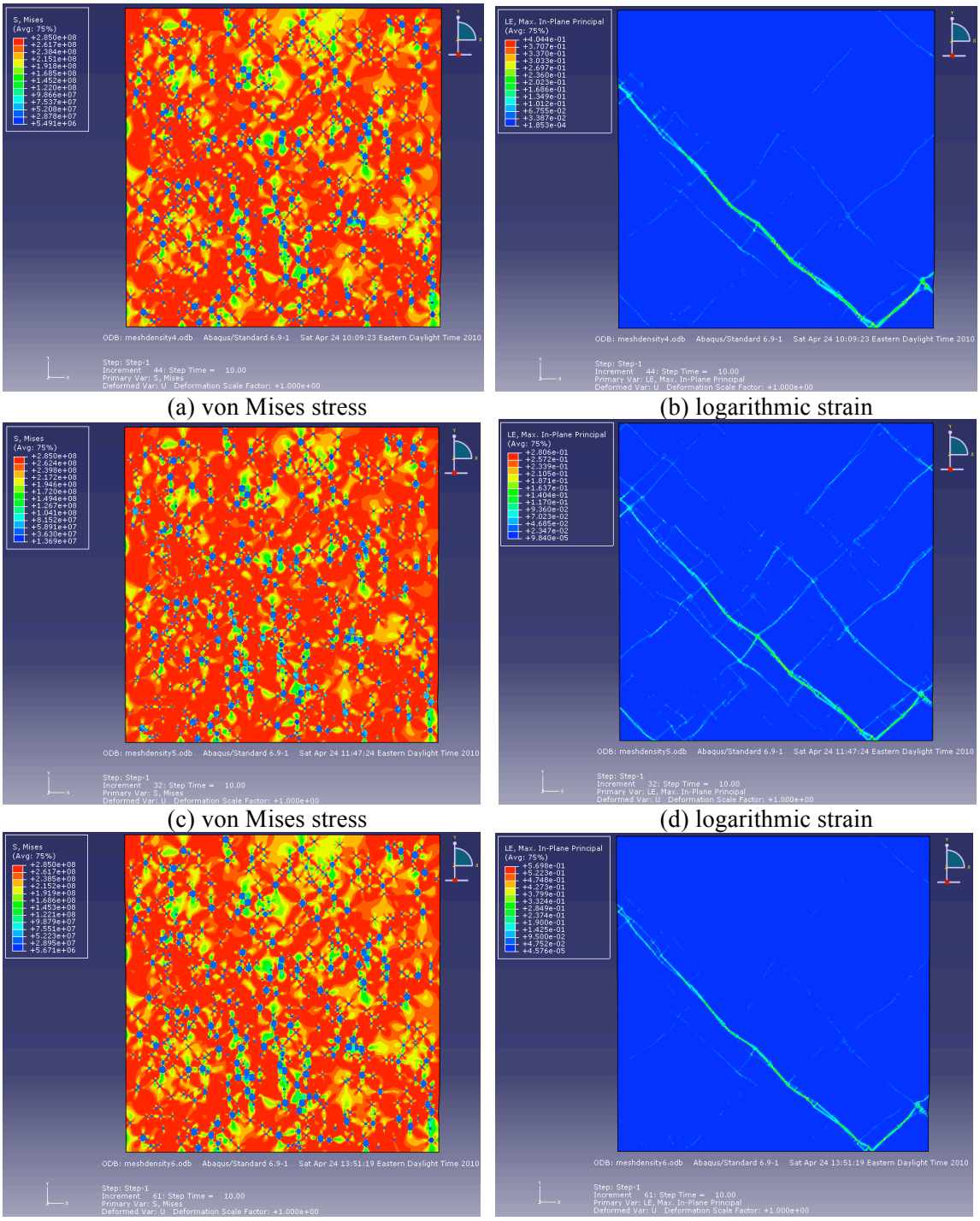

(a) von Mises stress (b) logarithmic strain

(c) von Mises stress (d) logarithmic strain

(e) von Mises stress (f) logarithmic strain

Figure 18. Final von Mises stress and logarithmic strain pattern for a material sample under maximum 0.6% axial tensile strain using mesh density of (a) and (b) 4, (c) and (d) 5, (e) and (f) 6 and (g) and (h) 7

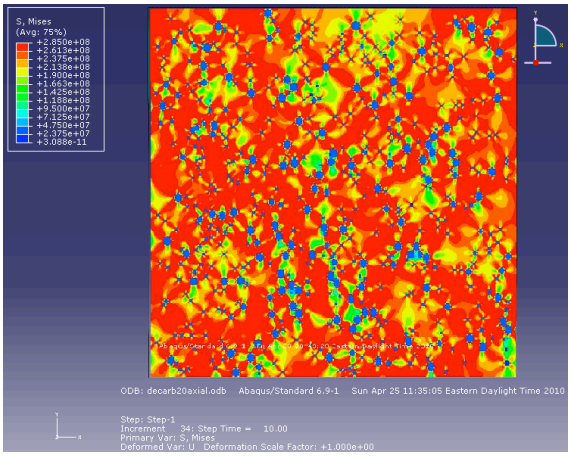

(g) von Mises stress

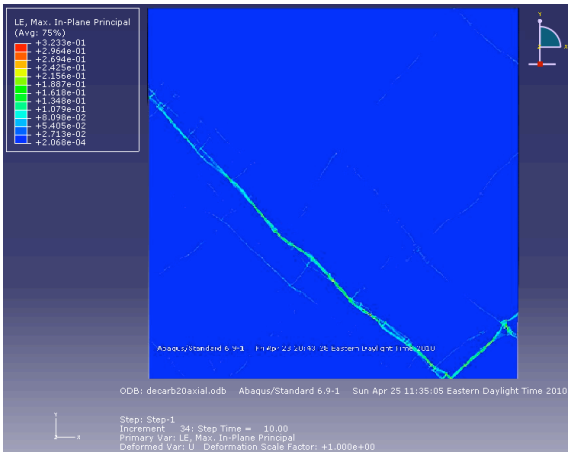

(h) logarithmic strain

Figure 18 continued

Table 9. Simulation results of mesh density convergence test

Mechanical properties	Young's modulus (GPa)	σ_y (MPa) - yield strength
Mesh density at 4	194.385	260.244
Mesh density at 5	191.687	269.296
Mesh density at 6	192.925	257.255
Mesh density at 7	196.218	256.919

The choice of von Mises stress deserves further elaboration here: using different mesh densities, shown in Figure 18 are the resulted final von Mises stress distributions, which is the most popular choice when it comes to delineating the elasto-perfectly plastic deformation of ductile material placed in an equilibrium loading environment, a description fitting for the scenario in this incidence. The von Mises yield criterion, developed based on the definition of von Mises stress, suggests that the yielding of materials begins when the second deviatoric stress invariant J_2 reaches the critical value, as shown in Figure 19.

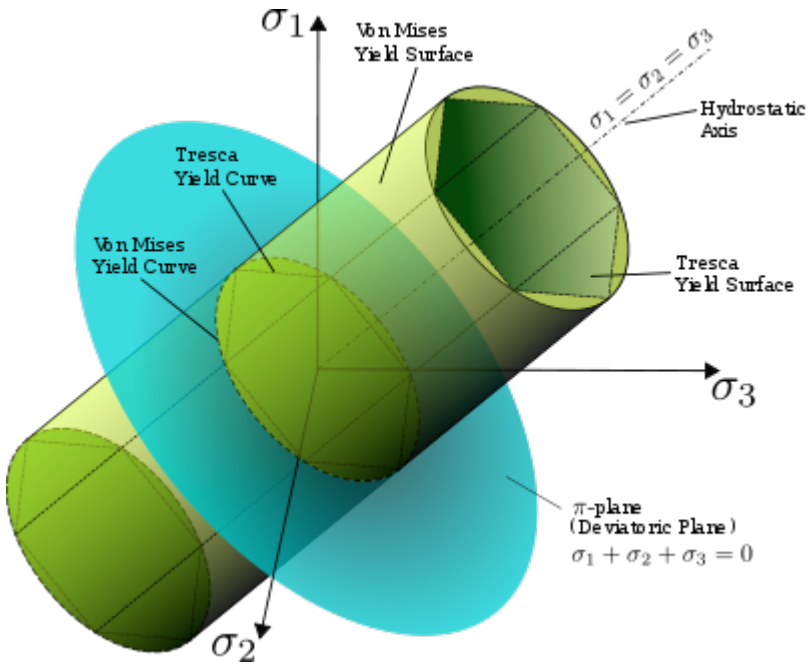

Figure 19. Illustration of von Mises yield criterion (cylindrical yield surface) and Tresca yield criterion (hexagonal yield surface) [46]

The deviatoric stress invariants are a set of invariants defined by subtracting the hydrostatic tensor λ from the stress tensor, as in Equations 14 and 15.

$$\begin{vmatrix} \sigma_{11} - \lambda & \sigma_{12} & \sigma_{13} \\ \sigma_{21} & \sigma_{22} - \lambda & \sigma_{23} \\ \sigma_{31} & \sigma_{32} & \sigma_{33} - \lambda \end{vmatrix} = 0 \qquad (14)$$

$$\lambda^3 - J_1\lambda^2 - J_2\lambda - J_3 = 0 \qquad (15)$$

Where J_1, J_2 and J_3 are the first, second and third deviatoric stress invariant, respectively; σ_{ij} is the stress tensor dependent on the coordinate system under consideration. If we choose a coordinate system with axes oriented towards the principal directions, the normal stresses will be the principal stresses and the stress tensor will regress into a diagonal matrix, as in Equation 16.

$$\begin{vmatrix} \sigma_1 & 0 & 0 \\ 0 & \sigma_2 & 0 \\ 0 & 0 & \sigma_3 \end{vmatrix} = \sigma_{ij} \qquad (16)$$

Mathematically, with the stress tensors in the three principal directions known, solving Equations 14, 15 and 16 will yield the expression for the second deviatoric stress invariant J_2 for von Mises yielding criterion, as displayed in Equation 17:

$$(\sigma_1 - \sigma_2)^2 + (\sigma_2 - \sigma_3)^2 + (\sigma_3 - \sigma_1)^2 = 6J_2 \qquad (17)$$

This equation encloses the von Mises yield surface whose yield curve, or intersection with the deviatoric yield surface, is a circular cylinder with radius $\sqrt{2J_2}$ as shown in Figure 19. This implies that the yield condition is independent of the hydrostatic stress λ, with J_2 solely dependent on the stress state. The von Mises stress is selected to describe the stress distribution in this case because all the materials involved in the analysis are assumed to be ductile, elasto-plastic and loaded in quasi-static conditions. An alternative criterion would be the Tresca stress criterion, which, however, sports a hexagonal cylinder-shaped deviatoric yield surface, instead of a circular cylinder. Rather than embody the synergistic effort of all three principal stresses, the Tresca stress emphasizes the maximum shear stress, as shown in Equation 18.

$$\max\left(|\sigma_1 - \sigma_2|, |\sigma_2 - \sigma_3|, |\sigma_3 - \sigma_1|\right) = \sigma_0 \qquad (18)$$

Observe in Figure 19 that the Tresca's yield surface is circumscribed by von Mises'. Therefore, it predicts plastic yielding already for stress states that are still elastic according to the von Mises criterion. As a model for plastic material behavior, Tresca's

criterion is consequently more conservative. More derivations and discussions on von Mises stress and Tresca stress are available in G. E. Dieter's Mechanical Metallurgy [47].

If somehow brittle materials become the object for similar FEM analysis, principal stress criterion needs to be considered for a more reliable judgment. Also, using the Ansys' featured “time” command enables special loading modes, including stepped loading, ramped loading among others.

5.1.4 Element Type Analysis

Once the optimal mesh density is determined in Section 5.1.3, the work moves on to finding out the most fitting FEM element to describe the mechanical behaviors of this system.

5.1.4.1 Linear plane stress vs. linear plane strain

In a two-dimensional case, the most conventional element choice would be linear plane strain and linear plane stress elements, code-named CPE4R (plane strain) and CPS4 (plane stress) in Abaqus. These two elements are the simplest 2D elements, both with four nodes in each element, as shown in Figure 20. Theoretically plane strain seems the anticipated choice as it deals with the scenarios in which the dimension of the structure in one direction, for instance the -z direction, is very large in comparison to the dimensions in the other two directions. In this particular work, no matter it is axial tensile stress, shear stress or transverse tensile stress being applied on the sample, it would be a baseless assertion to state that either of the two is the better option than the other one without testing. The actual sample material in question naturally is three-dimensional which for the time being we can only approach using the 2D elements due to the limited computing resources before segueing into the extra dimension. Therefore, out of discretion, a

comparison is made between the results obtained using the two elements, as well as the literature data.

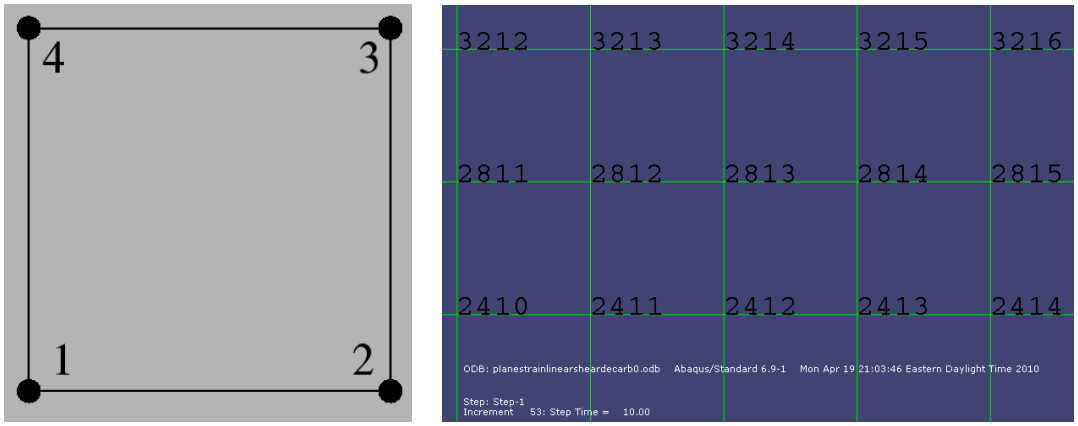

(a) element configuration (b) node-element connectivity

Figure 20. Linear plane strain and linear plane stress elements' configuration and node-element connectivity

The simulation results obtained with linear plane strain and linear plane stress elements under axial tensile stress are displayed in Figure 21. The simulation parameters are detailed in Table 10.

Table 10. Simulation parameters for linear plane strain and linear plane stress elements comparison (axial tension)

Parameters	Sample size	Stress type	Volume fraction of cementite	Average particle diameter (μm)	Volume fraction of voids	**Element type**	Total strain
Values	600 × 600 μm^2	axial tension	6.67%	2.14	0.000001%	**linear plane strain**	0.006
Values	600 × 600 μm^2	axial tension	6.67%	2.14	0.000001%	**linear plane stress**	0.006

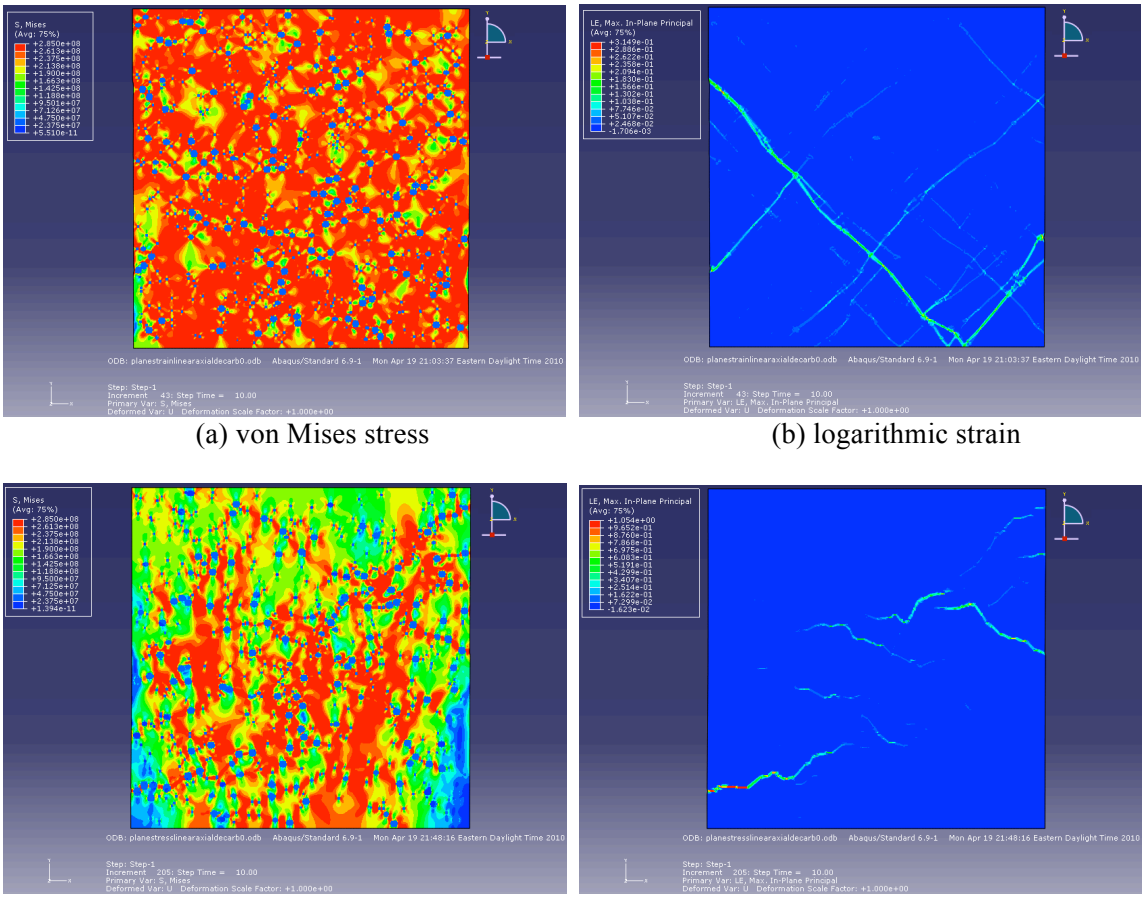

(a) von Mises stress (b) logarithmic strain

(c) von Mises stress (d) logarithmic strain

Figure 21. Final von Mises stress and logarithmic strain patterns for a material sample under maximum 0.6% axial tensile strain using (a) and (b) linear plane strain element and (c) and (d) linear plane stress element

Figure 22 shows the two axial tension stress-strain curves obtained using the two types of elements. The simulation parameters for the shear stress case using the two elements are listed in Table 11 and the results are shown in Figure 23. The comparison of the corresponding shear stress-strain curves is provided in Figure 24 and Table 12.

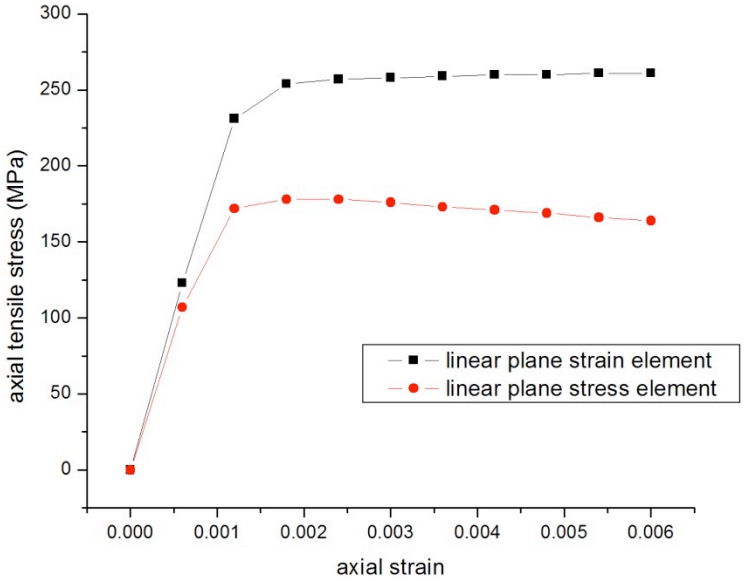

Figure 22. Comparison of the stress-strain curves obtained under axial tension using linear plane strain and linear plane stress elements

Table 11. Simulation parameters for linear plane strain and linear plane stress elements comparison (shear stress)

Parameters	Sample size	Stress type	Volume fraction of cementite	Average particle diameter (μm)	Volume fraction of voids	**Element type**	Total strain
Values	600 × 600 μm^2	shear	6.67%	2.14	0.000001%	**linear plane strain**	0.006
Values	600 × 600 μm^2	shear	6.67%	2.14	0.000001%	**linear plane stress**	0.006

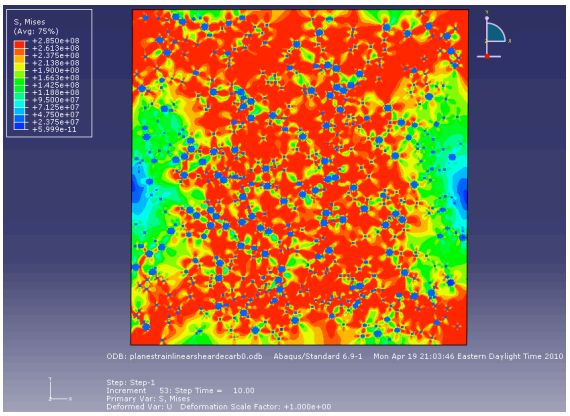

(a) von Mises stress

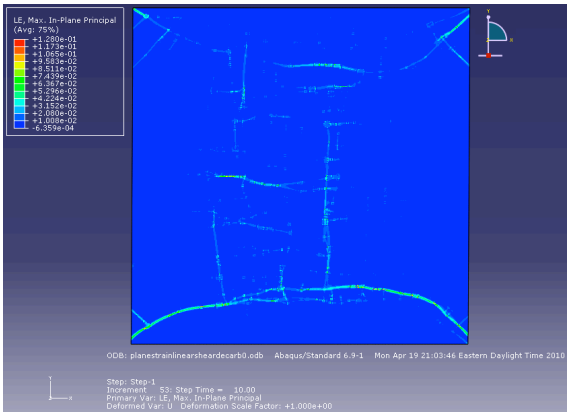

(b) logarithmic strain

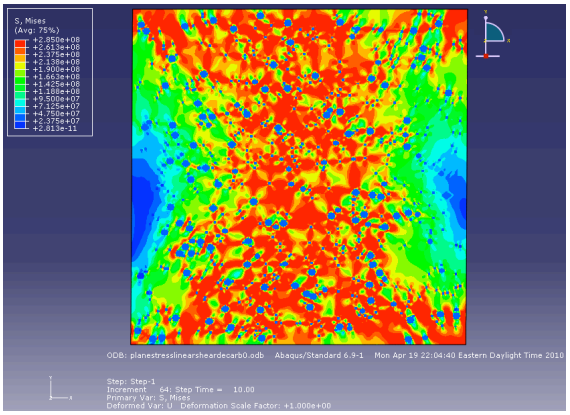

(c) von Mises stress

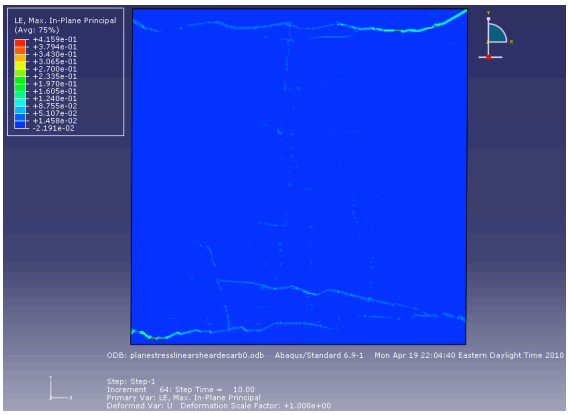

(d) logarithmic strain

Figure 23. Final von Mises stress and logarithmic strain distribution patterns for a material sample under maximum 0.6% shear strain using (a) and (b) linear plane strain element and (c) and (d) linear plane stress element

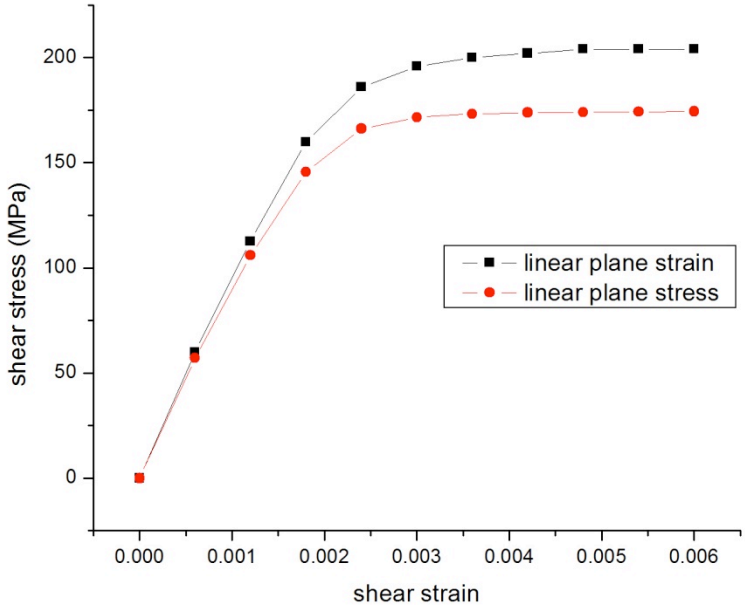

Figure 24. Comparison of the stress-strain curves obtained under shear stress using linear plane strain and linear plane stress elements

Table 12. Simulation results for linear plane strain and linear plane stress elements comparison (shear stress)

Mechanical property	Young's modulus (GPa)	σ_y (MPa) - axial tension	Shear modulus (GPa)	σ_y (MPa) - shear	Poisson's ratio
Plane strain	208.235	261	88.70	209.724	0.2738
plane stress	143.48	166	80.933	174.452	
Literature	~211	~250	~80	~200	~0.29

It is clear that the results acquired using linear plane strain element are much closer to the literature value, as listed in Table 12 [45, 48-50], than those obtained using linear plane stress element: the literature puts the Young's modulus of spheroidite steel at 200 GPa and beyond, depending on the specific carbon content. The Young's modulus gauged using plane strain element is at 208.2 GPa as opposed to 143.5 GPa, the modulus computed using plane stress element; as seen in Figure 21, the logarithmic strain patterns resulted from using the linear plane stress elements display worm-like configurations, very much unlike the expected 45º strain localization that the linear plane strain elements exhibit; in addition, the computing time for a model featuring plane strain element (approximately 40 minutes by a computer with 12 gigabyte memory) is much shorter

than that for one of the same size but using plane stress element (more than 3 hours). All the aforementioned reasons contributed to the decision of choosing plane strain element over plane stress element in the following analyses.

5.1.4.2 Linear element vs. quadratic element

In section 5.1.4.1 the results from linear plane strain and linear plane stress element are compared, with the former emerging as our choice element. To further consolidate this choice, we proceeded to test the quadratic elements in plane strain and plane stress states, to be more specific, CPE8 (plane strain) and CPS8 (plane stress) in Abaqus, element configuration and nodal connectivity shown in Figure 25.

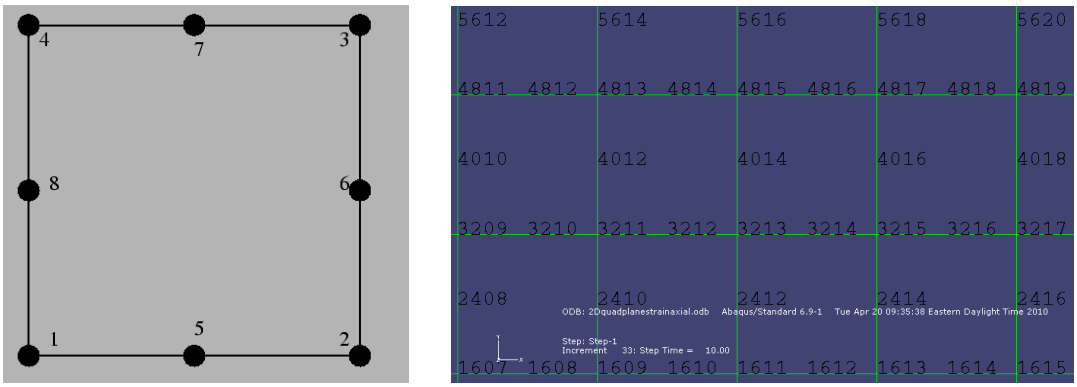

(a) element configuration (b) node-element connectivity

Figure 25. Quadratic plane strain and quadratic plane stress elements' configuration and node-element connectivity

Similar to the cases in Section 5.1.4.1, the plane strain and plane stress quadratic elements have the same configuration. The parameters used to perform this simulation are given in Table 13. The results computed with quadratic plane strain and quadratic plane stress element under axial tension are seen in Figure 26, including the final von Mises stress patterns and logarithmic strain distributions.

Table 13. Simulation parameters for quadratic plane strain and quadratic plane stress elements comparison

Parameters	Sample size	Stress type	Volume fraction of cementite	Average particle diameter (μm)	Volume fraction of voids	**Element type**	Total strain
Values	600 × 600 μm^2	axial tension	6.67%	2.14	0.000001 %	**quadratic plane strain**	0.006
Values	600 × 600 μm^2	axial tension	6.67%	2.14	0.000001 %	**quadratic plane stress**	0.006

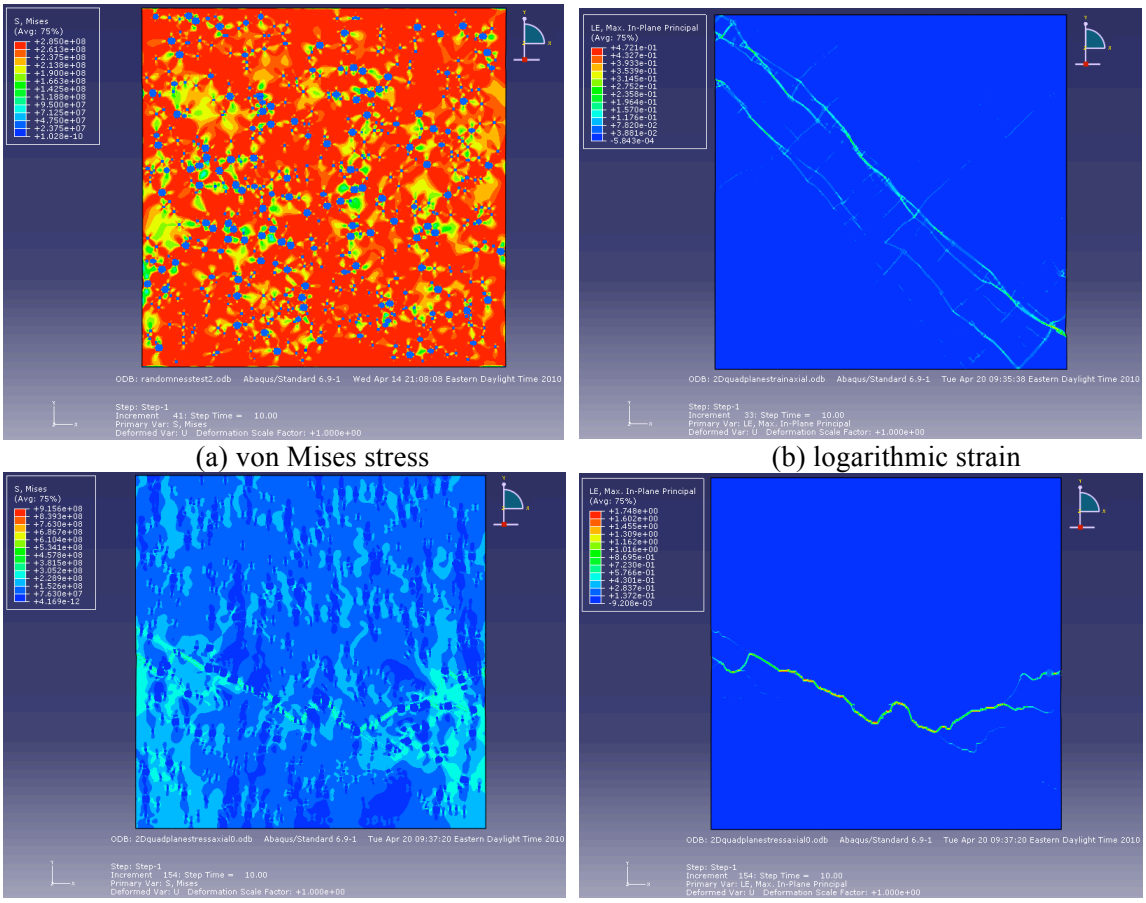

(a) von Mises stress (b) logarithmic strain

(c) von Mises stress (d) logarithmic strain

Figure 26. Final von Mises stress patterns and logarithmic strain distributions for a material sample under maximum 0.6% axial tensile strain using (a) and (b) quadratic plane strain element and (c) and (d) quadratic plane stress element

Figure 27 compares the axial stress-strain curves obtained using the two quadratic plane elements. Then the shear stress scenario is also examined using the two elements, with the resulted von Mises stress and logarithmic strain distributions given in Figure 28 and parameters shown in Table 14.

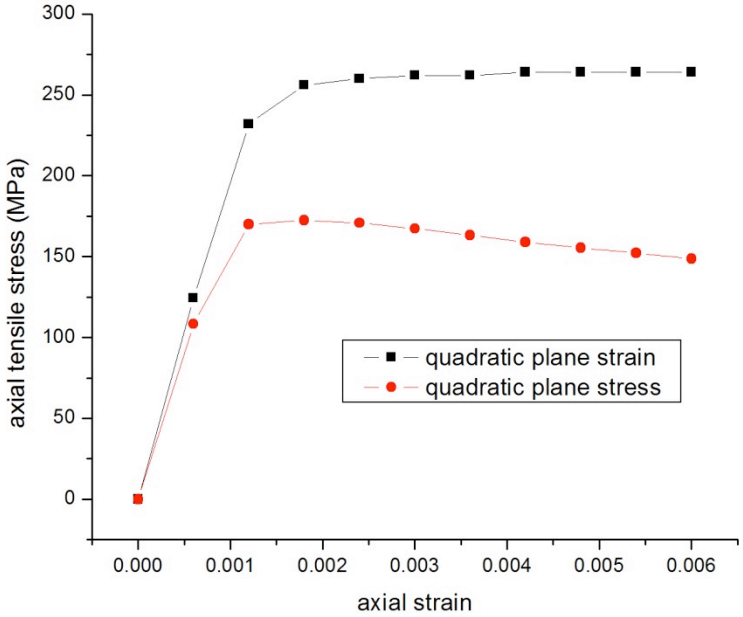

Figure 27. Comparison of the stress-strain curves obtained under axial tensile stress using quadratic plane strain and quadratic plane stress element

Table 14. Simulation parameters for quadratic plane strain and quadratic plane stress elements comparison

Parameters	Sample size	Stress type	Volume fraction of cementite	Average particle diameter (μm)	Volume fraction of voids	**Element type**	Total strain
Values	600 × 600 μm^2	shear	6.67%	2.14	0.000001%	**quadratic plane strain**	0.006
Values	600 × 600 μm^2	shear	6.67%	2.14	0.000001%	**quadratic plane stress**	0.006

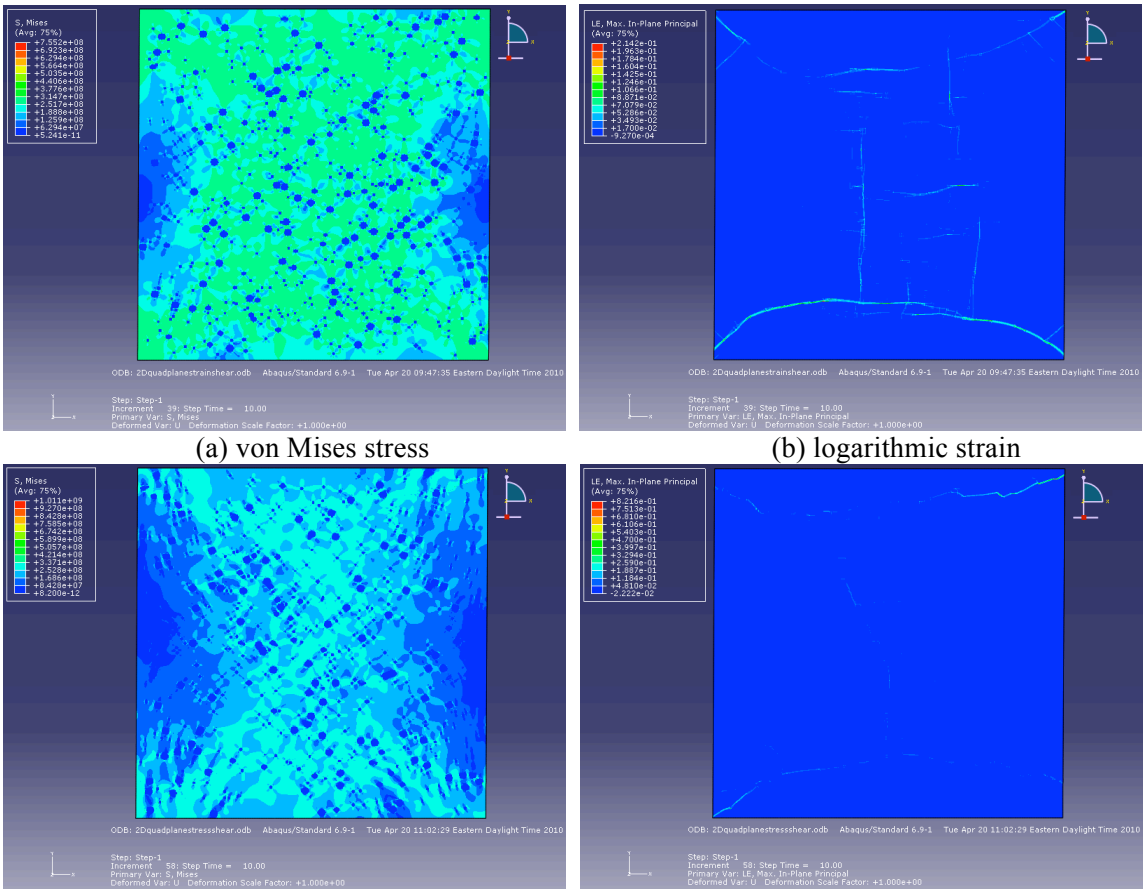

(a) von Mises stress (b) logarithmic strain

(c) von Mises stress (d) logarithmic strain

Figure 28. Final von Mises stress and logarithmic strain distribution pattern for a material sample under maximum 0.6% shear strain using (a) and (b) quadratic plane strain element and (c) and (d) quadratic plane stress element

Similarly, the resulted stress-strain curves are shown in Figure 29 for comparison.

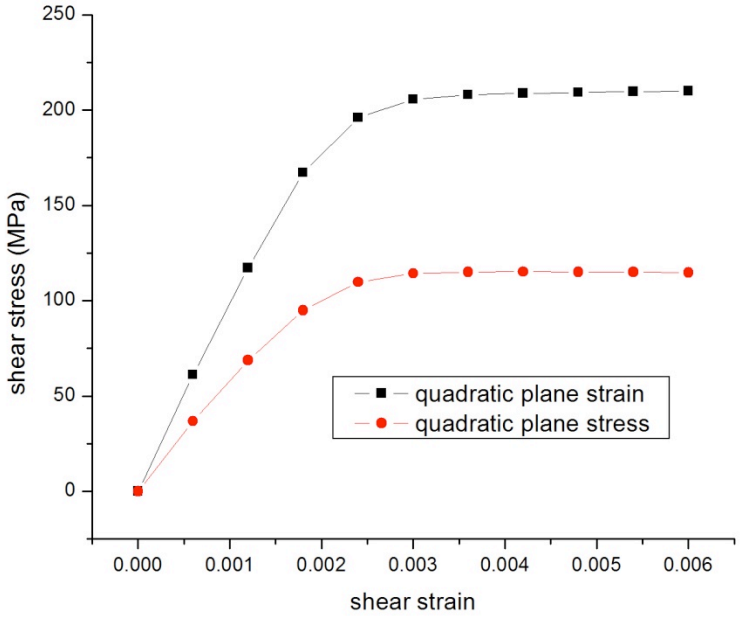

Figure 29. Comparison of the stress-strain curves obtained under shear stress using quadratic plane strain and quadratic plane stress elements

The results from using quadratic plane strain and quadratic plane stress element are compared in Table 15. Further comparisons with data obtained with linear plane strain are available in Figure 30, along with Tables 15 and 16, where it can be concluded that while the results calculated using quadratic plane strain element are very close to those yielded by using linear plane strain element, as well as the literature data, those acquired with quadratic plane stress element are far off of the acceptable range.

Table 15. Comparison between the results from quadratic plane strain and quadratic plane stress element with literature data

Mechanical properties	Young's modulus (GPa)	σ_y (MPa) - axial tension	Shear modulus (GPa)	σ_y (MPa) - shear	Poisson's ratio
Quadratic plane strain	208.666	264.028	92.933	211.064	0.12
Quadratic plane stress	145.933	148.651	52.833	91.824	0.381
Literature	~200	~250	~82	~200	~0.29

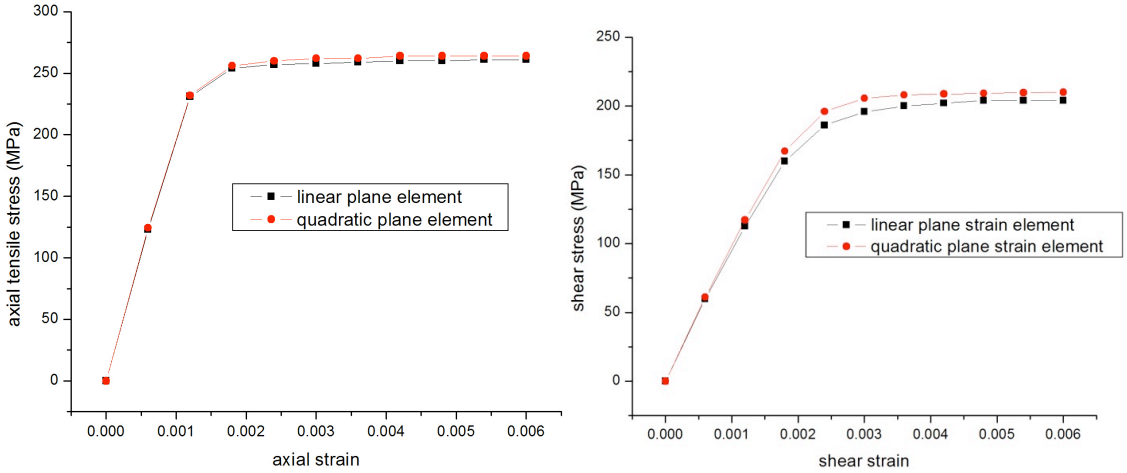

(a) axial tensile stress-strain curve (b) shear stress-strain curve

Figure 30. Comparison of the stress-strain curves obtained under axial tensile and shear stress using linear plane strain and quadratic plane strain elements

Table 16. Comparison between the results from linear plane strain and quadratic plane strain element with literature data

Mechanical properties	Young's modulus (GPa)	σ_y (MPa) - axial tension	Shear modulus (GPa)	σ_y (MPa) - shear	Poisson's ratio
Linear plane strain	208.235	261	88.70	209.724	0.2738
Quadratic plane strain	208.666	264	92.933	211.064	0.26
Literature	~200	~250	~82	~200	~0.29

The results from using the linear plane strain and quadratic plane strain elements basically land 10% within each other and both are very comparable to the literature data, implying that results achieved with either are valid. The mid-side nodes on the edges of the elements enable the models featuring the quadratic elements to describe bending and warpage effectively but since only tension and shear stress are involved in this case, quadratic element was deemed unnecessary. Also, the calculations involving quadratic elements are significantly more time-consuming: it typically takes 7 hours to run a 2-D quadratic model of 600 × 600 μm^2, as opposed to less than one hour using linear plane strain element of the same size with the same mesh density.

All the simulations in the upcoming sections were performed using linear plane strain element unless otherwise noted.

5.1.5 Computing Time Estimate

Having determined the optimal mesh density in Section 5.1.3, the work goes on to analyze the cases with four different sizes with the purpose of finding out the sample space size that is the most representative and that takes only manageable amount of time to compute. The parameters used are listed in Table 17.

Table 17. Simulation parameters

Average diameter of the spheres	2.14 μm
Mesh density	4 pixel/μm
Spheres' volume fraction	6.67%
Cavity void volume fraction	0.000001%

Cavities and voids with a volume fraction of approximately 0.0000001% are included as defects to approximate the actual scenario and reserved for more extensive analysis in Section 5.1.10.

The four different sample sizes being tested vary from 300 × 300 μm^2 to 600 × 600 μm^2, 1200 × 1200 μm^2 and 1800 × 1800 μm^2. The total calculation time of each scenario, including both geometry generation and model computing, is specified in Table 18.

Table 18. Comparison of the time consumed with different sample sizes

	Geometry generation (min)	FEM analysis (min)	Total (min)
300 × 300 μm^2	1	5	6
600 × 600 μm^2	11	30	41
1200 × 1200 μm^2	48	~180	~228
1800 × 1800 μm^2	116	~420	~536

Out of the consideration both for time and sample representativeness, the following analyses will be done using a sample size of 600 × 600 μm^2 unless noted otherwise.

5.1.6 Randomness Test

Multiple tests have been conducted to confirm that the system's properties of the sample simulated do not change notably with the various random distributions by which the cementite particles are placed in the sample space. The calculated final von Mises stress patterns and logarithmic strain distributions are plotted in Figure 31 and the parameters involved are listed in Table 19.

Table 19. Simulation parameters for randomness comparison

Parameters	Sample size	Stress type	Volume fraction of cementite	Average particle diameter (μm)	Volume fraction of voids	Element type	Total strain
values	600 × 600 μm^2	axial tension	6.67%	2.14	0.000001%	linear plane strain	0.006

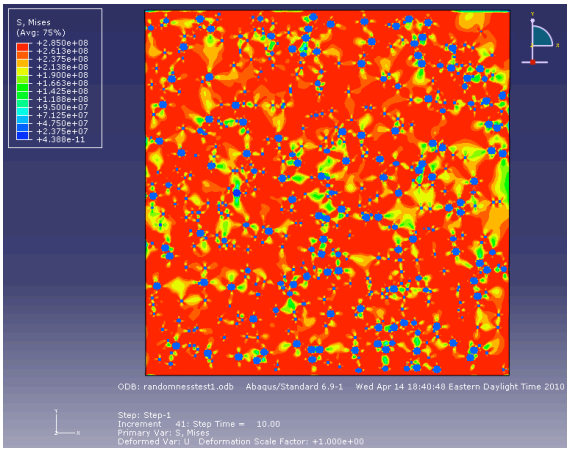

(a) von Mises stress

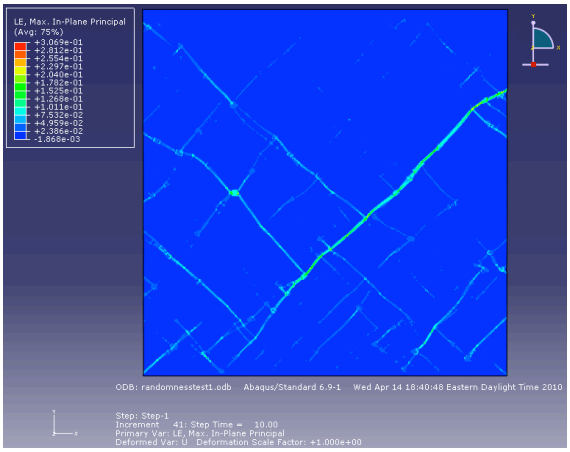

(b) logarithmic strain

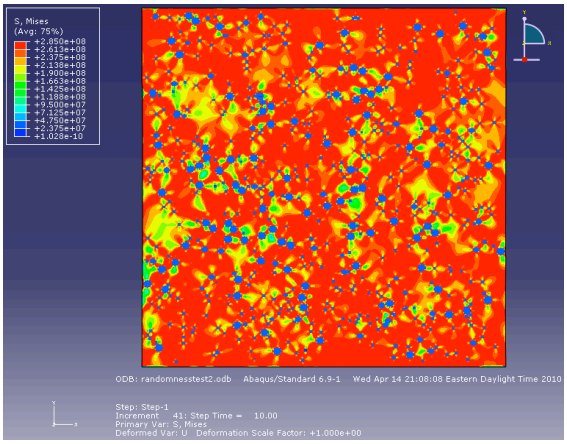

(c) von Mises stress

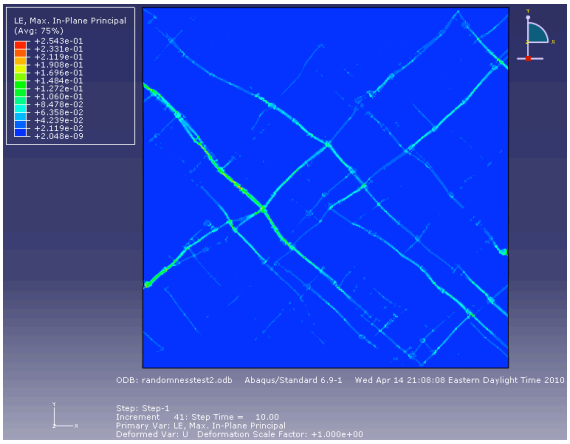

(d) logarithmic strain

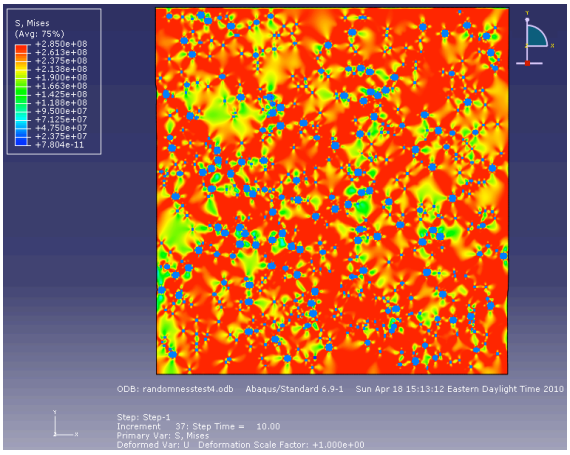

(e) von Mises stress

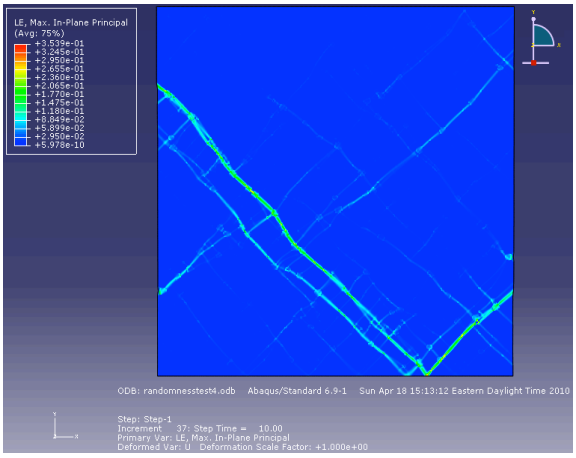

(f) logarithmic strain

Figure 31. Final von Mises stress and logarithmic strain distribution patterns for a material sample under maximum 0.6% axial tensile strain following (a) and (b) random distribution 1 (c) and (d) random distribution 2 (e) and (f) random distribution 3

The resulted stress-strain curves can be found in Figure 32.

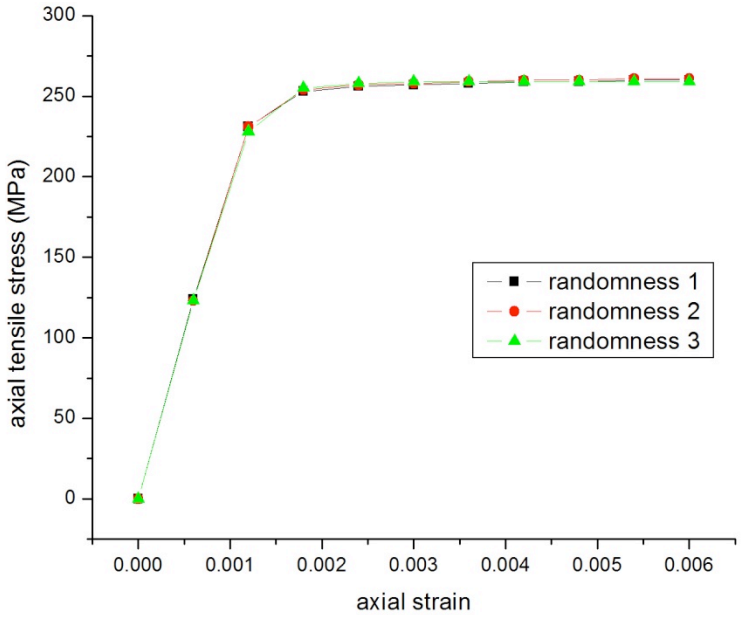

Figure 32. Comparison of the stress-strain curves obtained under axial tensile stress using three different random distributions for the spherical cementite particles

As shown in Figure 32, the three distributions result in practically identical stress-strain curves despite the dissimilar initial microstructures, which leads to the natural conclusion that the macroscopic properties of the sample will not change appreciably in spite of the particle distribution variation, as long as the total volume fraction and average particle size remain the same. However, the randomness test is performed only with this specific set of parameters. As the work proceeds, in the following analyses associated with larger particles and higher volume fraction, the axial tensile and shear behaviors are analyzed using the same configuration. Table 20 has the data results.

Table 20. Simulation results for randomness comparison

Mechanical properties	Young's modulus (GPa)	σ_y (MPa) - axial tension	Shear modulus (GPa)	σ_y (MPa) - shear	Poisson's ratio
Randomness1	208.235	261	88.70	209.724	0.2738
Randomness2	207.343	261	80.02	201.105	0.2755
Randomness3	208.329	260	79.93	200.985	0.2731
Experiment	~200	~250	~80	~200	~0.29

5.1.7 Axial Tension and Transverse Tension Comparison

For this simulation, the materials in study are assumed to be isotropic. Therefore, in theory the axial tensile stress and transverse tensile stress should yield the same results. However, in order to achieve maximum accuracy, this assumption cannot be taken for granted and two cases involved axial tensile stress and transverse tensile stress are analyzed and compared, with the simulation parameters listed in Table 21, the final von Mises stress patterns and the logarithmic strain distributions shown in Figure 33 and the corresponding stress-strain curves in Figure 34.

Table 21. Simulation parameters for axial tension and transverse tension comparison

Parameters	Sample size	**Stress type**	Volume fraction of cementite	Average particle diameter (μm)	Volume fraction of voids	Element type	Total strain
Values	600 × 600 μm^2	**axial tensile stress**	6.67%	2.14	0.000001%	linear plane strain	0.006
Values	600 × 600 μm^2	**transverse tensile stress**	6.67%	2.14	0.000001%	linear plane strain	0.006

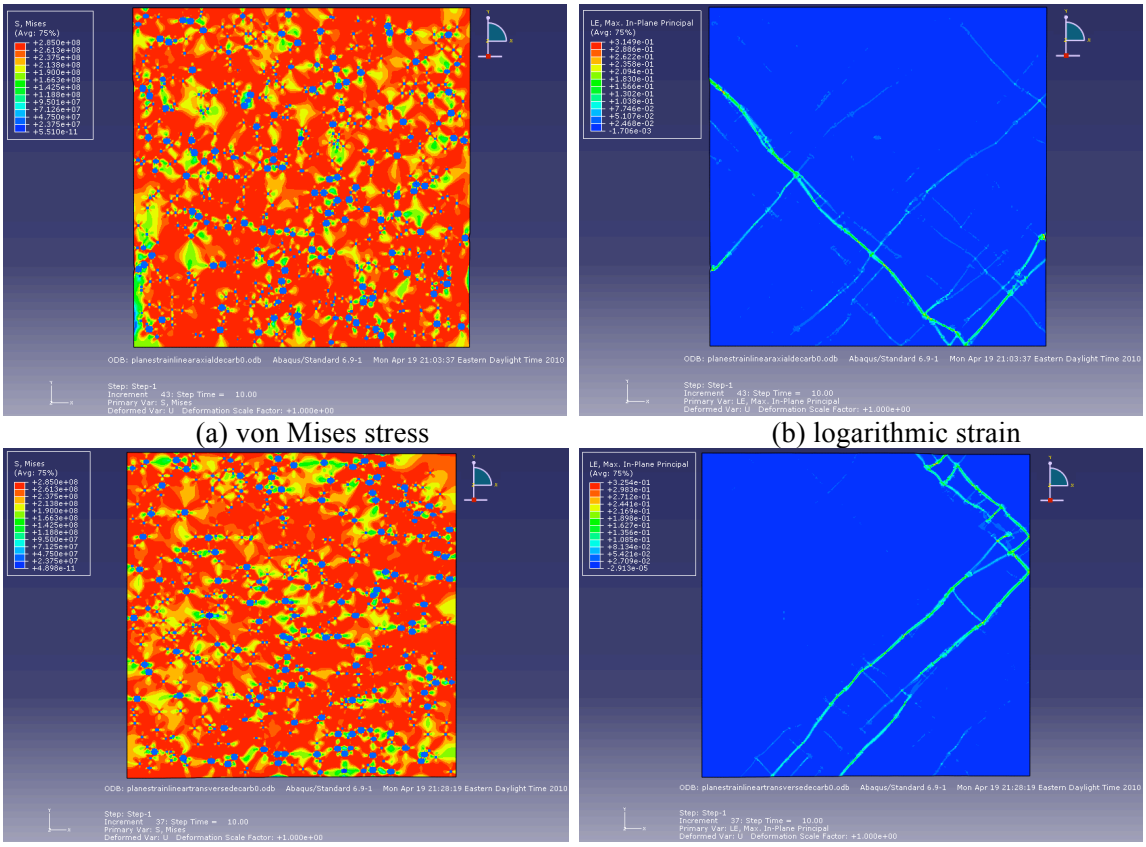

(a) von Mises stress (b) logarithmic strain

(c) von Mises stress (d) logarithmic strain

Figure 33. Final von Mises stress and logarithmic strain distribution patterns for a material sample under maximum 0.6% axial tensile strain using (a) and (b) axial tensile stress (c) and (d) transverse tensile stress

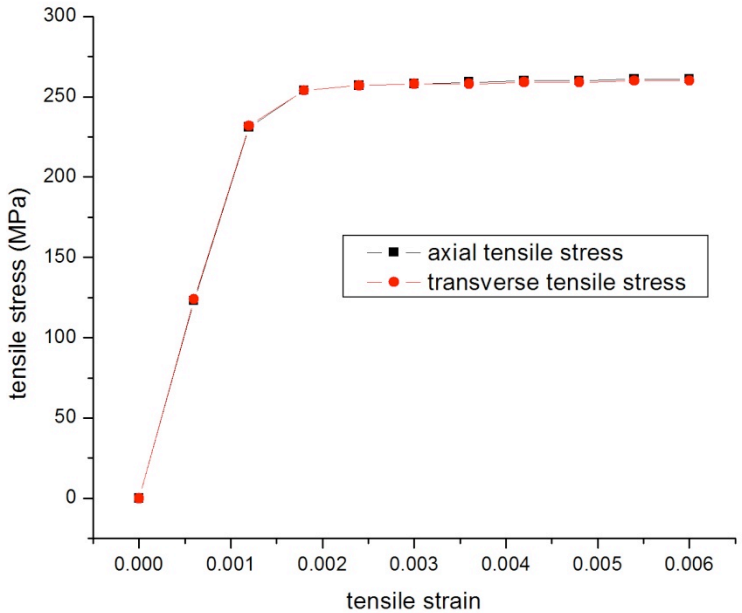

Figure 34. Comparison of the stress-strain curves obtained under axial tensile stress and transverse tensile stress

Although the 45º strain localizations in Figure 33(b) and (d) protract perpendicularly to each other, as is clearly demonstrated in Figure 34, the two stress-strain curves generated under axial tensile stress and transverse tensile stress take essentially the same shape, which is expected because the materials are assumed to be isotropic. This conclusion is further consolidated by the numbers compiled in Table 22.

Table 22. Simulation results for axial tension and transverse tension comparison

Mechanical properties	Young's modulus (GPa)	σ_y (MPa) - axial tension
Axial tensile stress	208.235	261
Transverse tensile stress	208.335	260
Literature	~200	~250

Therefore, in the following cases, the transverse tensile stress analysis is not specifically singled out due to the isotropic nature of the materials involved, except for the decarburization analysis section where the anisotropy needs to be considered for the obvious reasons (decarburization zones engendered at the surfaces break the isotropy).

5.1.8 Second Phase Particle Size

It is previously stated in Section 2.5 that the size distribution of the spherical cementite particles follows the Gaussian normal distribution function as in Equation 3. While keeping the total particle volume fraction constant, the average diameter of the cementite particles is increased from 2.14 μm to 4.28 μm (double), and then 8.56 μm (quadruple). Because in actuality, the average particle size distribution in spheroidite spans rather narrowly, instead of increasing it to an impractical value, only three different sizes are tested. In Figure 35, the final von Mises stress patterns and the logarithmic strain distributions are provided and parameters specified in Table 23.

Table 23. Simulation parameters for average particle size comparison (tensile stress)

Parameters	Sample size	Stress type	Volume fraction of cementite	**Average particle diameter (μm)**	Volume fraction of voids	Element type	Total strain
Values	600 × 600 μm^2	axial tension	6.67%	**2.14**	0.000001%	linear plane strain	0.006
Values	600 × 600 μm^2	axial tension	6.67%	**4.28**	0.000001%	linear plane strain	0.006
Values	600 × 600 μm^2	axial tension	6.67%	**8.56**	0.000001%	linear plane strain	0.006

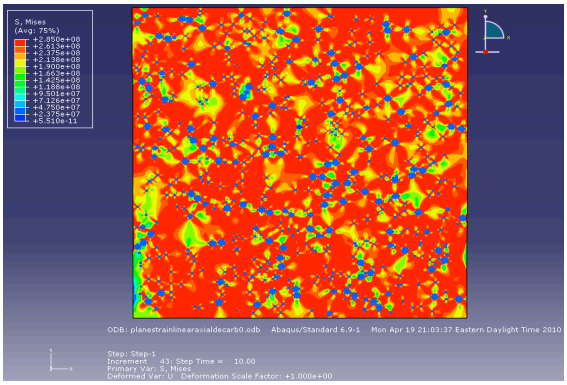

(a) von Mises stress

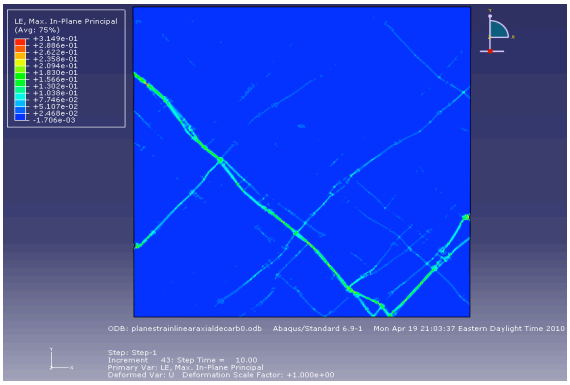

(b) logarithmic strain

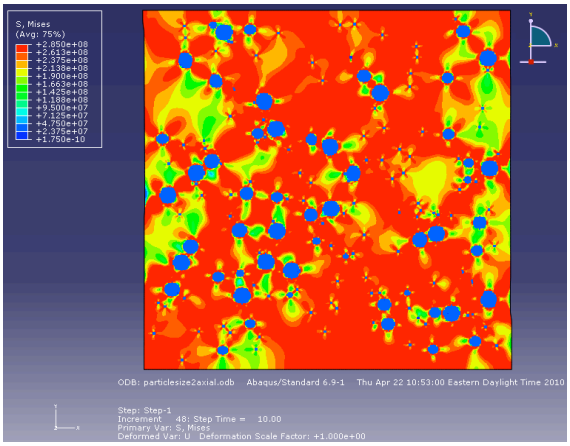

(c) von Mises stress

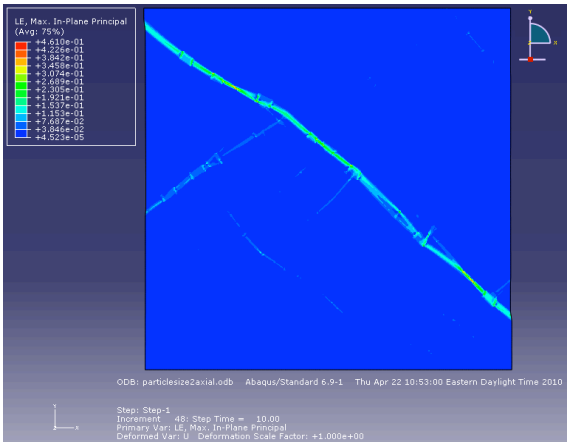

(d) logarithmic strain

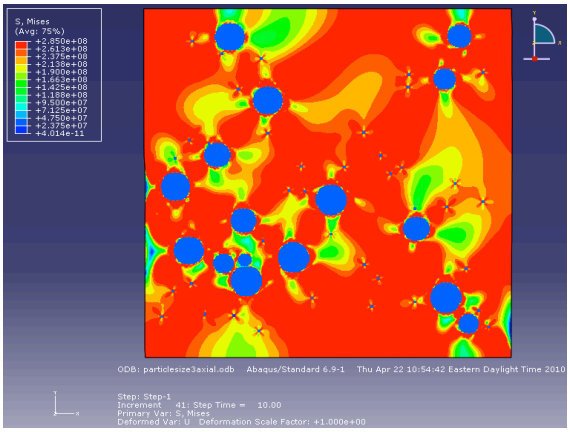

(e) von Mises stress

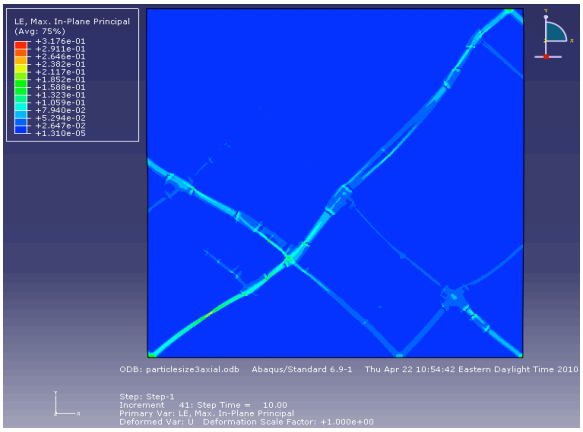

(f) logarithmic strain

Figure 35. Final von Mises stress and logarithmic strain distribution pattern for a material sample under maximum 0.6% axial tensile strain with (a) and (b) 2.14 µm average particle size (c) and (d) 4.28 µm average particle size (e) and (f) 8.56 µm average particle size

The increasing sphere size results in more concentrated strain localization. In Figure 35, it can be observed that when the average particle size is at 2.14 µm, there are

many secondary even tertiary branches intersecting with the primary strain localization; once the particle size increases, the smaller branches start to diminish, allowing the remaining stress concentration centers to become more prominent. The corresponding stress-strain curves are shown in Figure 36, where it is easy to see that the curve generated using the smallest average particle size has the highest Young's modulus and yield strength and, as the average particle size increases, the mechanical properties decrease significantly. This observation is well backed up by the theory of precipitation hardening, which is a heat treatment technique utilized to enhance the yield strengths of metals and metallic alloys, in the sense that second-phase particles, such as a proper amount of carbide (Fe_3C in this case), or intermetallic compounds, are precipitated from a supersaturated solid solution in the alloy at the grain boundaries and pin the dislocations. The smaller the second phase particles are, the more effectively they hinder the dislocation motion, therefore enhancing the overall mechanical strength of the system [51]. The final von Mises stress patterns, logarithmic strain distributions and stress-strain curves by the applied shear stress using different particle sizes are presented in Figures 37 and 38.

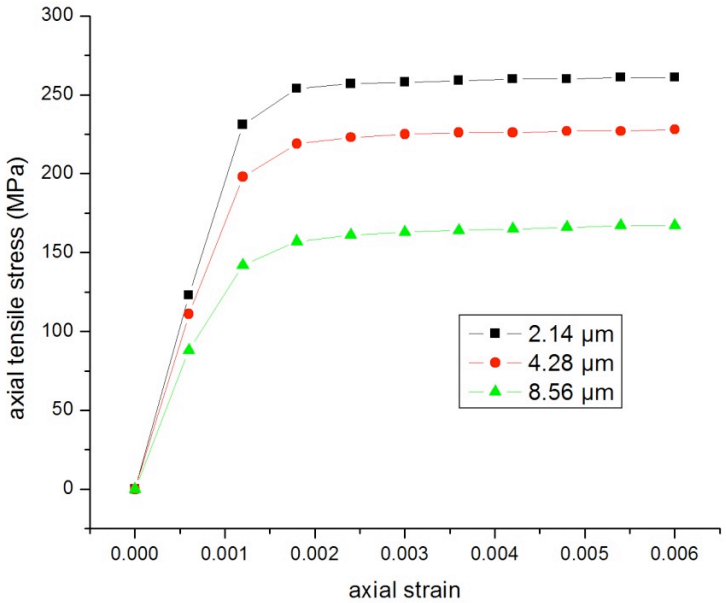

Figure 36. Comparison of the stress-strain curves obtained under axial tensile stress using spherical cementite particles of three different average particle sizes

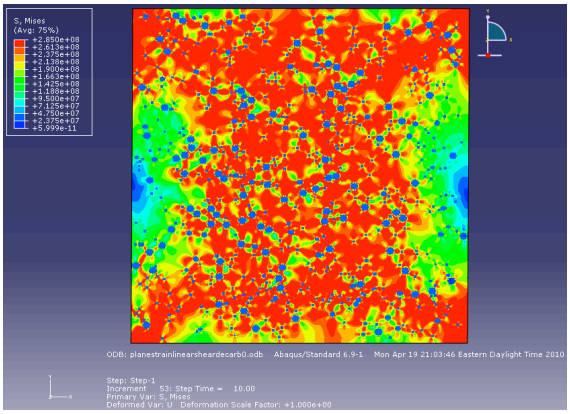

(a) von Mises stress

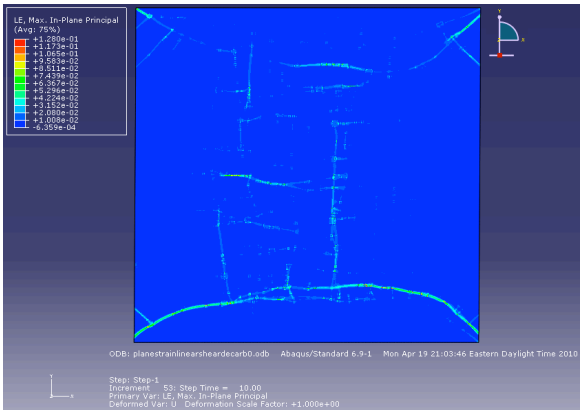

(b) logarithmic strain

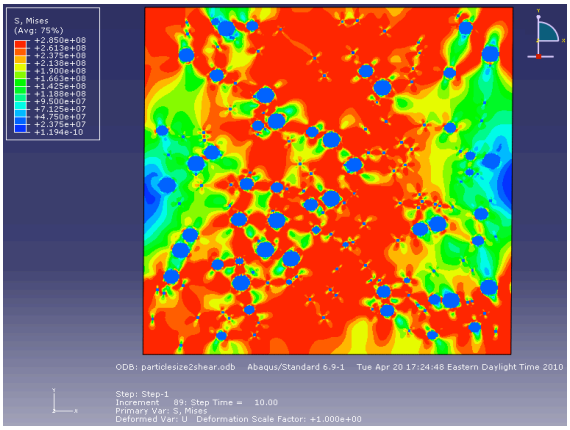

(c)von Mises stress

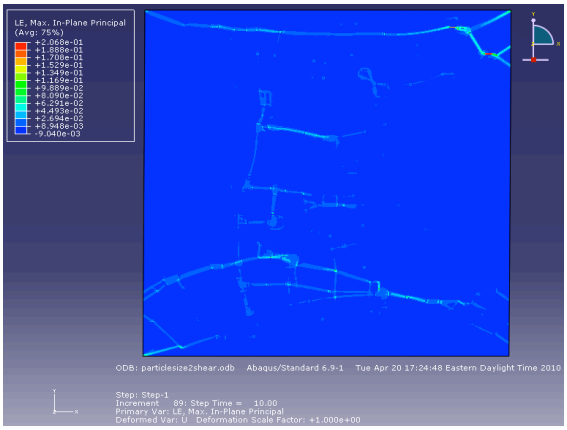

(d) logarithmic strain

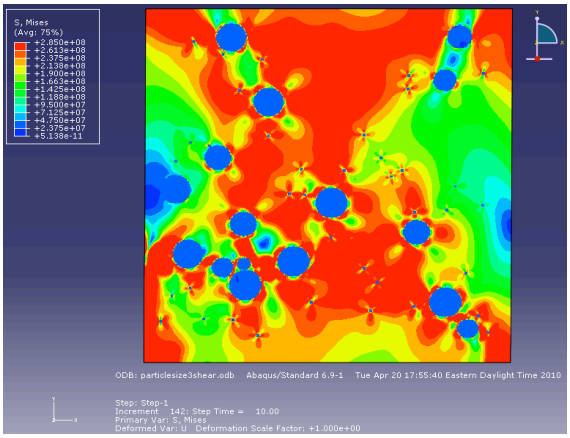

(e) von Mises stress

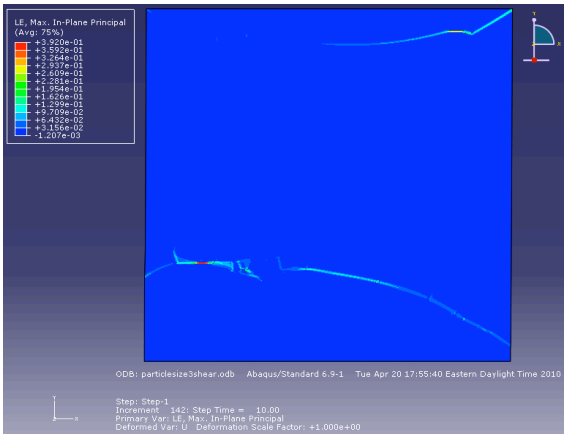

(f) logarithmic strain

Figure 37. Final von Mises stress and logarithmic strain distribution patterns for a material sample under maximum 0.6% shear strain with (a) and (b) 2.14 µm average particle size (c) and (d) 4.28 µm average particle size (e) and (f) 8.56 µm average particle size

When the average particle diameter increases from 2.14 µm, to 4.28 µm and then 8.56 µm, as can be observed in Figures 36 and 37, the impact of average particle size is rather obvious: with the total volume fraction fixed, the obtained overall mechanical properties deteriorate considerably with the increase of average particle size. The data comparison is summarized in Table 24.

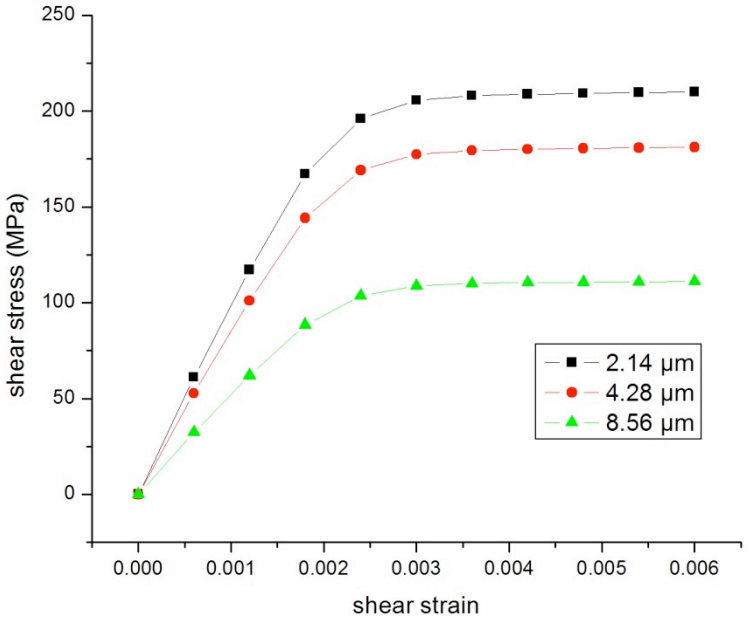

Figure 38. Comparison of the stress-strain curves obtained under shear stress using three different average particle sizes of spherical cementite particles

Table 24. Simulation results for average particle size comparison

Mechanical properties	Young's modulus (GPa)	σ_y (MPa) - axial tension	Shear modulus (GPa)	σ_y (MPa) - shear	Poisson's ratio
Diameter 2.14 µm	208.235	261	88.70	209.724	0.2738
Diameter 4.28 µm	183.903	226	84.25	181.138	0.1914
Diameter 8.56 µm	123.335	167	51.68	111.424	0.1932

5.1.9 Second Phase Particle Volume Fraction

Similar to Section 5.1.8, the effects of second-phase particle volume fraction are investigated by varying the fraction value from 0.0667 to 0.1334 and then 0.2668 while other parameters remain fixed. The final von Mises stress patterns and logarithmic strain distributions obtained with axial tension are illustrated in Figure 39. The parameters associated are provided in Table 25.

Table 25. Simulation parameters for particle volume fraction comparison (axial tensile stress)

parameters	sample size	stress type	**volume fraction of cementite**	average particle diameter (μm)	volume fraction of voids	element type	total strain
values	600 × 600 μm^2	axial tension	**6.67%**	2.14	0.000001%	linear plane strain	0.006
values	600 × 600 μm^2	axial tension	**13.34%**	2.14	0.000001%	linear plane strain	0.006
values	600 × 600 μm^2	axial tension	**26.68%**	2.14	0.000001%	linear plane strain	0.006

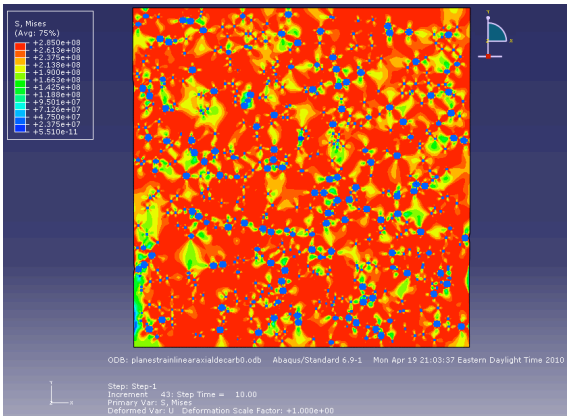

(a) von Mises stress

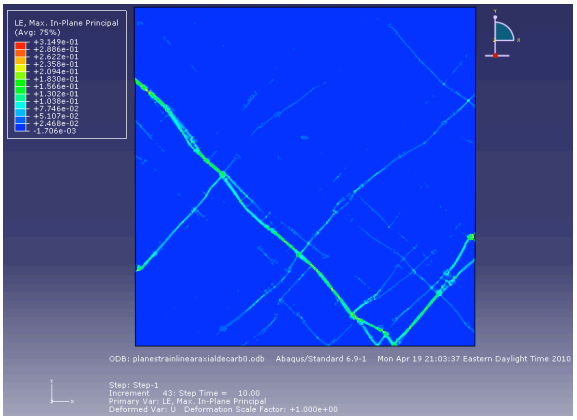

(b) logarithmic strain

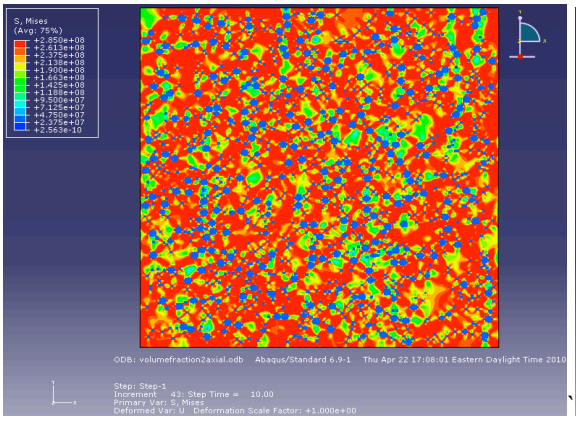

(c) von Mises stress

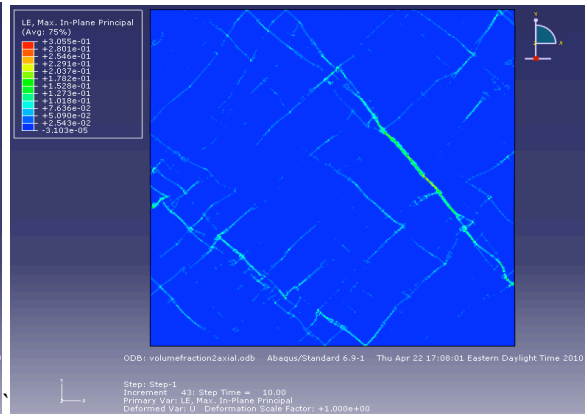

(d) logarithmic strain

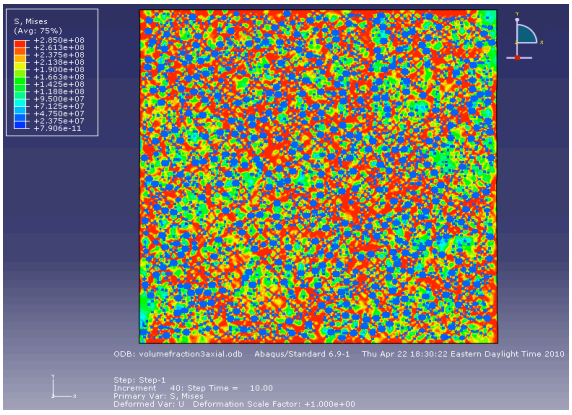

(e) von Mises stress

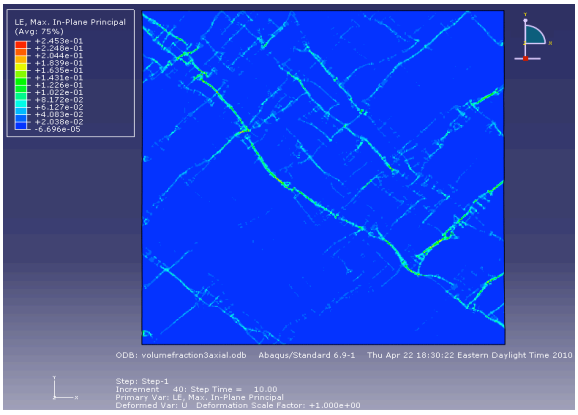

(f) logarithmic strain

Figure 39. Final von Mises stress and logarithmic strain distribution patterns for a material sample under maximum 0.6% axial tensile strain with volume fraction at (a) and (b) 0.0667 (c) and (d) 0.1337 and (e) and (f) 0.2668

The von Mises stress pattern and strain localization become more dispersed and decentralized as the total particle volume fraction increases. The erratic strain localization due to the numerous stress centers can be observed in Figure 39 (f). Figure 40 shows that

the yield strength of the simulated sample decreases precipitously with the increase of particle volume fraction, as well. A small amount of second phase particles can work as the precipitation hardening agent and hinder the slip of dislocations hence strengthening the material. However, when the volume fraction goes over a certain upper limit, continuing to increase it will only cause the overabundance of stress concentration centers and raise the probability of material failure.

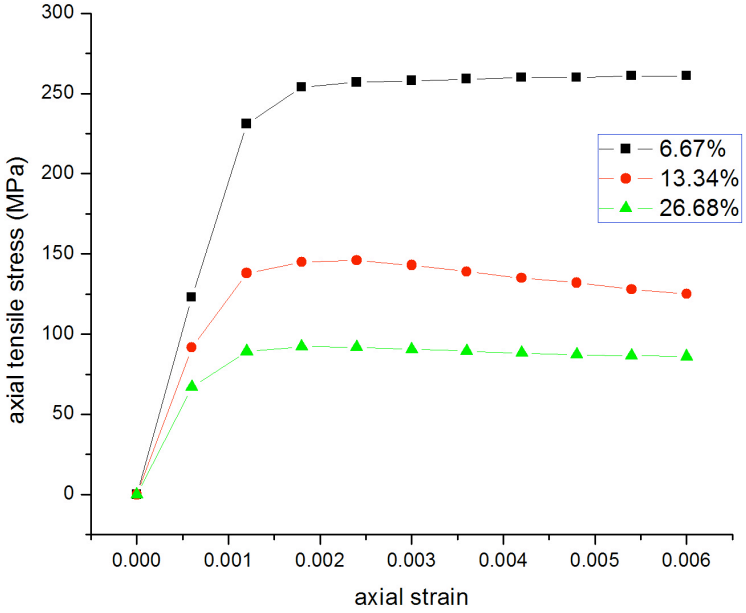

Figure 40. Comparison of the stress-strain curves obtained under axial tensile stress using three different volume fractions of spherical cementite particles

Then the shear stress is applied to find out how shear modulus varies in conjunction with the change of particle volume fraction, with the parameters listed in Table 26 and results shown in Figures 41 and 42.

Table 26. Simulation parameters for particle volume fraction comparison (shear stress)

Parameters	Sample size	Stress type	**Volume fraction of cementite**	Average particle diameter (μm)	Volume fraction of voids	Element type	Total strain
Values	600 × 600 μm^2	shear	**6.67%**	2.14	0.000001%	linear plane strain	0.006
Values	600 × 600 μm^2	shear	**13.34%**	2.14	0.000001%	linear plane strain	0.006
Values	600 × 600 μm^2	shear	**26.68%**	2.14	0.000001%	linear plane strain	0.006

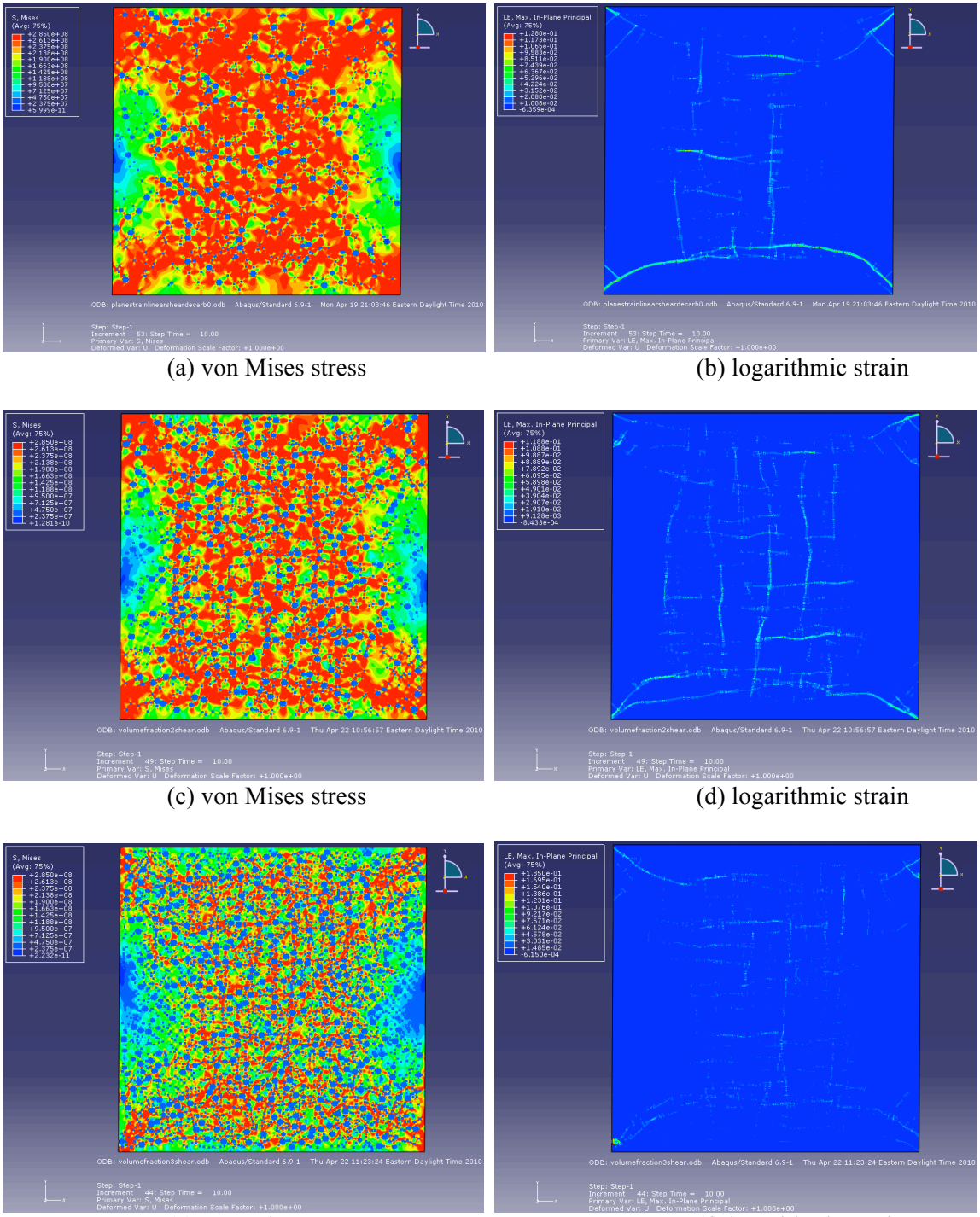

(a) von Mises stress (b) logarithmic strain

(c) von Mises stress (d) logarithmic strain

(e) von Mises stress (f) logarithmic strain

Figure 41. Final von Mises stress and logarithmic strain distribution patterns for a material sample under maximum 0.6% shear strain with (a) and (b) 0.0667 volume fraction (c) and (d) 0.1337 volume fraction (e) and (f) 0.2668 volume fraction

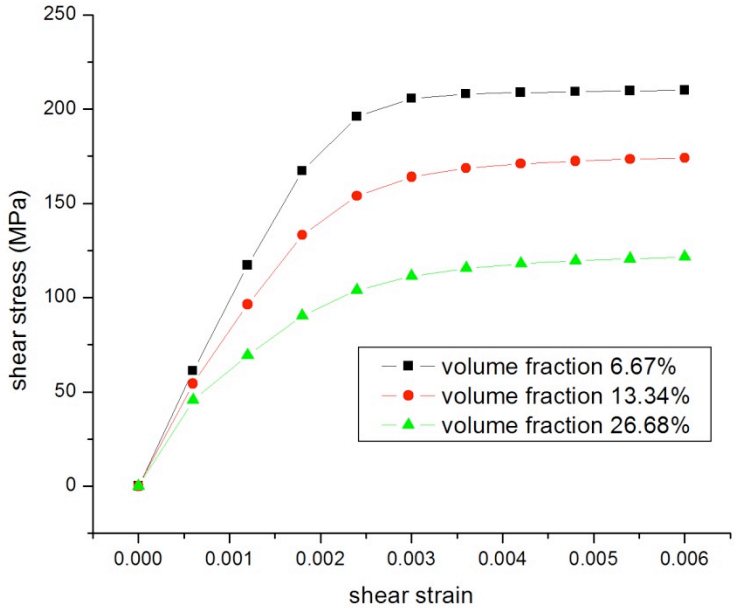

Figure 42. Comparison of the stress-strain curves obtained under shear stress using three different volume fractions of spherical cementite particles

As suggested by the simulation results in Figure 42, as the particle volume fraction changes, the resulted shear modulus and shear yield strength essentially follow the same trend established in the case of axial tensile stress: they decrease significantly with an increase in particle volume fraction. These observations echo the same conclusion about precipitation strengthening drawn from the previous case: when the total particle volume fraction is corralled within a certain range and form a discontinuous network adjacent to the grain boundaries, their presence can pin down the dislocations therefore hindering the deformation of material; however, when the volume fraction has increased to the extent where those particles not only appear in the grain boundary area but also in the grains, it could easily trigger cracking and negatively affect the material's ability to resist pressure [52]. The exact values of all the mechanical properties are shown in Table 27.

Table 27. Simulation results for particle volume fraction comparison

Mechanical properties	Young's modulus (GPa)	σ_y (MPa) - axial tension	Shear modulus (GPa)	σ_y (MPa) - shear	Poisson's ratio
Diameter 2.14 μm	208.235	261	88.707	209.724	0.2738
Diameter 4.28 μm	115.300	146	80.335	174.05	
Diameter 8.56 μm	74.357	92.2	49.171	121.601	

Using second-phase particle precipitation hardening to improve the material's strength has always been an intriguing topic in the physical metallurgy discipline [53-58]. The question of how best to control the morphology of second-phase precipitation remains to be solved. It is believed that in the vicinity of 6.67%, which is the natural content of cementite particles in spheroidite, an optimal value could be found that can pin down the dislocations, enhance the overall strength while not acting as fracture nuclei and triggering intra-granular fracture. Constrained by time and resources, this topic was not fully covered but it could easily be explored using the same approach.

5.1.10 Cavity and Void Volume Fraction

In addition, the presence of cavities and voids are also taken into consideration. These imperfections are inherent in materials, fabricated using the process developed at GT. The inclusion of cavities and voids is essential to the characterization of the materials' properties because these three-dimensional defects significantly alter the occurrence of stress concentrations, strain localization, crack initiation and sometimes total failure. The voids are distributed in the sample following the same distribution function (Equation 3) as the second phase particles, only with a much lower volume fraction. Based on Cramer's ASM handbook [59], the volume fraction of voids present in AISI 1074 spheroidite is approximately 10^{-8}. In this work, the volume fraction of void varies from 0 to 10^{-8}, 10^{-6}, up to 10^{-4} and the resulted logarithmic strain patterns are plotted in Figure 43. Because in practice, the estimate of the average volume fraction of voids and cavities

in dense material such as spherodite can be tricky and hardly very accurate, this section of analysis is performed aiming to roughly determine the impact of the void and cavity volume fraction.

Table 28. Simulation parameters for average particle size comparison (tensile stress)

Parameters	Sample size	Stress type	Volume fraction of cementite	Average particle diameter (μm)	**Volume fraction of voids**	Element type	Total strain
Values	600 × 600 μm^2	axial tension	6.67%	2.14	**0**	linear plane strain	0.006
Values	600 × 600 μm^2	axial tension	6.67%	2.14	**0.000001%**	linear plane strain	0.006
Values	600 × 600 μm^2	axial tension	6.67%	2.14	**0.0001%**	linear plane strain	0.006
Values	600 × 600 μm^2	axial tension	6.67%	2.14	**0.01%**	linear plane strain	0.006

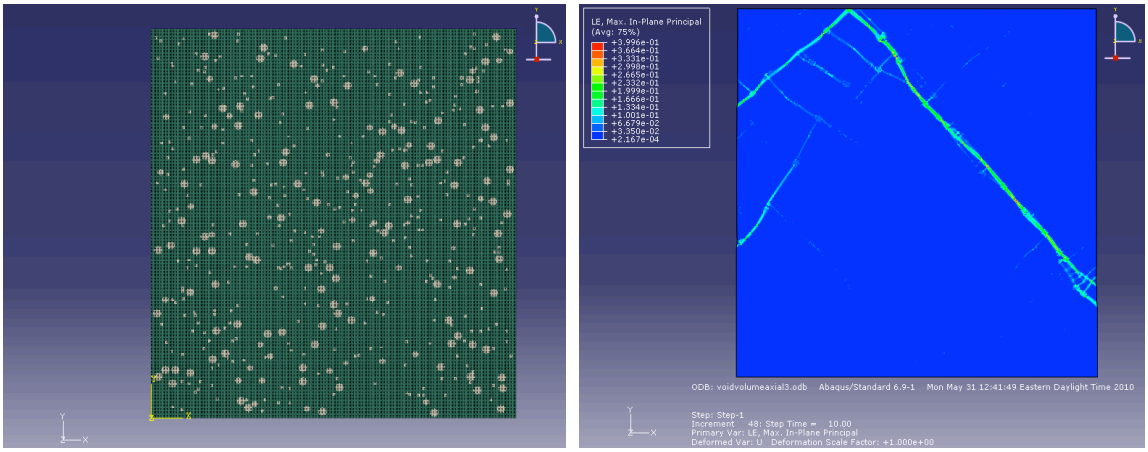

(a) sample microstructure (b) logarithmic strain

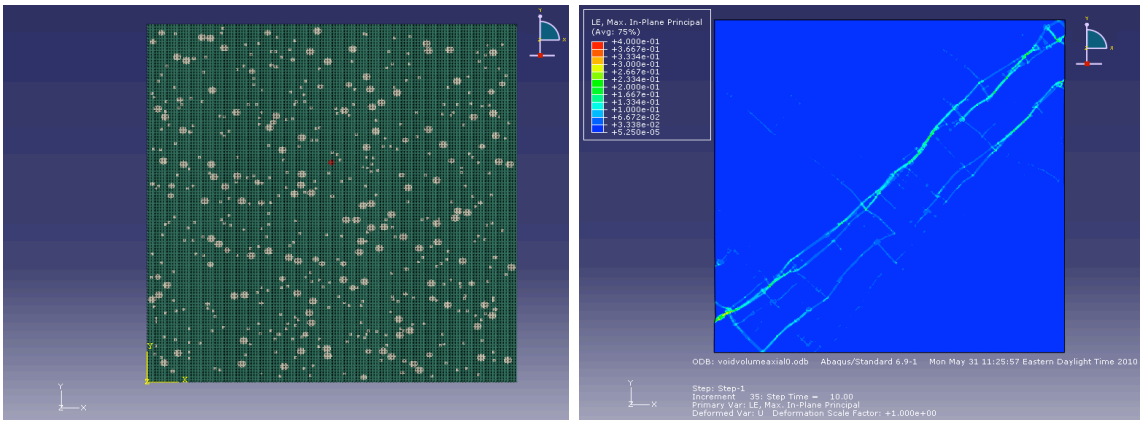

(c) sample microstructure (d) logarithmic strain

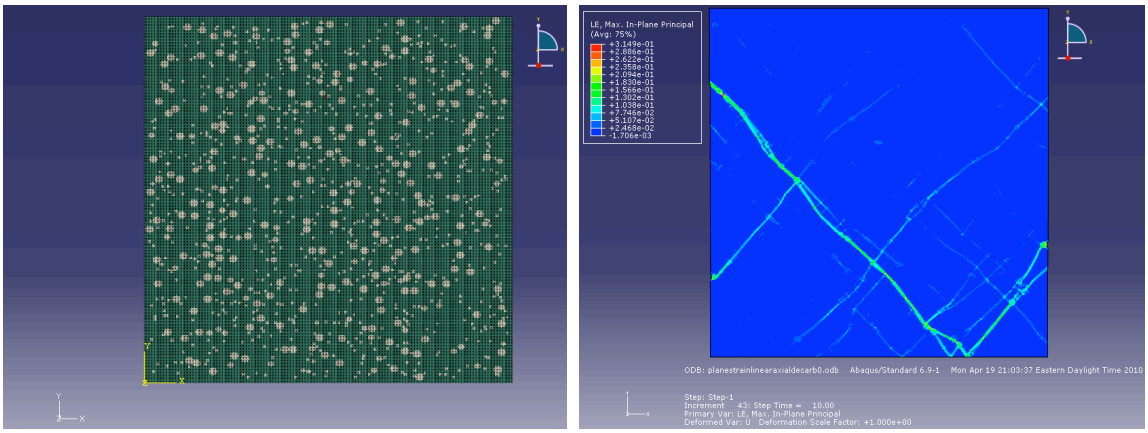

(e) sample microstructure (f) logarithmic strain

Figure 43. Simulated sample geometry and logarithmic strain distribution patterns for a material sample under maximum 0.6% axial tensile strain with cavity and void volume fraction at (a) and (b) 0, (c) and (d) 0.000001%, (e) and (f) 0.0001% and (g) and (h) 0.01%

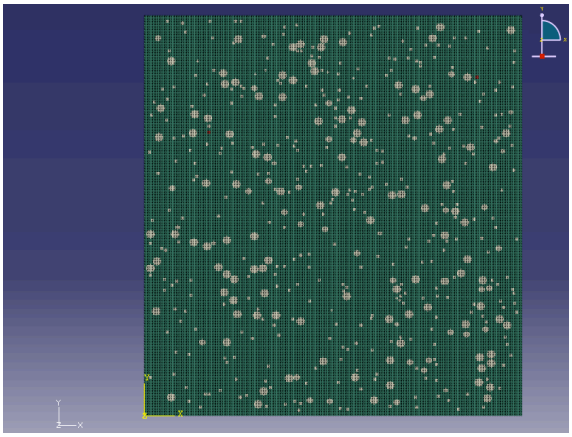

(g) sample microstructure

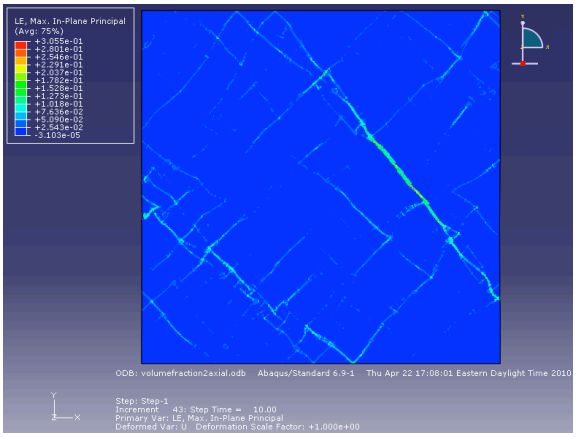

(h) logarithmic strain

Figure 43 continued

The accompanying stress-strain curves are shown in Figure 44. An obvious conclusion can be reached from those plots that without the cavities and voids, the strain localization tends to form in accordance with the second phase-particle-arrays in the directional permutation closest to 45º with respect to the direction in which the tension is applied; once the voids are present, they tend to act as the initiation centers for strain localization. Also as suggested in Figure 43, higher cavity volume fraction induces more frequent strain localization occurrence and lower yield strength, largely owing to the high number of initiation centers but the obtained Young's moduli are practically the same, meaning that while in the elastic deformation range, a cavity percentage less than 0.01% does not cause major shift in the modulus.

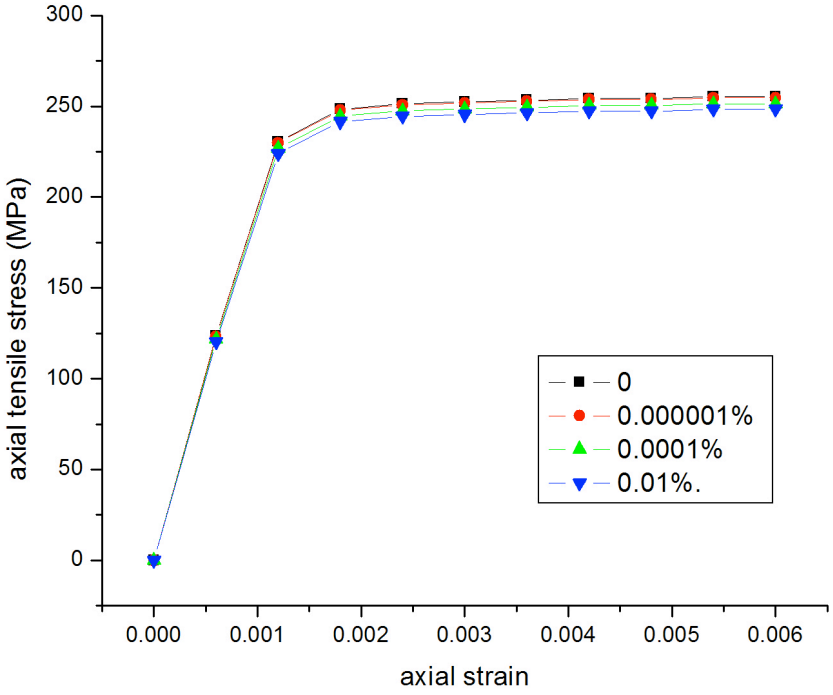

Figure 44. Comparison of the stress-strain curves obtained under axial stress using four different volume fractions of voids and cavities

Similarly, the accompanying plots for the resulted strain localization patterns obtained under shear stress are provided below in Figure 45.

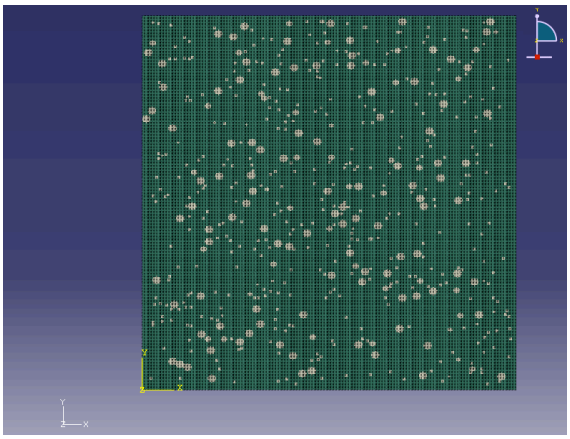

(a) sample microstructure

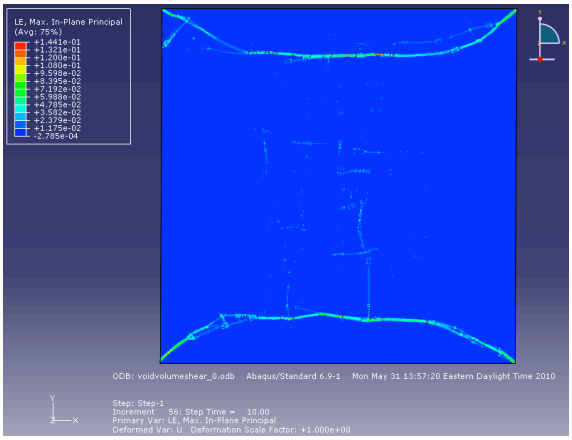

(b) logarithmic strain

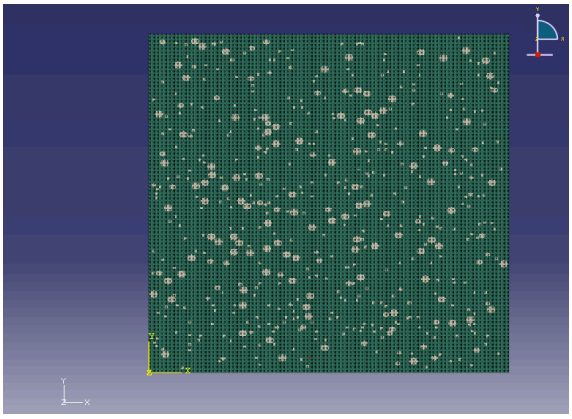

(c) sample microstructure

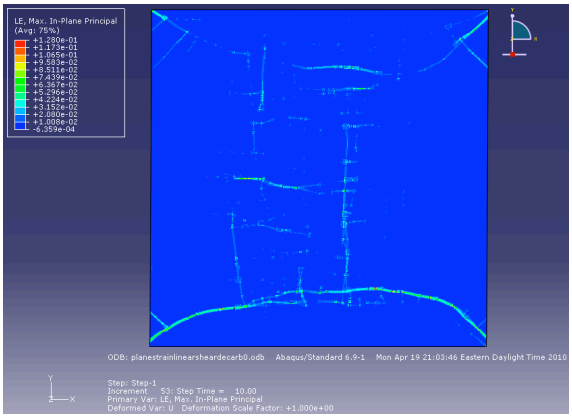

(d) logarithmic strain

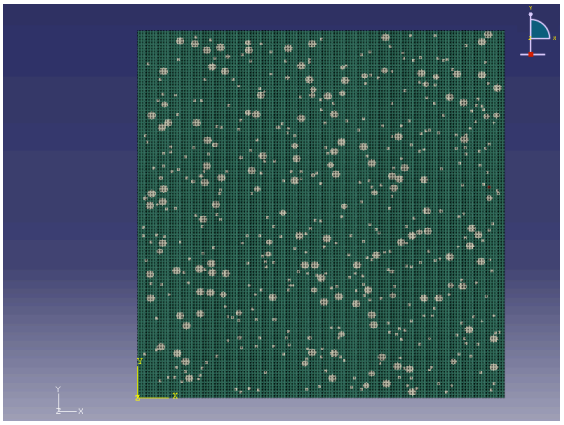

(e) sample microstructure

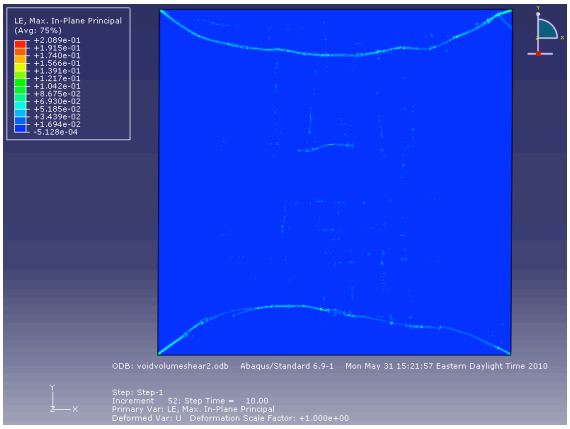

(f) logarithmic strain

Figure 45. Simulated sample geometry and logarithmic strain distribution patterns for a material sample under maximum 0.6% shear strain with cavity and void volume fraction at (a) and (b) 0, (c) and (d) 0.000001%, (e) and (f) 0.0001% and (g) and (h) 0.01%

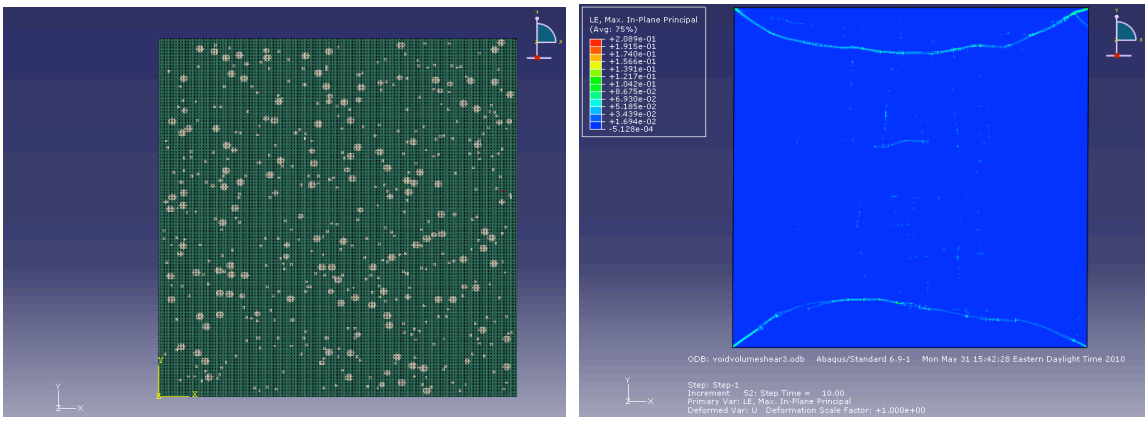

(g) sample microstructure (h) logarithmic strain

Figure 45 continued

Following the same trend as in the case of axial tensile stress, when the total volume fraction of cavities increases from 0 to 0.01%, the obtained stress-strain curves display discernable decrease, as demonstrated in Figure 46. The effects of void volume fraction in the cases of shear stress are comparable to that in the axial stress case: the shear stress of spheroidite decreases as the void volume fraction increases, but not to a significant extent.

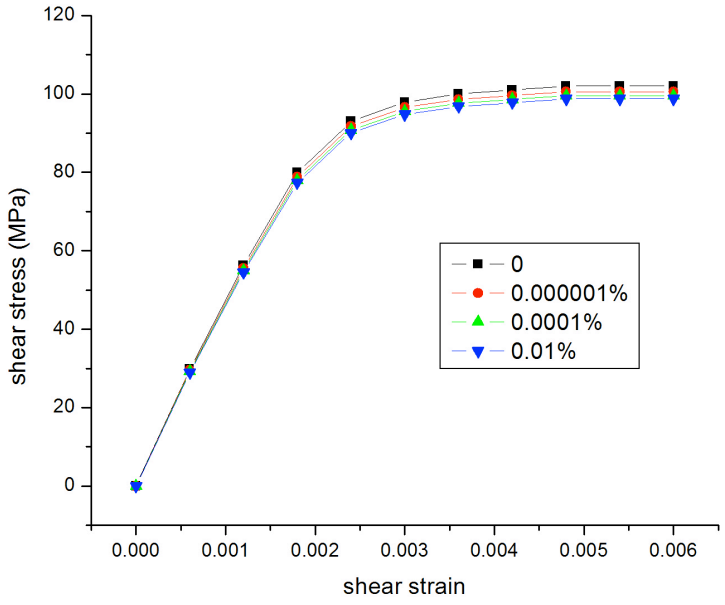

Figure 46. Comparison of the stress-strain curves obtained under shear stress using four different volume fractions of voids and cavities

The exact values of each mechanical property in all four scenarios are shown in Table 29.

Table 29. Simulation results for particle volume fraction comparison

Void volume fraction	Young's modulus (GPa)	σ_y (MPa) - axial tension	Shear modulus (GPa)	σ_y (MPa) - shear	Poisson's ratio
0	208.235	255.360	88.707	102.04	
0.000001%	203.587	254.728	86.255	100.172	
0.0001%	202.191	251.392	84.398	99.552	
0.01%	198.670	248.32	83.109	98.736	

5.1.11 Decarburization Analysis

Just to refresh, during the heat treatment, decarburization occurs as the carbon element at the surface reacts with certain components in the atmosphere, forming the carbon-depleted zones in the process. According to previous discussion, the decarburization layers proceed into the sample following the models detailed in Chapter IV, with the data comparison compiled from the modeling results and experiment provided in Table 30.

Table 30. Change of decarburization depth with time in AISI 1074 samples heat treated at 700 ºC

Processing time (mins)	0	20	40	60	80	100
decarburization layer thickness (μm)	0	9.6	23.5	39.3	55.8	81.2

In each case, the area within the decarburization zones is treated as pure iron without second-phase particles because both the fraction of carbon element dissolved in the original ferrite matrix (Fe-0.02%C) solid solution and the fraction fixated in Fe_3C particles are consumed. In the meantime, cavities and voids are still scattered throughout the sample space as they will not disappear or migrate during decarburization.

The mechanical behaviors of the spheroidite with decarburization zones under axial tension are analyzed and results are shown in Figure 47. The parameters involved are listed in Table 31

.

Table 31. Simulation parameters for decarburization depth analysis (axial tensile stress)

Parameters	Sample size	Stress type	Volume fraction of cementite	Average particle diameter (μm)	Volume fraction of voids	Element type	Total strain
Values	600 × 600 μm^2	axial tensile stress	6.67%	2.14	0.000001%	linear plane strain	0.006

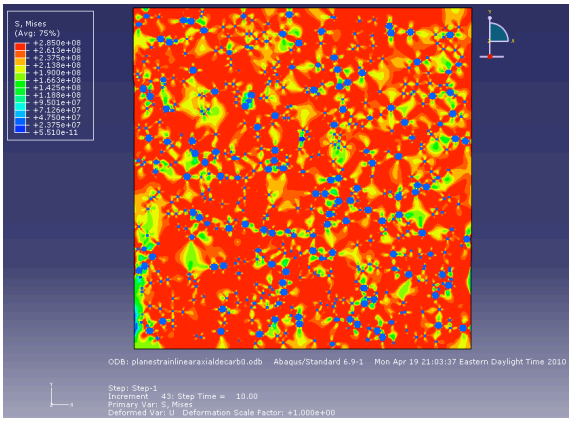

(a) von Mises stress at 0 decarb. depth

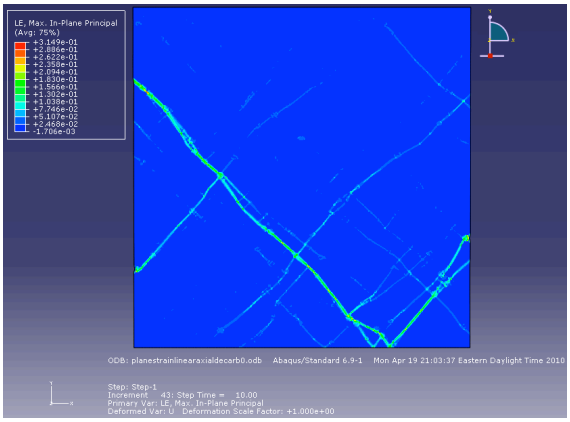

(b) logarithmic strain at 0 decarb. depth

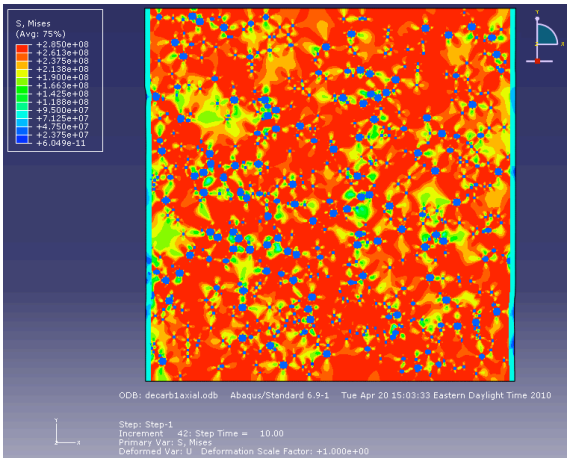

(c) von Mises stress at 9.6 µm decarb. depth

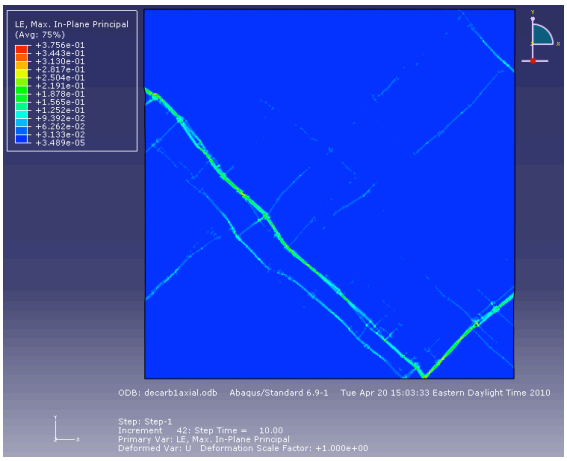

(d) logarithmic strain at 9.6 µm decarb. depth

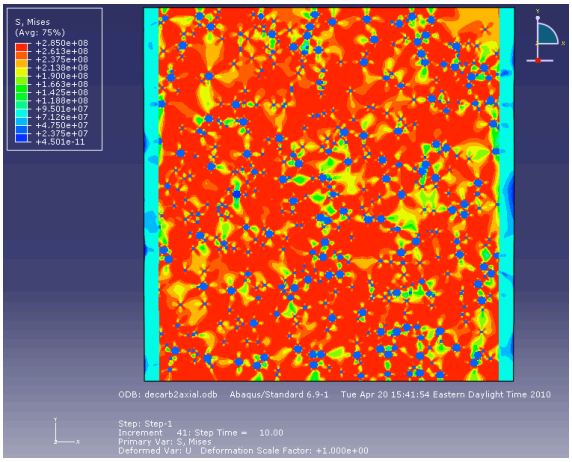

(e) von Mises stress at 23.5 µm decarb. depth

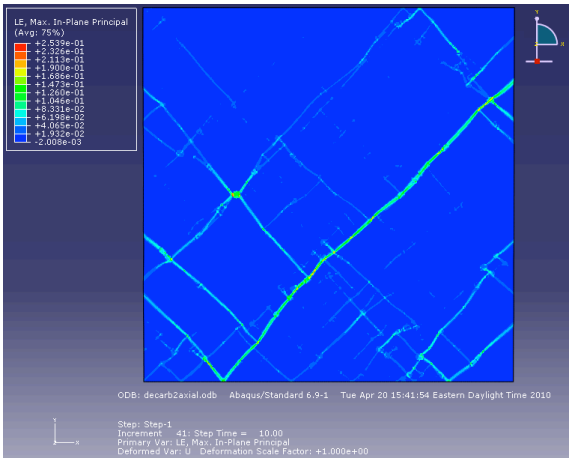

(f) logarithmic strain at 23.5 µm decarb. depth

Figure 47. Final von Mises stress and logarithmic strain distribution patterns for a material sample under maximum 0.6% axial tensile strain after (a) and (b) 0 (c) and (d) 20 minutes (e) and (f) 40 minutes (g) and (h) 60 minutes (i) and (j) 80 minutes (k) and (l) 100 minutes decarburization time

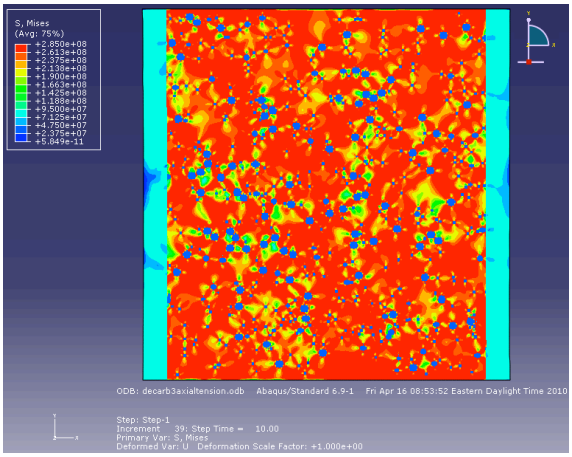

(g) von Mises stress at 39.3 µm decarb. depth

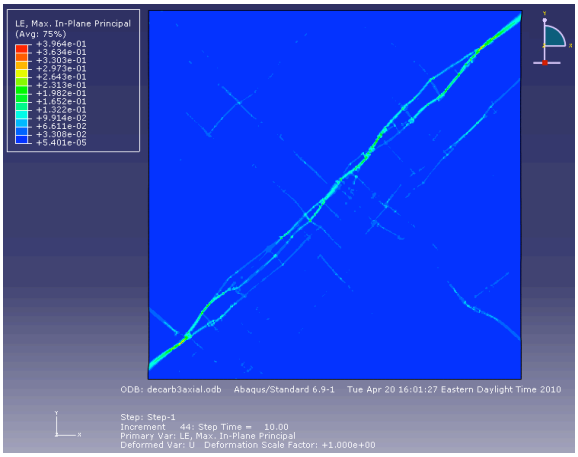

(h) logarithmic strain at 39.3 µm decarb. depth

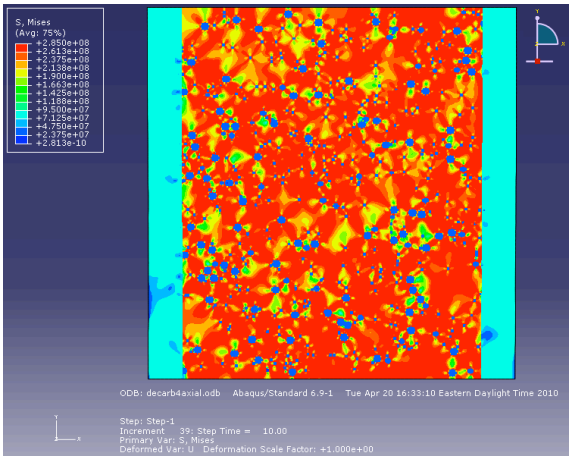

(i) von Mises stress at 55.8 µm decarb. depth

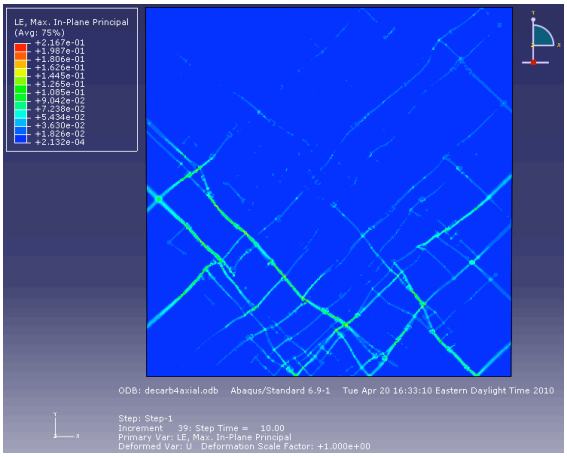

(j) logarithmic strain at 55.8 µm decarb. depth

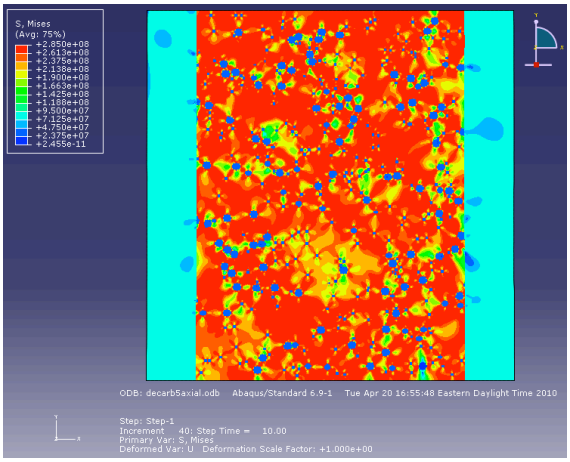

(k) von Mises stress at 81.2 µm decarb. depth

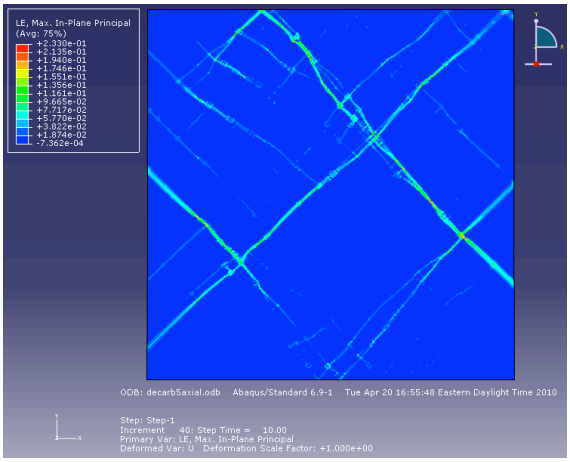

(l) logarithmic strain at 81.2 µm decarb. depth

Figure 47 continued

As concluded with the theoretical simulation results, as well as the experimental observations, the mechanical strength decreases substantially as the decarburization zones augment. Then the mechanical behaviors of samples undergoing axial tensile stress are depicted in Figure 48.

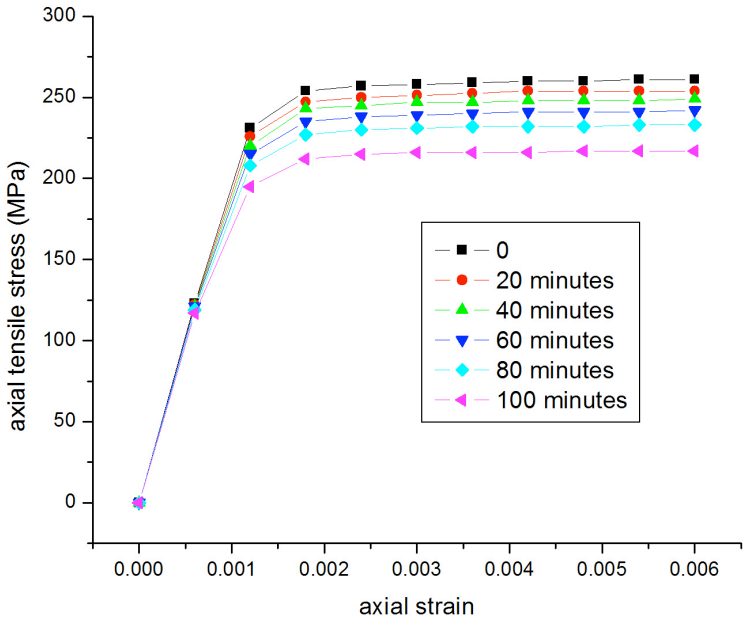

Figure 48. Comparison of the stress-strain curves obtained under axial tensile stress with different decarburization depth

Then the behaviors of the material samples under shear stress are explored with parameters listed in Table 32 and the results are presented in Figure 49.

Table 32. Simulation parameters for decarburization depth analysis (shear stress)

Parameters	Sample size	Stress type	Volume fraction of cementite	Average particle diameter (μm)	Volume fraction of voids	Element type	Total strain
Values	600 × 600 μm^2	Shear	6.67%	2.14	0.000001%	linear plane strain	0.006

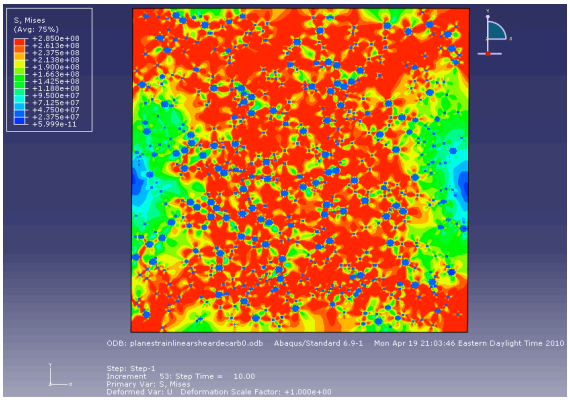

(a) von Mises stress at 0 decarb. depth

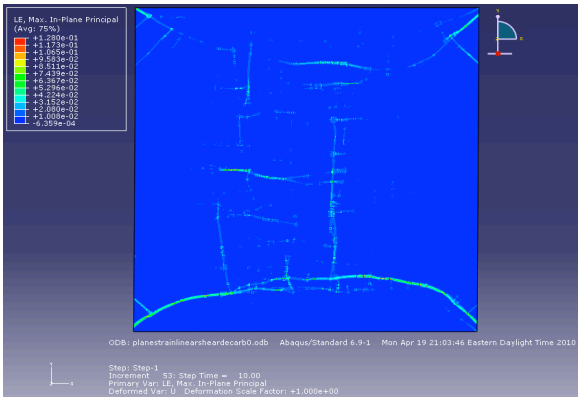

(b) logarithmic strain at 0 decarb. depth

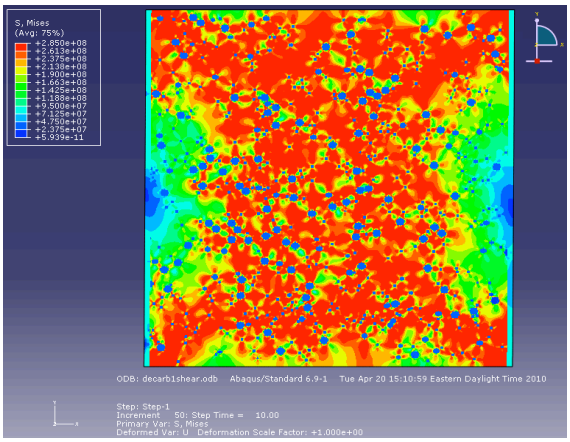

(c) von Mises stress at 9.6 µm decarb. depth

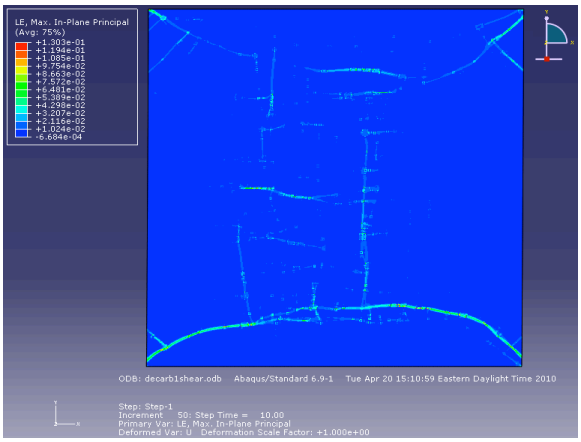

(d) logarithmic strain at 9.6 µm decarb. depth

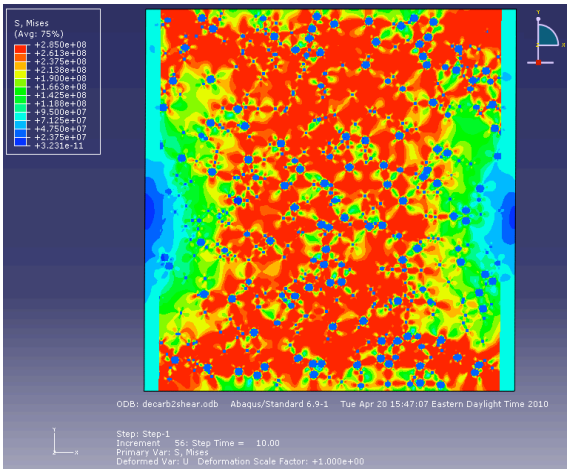

(e) von Mises stress at 23.5 µm decarb. depth

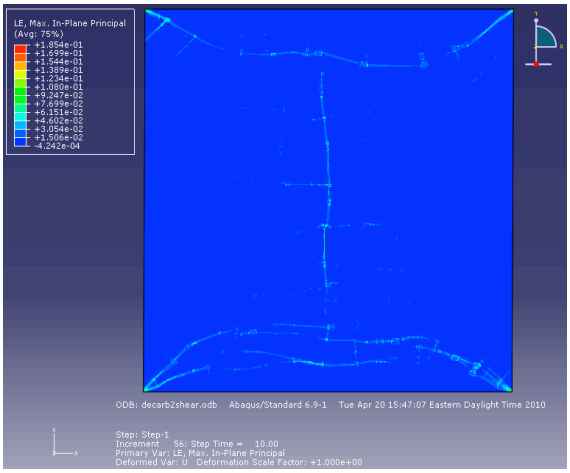

(f) logarithmic strain at 23.5 µm decarb. depth

Figure 49. Final von Mises stress and logarithmic strain distribution patterns for a material sample under maximum 0.6% shear strain after (a) and (b) 0 minute, (c) and (d) 20 minutes (e) and (f) 40 minutes, (g) and (h) 60 minutes, (i) and (j) 80 minutes, (k) and (l) 100 minutes decarburization time

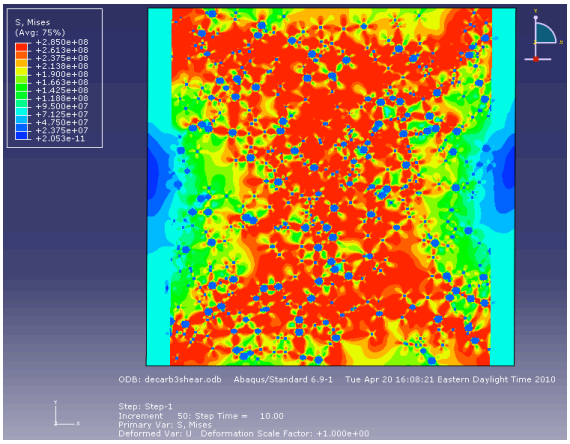

(g) von Mises stress at 39.3 µm decarb. depth

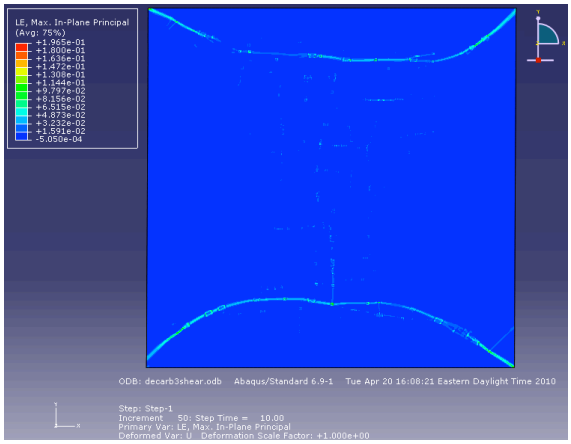

(h) logarithmic strain at 39.3 µm decarb. depth

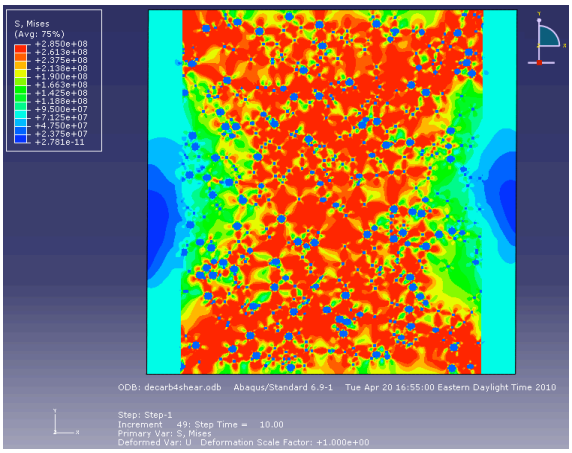

(i) von Mises stress at 55.8 µm decarb. depth

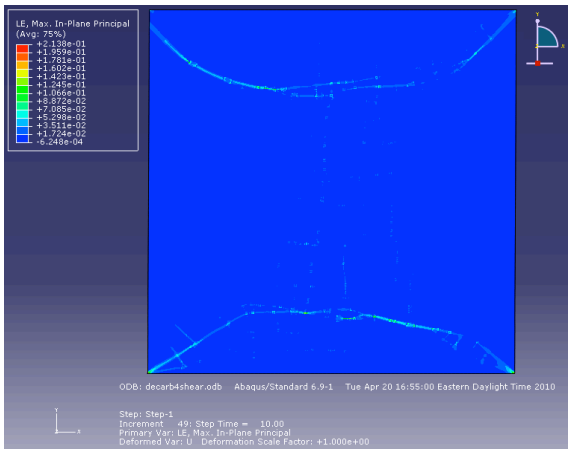

(j) logarithmic strain at 55.8 µm decarb. depth

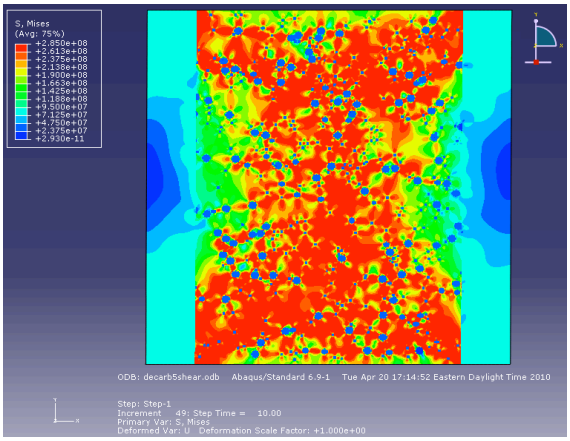

(k) von Mises stress at 81.2 µm decarb. depth

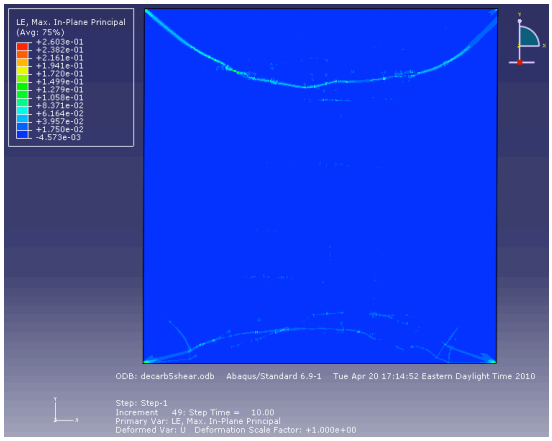

(l) logarithmic strain at 81.2 µm decarb. depth

Figure 49 continued

The obtained shear stress-strain curves are shown in Figure 50, where the decline of spheroidite's shear modulus with the increase of decarburization time is evident.

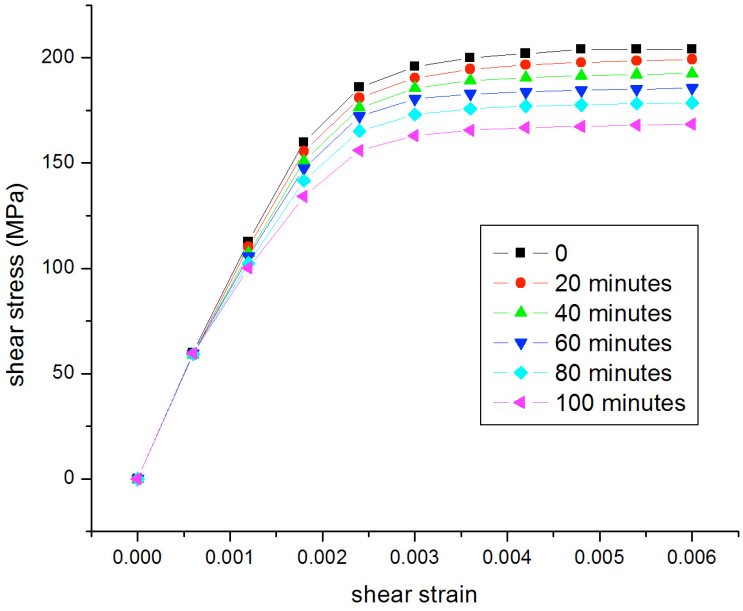

Figure 50. Comparison of the stress-strain curves obtained under shear stress with different decarburization depths

The transverse tensile mode is also analyzed with growing decarburization depths, the material is apparently weaker in the transverse direction thanks to the newly generated decarburization zones. The parameters associated are specified in Table 33 and results shown in Figure 51.

Table 33. Simulation parameters for decarburization depth analysis (transverse tensile stress)

Parameters	Sample size	Stress type	Volume fraction of cementite	Average particle diameter (μm)	Volume fraction of voids	Element type	Total strain
Values	600 × 600 μm^2	transverse tensile stress	6.67%	2.14	0.000001%	linear plane strain	0.006

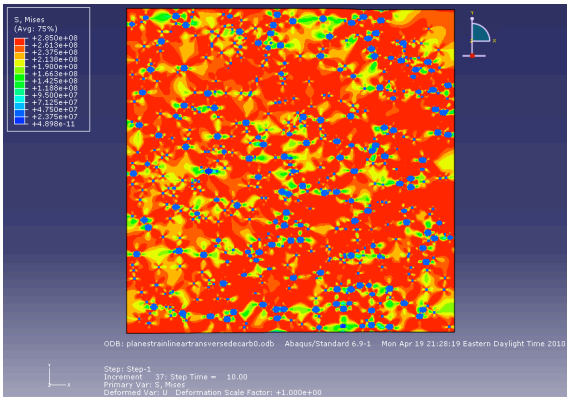

(a) von Mises stress at 0 decarb. depth

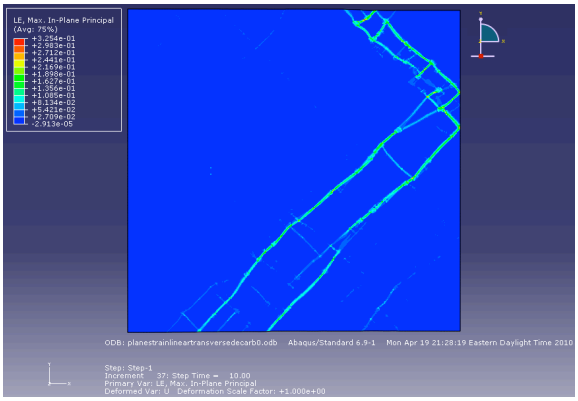

(b) logarithmic strain at 0 decarb. depth

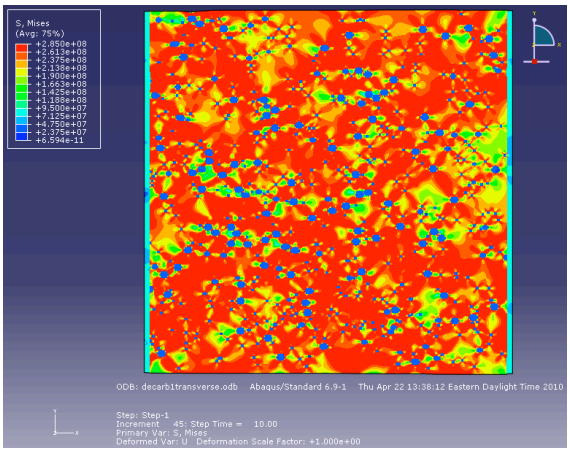

(c) von Mises stress at 9.6 µm decarb. depth

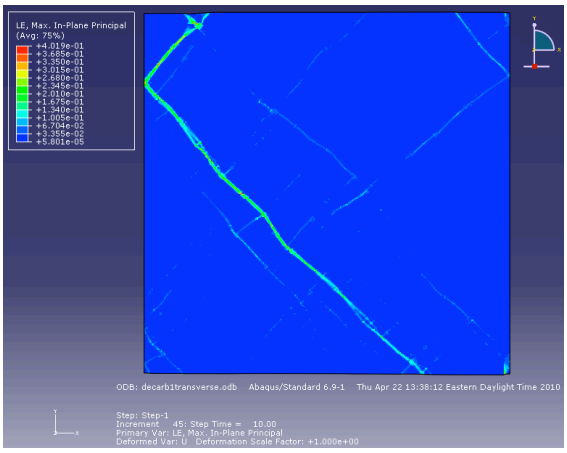

(d) logarithmic strain at 9.6µm decarb. depth

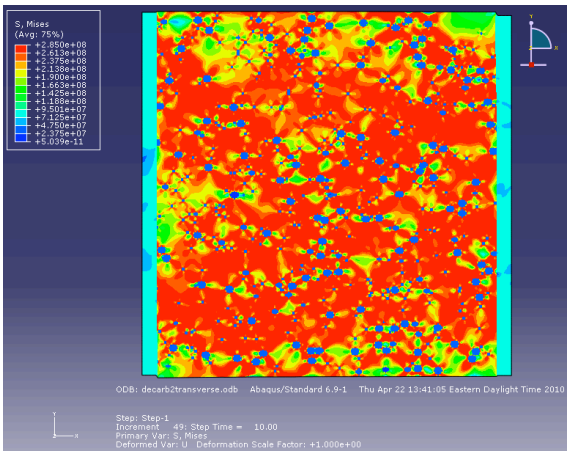

(e) von Mises stress at 23.5 µm decarb. depth

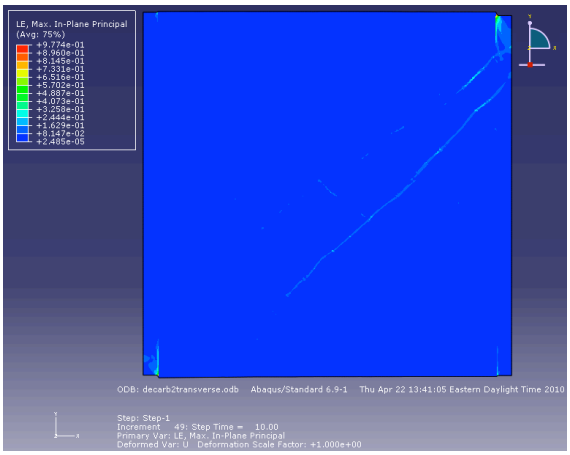

(f) logarithmic strain at 23.5 µm decarb. depth

Figure 51. Final von Mises stress and logarithmic strain distribution patterns for a material sample under maximum 0.6% transverse tensile strain after (a) and (b) 0 minute, (c) and (d) 20 minutes (e) and (f) 40 minutes, (g) and (h) 60 minutes, (i) and (j) 80 minutes, (k) and (l) 100 minutes decarburization time

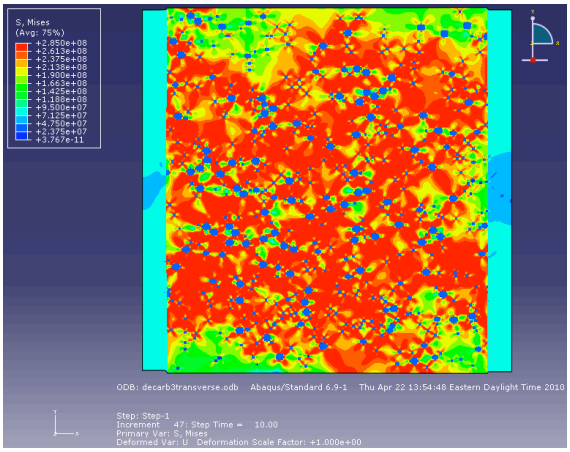

(g) von Mises stress at 39.3 µm decarb. depth

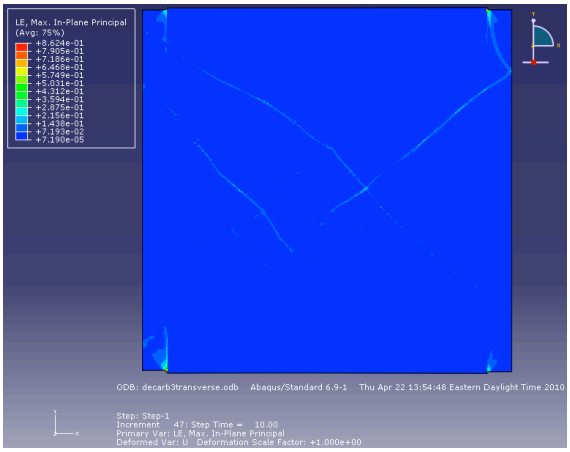

(h) logarithmic strain at 39.3 µm decarb. depth

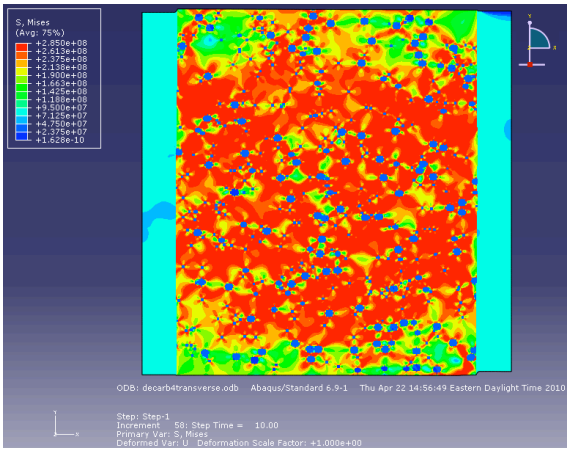

(i) von Mises stress at 55.8 µm decarb. depth

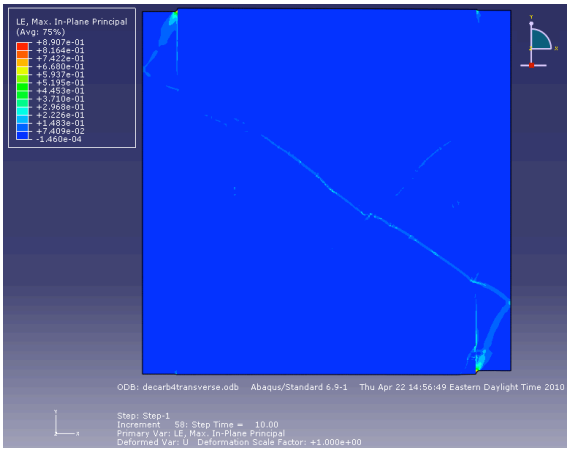

(j) logarithmic strain at 55.8 µm decarb. depth

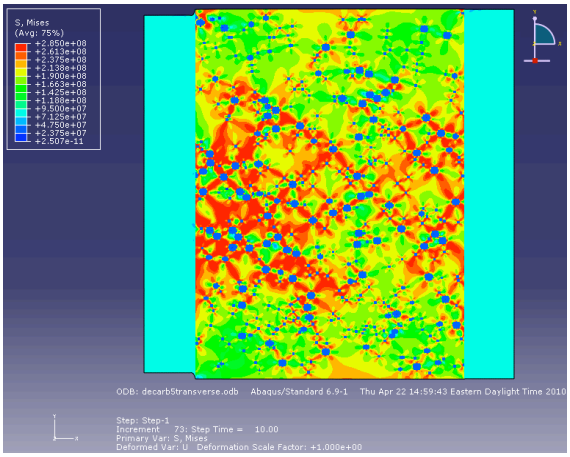

(k) von Mises stress at 81.2 µm decarb. depth

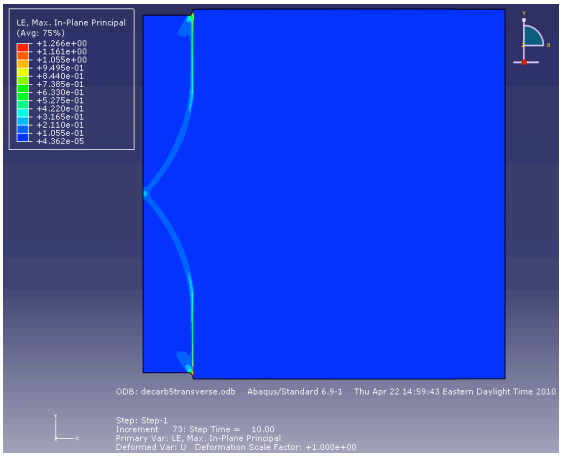

(l) logarithmic strain at 81.2 µm decarb. depth

Figure 51 continued

According to Figure 51, early on in decarburization the strain localization remains in 45º. Once the thickness of decarburization layer becomes comparable to the size of the entire sample, the stress seems to intensify in the joining area between the matrix and the decarburization layers, with the carbon-depleted zones deformed much more prominently than the rest of the sample space. As indicated by the stress-strain curves in Figure 52, similar to what happens to the axial Young's modulus and shear modulus in the axial tension scenario, the transverse Young's modulus of spheroidite also decreases as decarburization zones expand into the sample, only to a larger extent. Between the axial tensile and the transverse tensile cases, the decay of mechanical properties is more obvious in the latter due to the fact that the weaker decarburization zones are subject to the tension alone when the transverse tensile stress is applied, whereas with axial tension it could have other parts of the sample share the load. The quantitative comparison is provided in Table 34.

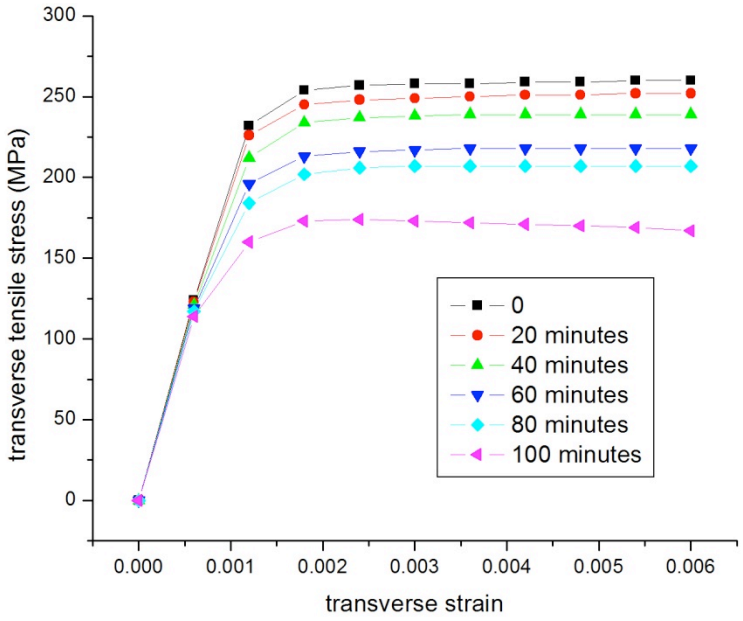

Figure 52. Comparison of the stress-strain curves obtained under transverse tensile stress with different decarburization depths

Table 34 Simulation results of decarburization depth comparison

	0	20	40	60	80	100
Simulated decarb. depths (μm)	0	1.6	3.917	6.55	9.3	13.53
E-axial (GPa)	208.235	203.337	202.191	201.478	198.670	195.374
σ_y-axial (MPa)	261.332	248.154	241.384	233.057	217.643	191
S (GPa)	88.66	86.286	83.57	81.446	78.002	73.844
E-transverse (GPa)	208.335	187.926	176.421	163.356	153.008	133.067
σ_y-transverse (MPa)	260.232	251.931	238.655	217.981	206.820	173.576

5.1.12 Three-Dimensional Analysis

5.1.12.1 Geometry generation

Three dimension should be the obvious choice for simulating the mechanical behaviors of the material system in study, as the thickness of the sample are comparable in all three dimensions. However, with a three-dimensional model, the available computing resources cannot support bigger-scale or higher-mesh-density calculation (a model with 50 × 50 × 50 linear elements with a mesh density of 1 takes 13 hours to compute while a model with 8 × 8 × 8 quadratic elements with a mesh density of 4 takes approximately 17 hours to complete. A model with 100 × 100 × 100 linear elements with a mesh density of 1 was attempted using a 20-gigabyte computer and it reached only 14% completion after 5 days before termination), so it is decided that only a few simple cases will be examined in the extra dimension for the sake of comparison with 2D cases.

Similar algorithm used for microstructure generation for the 2D cases is used here as well: the origins of spheres are randomly placed in the sample space while their radii are determined following the Gaussian normal distribution, as in Equation 3; the sphere size grows until they start to overlap or the preordained total particle volume fraction has been reached, whichever comes first. The generated geometry can be seen in Figure 53.

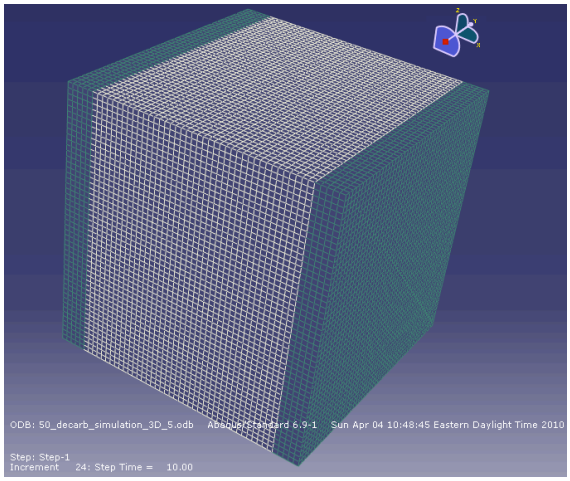

(a) 3D perspective view

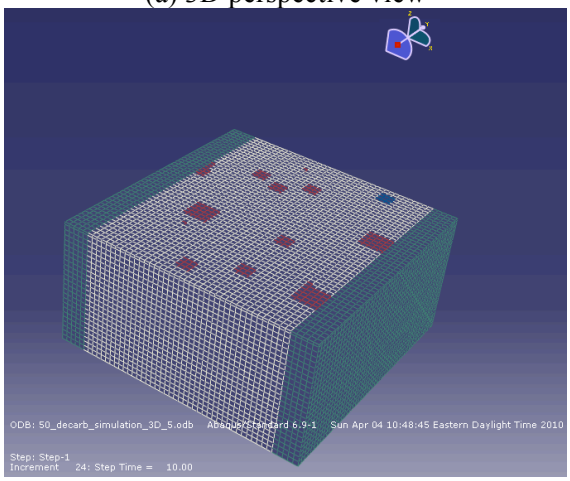

(b) x-y cross-section view

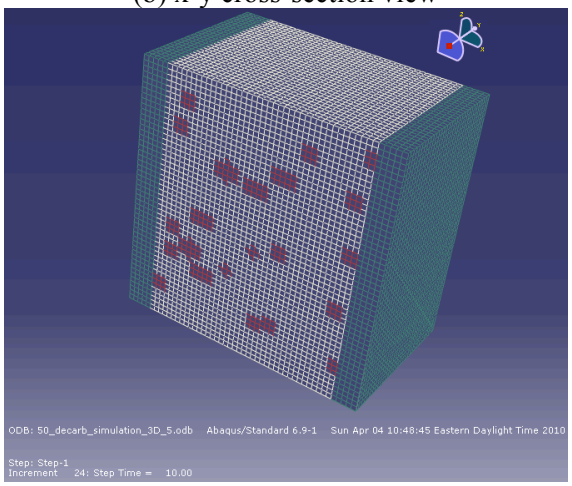

(c) x-z plane cross-section view

Figure 53. Generated geometry for (a) 3D perspective view (b) x-y plane cross-section view (c) x-z plane cross-section view

5.1.12.2 Element type

The most popular 3D linear element in Abaqus is C3D8, whose element configuration and node-element connectivity are shown in Figure 54.

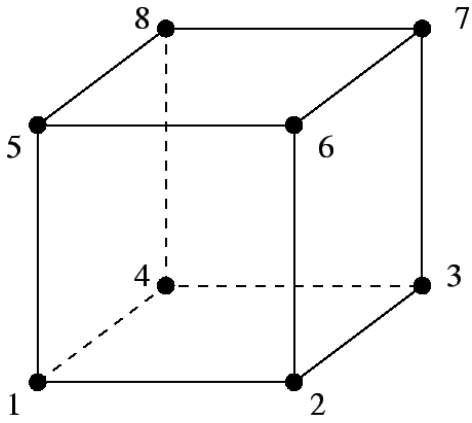

(a) element configuration

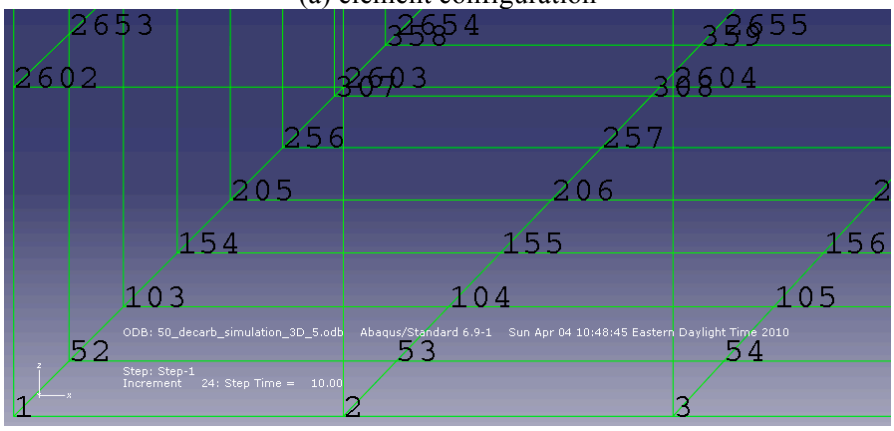

(b) node-element connectivity

Figure 54. Linear three dimensional element C3D8 (a) element configuration (b) node-element connectivity

5.1.12.3 Convergence test

The convergence test in 3D is performed using a cube containing 10 × 10 × 10 elements, with the mesh density varying from 1 to 2, 4 and 6. The final von Mises stress patterns and logarithmic strain distributions are compared in Figure 55. The involved parameters are summarized in Table 35.

Table 35. Simulation parameters for 3D convergence test (axial tensile stress)

Parameters	Sample size	Stress type	Volume fraction of cementite	Average particle diameter (μm)	Volume fraction of voids	Element type	Total strain
Mesh density of 1	10 × 10 × 10 μm^3	axial tension	6.67%	2.14	0.000001%	linear 3D	0.006
Mesh density of 2	10 × 10 × 10 μm^3	axial tension	6.67%	2.14	0.000001%	linear 3D	0.006
Mesh density of 4	10 × 10 × 10 μm^3	axial tension	6.67%	2.14	0.000001%	linear 3D	0.006
Mesh density of 6	10 × 10 × 10 μm^3	axial tension	6.67%	2.14	0.000001%	linear 3D	0.006

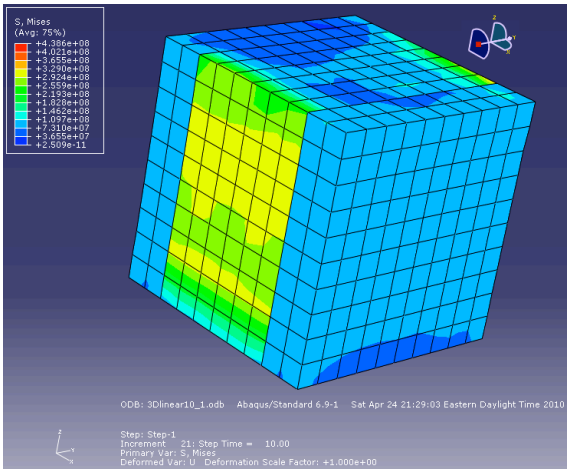

(a) von Mises stress with mesh density at 1

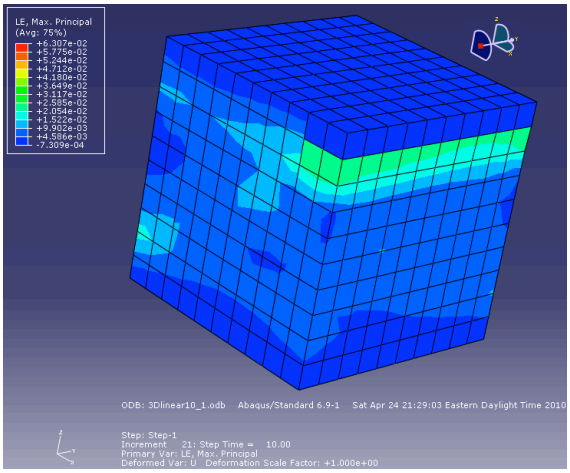

(b) logarithmic strain with mesh density at 1

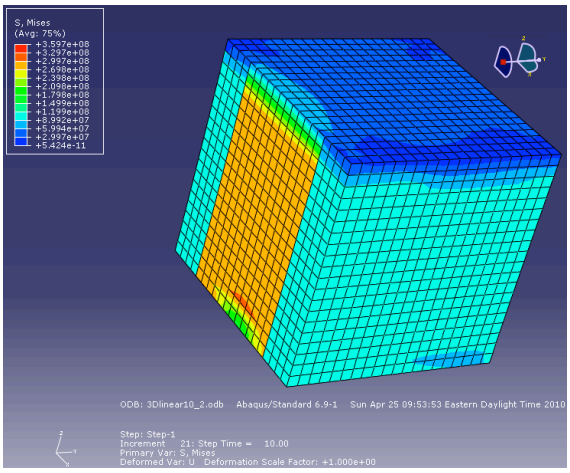

(c) von Mises stress with mesh density at 2

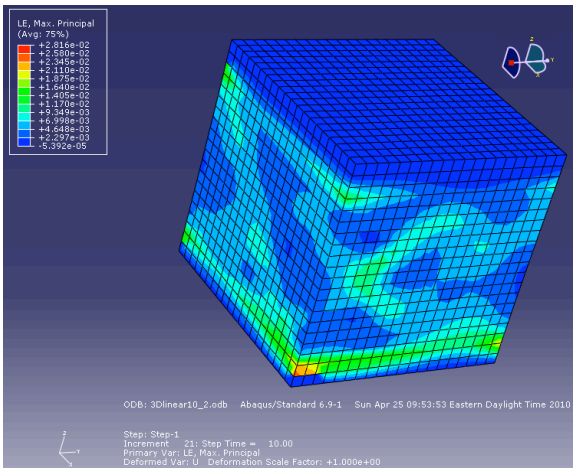

(d) logarithmic strain with mesh density at 2

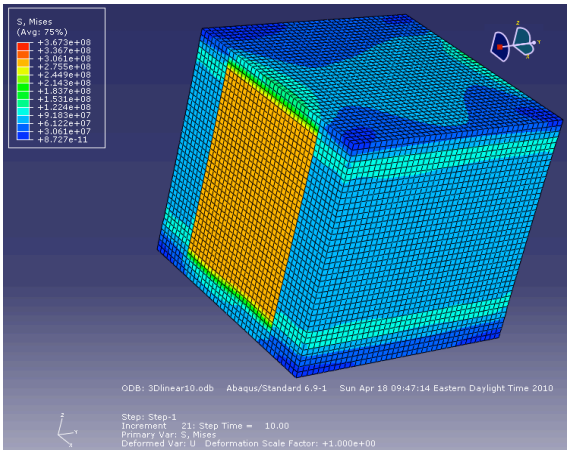

(e) von Mises stress with mesh density at 4

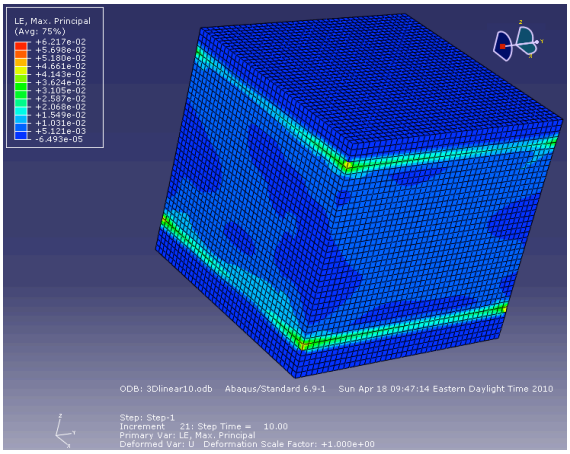

(f) logarithmic strain with mesh density at 4

Figure 55. The final von Mises stress patterns and logarithmic strain distributions for a 3D material sample under maximum 0.6% axial tensile strain with (a) and (b) mesh density of 1, (c) and (d) mesh density of 2 (e) and (f) mesh density of 4 and (g) and (h) mesh density of 6

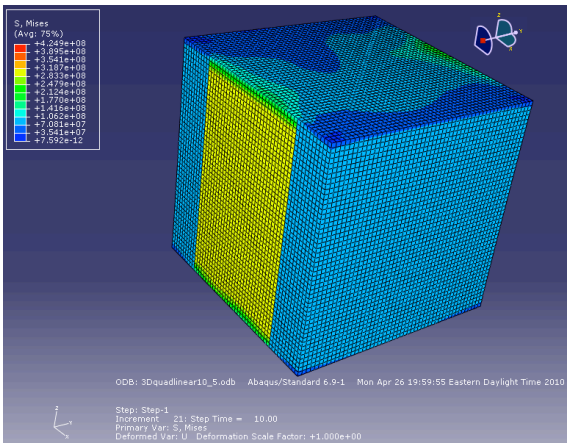

(g) von Mises stress with mesh density at 6

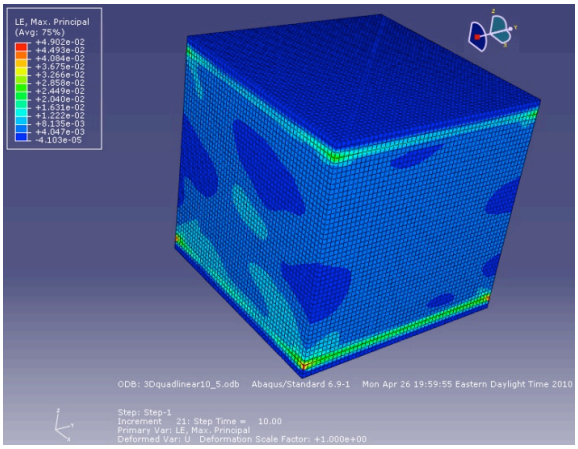

(h) logarithmic strain with mesh density at 6

Figure 55 continued

The resulted stress-strain curves are summarized in Figure 56. Under the same magnitude of maximum strain (0.6%), the maximum stresses reached using different mesh densities reflect the tendency of convergence. Note that the stress-strain data are collected using the same method used in the 2D cases: calculate the collective stress over the top surface of the sample, as opposed to the top edge in 2D, at each given step and plot the results against the strain, which increases at a constant pace.

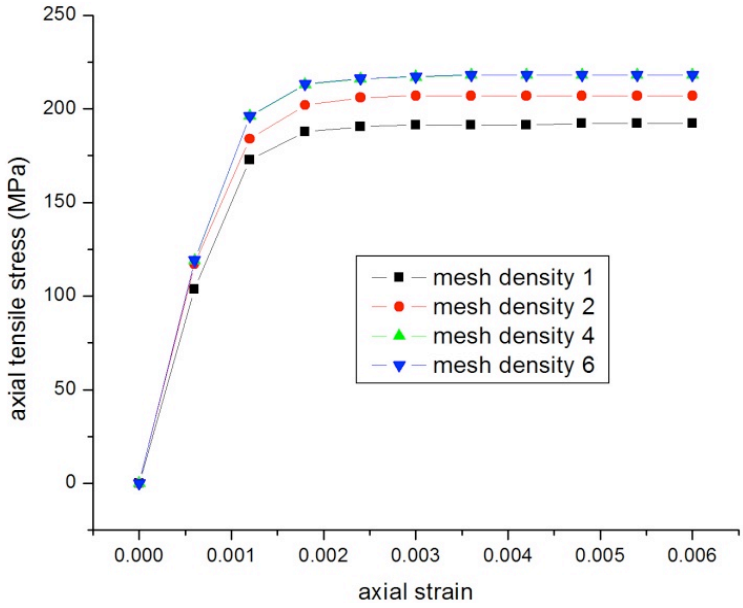

(a)

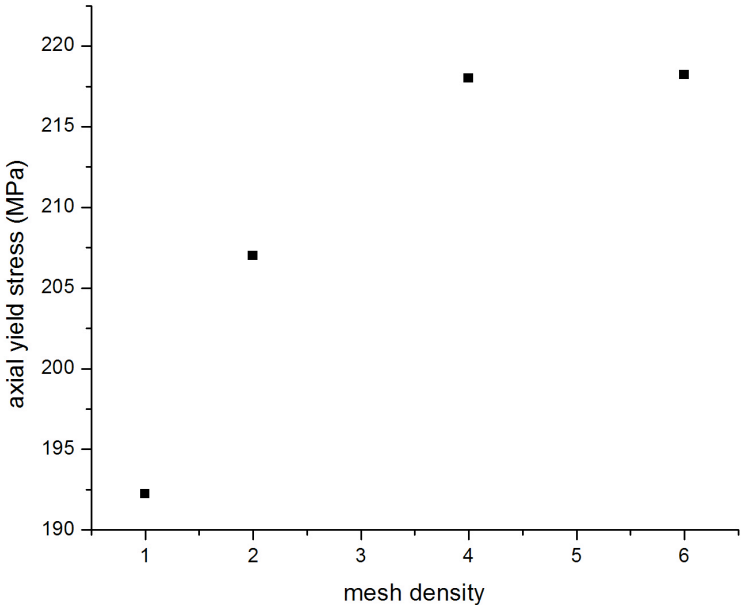

(b)

Figure 56. Convergence of cases with different mesh densities (a) stress-strain curves convergence (b) maximum yield strength convergence

The maximum tensile stress tends to converge after the mesh density is increased to 4 pixels/micron, as evidenced by the overlapping of the stress-strain curves obtained with the densities of 4 and 6 in Figure 56(a). As the mesh density increases, the maximum tensile stress converges in the vicinity of 218 MPa and the results from using mesh density 2 falls within 10% of what is obtained with mesh density 4. The modeling would exceed the computing power limit if the $10 \times 10 \times 10$ μm^3 sample size is retained

while using a mesh density higher than 6, so while what was presented so far may not be the ideal approach to ascertain the convergence tendency, it is the best possible way to balance between the number of elements required to properly embody the heterogeneity of the material in question and the preciseness and accuracy of the simulation results. Therefore, density of 4 is chosen for the rest of the simulation unless stated otherwise. The comparison of results is shown in Table 36.

Table 36. Simulation results of 3D convergence test

Mechanical properties	Young's modulus (GPa)	σ_y (MPa) - yield strength
Mesh density at 1	172.744	192.234
Mesh density at 2	195.006	207.241
Mesh density at 4	198.333	218.02
Mesh density at 6	198.382	218.22

5.1.12.4 Comparison with two-dimensional elements

A comparison between results obtained with 2D and 3D elements is compiled in Figures 57, 58 and Table 38. Involved parameters are listed in Table 37.

Table 37. Simulation parameters for 2D and 3D comparison (axial tensile stress)

Parameters	**Sample size**	Stress type	Volume fraction of cementite	Average particle diameter (μm)	Volume fraction of voids	Element type	Total strain
2D mesh density of 4	**600 × 600 μm^2**	axial tension	6.67%	2.14	0.000001%	linear 3D	0.006
3D mesh density of 4	**10 × 10 × 10 μm^3**	axial tension	6.67%	2.14	0.000001%	linear 3D	0.006

The two models are calculated and compared, one with decarburization zones and the other without them. In the group without decarburization, as in Figure 57, the final von Mises stress patterns and logarithmic strain distributions are shown for both two- and

three-dimensional scenarios, as opposed to Figure 58, which shows those resulted von Mises stress patterns and strain distributions with decarburization.

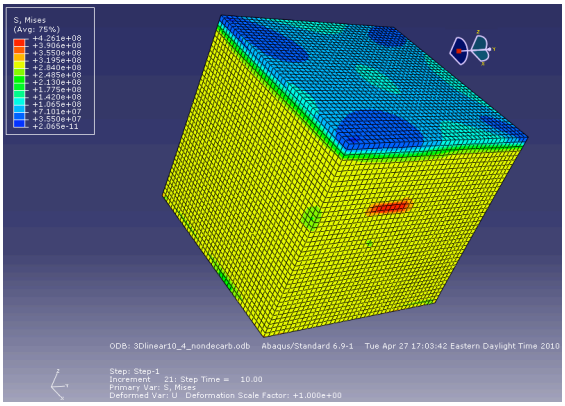

(a) von Mises stress with 3D linear element

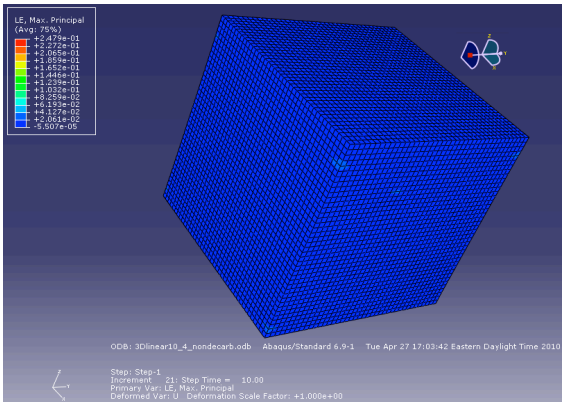

(b) logarithmic strain with 3D linear element

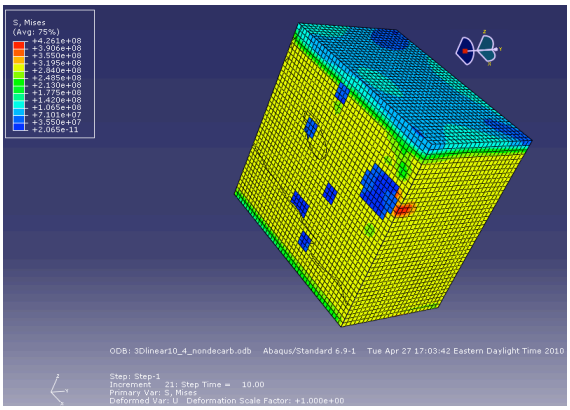

(c) von Mises stress with 3D linear element (x-z cross section view 40% at the -y length)

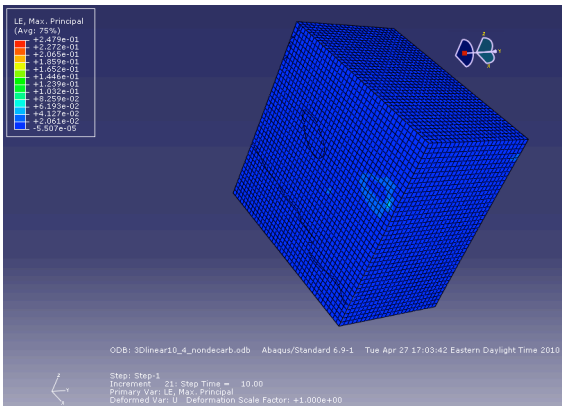

(d) logarithmic strain with 3D linear element (x-z cross section view 40% at the -y length)

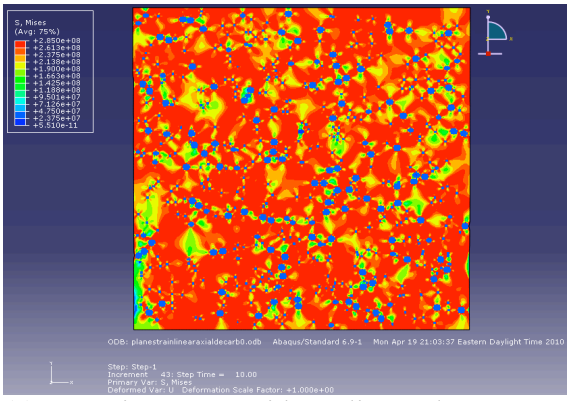

(e) von Mises stress with 2D linear element

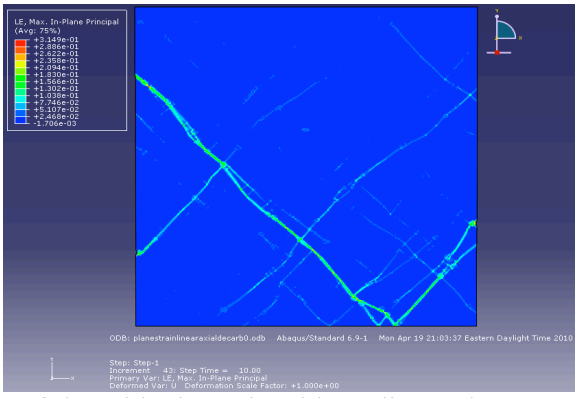

(f) logarithmic strain with 2D linear element

Figure 57. Final von Mises stress and logarithmic strain distribution patterns for a sample material without decarburization under maximum 0.6% axial tensile strain in (a) and (b) 3D linear element overview, (c) and (d) 3D element cross-section view (e) and (f) 2D linear element plane view

Note that the decarburization depth in the 3D model is set as 2 μm on each side out of 10 μm total edge length, and the depth in the two-dimensional model is set as 120 μm on each side out of 600 μm total edge length. The two scenarios are not totally

comparable but given that the decarburization zones occupy an invariable 20% of their respective total area/volume, it is safe to assume that to some extent the setting could provide a telling comparison regardless, as the stress-strain curves would suggest in Figure 59.

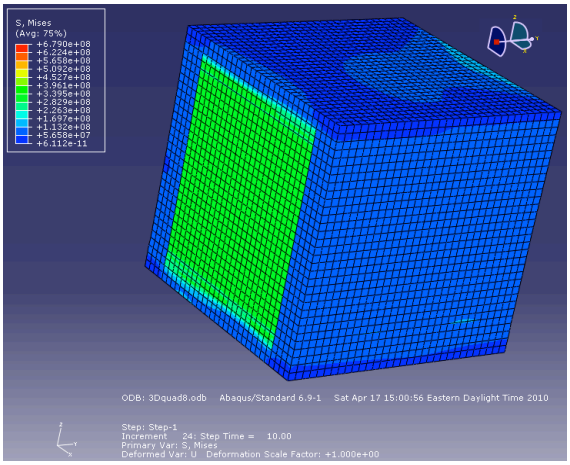

(a) von Mises stress with 3D linear element

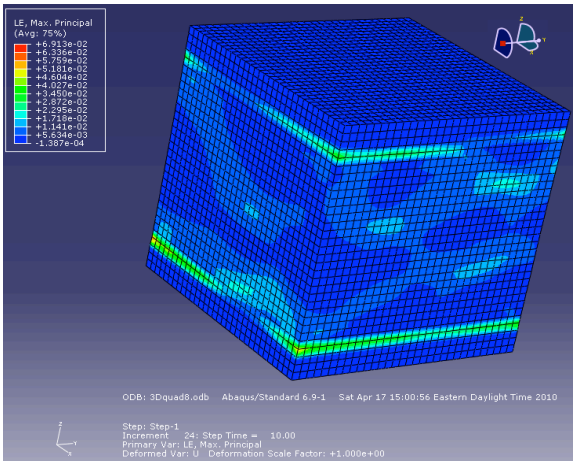

(b) logarithmic strain with 3D linear element

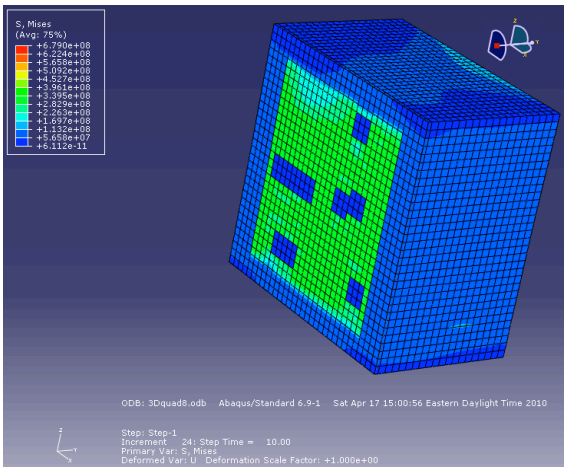

(c) von Mises stress with 3D linear element (x-z cross section view 40% at the -y length)

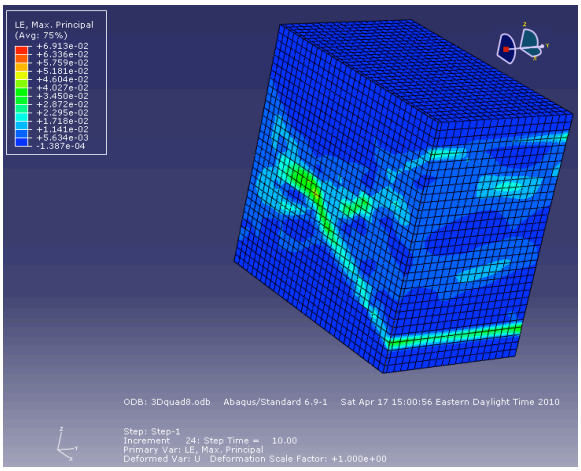

(d) logarithmic strain with 3D linear element (x-z cross section view 40% at the -y length)

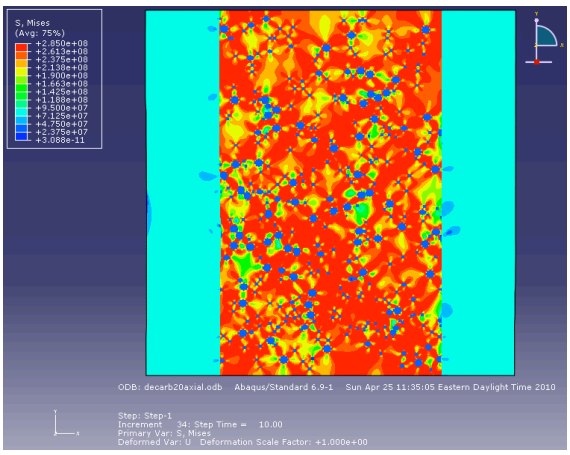

(e) von Mises stress with 2D linear element

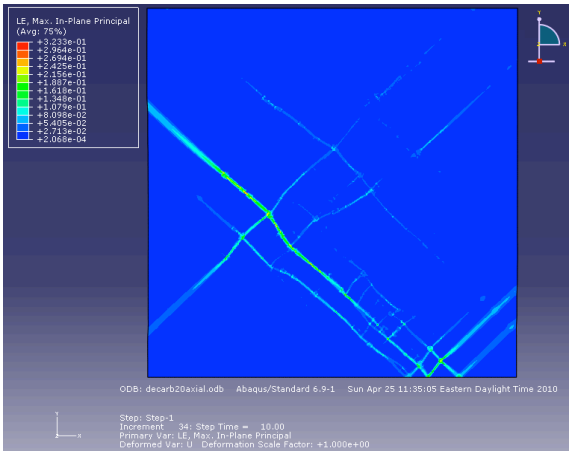

(f) logarithmic strain with 2D linear element

Figure 58. Final von Mises stress and logarithmic strain distribution patterns for a sample with decarburization under maximum 0.6% axial tensile strain in (a) and (b) 3D linear element overview, (c) and (d) 3D element cross-section view (e) and (f) 2D linear element plane view

The obtained data of related mechanical properties are shown in Table 38.

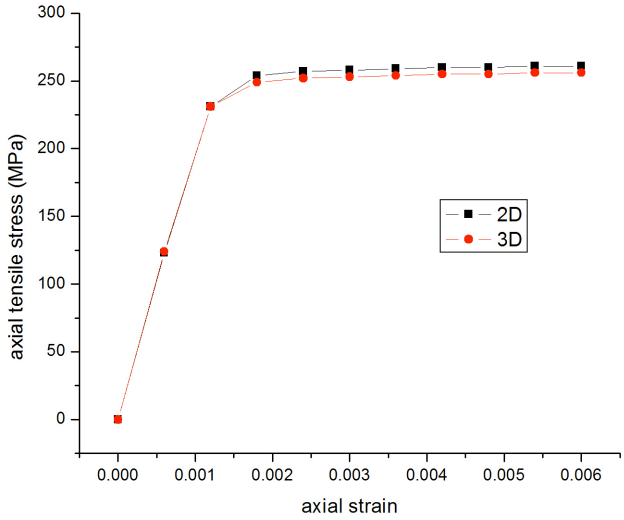

(a) without decarburization

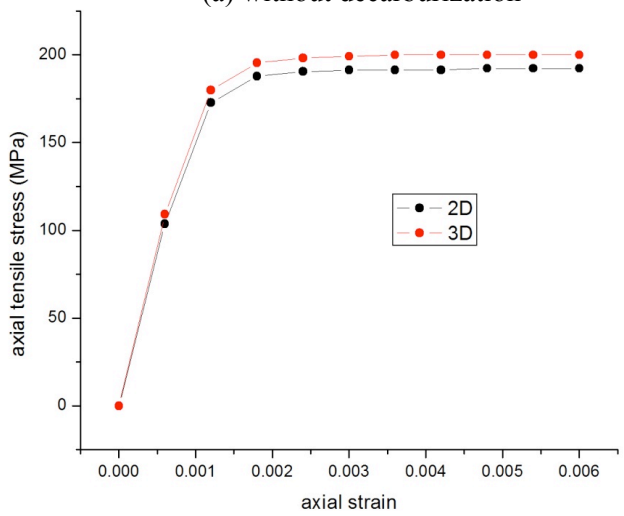

(b) with decarburization

Figure 59. Stress-strain curve comparison between 2D linear element and 3D linear element comparison (a) without decarburization (b) with decarburization

Table 38. Simulation results of 2D and 3D element comparison

Mechanical properties	Young's modulus (GPa)	σ_y (MPa) - yield strength
3D linear element with decarburization	181.951	199.993
2D linear element with decarburization	172.744	192.234
3D linear element without decarburization	192.500	256.452
2D linear element without decarburization	190.268	261.854

As is evidenced in Table 38, the Young's moduli and yield strengths calculated with two- and three-dimensional elements fall about 10% within each other. Despite the fact that 2D and 3D elements are not directly comparable, the size of the 3D model ($10 \times 10 \times 10\ \mu m^3$) is much smaller than that of the 2D model ($600 \times 600\ \mu m^2$), in the sense that it contains significantly fewer elements (1000 vs. 360000) but the obtained mechanical properties drops off more slowly with decarburization growth in the 3D case. Both the Young's modulus and yield strength calculated with 3D element drop less when compared to 2D after adding the same percentage of decarburization, despite the fact that the 3D model contains much fewer elements. It implies that the 3D model is less sensitive to the variation of material properties. A systematic decarburization series analysis with models big enough could shed more light on this topic.

5.1.12.5 3D linear element vs. 3D quadratic element

The last to be compared are a pair of 3D elements. As previously stated in Section 5.1.12.2, C3D8 is the simplest 3D element primarily employed to describe translational motions of three-dimensional objects. While C3D8 is robust enough to describe all the mechanical behaviors involved in this study, C3D20, the quadratic element in 3D configuration, whose node-element connectivity is depicted in Figure 60, is investigated and compared in this section.

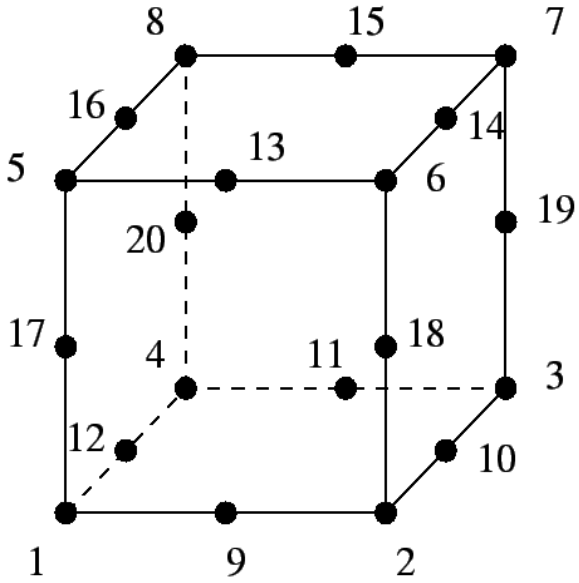

(a) element configuration

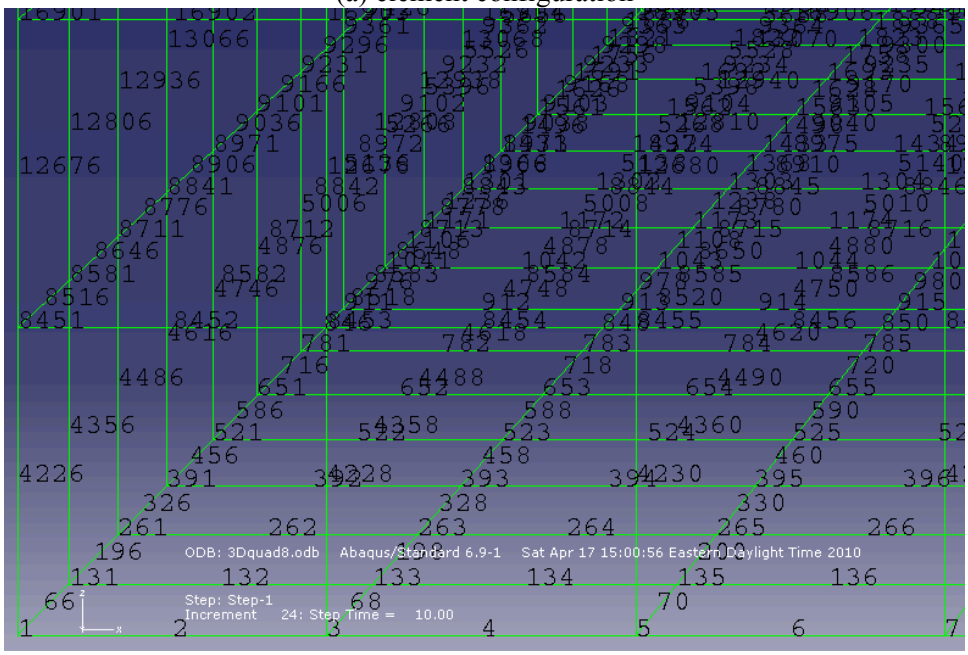

(b) node-element connectivity

Figure 60. Three-dimensional quadratic element C3D20 (a) element configuration (b) node-element connectivity

With the density set at 4, the available computing resources are only able to run a model with a maximum of 8 × 8 × 8 quadratic elements, with a geometrically identical model using 8 × 8 × 8 linear element C3D8 built for comparison. The parameters are specified in Table 39 and the resulted von Mises stress patterns and logarithmic strain distributions are shown in Figure 61.

Table 39. Simulation parameters for 3D linear and 3D quadratic element comparison (axial tensile stress)

Parameters	Sample size	Stress type	Volume fraction of cementite	Average particle diameter (μm)	Volume fraction of voids	**Element type**	Total strain
3D	8 × 8 × 8 μm^3	axial tension	6.67%	2.14	0.000001%	**linear 3D**	0.006
3D	8 × 8 × 8 μm^3	axial tension	6.67%	2.14	0.000001%	**quadratic 3D**	0.006

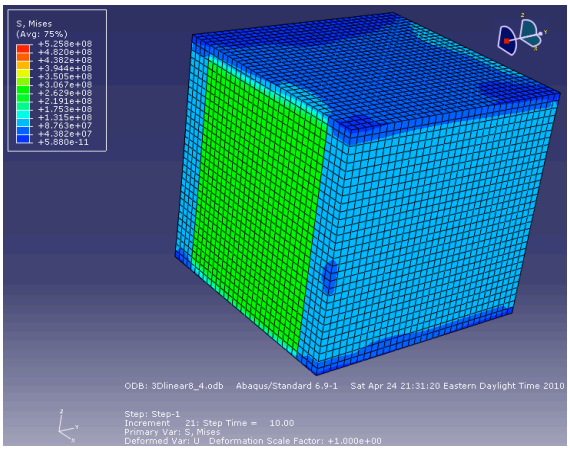

(a) Final von Mises stress with 3D linear element

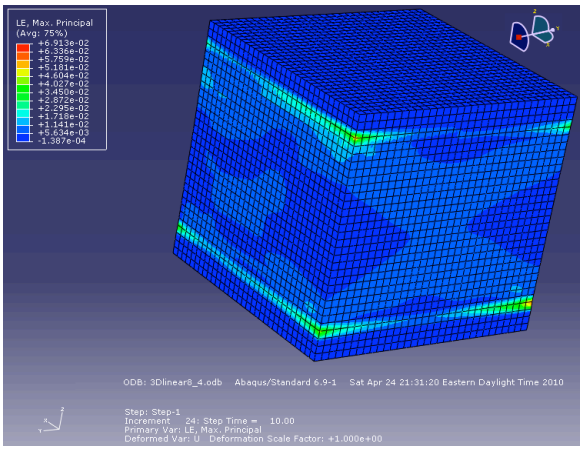

(b) Final logarithmic strain with 3D linear element

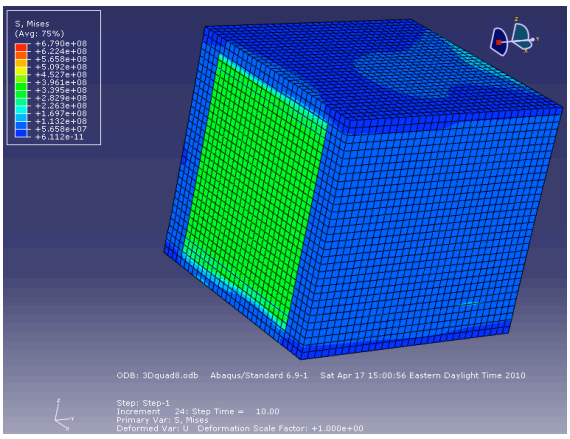

(c) Final von Mises stress with 3D quadratic element

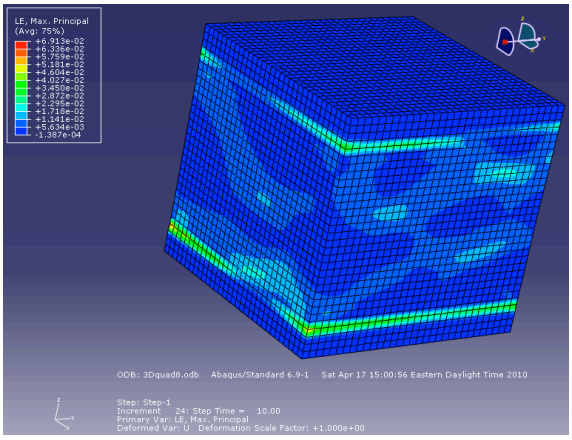

(d) Final logarithmic strain with 3D quadratic element

Figure 61. Final von Mises stress and logarithmic strain distribution pattern for a sample material under maximum 0.6% transverse tensile strain using (a) and (b) 3D linear element (c) and (d) 3D quadratic element

The resulted stress-strain curves are shown in Figure 62. Not surprisingly, those two curves fall about 1% within each other and display very similar mechanical behavior tendency, as presented in Figure 62. C3D20 is an excellent element for linear elastic calculations especially on the occasions where complex behaviors such as bending and warpage are involved [60]. Thanks to the mid-edge integration nodes in C3D20, stress concentration in the sample, as well as at the surface, can be accurately captured. It displays a lot more flexibility in bending, which is why when it comes to slender beam or thin plate structures, C3D20 is a much more powerful tool than C3D8. However, in this case, such scenarios are not involved.

Result data are provided in Table 40.

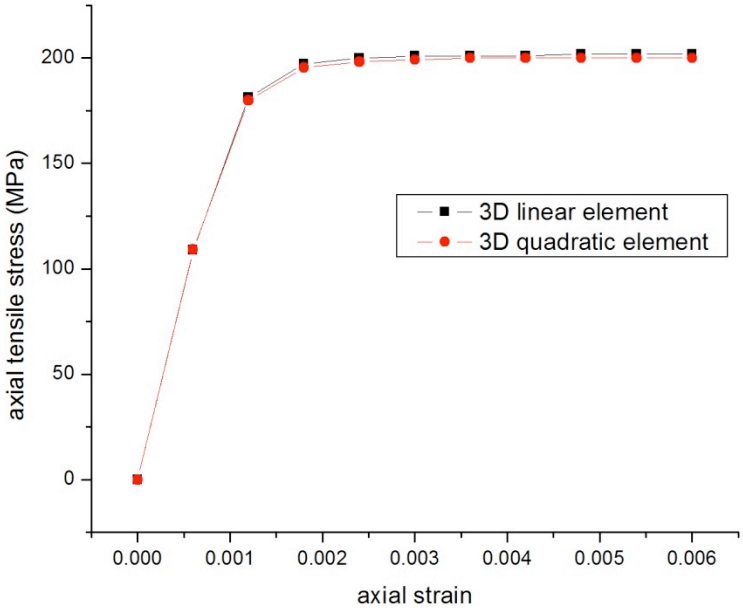

Figure 62. Stress-strain curve comparison with 2D linear element and 3D linear element

Table 40. Simulation results of 3D linear and 3D quadratic element comparison

Mechanical properties	Young's modulus (GPa)	σ_y (MPa) - yield strength
3D linear element	181.951	199.993
3D quadratic element	181.382	201.845

5.1.12.6 Crack opening propagation

As much reiterated in the previous sections, simulation can only represent the scenarios without imperfections whereas in fact, imperfections in all shape and form are commonly encountered in actuality. It makes sense to find out what impact a crack opening would have on the sample's mechanical behaviors. This section aims to tap a little on the topic of fracture analysis associated with metallurgical mechanics.

Fracture mechanics is the field of mechanics in relation to the study of the propagation of cracks in materials. It uses methods of analytical solid mechanics to calculate the driving force on a crack and those of experimental solid mechanics to characterize the material's resistance to fracture. In modern materials science, fracture mechanics is an important tool in determining the accurate mechanical properties of materials and components. This discipline was first developed during World War I by British aeronautical engineer, A. A. Griffith, to explain the failure of brittle materials [61], which later evolved into the Griffith theory as we know it.

The Griffith crack theory surmises that a balance must be struck between the decrease in the potential energy (U_{SE}) and the increase in surface energy (U_S) resulted from the presence of a crack. The surface energy arises from the fact that there is a non-equilibrium configuration of the nearest neighboring atoms at any surface in a solid body, where there exists an energy balance between the strain energy released as the crack length ($2a$) extends, as in Equation 19 and Figure 63.

$$U_{SE} = \frac{\pi\sigma^2 a^2 t}{E} \tag{19}$$

And the energy absorbed as crack grows, as in Equation 20, due to the creation of new surface.

$$U_S = 4\gamma at \qquad (20)$$

Where γ is the surface energy coefficient, σ is the applied stress, E is the Young's modulus and t is the time.

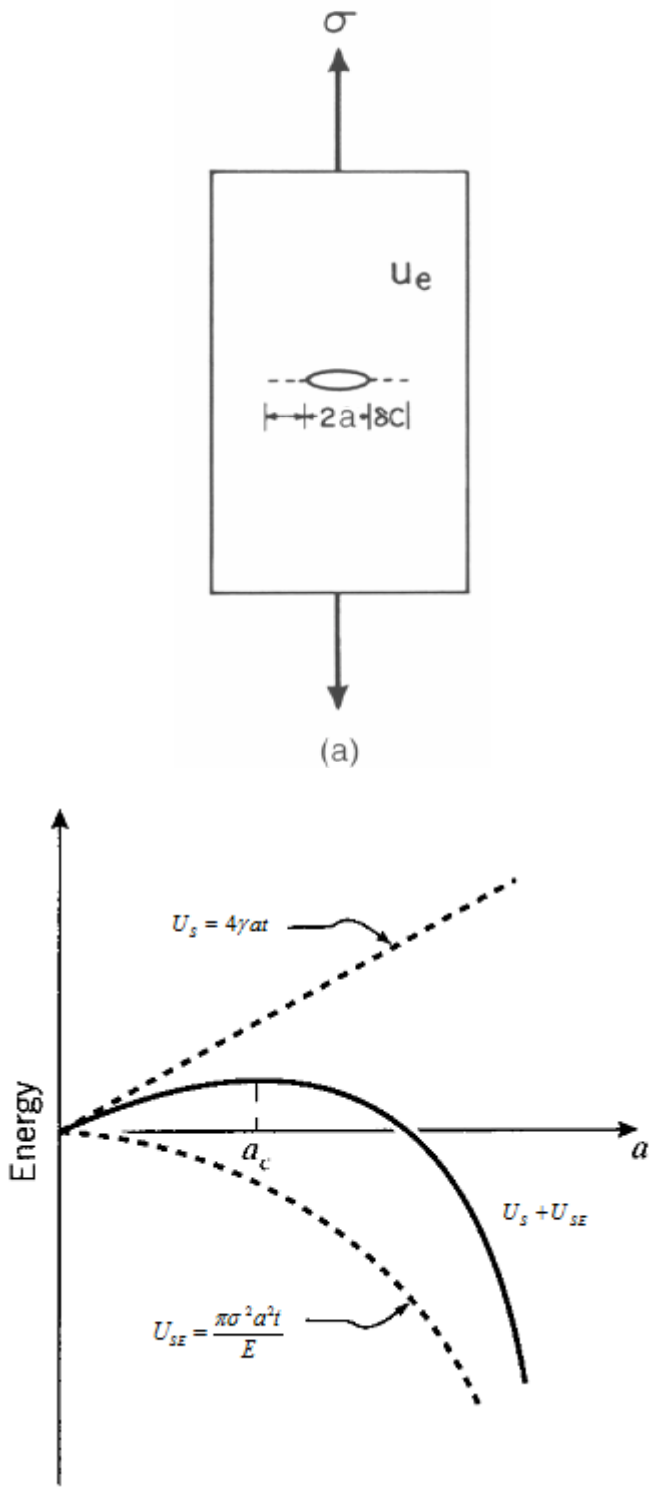

Figure 63. (a) The Griffith model for a crack propagation in a plate material (b) the development of system energy in a fracture system with respect to the half crack length *a* [62]

The next step in the development in the Griffith theory is the consideration of the energy release rate in conjunction with the crack extension, because the critical state occurs in correspondence to the maximum point in the total energy curve, i.e. $dU/da = 0$, where $U = U_{SE} + U_S$ and a is equal to a_c, the critical half crack length. As the crack continues to grow, the strain energy eventually begins to dominate the surface energy and the system can lower its total energy by letting the crack grow longer. Beyond a_c, the crack growth is spontaneous. When the $dU/da = 0$ condition is satisfied, the stress is written as σ_f and solved as in Equation 21.

$$\sigma_f = \sqrt{\frac{2E\gamma}{\pi a}} \qquad (21)$$

The original work of Griffith was meant to deal with very brittle materials, specifically glass rods [61]. This deficiency was later remedied by Irwin and Orowan that the vast majority of the released energy was not absorbed by creating new surfaces, but by energy dissipation due to the plastic flow in the material adjacent to the crack tip [63]. It was later suggested that the spontaneous fracture occurs when the strain energy is released at a rate sufficient to satisfy all the energy dissipation, which then introduced another important parameter, the energy release rate G, defined as the energy dissipated during fracture per unit of newly created fracture surface area [64-66]. The energy release rate G is of central importance to fracture analysis because the energy that must be provided to a crack tip for it to propagate must be balanced by the amount of energy dissipated due to the formation of new surfaces. The expression of G is shown in Equation 22.

$$G = -\left[\frac{\partial U}{\partial a}\right] \qquad (22)$$

Where, as stated previously, U is the elastic energy of the system and a is the half crack length. The unit of G is J/m^2. Using the stress value σ_f acquired before, the critical strain energy release rate is denoted by the parameter G_c and the Griffith equation in Equation 21 can be rewritten in the form of Equation 23:

$$\sigma_f = \sqrt{\frac{EG_c}{\pi a}} \qquad (23)$$

Equation 23 in a very succinct way describes the relations between the three important aspects of a fracture process: the material, as represented by G_c; the stress level, by σ_f; and the size of the initial crack, by a. For a given material with its associated value of G_c, the safe level of stress could be determined.

Another important concept of J-integral was first established in 1967 by Cherepanov [67] and in 1968 by Jim Rice, independently [68]. It represents a way to calculate the strain energy release rate or the energy per unit fracture surface area in a material, which is independent of the integration path around a crack. The J-integral expression for a two-dimensional crack in the x-y plane with the crack parallel to the -y axis is the line integral form as in Equation 24:

$$J = \int_{\gamma} \left(W_{dy} - T \frac{\partial \mu}{\partial x} ds \right) \qquad (24)$$

where

W = loading work per unit volume or for elastic bodies, strain energy density

γ = path of the integral which encloses or contains the crack tip

ds = increment of the contour path

T = outward traction vector on ds

μ = displacement vector at ds

There are three major modes of loading as illustrated in Figure 64:

mode I - opening or tensile mode, where the crack surfaces move directly apart;

mode II - sliding or in-plane shear mode, where the crack surfaces slide over one another in a direction perpendicular to the leading edge of the crack;

mode III - tearing shear mode, where the crack surfaces move relative to one another and parallel to the leading edge of the crack.

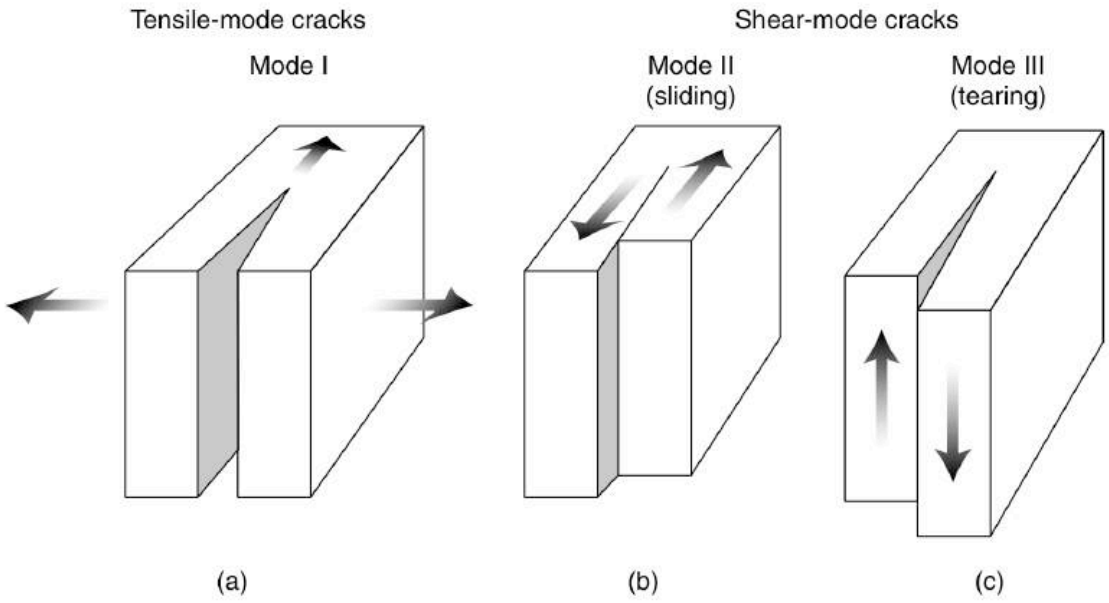

Figure 64. Three fracture modes (a) tensile mode (b) sliding mode (c) tearing mode [69]

Only mode I is simulated in this work, given the premise of linear elastic analysis and elasto-perfectly plastic material system. Under such premise, the J-Integral expression as in Equation 23 can be analytically integrated and solved [70].

While the energy-balanced approach by Equations 19 and 20 provides a great deal of insight as to the fracture process, an alternative and more practical criterion that is used to examine the stress state near the tip of a sharp crack directly has proven more useful in engineering practice. For mode I, the stress level close to the tip of the opening is characterized by Westergaard [71] as Equation 25:

$$\sigma_x = \frac{K_I}{\sqrt{2\pi r}} \cos\frac{\theta}{2}\left(1 - \sin\frac{\theta}{2}\sin\frac{3\theta}{2}\right) \qquad (25)$$

Equation 25 is defined within an axisymmetric coordinate system, with r being the distance from the origin, in this case, the crack tip and θ being the directional angle. The K_I in Equation 25 is a very important parameter known as the stress intensity factor that predict the stress state near the tip of a crack and relates the J-integral to the energy release rate G. The subscript I denotes the tensile opening mode. In the tensile opening mode, Irwin showed [72] that the stress intensity factor for a through crack of length $2a$ in an infinite plane to a uniform tensile stress α is

$$K_I = \sigma\sqrt{\pi a} = \sqrt{EJ} \qquad (26)$$

and

$$J_{IC} = G_{IC} = \begin{Bmatrix} \dfrac{K_I^2}{E} \\ \dfrac{\left(1-\nu^2\right)K_I^2}{E} \end{Bmatrix} \begin{matrix} plane\ stress \\ plane\ strain \end{matrix} \qquad (27)$$

Equations 26 and 27 serve as the juncture between the J-Integral, the crack length, the stress around the crack tip and the energy release rate G. The complete derivation process and discussions regarding other scenarios are available in a variety of materials on fracture mechanics [73, 74].

The crack propagation is then simulated based on a model of 20 × 20 μm^2. The generation of the model is similar to the previous cases except a few alterations: a small portion of the model is replaced with mesh constituted by modified quadratic elements to imitate the configuration of the seam of a crack opening, as shown in Figure 65.

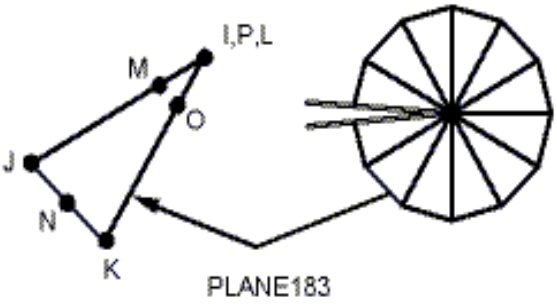

(a)

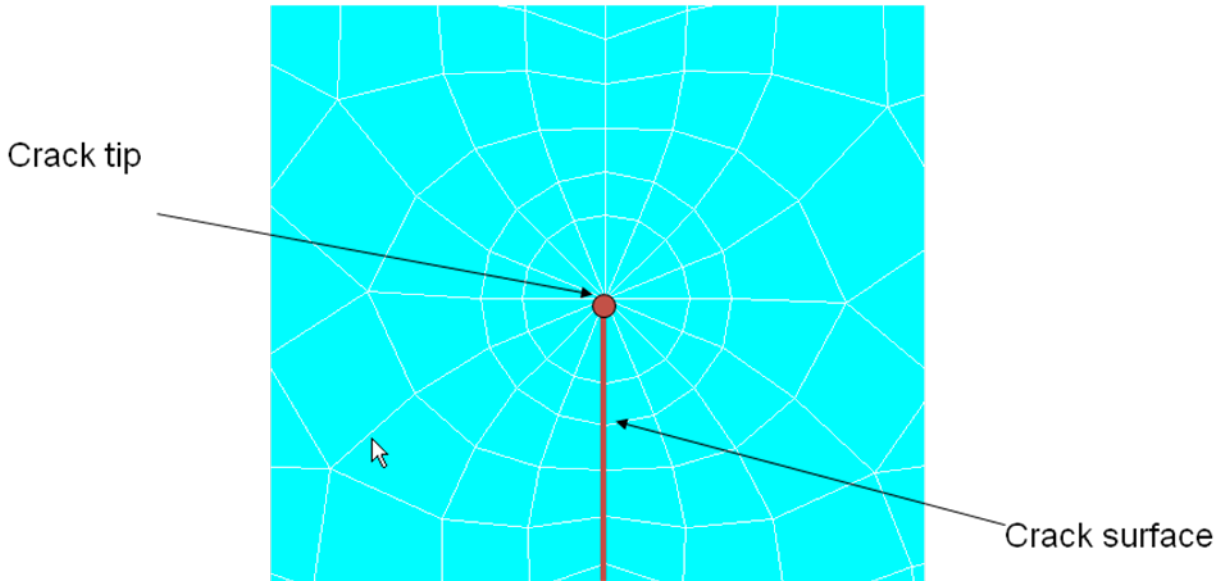

(b)

Figure 65. (a) Choice of element and modification of mid-side nodes (b) crack tip and crack surface

Figures 65 and 66 provide the details of element type and element configurations around the tip of the crack. As shown in Figure 65(a), these quadratic quadrilateral elements have one of their edges collapse to a single point (plane 183) and also have their mid-side nodes moved to one quarter of the length of the neighboring sides away from the collapsed edges to represent the crack tip.

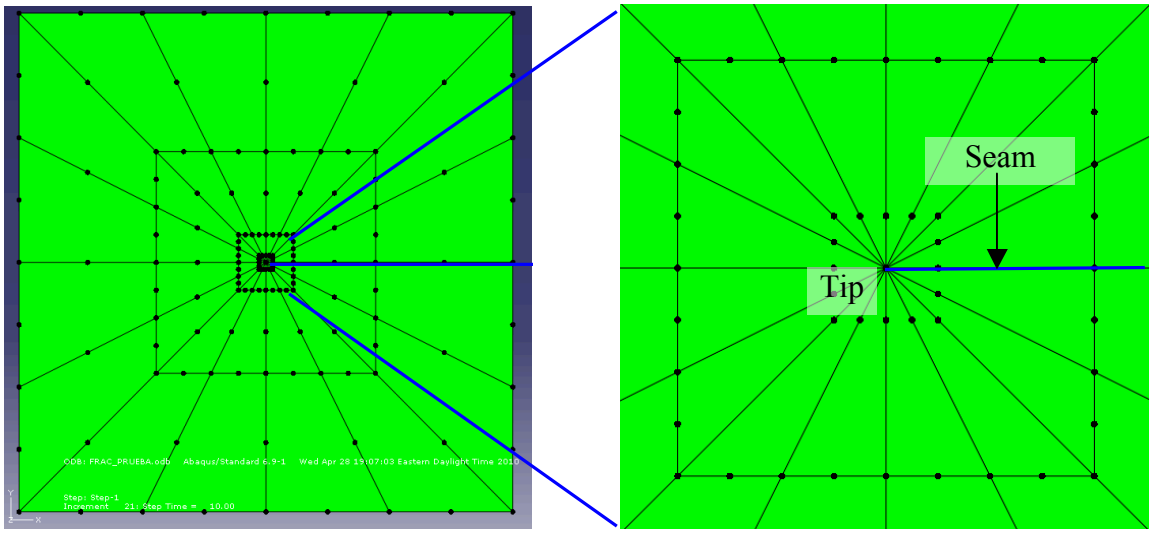

Figure 66. Mesh used in and around the crack tip

Figure 66 provides the details of element configurations around the tip of the crack. The overall geometry, including the crack area, is shown in Figure 67. Unlike the perfect mesh generated automatically by Matlab codes that arrange and label elements and nodes sequentially, the altered mesh here is generated manually. The method of "brute force" is used to reposition the nodes involved in the local area to resemble the configuration of the crack tip and the seam.

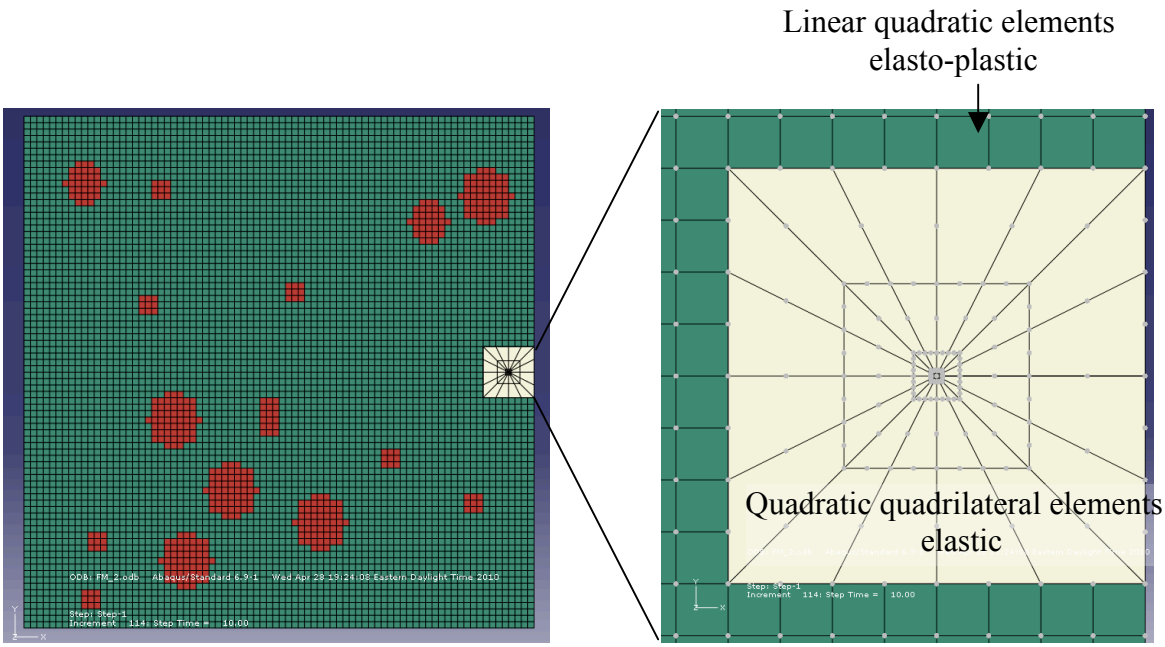

Figure 67. Overall geometry of the fracture analysis model and elements of choice

With this configuration, Abaqus is able to simulate the $1/\sqrt{r}$ stress singularity for an elastic fracture. Consequently, the material is assumed to be elastic-plastic while using the same material constants as the previous models (the Young's modulus = 211 GPa, the Poisson's ratio = 0.29). Similar to the previous axial tension tests, the boundary conditions applied to the model correspond to 10 discrete increments of 1.2×10^{-7} m, from 0 to 0.6% axial strain.

Results show that the model is able to reproduce the stress concentration at the tip, as in Figure 68. As it turns out, while the von Mises stress in the surrounding elastic zone is largely equal to the yield strength, the stress at the tip is up on the magnitude of 10 GPa. As far as the author is aware, while FEM is able to calculate the extreme stress responses under some unusually large applied load by stretching the elements, it is not able to actually have the elements break apart to embody the material failure scenario. It requires constant checking on the stress level to precisely pinpoint the exact location and moment at which the failure occurs.

The J-Integral value at the tip is illustrated as a function of the axial strain of the sample in Figure 69. As expected for a model I type of loading, the J-integral increases with the axial strain. However, the increments are decelerating as the strain increases due

to the presence of second-phase particles that deviate the strain localization from the ideal 45º. The butterfly-shaped plastic zone in Figure 68(b) resembles what is obtained under the same circumstances but using a different software (Ansys) in Figure 68(c).

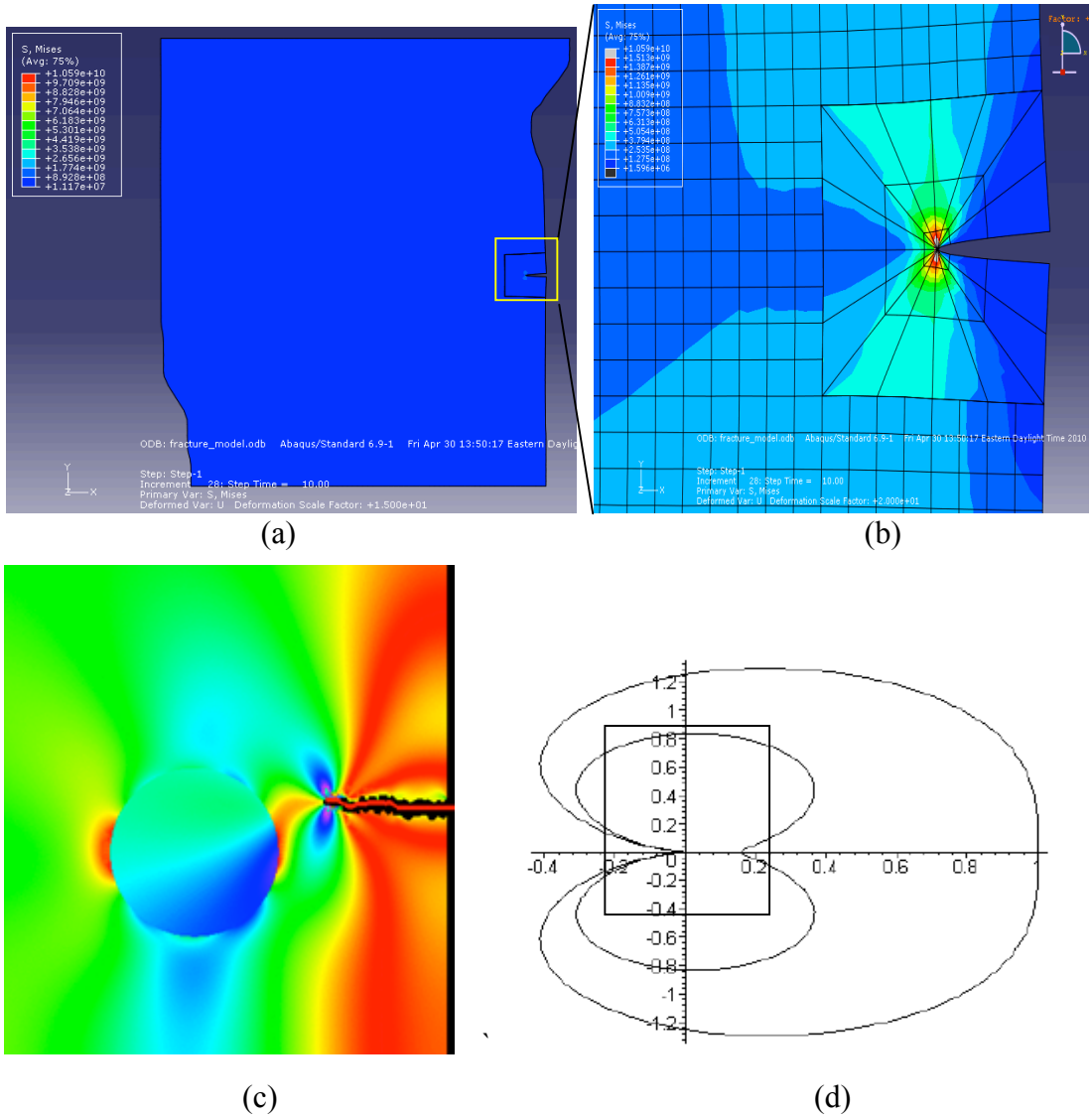

Figure 68. (a) Final logarithmic strain in the model (b) von Mises stress at the tip of the crack (c) plastic zone distribution around a crack opening obtained using Ansys (d) normalized plastic zone shapes for plane strain (inner contour) and plane stress (outer contour) for mode I opening [62]

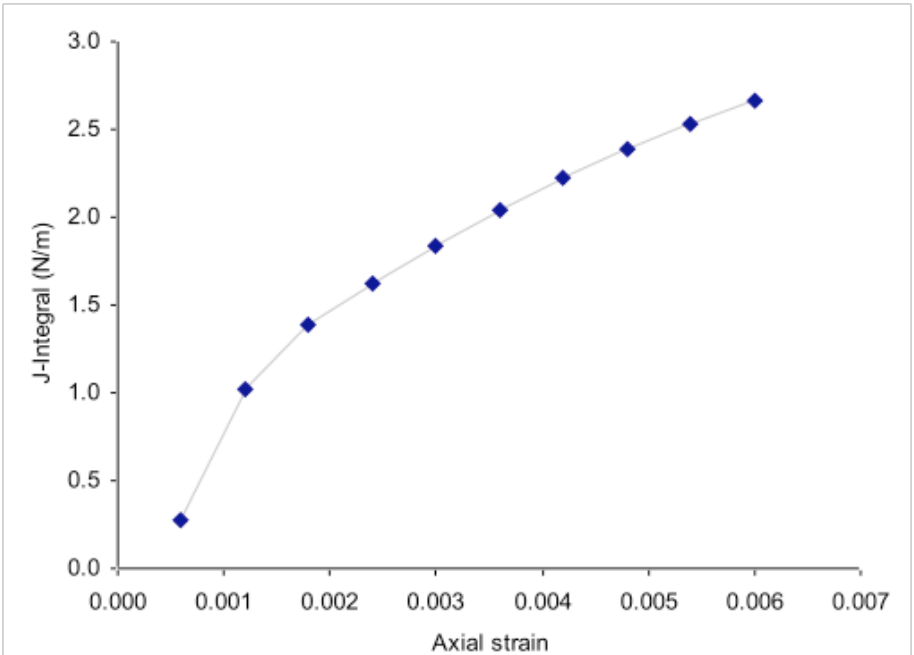

Figure 69. The J-Integral calculated at the first contour of elements surrounding the tip

The resulted stress-strain curves are shown in Figure 70, in which it is observed that with the initial crack the obtained Young's modulus value and yield strength are noticeably lower than their counterparts in a model with ideally shaped elements and closer to the literature values.

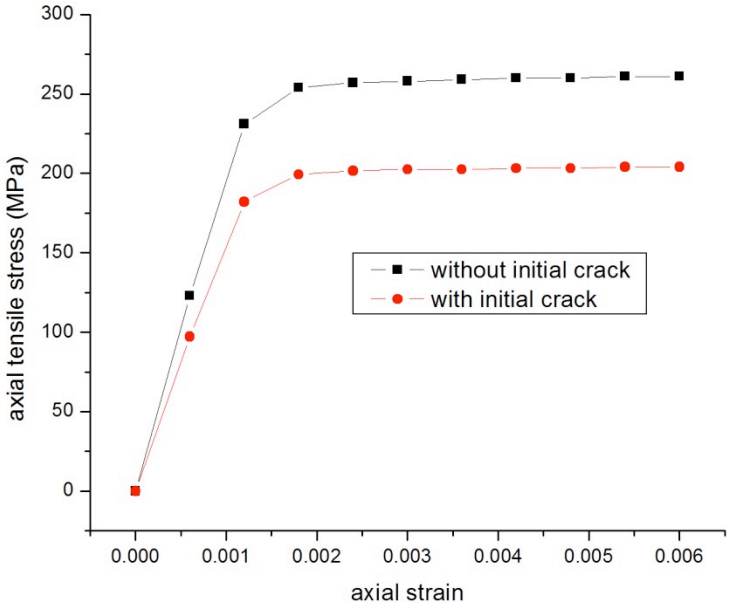

Figure 70. Comparison between the stress-strain curves obtained with and without initial crack

5.1.13 Mechanical Properties of Decarburized Spheroidite

The experiment was conducted on mechanical testing instrument (MTI) that can perform tension and shear tests with external force up to 30,000 lb. MTI is able to record the instant changes during deformation but its results are hardly very accurate for it can only document the actual force and displacement values, which later need to be converted into stresses and strains manually. The data are relatively inaccurate as the converted stress-strain curves are engineering stress-strain curves, while the cross-section area of the sample hardly remains constant throughout the test. Then again, as the samples experimented on assume the shape of a thin sheet that does not exhibit much deformation in the cross section, the converted stress-strain curve should be able to provide a relatively authentic description of the sample's mechanical properties nonetheless. In the experiment the maximum strain of 0.6%, so no material failure is observed.

The collected force-displacement data were converted to stress-strain curves and shown in Figure 71. Also included in Figure 71 for comparison is the stress-strain curves for simulated axial tension in decarburized spheroidite. The values of the acquired mechanical properties by both approaches are provided in Table 41.

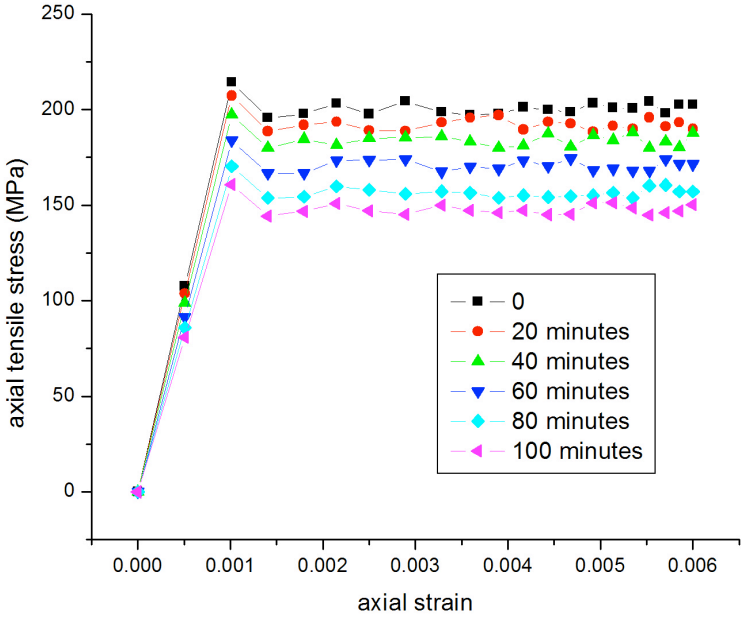

(a) experimental data

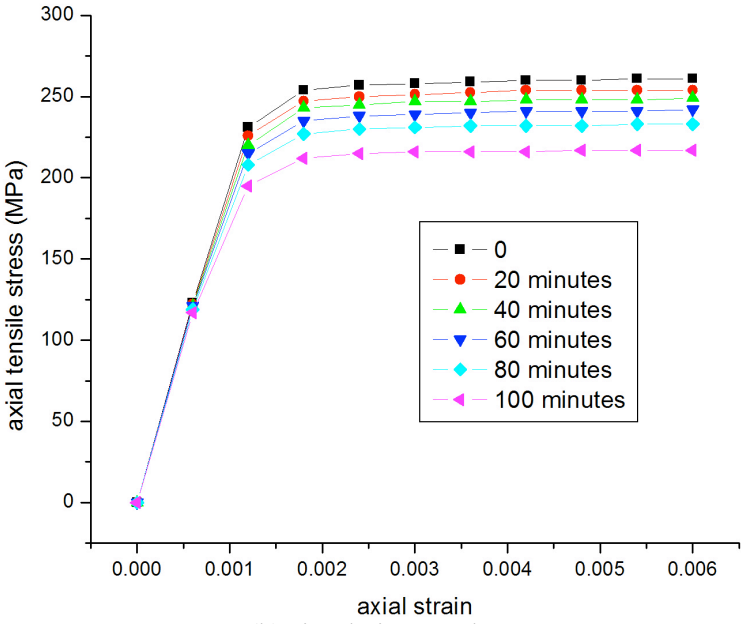

(b) simulation results

Figure 71. Comparison of experimentally obtained and simulated axial tensile stress-strain curves for the decarburized spherodite (a) experimental results (b) simulation results

Table 41. Comparison of simulation results and experiment data (axial tension)

	0	20	40	60	80	100
Simulated decarb. depths (μm)	0	1.6	3.917	6.55	9.3	13.53
E-axial (GPa) - simulation	208.235	203.337	202.191	201.478	198.670	195.374
E-axial (GPa) - experiment	214.778	207.127	197.067	183.476	170.305	160.398
σ_y-axial (MPa) - simulation	261.014	253.829	239.002	221.194	209.852	195.181
σ_y-axial (MPa) - experiment	228.670	219.476	204.995	195.700	171.008	157.717

In Figure 71(a), the upper yield point of each stress-strain curve is clearly visible. In practice, after reaching the upper yield point, elastic-plastic metallic material tends to witness a substantial drop in stress because of the dislocations escaping from the Cottrell atmosphere and then the material enters a period called yield point elongation, where the stress remains roughly constant while fluctuating insignificantly, as the strain keeps increasing until reaching the lower yield point [75-79]. This process results from dynamic strain aging, formation of deformation twinning, slipping among other phenomena and is too complicated for FEM to approximate but the elastic parts of two sets of curves coincide well.

Table 41 shows that the difference of the Young's moduli obtained from experiment and simulation ranges from 1.83% to 21.83% and that of yield strengths falls between 13.02% and 23.08%. Both the Young's modulus and axial yield strength values are lower than their simulation counterparts because the model assumes materials are perfect whereas in reality the voids, surface defects, crack openings and other imperfections that could lead to low modulus and early yielding are very common. The two series of data decrease approximately at the same rate. With the growing decarburization depth, the values of E and σ_y obtained using 3D elements are clearly higher than those with 2D elements through the same point, implying that the model using 3D elements displays less sensitivity and could potentially provide better results. Similar comparisons have been made with shear stress and transverse tension as well, as

illustrated in Figure 72, the corresponding stress-strain data compiled in Tables 42 and 43.

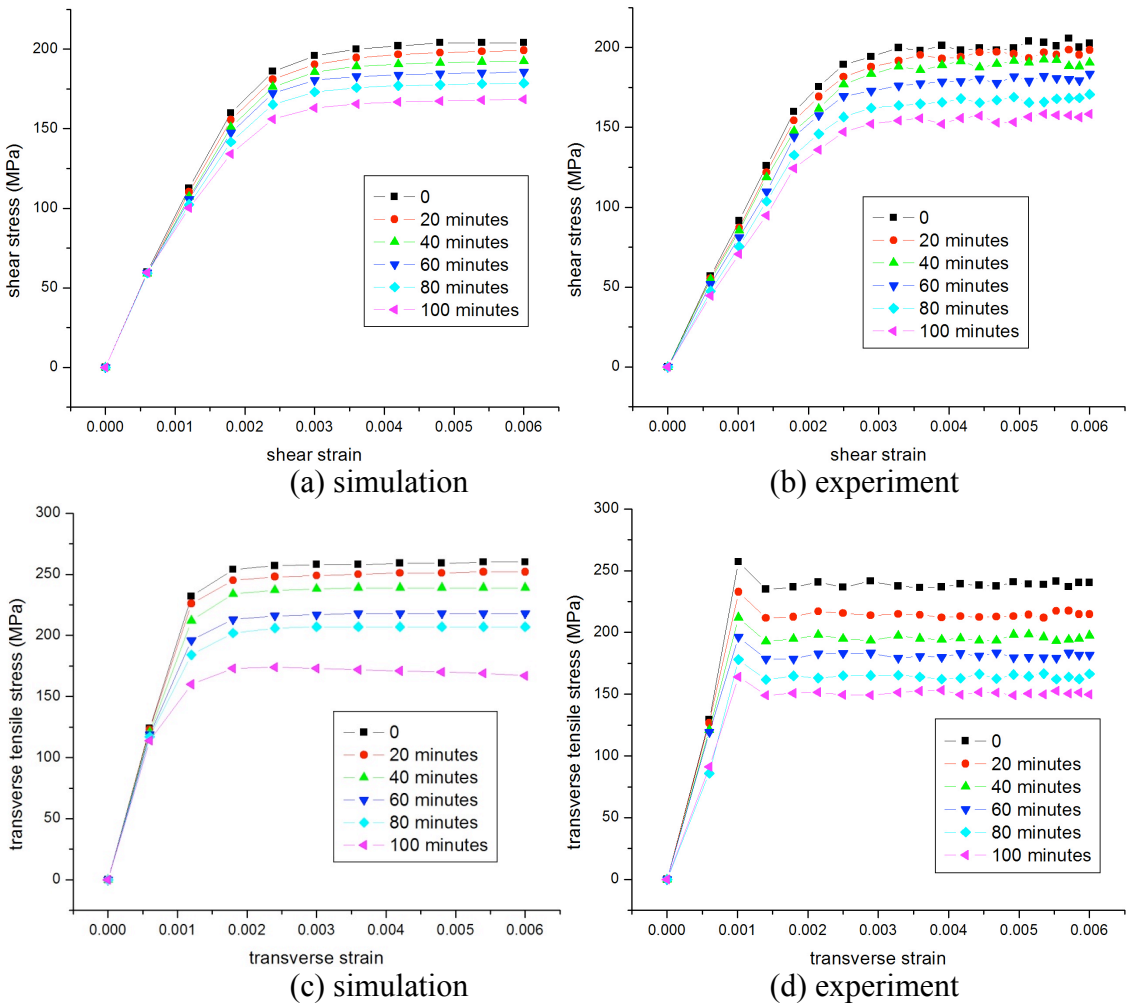

Figure 72. Comparison of experimentally obtained and simulated stress-strain curves, (a) and (b) shear stress and (c) and (d) transverse tensile stress for the decarburized spherodite sample

Table 42. Comparison of simulation results and experiment data (shear stress)

	0	20	40	60	80	100
Simulated decarb. depths (μm)	0	7	19	33	53	80
S - shear (GPa) - simulation	88.66	86.286	83.57	81.446	78.002	73.844
S - axial (GPa) - experiment	89.566	86.225	86.225	78.042	73.706	67.690
σ_y - axial (MPa) - simulation	204.2	199.2	192.4	185.6	178.6	168.6
σ_y - axial (MPa) - experiment	202.559	198.381	190.464	183.445	170.692	158.357

Table 43. Comparison of simulation results and experiment data (transverse tension)

	0	20	40	60	80	100
Simulated decarb. depths (μm)	0	7	19	33	53	80
E-transverse (GPa) - simulation	208.335	187.926	176.421	163.356	153.008	133.067
E- transverse (GPa) - experiment	210.741	190.694	173.620	160.613	145.915	134.331
σ_y - transverse (MPa) - simulation	260.232	251.931	238.655	217.981	206.820	173.576
σ_y - transverse (MPa) - experiment	240.175	214.724	197.471	181.898	162.338	151.456

The results obtained under shear stress and transverse tension match even better with the simulation results, with the differences of the values of the Young's moduli and yield strength falling about 5% within experiment results. Unfortunately, the values of the Poisson's ratio obtained from those simulations do not seem very accurate, with some far off of the normal range. This is mostly likely because of the small scale of simulated samples which are in the range of 0.6 mm. In this case, localization of embedded particles will considerably affect the expansion and contraction in the local area. Besides, the average size of second-phase particles and the total volume fraction are not experimentally controllable variables so the validation of those parameters' impacts is not explicitly available until we manage to develop more flexible and more powerful processing approaches.

5.2 Finite Element Modeling Uniaxial Deformation of Hollow Spheres

5.2.1 Compressive Pressure from Conceptual Stress

An FEM model is implemented to provide a theoretical portrait for the deformation of a maraging steel hollow sphere under compressive stress. The research conducted so far focuses on assessing the resulted mechanical properties of the steel samples after certain heat treatments. Now it behooves the researchers to gain a quantitative understanding of the deformation behaviors and compression-resistant capabilities of the said spheres, both experimentally and theoretically. At this stage, the sphere is made of M350 steel, with a diameter varying between 1.8 and 2.7 mm, with the density ranging from 2.0 to 2.3 g/cm^3, respectively. As can be seen from Figure 73, the wall thickness increases linearly with diameter as would be expected from equations 28, 29 and 30.

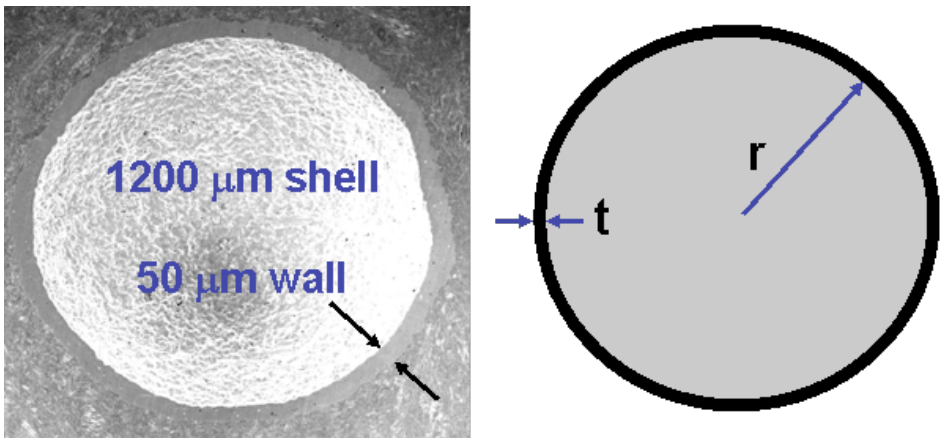

Figure 73. Cross section of typical M350 sphere with 25% relative density [80]

$$\rho_s = \frac{m}{\frac{4}{3}\pi\left(\frac{d_{avg}}{2}\right)^3} \qquad (28)$$

$$f_v = \frac{\rho_s}{\rho_0} \qquad (29)$$

$$t = \frac{\left(\frac{d_{avg}}{2}\right) f_v}{3} \qquad (30)$$

For each sphere, the sphere's mass (m) and average diameter (d_{avg}) are measured, with which the sphere density (ρ_s) is calculated, as well as the relative density (f_v) and wall thickness (t_w). Here the term "maraging" refers to martensite that is produced through an aging process. When aging is applied, the samples are maintained at an elevated temperature over a prolonged period of time before they cool to the ambient temperature, the outcome of which is crystalline and appears harder and stronger than it would were the steel allowed to cool off naturally in air. Among all maraging steels, M350 has become an integral alloy in the aviation and aerospace industry due to its strength and its ability to withstand extreme conditions including frequent and sudden changes in speed, temperature and pressure, making it an ideal candidate for rocket motor casings, takeoff and landing gears, and certain munitions and weaponry for defense companies, as well as the natural choice for proppant production [81].

In Figure 74, four proppants deformed under different compressive stress levels are presented for comparison. In the actual test, the compressive pressure is applied via two rigid alumina plates that are positioned parallel to each other, above and below the hollow spheres respectively. The top alumina plate moves down perpendicularly towards the bottom plate causing the sphere to deform in the process, approximating what happens in the compression test.

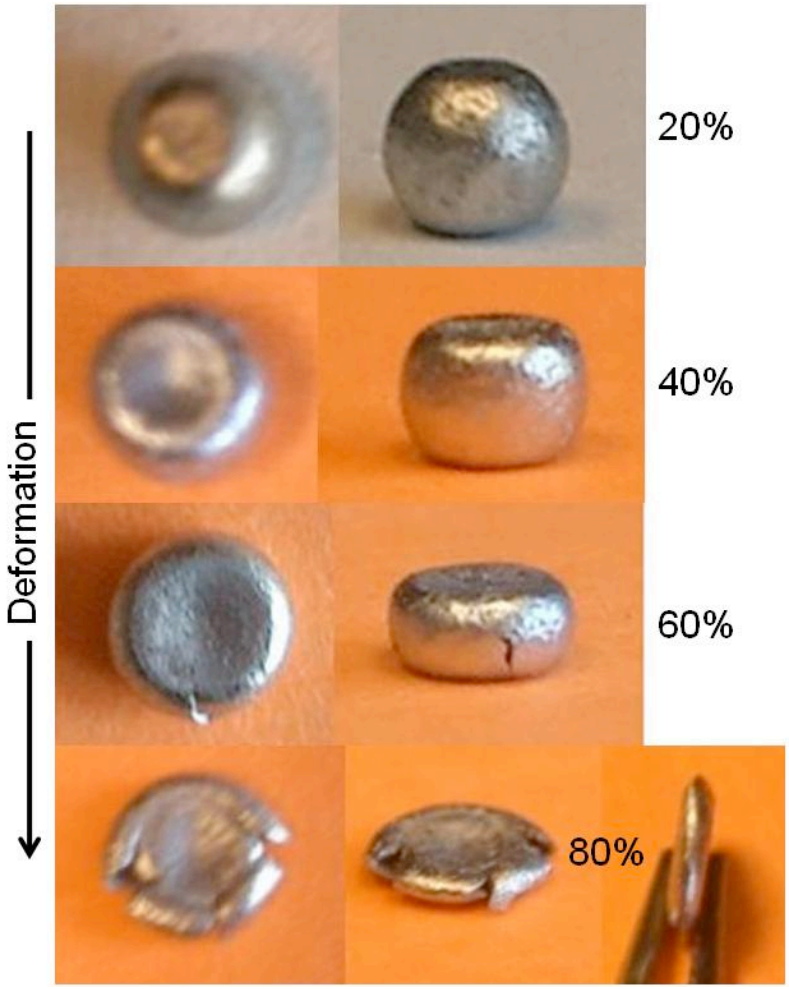

Figure 74. Images of thin wall, M350, hollow spheres over large ranges of deformation [82]

For this model, it is assumed that the hollow sphere is with an inner radius of 1.215 mm and an outer radius of 1.265 mm, which are also the sizes of the spheres used for experiment. The material is assumed to be maraging steel M350 in this model with the Young's modulus at 200 GPa and the Poisson's ratio 0.29. Only a quarter sphere is simulated to expose the internal stress distribution. Encastré boundary conditions are applied on the sphere where it is supposed to join the other three quadrants to ensure no translation or rotation occurs on those interfaces. The resulted deformation plots are shown in Figure 75.

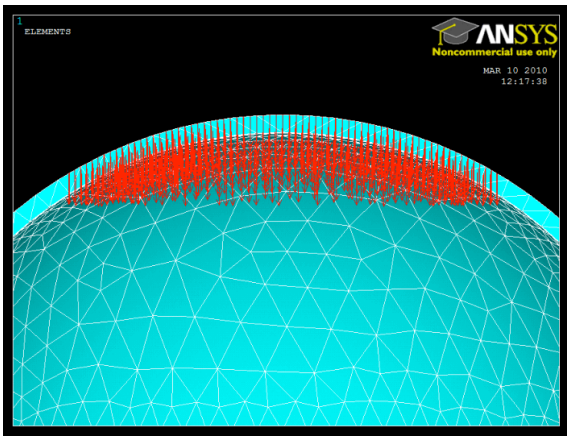

(a) Status of applied stress

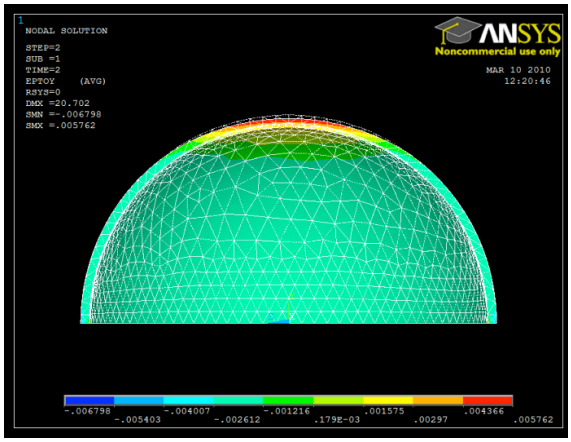

(b) Total mechanical strain under 50 GPa

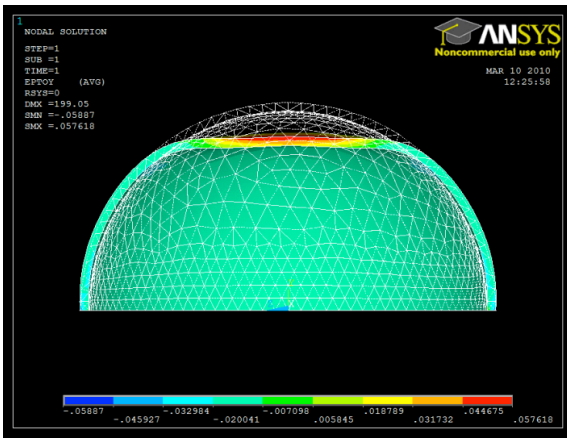

(c) Total mechanical strain under 500GPa

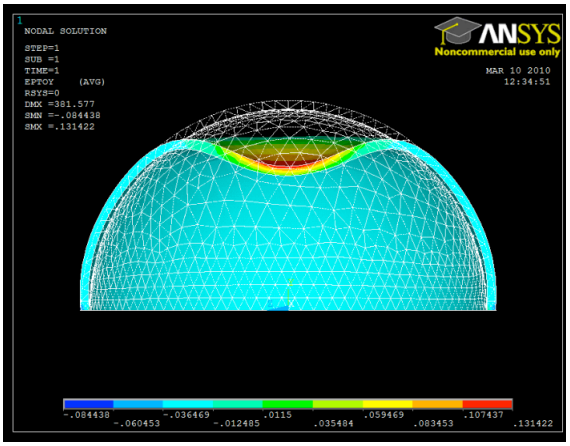

(d) Total mechanical strain under 1000GPa

Figure 75. Deformation and strain status of a hollow steel proppant in contrast with its undeformed model (a) stress distribution (b) total mechanical strain under 50 GPa (c) total mechanical strain under 500 GPa (d) total mechanical strain under 1000 GPa

Under 50 GPa, the maximum strain at the top of the sphere is 0.437%, whereas when the applied stress is increased to 500 GPa and 1000 GPa, the total strain at the same location has reached 4.47% and 10.74%, respectively. This model provides us immense freedom in varying the material's dimensions, property parameters, stress types, stress distributions among many others. However, all the deformation is set to occur within the elastic range and the compression is applied as abstract force vectors instead of actual rigid alumina plates, which leaves a lot of room for improvement. In the next step, the plastic deformation will be included as well as the interactions between the hollow sphere and the plates.

5.2.2 Contact Element

In order to properly simulate the interactions between the rigid plates and the hollow sphere, as well as provide the most accurate possible stress-strain curve for the sphere deformation, contact elements are adopted to correctly depict the deformation process of the hollow spheres.

5.2.2.1 Contact problem

Vastly different from the single-body FEM models previously discussed, contact is a problem involving load transferring between different bodies. It could be the convection and radiation between adjacent surfaces with small gap in between [83], the heat generation issue due to frictional dissipation [84-85] or the structural problems where surfaces belonging to different bodies come into contact with each other [86-89]. The mechanism of that kind of load transferring depends on the nature of interaction between two or more contact surfaces. The direct observation of the contact phenomenon and the measuring of certain quantities is often impractical. Contact problem is also further complicated by the fact that the behaviors of the elements, including but not limited to the slipping and scraping between the two joining objects, depend very much on the specific properties of the materials: the state of target bodies (rigid or deformable relative to each other), the friction coefficient between adjoining surfaces (smooth or rough surfaces), the type and intensity of loading (equilibrium, ramp or stepped), the tangent modulus (both within and beyond the elastic range), the direction of loading in relation to contact surfaces (normal, shear or otherwise) and how the boundary elements are fastened.

Specifically, the contact problem we are discussing here is a non-conformal problem with friction, which necessitates the introduction of the iteration procedures. The geometry of the setting and the corresponding mesh is illustrated in Figure 76 and the failure to choose proper contact elements between the contacting surfaces will cause the

structure to deform unnaturally and the components to cut into each other as if other components did not exist, as illustrated in Figure 77.

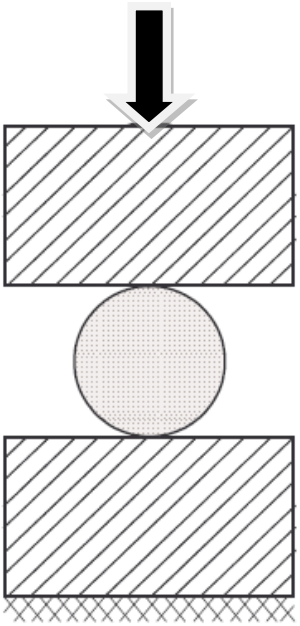

(a)

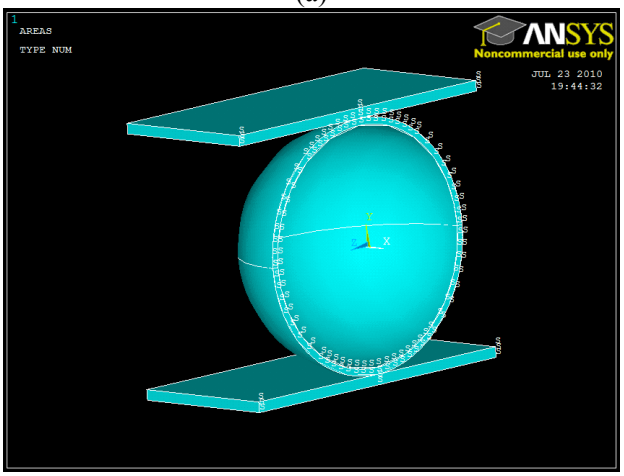

(b)

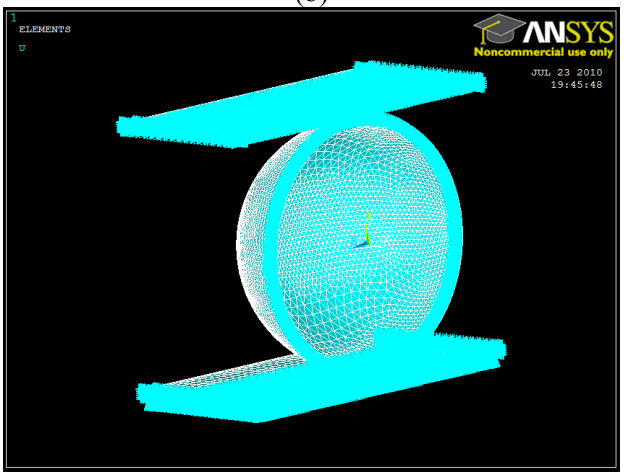

(c)

Figure 76. (a) The cartoon illustration of the plate-sphere-plate structure (b) unmeshed (c) meshed half-sphere-plate structure

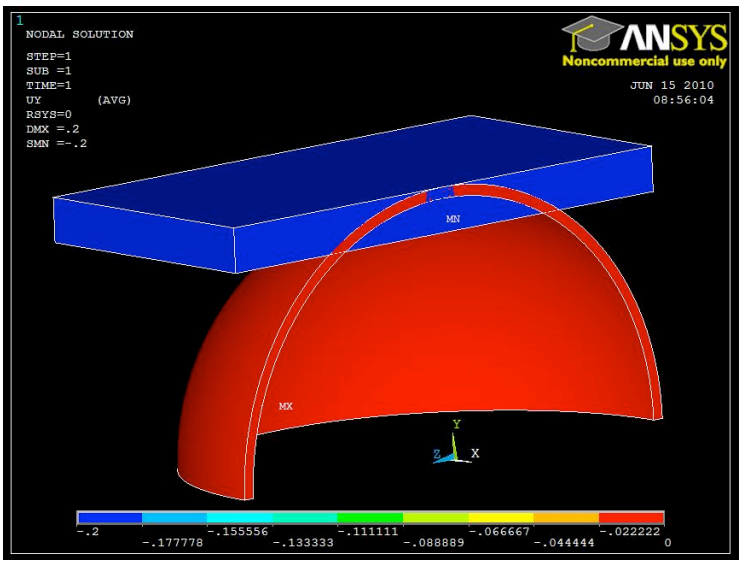

(a)

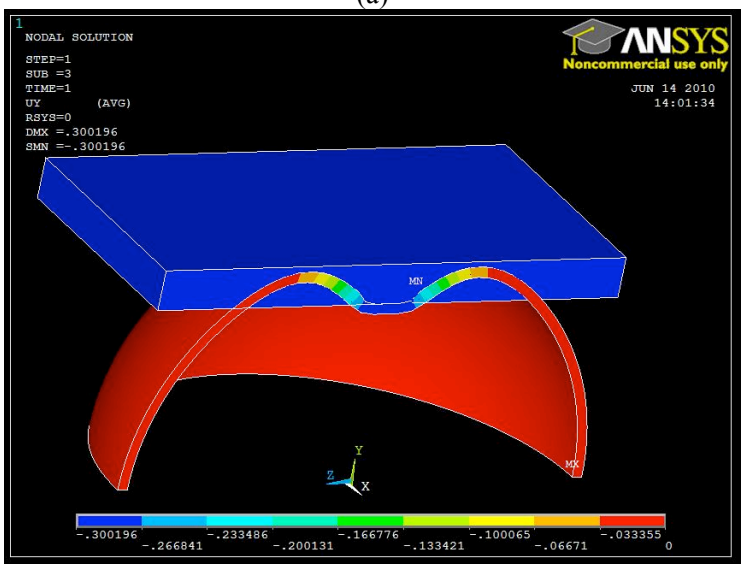

(b)

Figure 77. Results obtained (a) without contact elements (b) with contact elements only applied locally

5.2.2.2 Numerical solutions

As detailed in Section 3.2, for each element there is an equation $[K]\{u\}=\{F\}$ that governs the relations between the key variables. The incremental-iterative method for solving the system of non-linear equations specific to an elastic-perfect plastic system is as following:

1. Known: displacement of nodes $u_{t+\Delta t}^{i-1}$

2. Solve: stresses $F_{t+\Delta t}^{i-1}$

3. Solve: $[K_{t+\Delta t}^{i-1}]\left\{u_{t+\Delta t}^{i-1}\right\}=\left\{F_{t+\Delta t}^{i-1}\right\}$

4. Solve: $u_{t+\Delta t}^{i}=u_{t+\Delta t}^{i-1}+\Delta u$, and $[K_{t+\Delta t}^{i-1}]\left\{u_{t+\Delta t}^{i}\right\}=\left\{F_{t+\Delta t}^{i}\right\}$

Repeat steps from 1 to 4 till convergence is achieved. Note that in most FEM cases, the stiffness matrix $\left[K_{t+\Delta t}^{i}\right]$ remains constant throughout. However, there exists a more advanced FEM technique named adaptive mesh that can adjust the attributes of elements based on the latest computed results to obtain the highest precision and accuracy, during which process the stiffness matrix, which is closely related to the shape of elements, changes as well. Especially so in the case of contact problems, the topographic variations at the contact area are even more prominent, which naturally commands the application of contact elements.

The aforementioned procedure is for solving a set of regular non-linear equations but in order for this procedure to work for contact problems, the numerical solution uses Updated Lagrange Formulation (ULF), which is very convenient for modeling the contact behaviors between non-conform elastic bodies especially when friction is considered [90-94].

1. Known: the system equation has been altered by including an external force term, as shown in Equation 31.

$$[K_{t+\Delta t}^{i-1}]\left\{u_{t+\Delta t}^{i}\right\} = \left\{R_{t+\Delta t}^{i}\right\} - \left\{F_{t+\Delta t}^{i}\right\} \qquad (31)$$

$\left\{R_t^i\right\}$ stands for the external load, as in Equation (32), with the three components representing volume, surface and concentrated forces.

$$R_t^i = R_{Vt}^i + R_{St}^i + R_{Ct}^i \qquad (32)$$

2. Solve: the linear transformation equation from step 1 is altered to Equation 33:

$$\left[K^{i-1}\right]\left\{\Delta u^i\right\} = \left\{R_{t+\Delta t} - F_{t+\Delta t}^i\right\} - \left\{R_t - F_t^i\right\} \qquad (33)$$

Δu^i consists of required degree of freedom potential contact nodes.

In this case of contact with fraction, $F_{t+\Delta t}^{i-1}$ is the force that causes friction in the slipping zone, and solved with the normal contact force from previous iteration

3. Solve: the system of equation is solved by Gauss iteration method

4. Control of contact status:

In the case of fraction the pairs of nodes inside the contact area must satisfy the following conditions:

1) in the sticking zone,

$$R_{St}^i < \mu\left|F_{t+\Delta t}^{i-1}\right| \qquad (34)$$

2) in the slipping zone,

$$R_{St}^i = \mu\left|F_{t+\Delta t}^{i-1}\right| \qquad (35)$$

μ is the friction coefficient.

The numerical algorithm presented above lays the foundation for writing the program analyzing the contact between two or more non-conformal elastic bodies. When contact is assumed friction-less, constant-iteration would suffice, but for contact with friction it calls for an incremental-iterative methods.

The above introduction for the algorithm for solving the contact problem is the simplified principle. Ansys' manual on contact element lays out more detailed derivations [95-96]. Both Abaqus and Ansys have developed complex features for the contact element selection, analysis options (large/small static/transient displacement), time control, damping coefficients, midstep criteria, time integration, creep option, cutback control, termination criteria among many others. These features will not be extensively discussed except for the element choice as the discontinuities along the contacting surfaces need to be addressed with specially refined grid and mesh.

5.2.2.3 Element selection and model generation

In order to simulate the interactions between contacting surfaces, proper elements have to be selected to fill up the geometries of the simulated objects. The friction and sliding behaviors are non-linear in nature so all linear elements are ruled out. Quadratic quadrilateral element is chosen over quadratic tetrahedral element to simulate the contacting behaviors, with the reason being that tetrahedral elements generate meshes as subparametric quadratic elements, which means that the edges of the triangles are always straight, as shown in Figure 78 (a), such that the subparametric elements are actually functionally identical to linear elements [97], even though they sometimes can be used for quadratic interpolating functions. Also contributing to the decision is the fact that the basic geometry of the rigid bodies involved are more cubic than triangular, making it easier to fill the structure up with the formal.

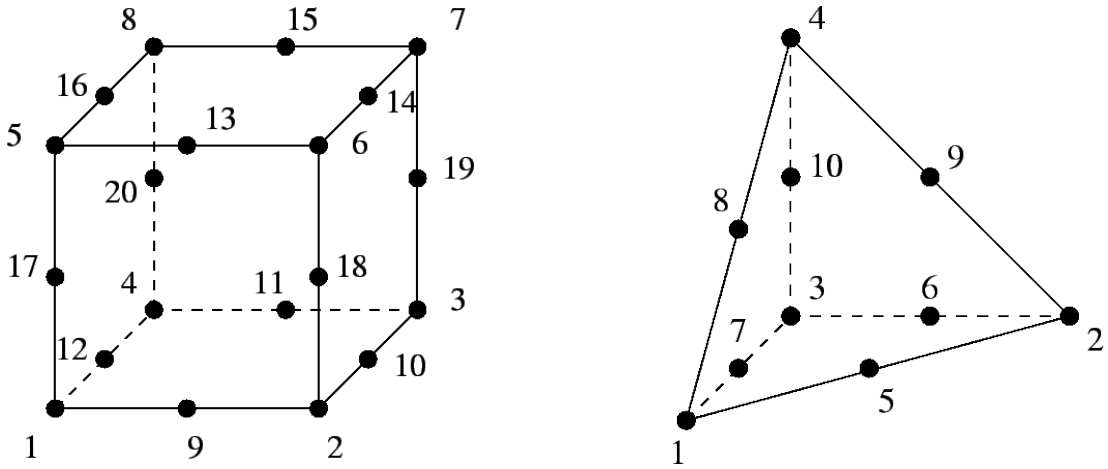

(a) (b)

Figure 78. Elements under consideration for the simulation (a) quadratic quadrilateral element (b) quadratic tetrahedral element

On the other hand, as seen in Figure 78 (a), the locations of the mid-side nodes in a quadratic quadrilateral element enable it to accurately describe bending, warpage, contact interactions, opening of a fracture in an elastic material, among other non-linear mechanical phenomena. In addition to that, quadratic quadrilateral elements are capable of having faces of the element collapse into edges, consequently forming wedge-shaped elements to conform to the most peculiar geometries, a fact that makes the element the ideal choice for this simulation.

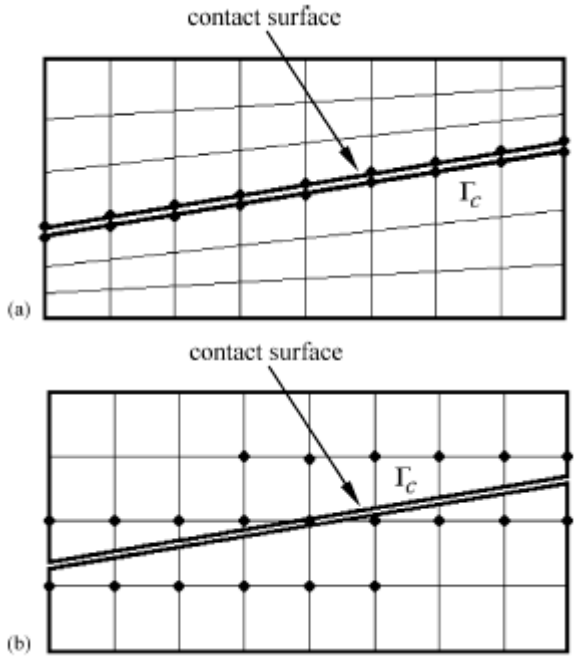

Figure 79. The mesh adjacent to the contact surface between two bodies (a) a mesh that conforms to the geometry of the contact pair (b) a mesh that is enriched and refined by using enrichment functions [89]

The conventional approach is to generate the contact elements along the contact surface, as shown in Figure 79(a). However, besides creating a discontinuity in the approximation, this strategy is very cumbersome and potentially problematic if the contact surface evolves and the topography changes as simulation proceeds, or if non-conformal configurations are to be considered. In this study, the modeling of the discontinuity along the contact surface is addressed using extrinsic enrichment, where the contact elements distribution across the contact surface as in Figure 79 (b) is capable of modeling the evolution of the contact surface when the dotted nodes are enriched with functions which are discontinuous across the contacting surface.

Furthermore, for the elements intercepted by the contact surface, the nodal distribution in the quadratic elements sometimes is insufficient for precise numerical integration, and it is necessary to modify the quadratic points on the edges of the elements to accurately evaluate the contribution from both sides of the contact surface.

Figure 80 presents the modified node points of sub-triangular elements used for numerical integration across the contact surface.

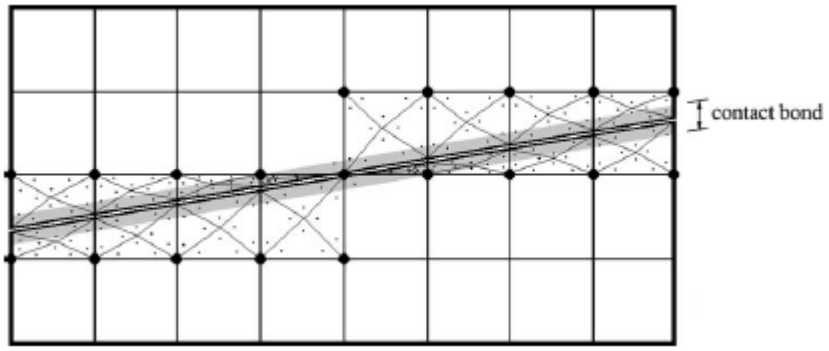

Figure 80. The sub-triangles associated with elements cut by contact surface and enriched by adding Gauss points in the sub-triangles [89]

For those elements intersected by the contact surface, the concept of the partition of unity is used to generate the sub-triangles. The Gauss points of sub-triangles are then employed to evaluate the stiffness matrix with friction in effect.

The basic steps to be taken:

1. Create geometry and mesh

2. Identify contact pairs, including the contact region (typically the deformable object) and the target region (usually the rigid object)

3. Superimpose contact elements onto the existing mesh and set the simulation constants and material properties

4. Apply loads, boundary conditions and solve

5. Post process.

5.2.2.4 Simulation results

The contact elements have been so utilized that the interactions between the surfaces that come in contact with each other during the deformation, including the lower surface of the top plate and the outer surface of the sphere, as in Figure 76, the upper surface of the bottom plate and the cross-section area of the quarter sphere, and the inner

surface of the sphere and the upper surface of the bottom plate, can be properly described. The plates are only allowed to move perpendicularly with respect to the sphere while being fixed in the other two directions. Symmetrical boundary conditions are applied on the surfaces where the simulated parts join the other parts not displayed in the model. The material properties are summarized in Table 44. Note that the yield strength and plastic tangent modulus values are not provided for the rigid plates, granted the plates are supposed to be infinitely rigid and will not deform against the sphere regardless.

Table 44. Parameters used for the deformation simulation [45]

	Young's Modulus (GPa)	Yield strength (MPa)	Poisson's ratio	Plastic tangent modulus (MPa)	Friction coefficient
sphere	211	827	0.29	1758.4	0.4
plate	370		0.22		

Altogether six levels of deformation were captured during the loading process as shown in Figure 81 (a)-(f). The total displacement is 1.1 mm in the perpendicular direction. The obtained stress-strain curve is given in Figure 82.

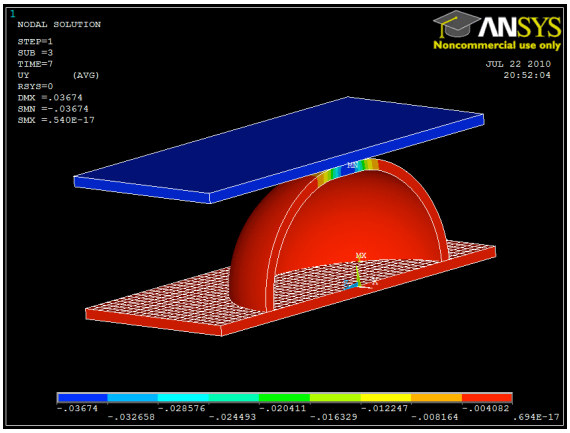

(a) 0.037 mm (3% strain)

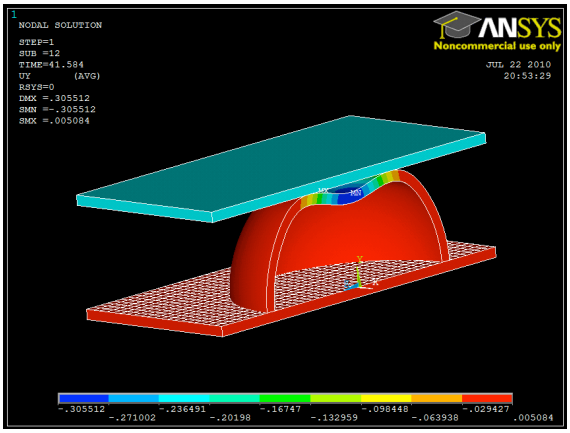

(b) 0.306 mm (25% strain)

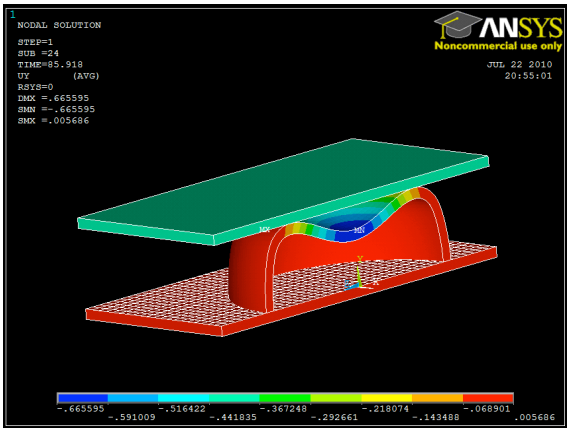

(c) 665 mm (55% strain)

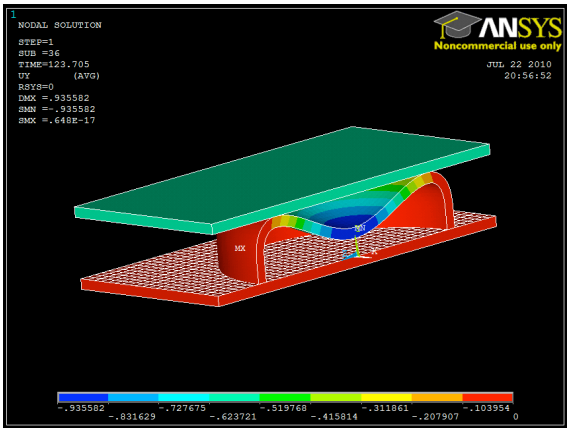

(d) 0.936 mm (78% strain)

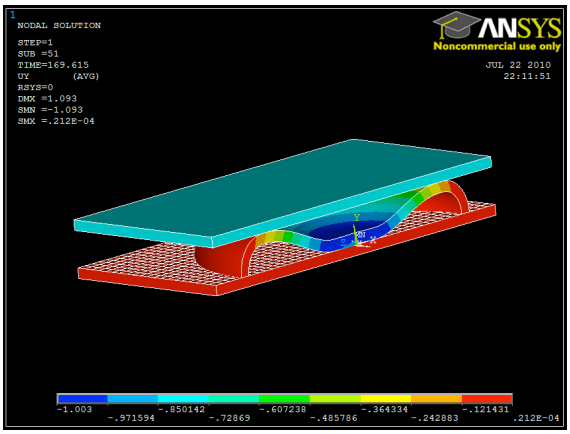

(e) 1.003 mm (84% strain)

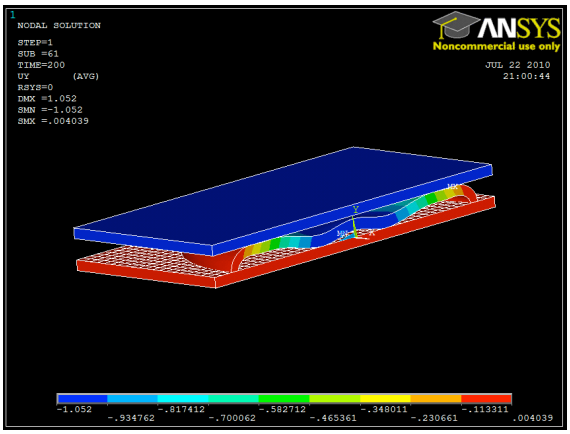

(f) 1.053 mm (88% strain)

Figure 81. Deformation status of a hollow sphere with perpendicular displacement of the top plate at (a) 0.037 mm (b) 0.306 mm (c) 0.665 mm (d) 0.936 mm (e) 1.003 mm (f) 1.053 mm

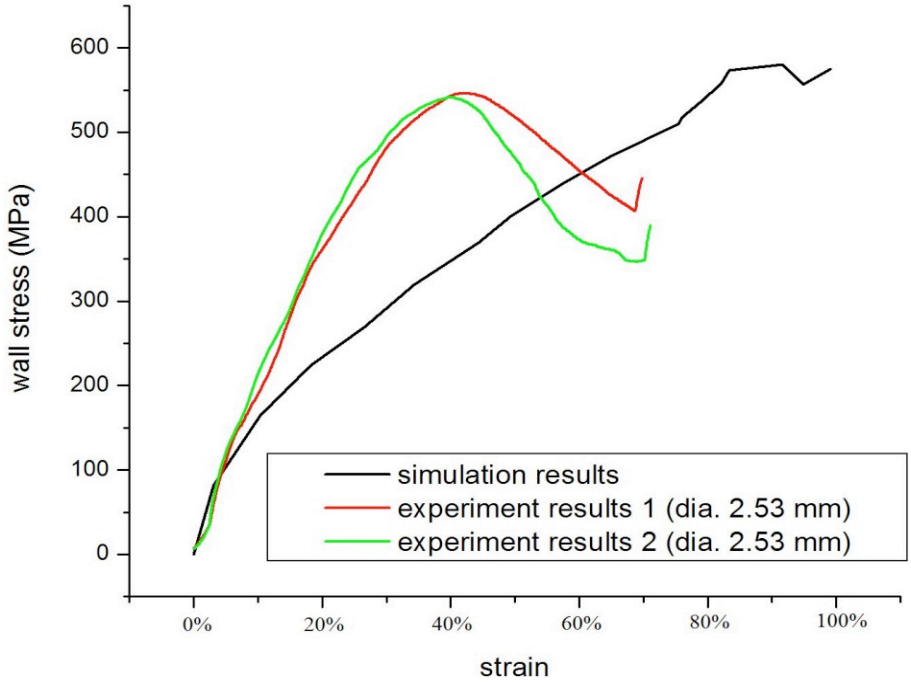

Figure 82. Comparison of stress-strain curves obtained through simulation and experiments

The comparison between the simulation and experimental results, including the Young's modulus and the yield strength is shown in Table 45.

Table 45. Comparison of simulation results and experiment data (deformation of M350 hollow sphere)

	Young's Modulus (GPa)	Yield strength (MPa)
Simulation	1.16	580
Experiment 1	1.36	546
Experiment 2	1.42	541

The model presented in this section so far is flawed in the sense that all the deformations presented are elastic, whereas in this model, once the yield limit is reached, the yielded parts continue to deform plastically. The resulted elastic strain and plastic strain are shown in Figure 83. Obviously, the highest strain appears where the sphere's inner top and the lower plate come in contact with each other and the hollow sphere starts to buckle, with the majority of the strain being plastic.

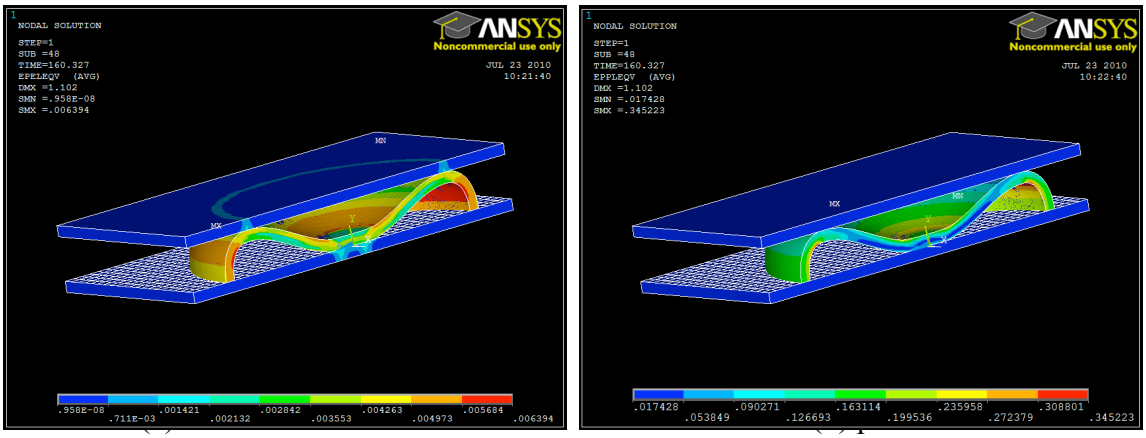

Figure 83. Distributions of (a) elastic strain and (b) plastic strain when the displacement of the top plate is at 0.85 mm

Also, this model may be able to approximate the behaviors of a hollow metal sphere early on in its deformation process. However, lacking the lower half of the hollow sphere deviates the stress-strain curve after the strain has reach 20% and beyond, as also clearly seen in Figure 82.

After the enhancement of the computing power and algorithm, a more proper model was developed to assess the deformation process and the stress-strain curve associated. Figures 84 and 85 show the von Mises stress distribution at progressive deformation stages. In Figure 84, the outer diameter of the hollow sphere is 2.4 mm and the inner diameter is 2.2 mm, as opposed to 2.53 mm and 2.42 mm in the experiment. Then in Figure 85, the dimension of the sphere is rendered exactly as in the experiment, just to help put the impact of sphere diameter in perspective. The resulted stress-strain curves of the two spheres are compared with two experiment results, as illustrated in Figure 86.

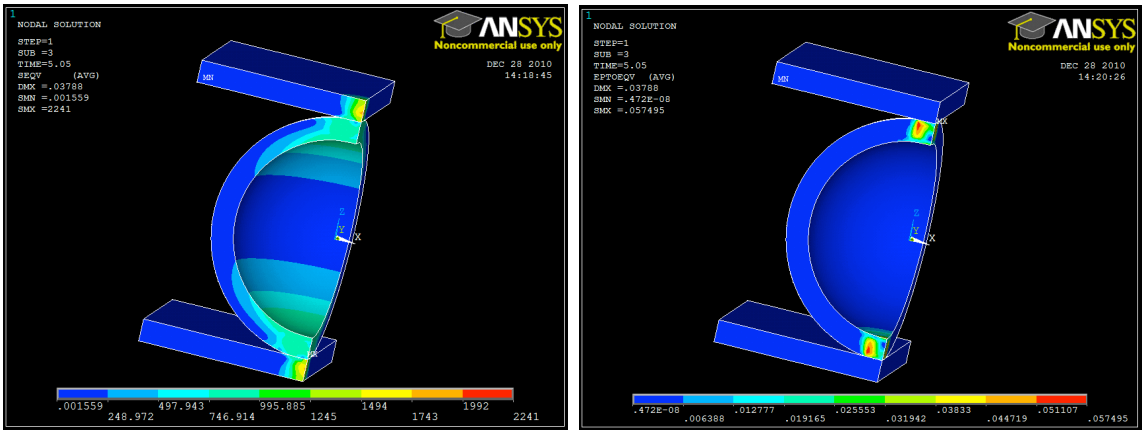

(a) von Mises stress pattern (perpendicular displacement 0.038 mm) (b) corresponding total mechanical strain distribution

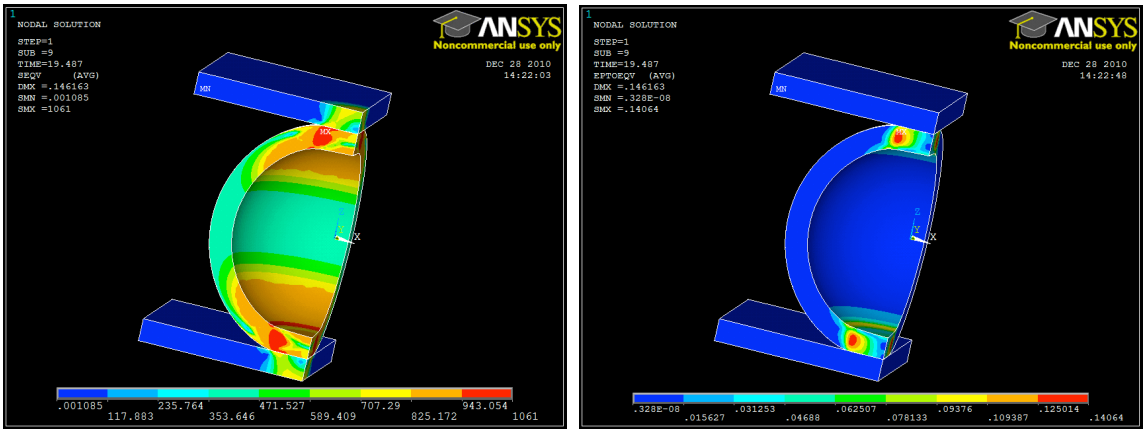

(c) von Mises stress pattern (perpendicular displacement 0.146 mm) (d) corresponding total mechanical strain distribution

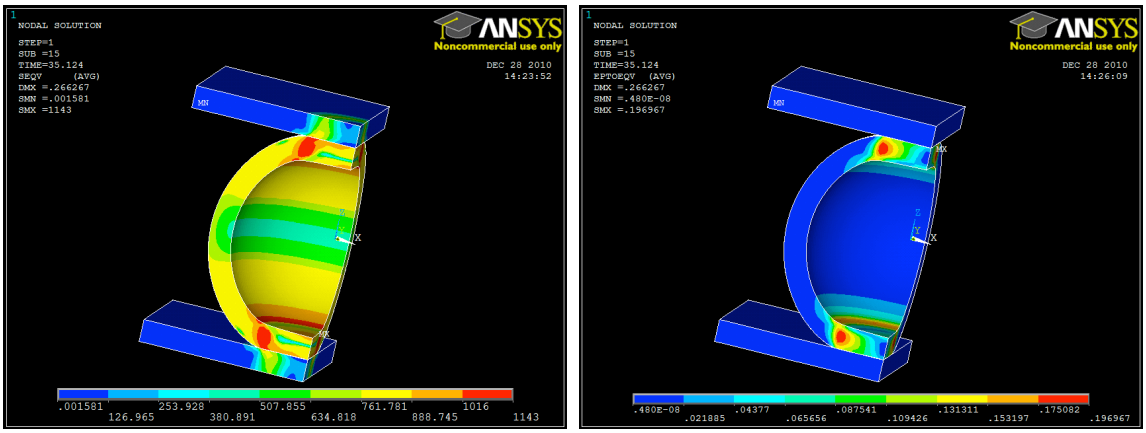

(e) von Mises stress pattern (perpendicular displacement 0.266 mm) (f) corresponding total mechanical strain distribution

Figure 84. The von Mises stress patterns and total logarithmic strain distributions of a deformed hollow sphere with perpendicular displacement of the top plate at (a) (b) 0.038 mm (c) (d) 0.146 mm (e) (f) 0.266 mm (g) (h) 0.517 mm (i) (j) 0.746 mm (k) (l) 1.06 mm (m) (n) 1.34 mm (o) (p) 1.57 mm (q) (r) 1.63 mm

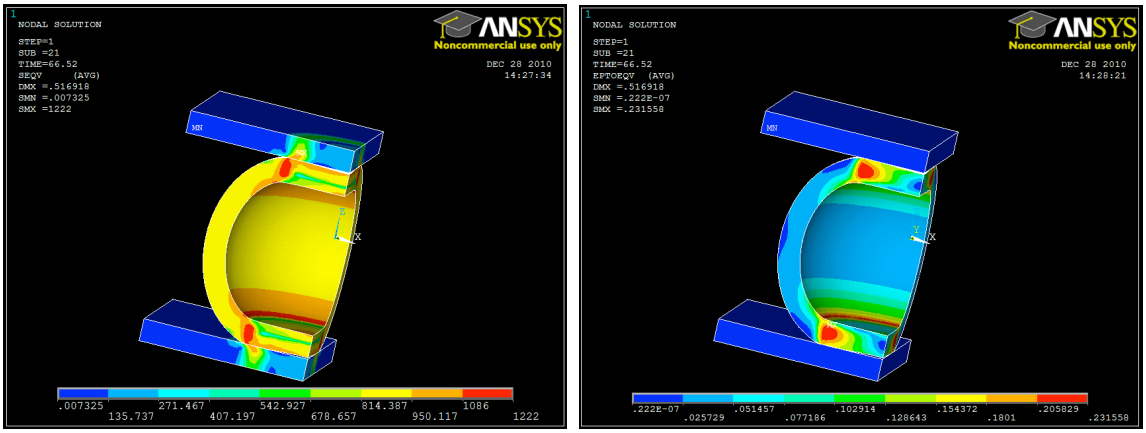

(g) von Mises stress pattern (perpendicular displacement 0.517 mm) (h) corresponding total mechanical strain distribution

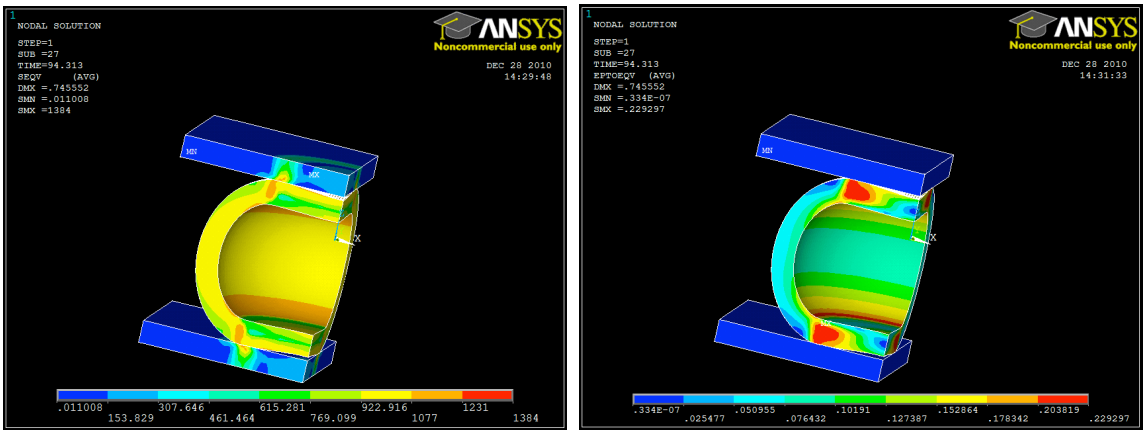

(i) von Mises stress pattern (perpendicular displacement 0.746 mm) (j) corresponding total mechanical strain distribution

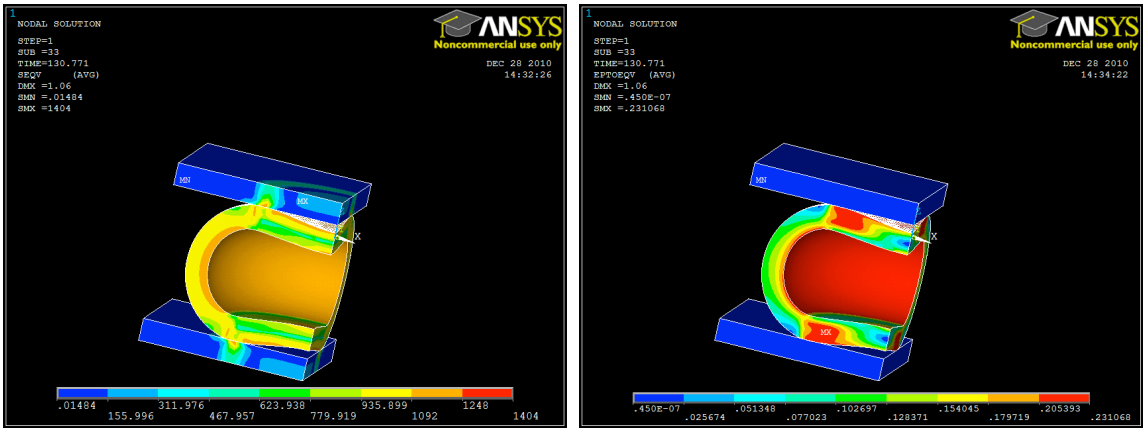

(k) von Mises stress pattern (perpendicular displacement 1.06 mm) (l) corresponding total mechanical strain distribution

Figure 84 continued

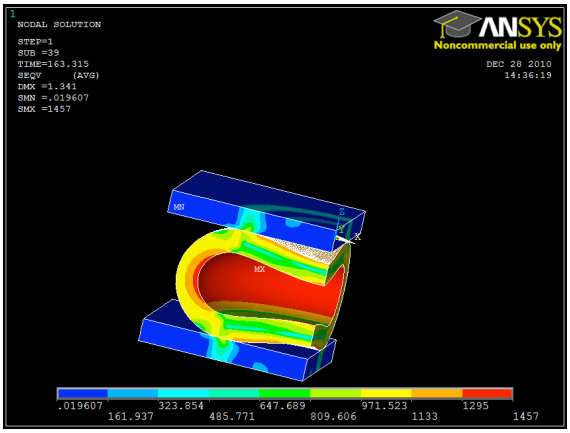

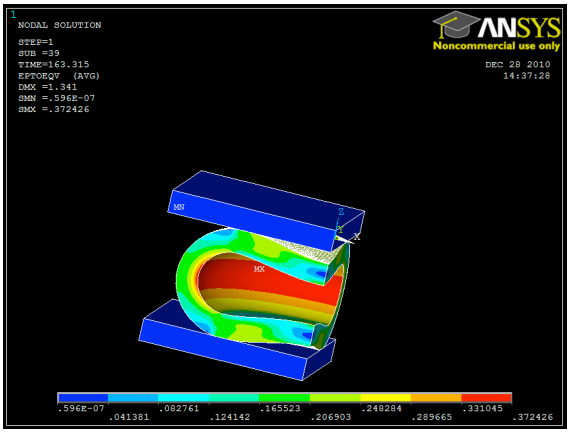

(m) von Mises stress pattern (perpendicular displacement 1.34 mm) (n) corresponding total mechanical strain distribution

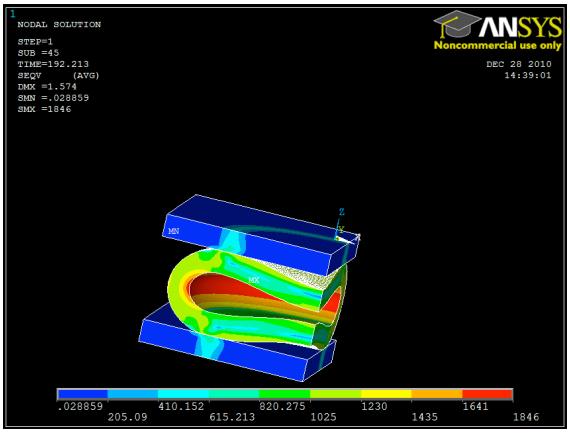

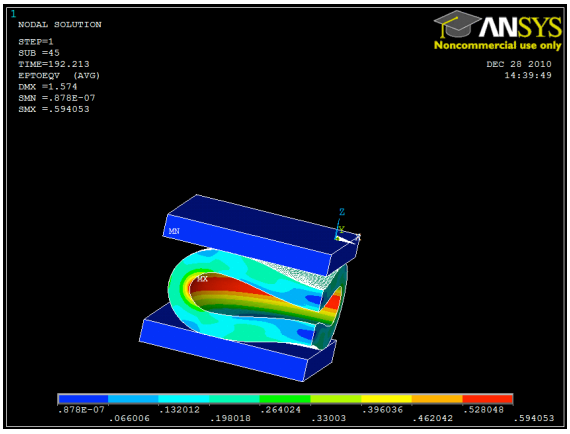

(o) von Mises stress pattern (perpendicular displacement 1.57 mm) (p) corresponding total mechanical strain distribution

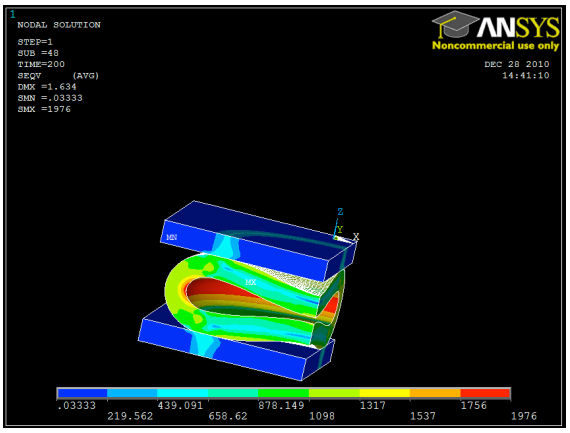

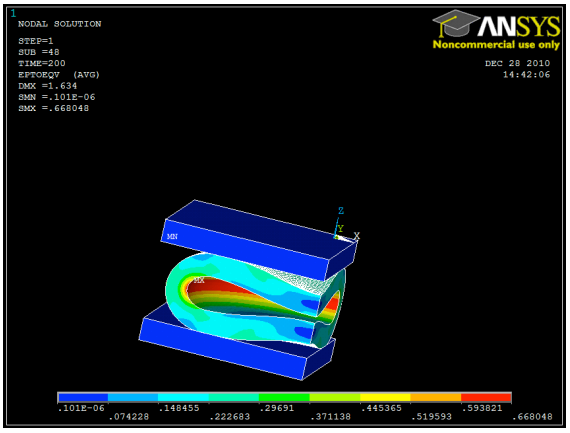

(q) von Mises stress pattern (perpendicular displacement 1.63 mm) (r) corresponding total mechanical strain distribution

Figure 84 continued

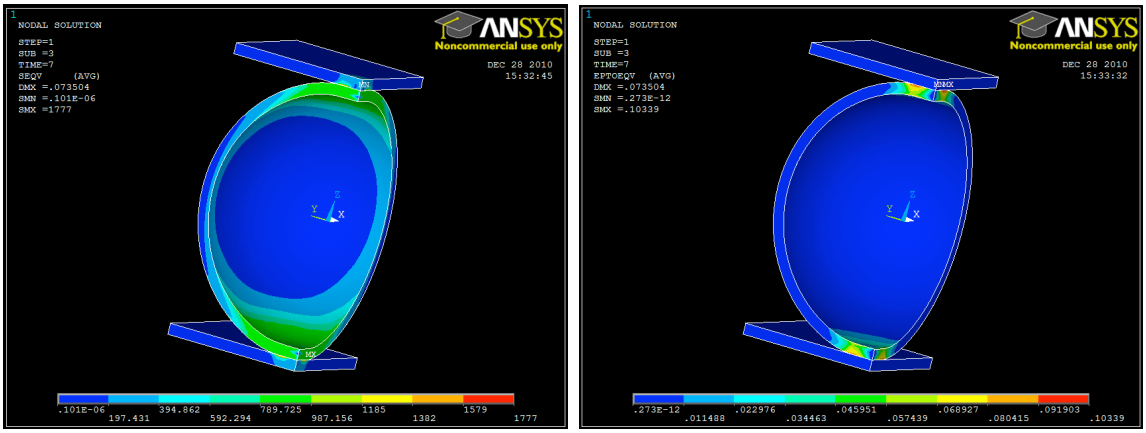

(a) von Mises stress pattern (perpendicular displacement 0.0735 mm) (b) corresponding total mechanical strain distribution

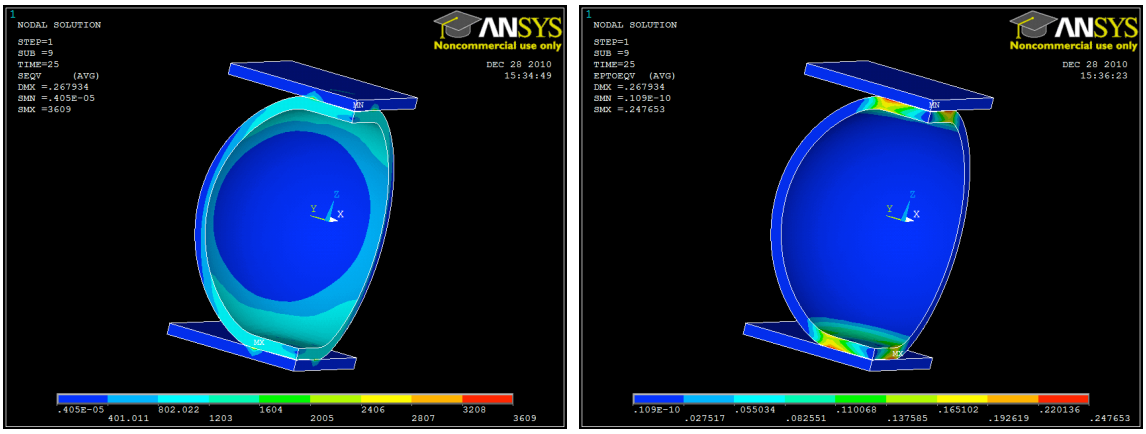

(c) von Mises stress pattern (perpendicular displacement 0.268 mm) (d) corresponding total mechanical strain distribution

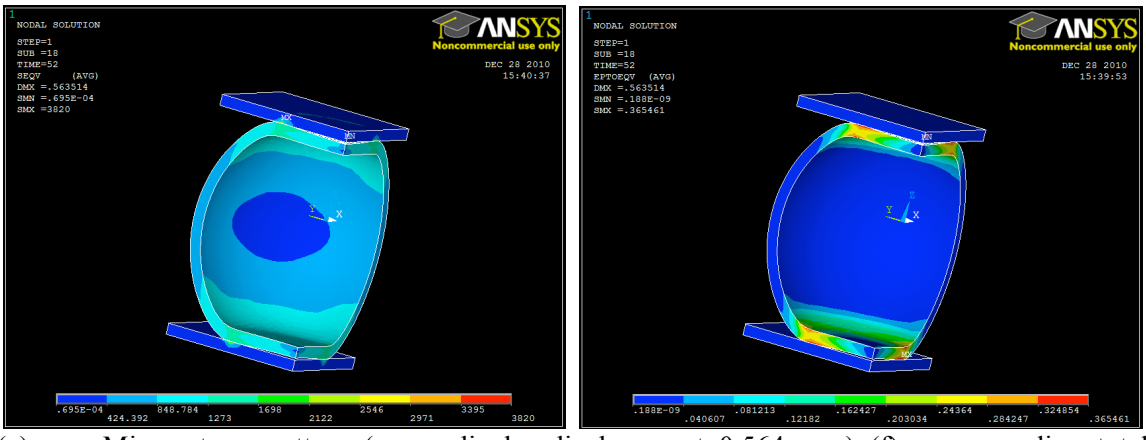

(e) von Mises stress pattern (perpendicular displacement 0.564 mm) (f) corresponding total mechanical strain distribution

Figure 85. The von Mises stress patterns and total logarithmic strain distributions of a deformed hollow sphere with perpendicular displacement of the top plate at (a) (b) 0.0735 mm (c) (d) 0.268 mm (e) (f) 0.564 mm (g) (h) 0.837 mm (i) (j) 1.10 mm (k) (l) 1.41 mm (m) (n) 1.66 mm (o) (p) 2.03 mm (q) (r) 2.14 mm

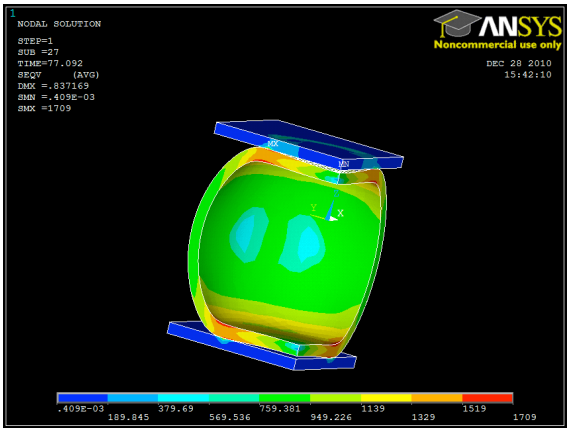

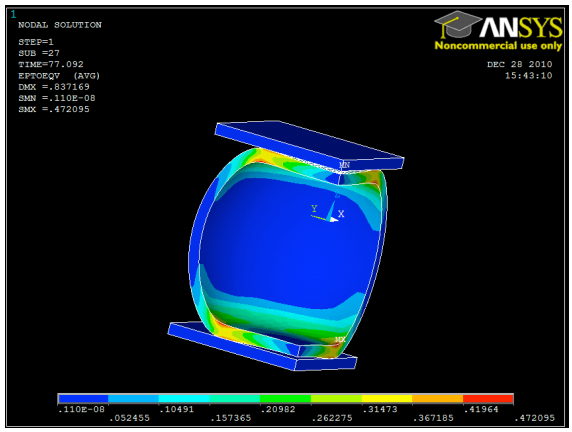

(g) von Mises stress pattern (perpendicular displacement 0.837 mm) (h) corresponding total mechanical strain distribution

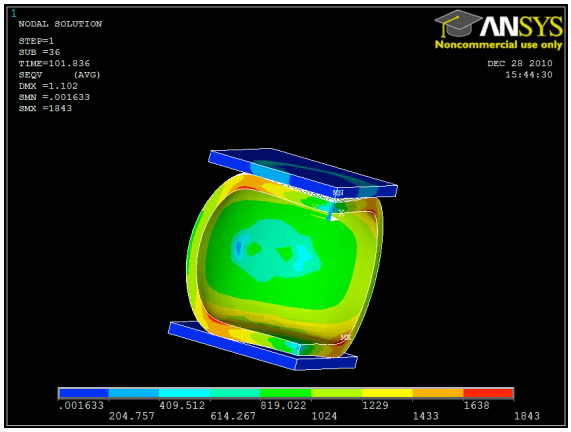

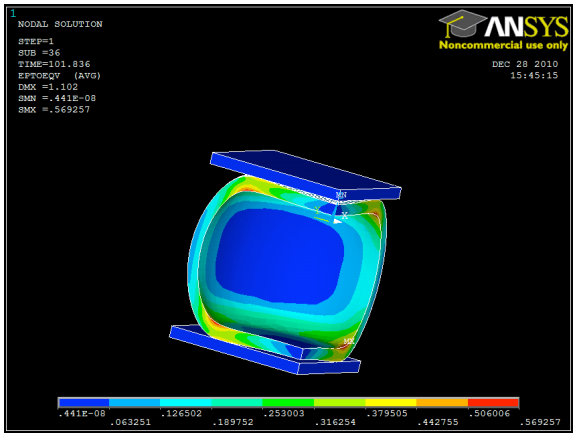

(i) von Mises stress pattern (perpendicular displacement 1.10 mm) (j) corresponding total mechanical strain distribution

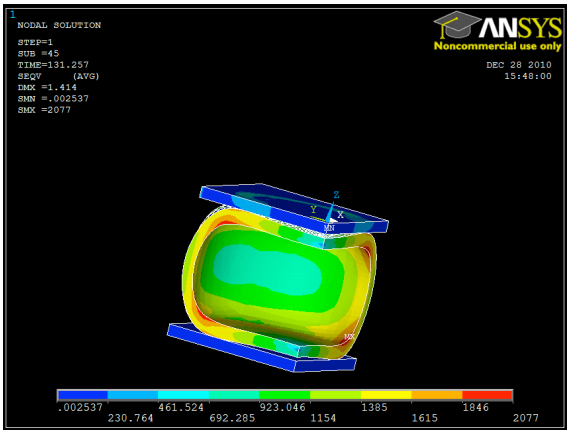

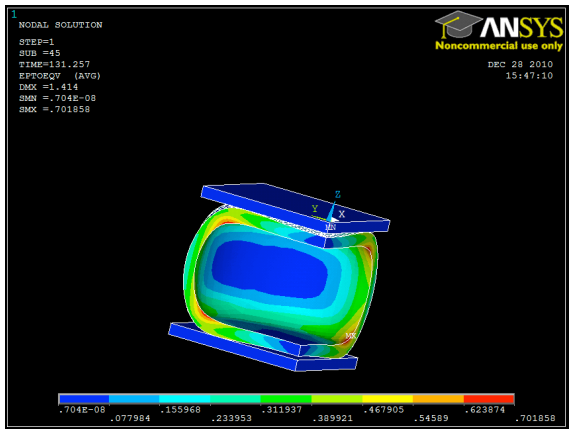

(k) von Mises stress pattern (perpendicular displacement 1.41mm) (l) corresponding total mechanical strain distribution

Figure 85 continued

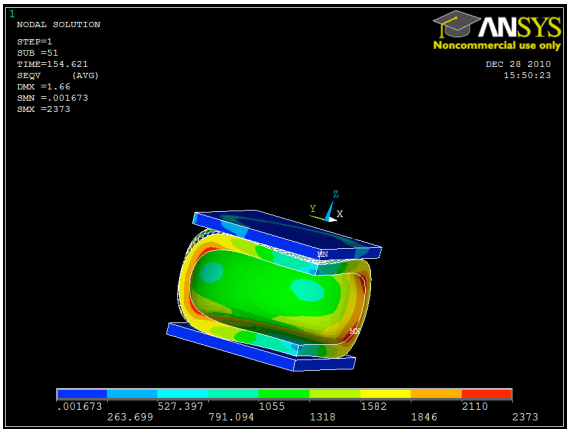

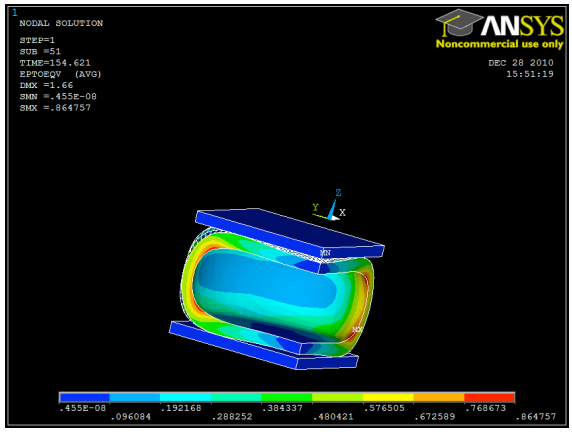

(m) von Mises stress pattern (perpendicular displacement 1.66 mm) (n) corresponding total mechanical strain distribution

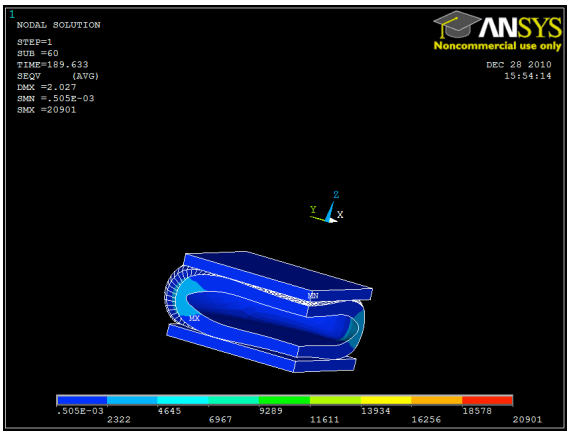

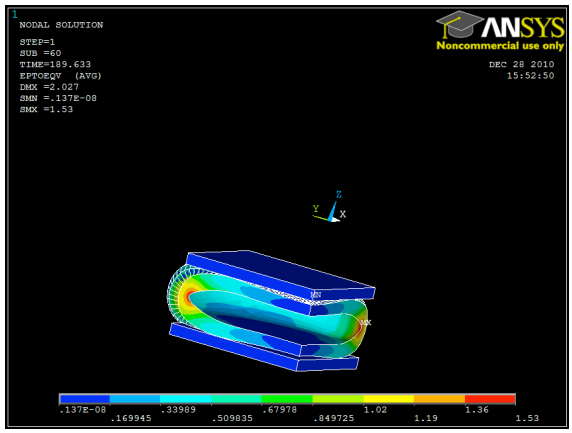

(o) von Mises stress pattern (perpendicular displacement 2.03 mm) (p) corresponding total mechanical strain distribution

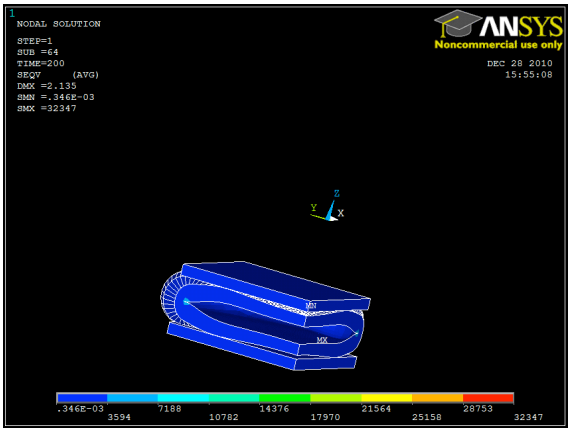

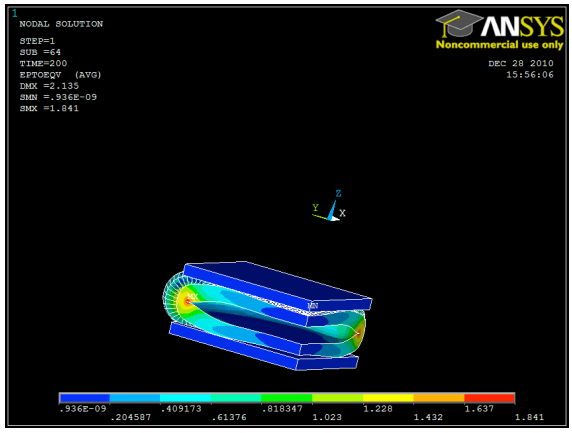

(q) von Mises stress pattern (perpendicular displacement 2.14 mm) (r) corresponding total mechanical strain distribution

Figure 85 continued

The collective stress over the top plate has been calculated and divided by the area of the plate in order to obtain the strain values, with the stress-strain pattern provided in Figure 86.

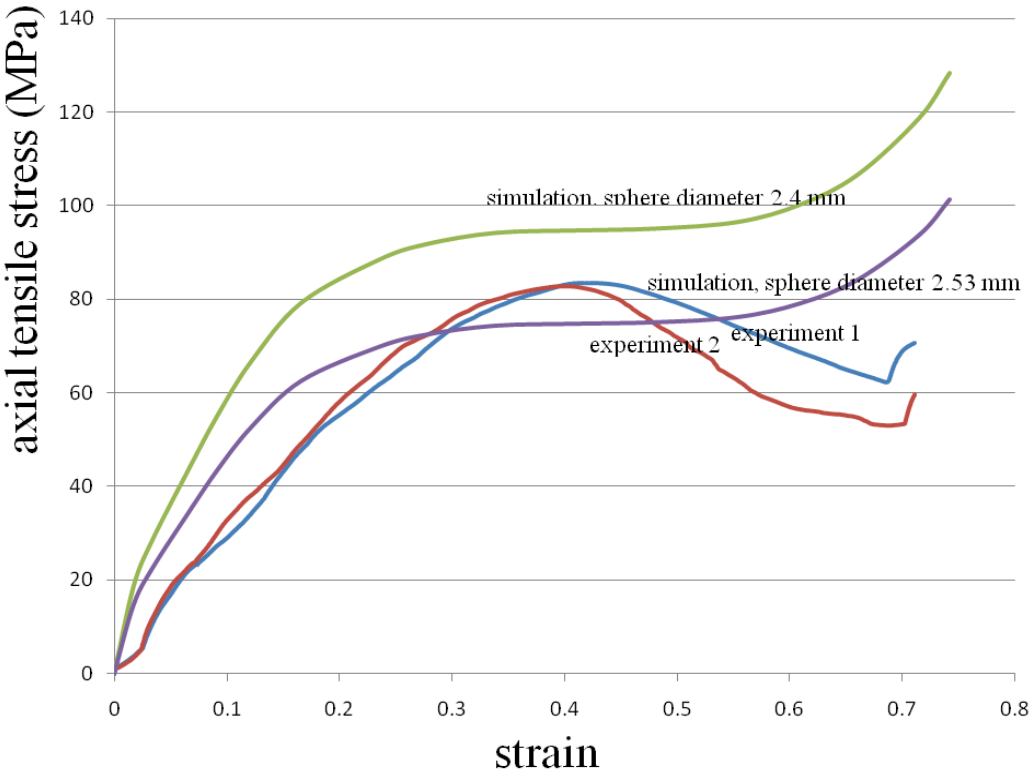

Figure 86. Stress-strain curves of spheres tested experimentally as compared to simulation results

The curves shown in Figure 86 imply that the results from simulation match well those obtained with hollow steel sphere of the same diameter, except in the final stage when the experiment results start acting erratically. That can be explained by the fact that when the total strain of sphere has reached 60% and beyond, in actuality the sphere has started to crack open and ultimately break apart, as shown in Figure 74, whereas in FEM modeling the elements, instead of becoming detached from each other, simply deform infinitely while maintaining the connectivity. Besides, the material properties from literature could be different from that of the spheres actually being tested, which could also contribute to the discrepancy.

It is evident that the sphere with smaller diameter and thicker wall displays higher modulus than the one with larger radius and thinner wall, which is natural thinking as thicker wall provides more resistance to the compressive force.

Up to this point, the application of contact element has been proved to work well and produce reasonable results. This model can be expanded by varying all the parameters including material types, sphere dimension and the friction coefficient between the touching surfaces.

5.3 Modeling Mg/Al/Maraging Steel Hollow Spheres Composite Materials

5.3.1 Significance

Using the previously established prototypical model for decarburization and the obtained mechanical properties of the hollow M350 spheres, this section focuses on deconstructing the development of lightweight, energy-absorbing, impact-resistant magnesium/aluminum alloy composites, in which the hollow M350 spheres are embedded, a design to ultimately produce a low-density material with high compressive strength and impact resistance [98-99]. The selected maraging steel acquires its superior strength, toughness and ductility from processes including annealing, air cooling and subsequent aging to achieve a fine dispersion of intermetallic phases along dislocations left by martensitic transformation [100]. Besides the mentioned properties, one additional advantage would be that the maraging steel displays very low thermal expansion coefficient therefore causing little dimensional variation, such that when the ambient temperature changes the spheres will not exert internal stress on the surrounding magnesium\aluminum matrix and cause cracks. The following considerations are necessary for the optimization of the composite:

1) The alloy composite chosen for the matrix and hollow sphere materials

2) The fabrication of hollow spheres such that uniform wall thickness and low porosity are maintained

3) Casting parameters such that there is low porosity in the matrix and good interfacial properties between the spheres and the matrix

4) Subsequent heat treatment parameters of the composite to achieve the desired mechanical properties

While the above considerations are ultimately to be investigated through experimentally casting maraging steel spheres in a Mg-Al alloy matrix, FEM modeling needs to be implemented to outline the most productive and cost-effective strategies before any actual steps are taken. So far, the compressive stress-strain data for the

individual components of the composite (hollow spheres and matrix alloys, as well as various heat treatments) have been incorporated into the preliminary models that can be expanded with the acquisition of more computing power. The parameters used and details of these models are described in the following sections.

5.3.2 Material Geometry and Parameters Used for Modeling

Out of budgetary concerns, the composite material is first attempted with aluminum alloy AA5083 which is less costly than the magnesium alloys. Figure 87 shows part of the cross-section of a composite with maraging steel hollow spheres of M350 composition that were cast in a matrix of aluminum alloy AA5083.

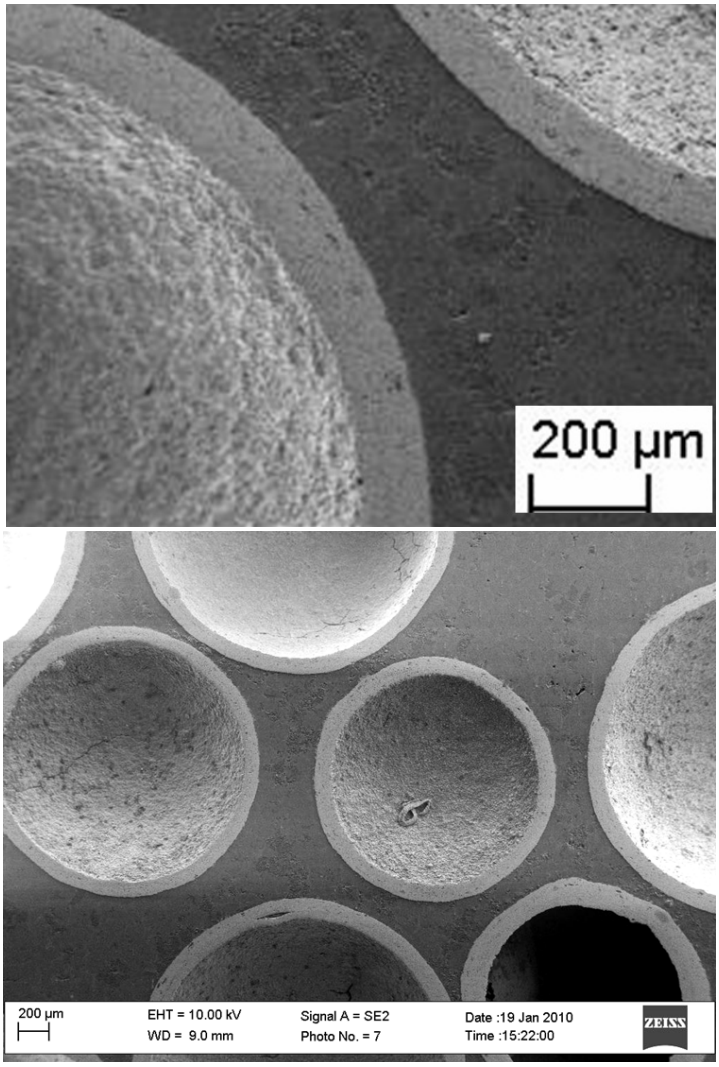

Figure 87. SEM images of the cross-section of a composite produced through the casting of a aluminum alloy of AA5083 composition around maraging steel spheres of M350 composition. The spheres in the composite were not aged prior to casting [100]

For the preliminary modeling of this AA5083/M350 hollow sphere composite, the hollow spheres are assumed to be perfectly spherical with a diameter of approximately 2.5 mm and wall thickness 0.12 mm. The size of the 2D sample simulated is set at 20 × 20 mm^2, with a mesh density of 20 pixels/mm. The details about the parameters involved in the simulation are listed in Table 46.

Table 46. Parameters used for the modeling of M350 maraging steel spheres embedded in an AA5083 alloy matrix

	AA5083	M350
Yield tensile strength (MPa)	230	827
Young's modulus (GPa)	75	211
Poisson's Ratio	0.33	0.3
Density (g/cm^3)	2.66	8.08
Tangent modulus (MPa)	2327.58	1758.4
Elongation percentage at break	0.06	0.18

A program has been written to create the two-dimensional geometry for the AA5083 alloy/maraging steel hollow sphere composite material. Figure 88 shows an example of the geometry that is being investigated. The spheres are placed in the sample space following Gaussian normal distribution and the total volume accrues as more spheres are added until the total volume fraction is reached, which is 50% in this case. The deformation progress is displayed in Figure 89 with the von Mises stress pattern and logarithmic strain distribution at each step till the tensile strain reaches 40%.

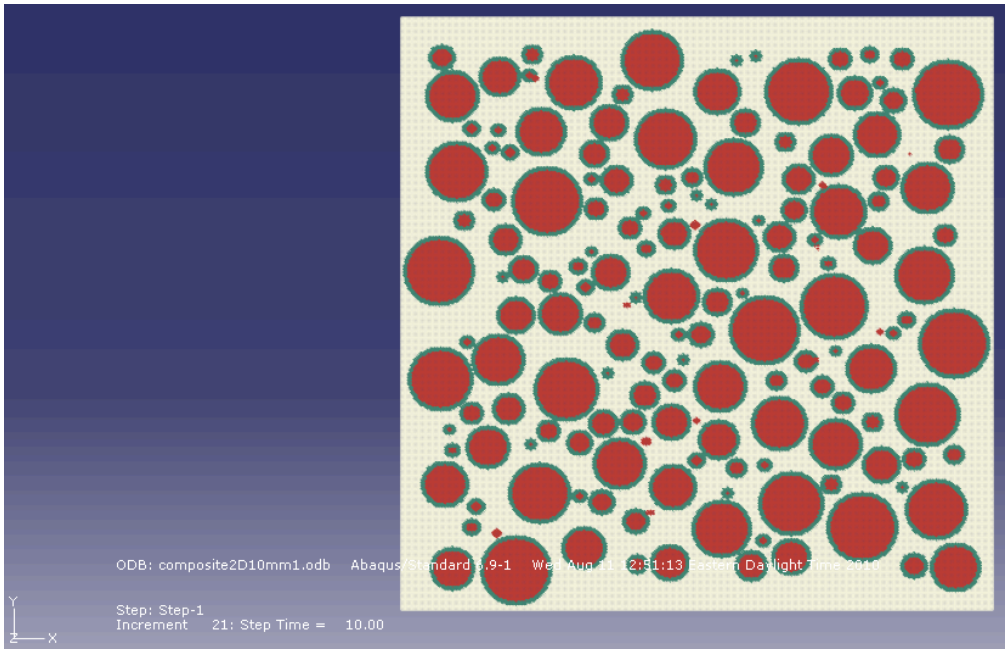

Figure 88. 2D geometry of Mg/Al/Maraging steel hollow sphere (20 × 20 mm^2)

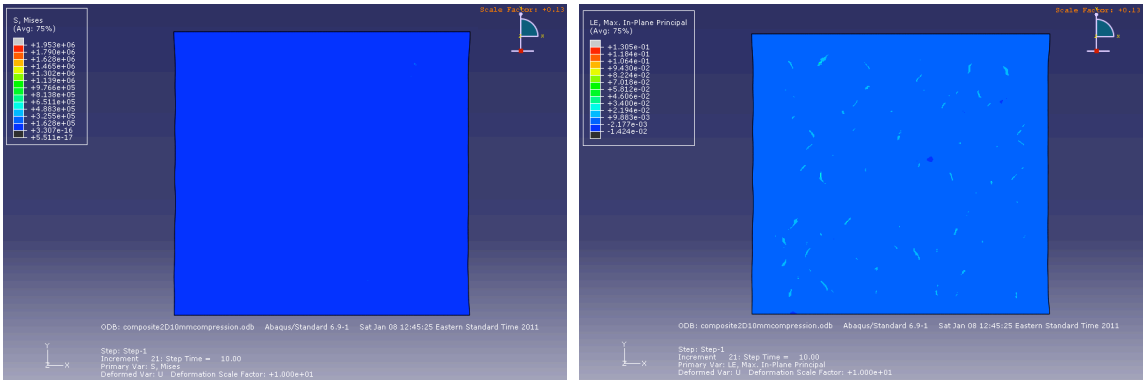

(a) von Mises stress pattern (total strain in -y direction -0.05) (b) corresponding logarithmic strain distribution

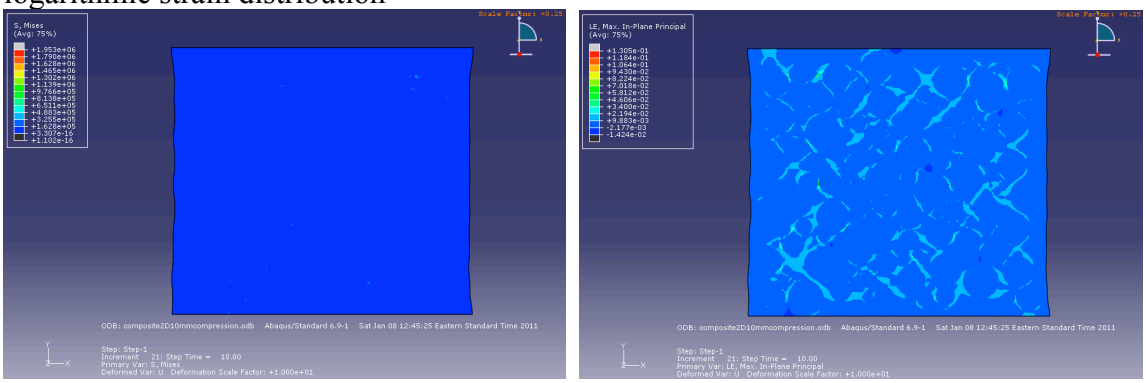

(c) von Mises stress pattern (total strain in -y direction -0.1) (d) corresponding logarithmic strain distribution

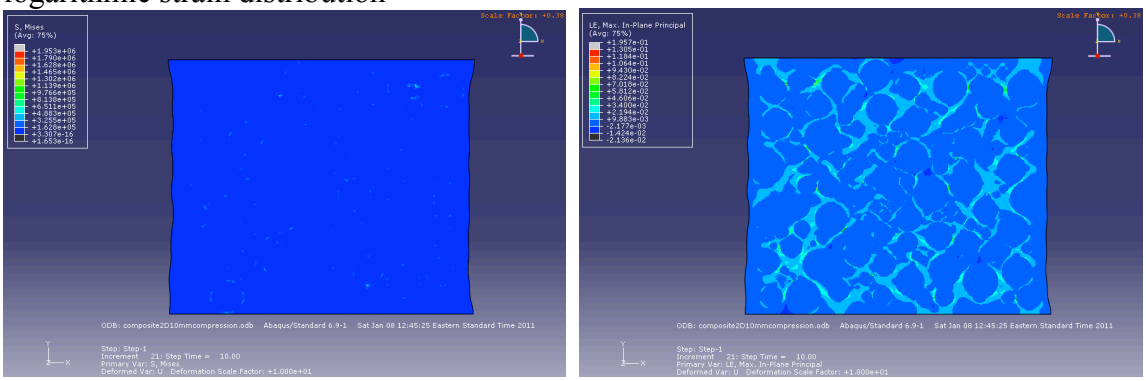

(e) von Mises stress pattern (total strain in -y direction -0.15) (f) corresponding logarithmic strain distribution

Figure 89. The von Mises stress patterns and total logarithmic strain distributions of 20 × 20 mm^2 Mg/Al/M 350 hollow sphere composite material under tensile strain in -y direction at (a) (b) -0.05 (c) (d) -0.1 (e) (f) -0.15 (g) (h) -0.20 (i) (j) -0.25 (k) (l) -0.30 (m) (n) -0.35 (o) (p) -0.40

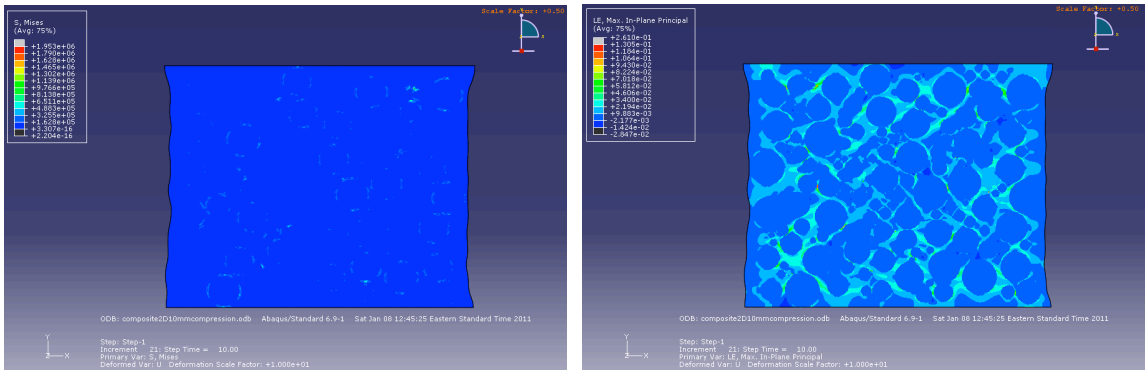

(g) von Mises stress pattern (total strain in -y direction -0.2) (h) corresponding logarithmic strain distribution

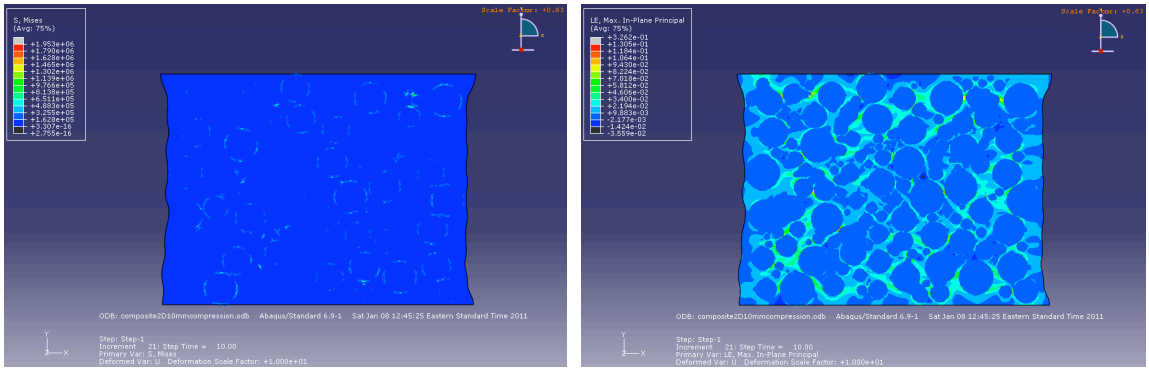

(i) von Mises stress pattern (total strain in -y direction -0.25) (j) corresponding logarithmic strain distribution

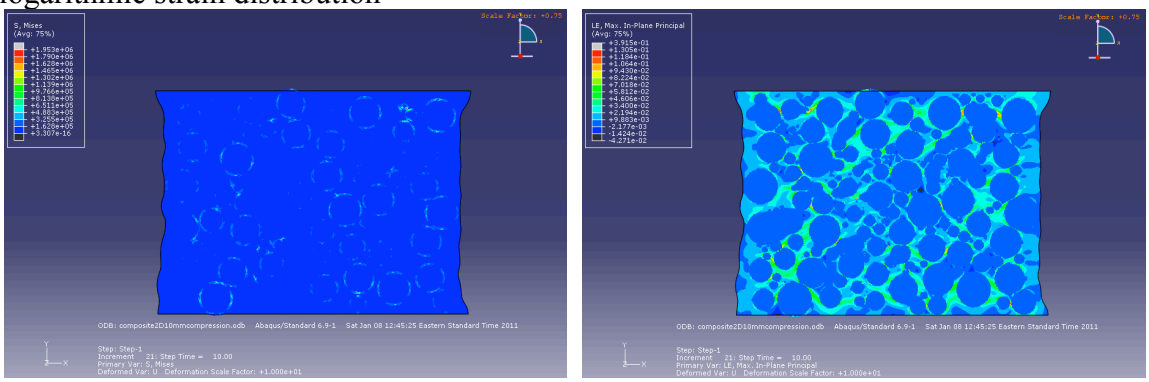

(k) von Mises stress pattern (total strain in -y direction -0.30) (l) corresponding logarithmic strain distribution

Figure 89 continued

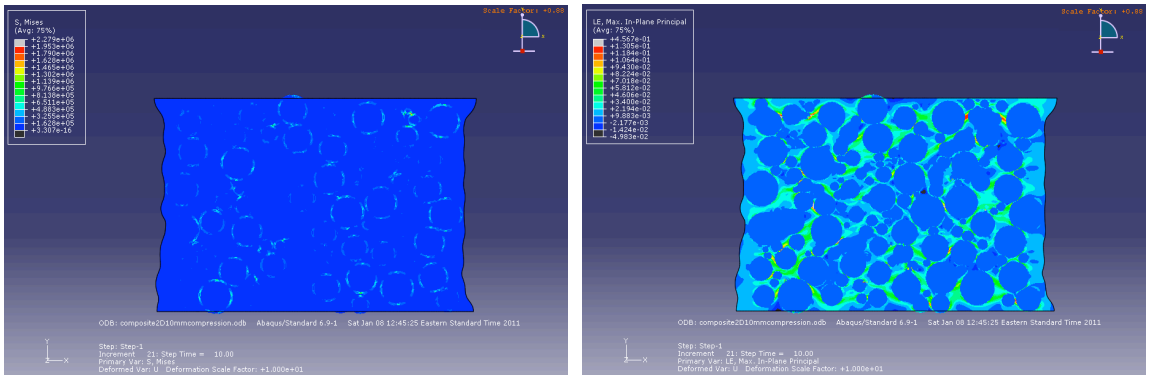

(m) von Mises stress pattern (total strain in -y direction -0.35) (n) corresponding logarithmic strain distribution

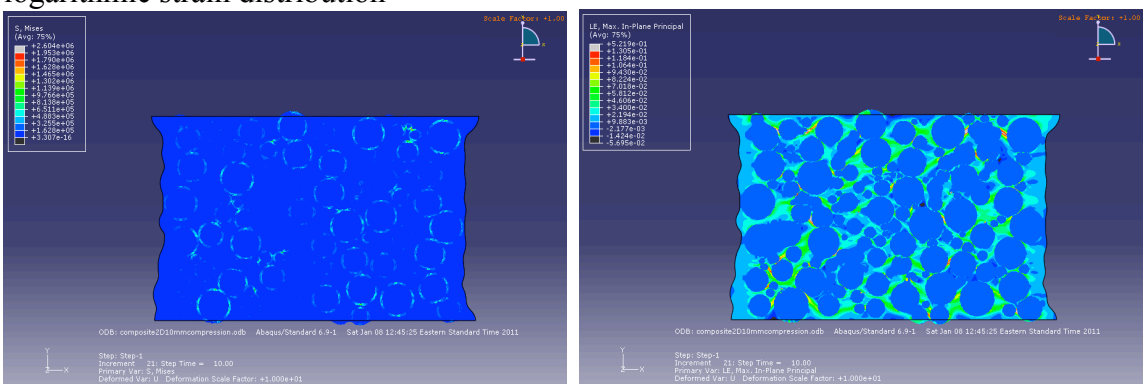

(o) von Mises stress pattern (total strain in -y direction -0.40) (p) corresponding logarithmic strain distribution

Figure 89 continued

The total maximum strain in -y direction is 40%. As clearly seen in the stress pattern, the circumferences of the embedded spheres are the places where the stress congregates, whereas the alloy matrix sustains most of the strain. The alloy matrix can be compared to relatively "soft" rice cake while the M350 spheres are "hard" peanuts embedded in the rice cake. The compressive stress mostly concentrates around the interface between the embedded spheres and the alloy matrix while the matrix exhibits the majority of the deformation. The resulted stress-strain curve is provided in Figure 90.

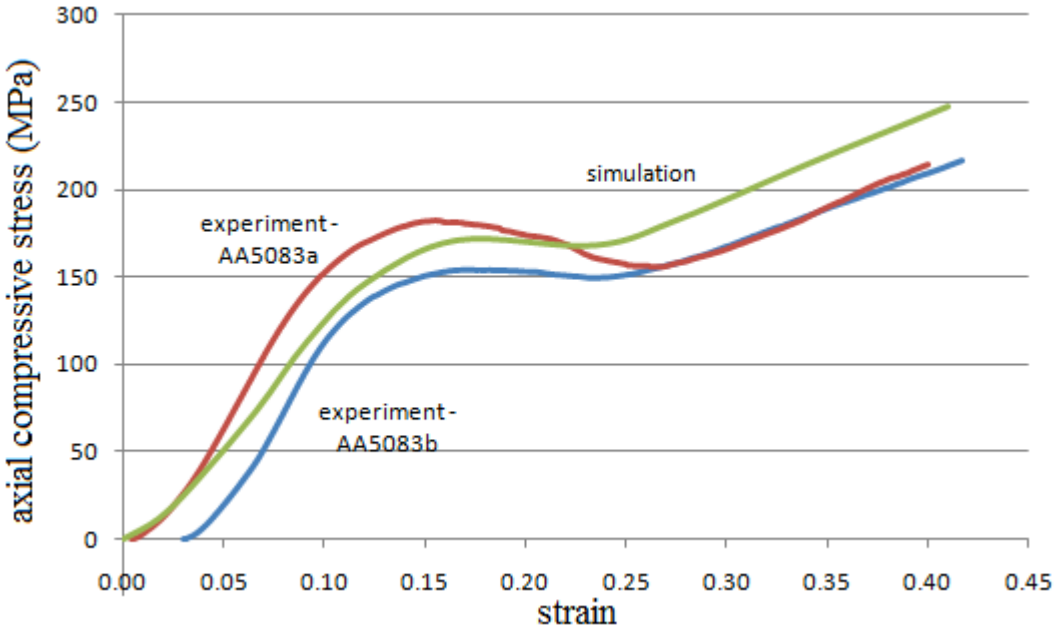

Figure 90. Compressive stress-strain curves of the Al/M350 sphere composite material tested as compared to simulation results

The strain is only modeled up to 40%, which has exceeded the material's elastic limit though. The coincidence of the simulated stress-strain curves with the curves obtained experimentally is good (~170 MPa for the Young's modulus). However, due to the uncontrollable factors such as the actual volume fraction of hollow spheres, the normalization of force-stress, displacement-strain conversions, the actual properties of the material experimented on among others, the as-cast material's properties are rather volatile, heavily dependent on the aforementioned factors among others. The simulation can only provide a semi-quantitative estimate.

Similarly, the von Mises stress patterns and logarithmic strain distributions from the simulated tension test are provided in Figure 91.

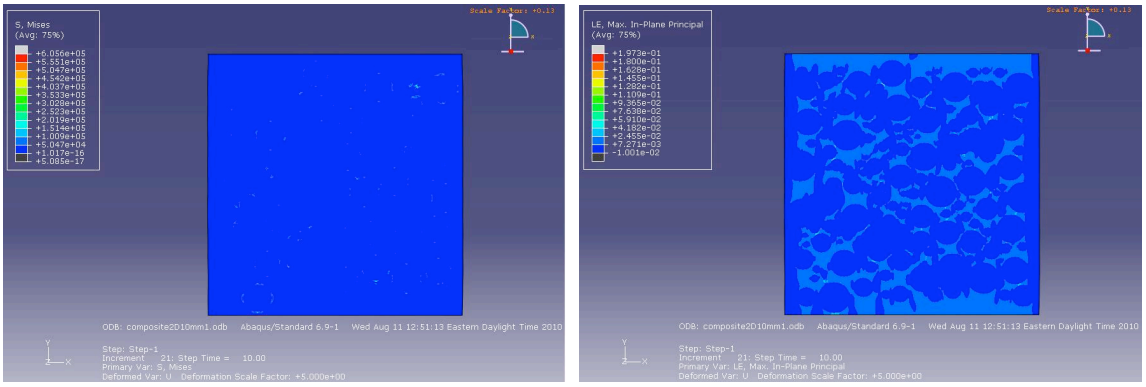

(a) von Mises stress pattern (total strain in -y direction 0.05) (b) corresponding logarithmic strain distribution

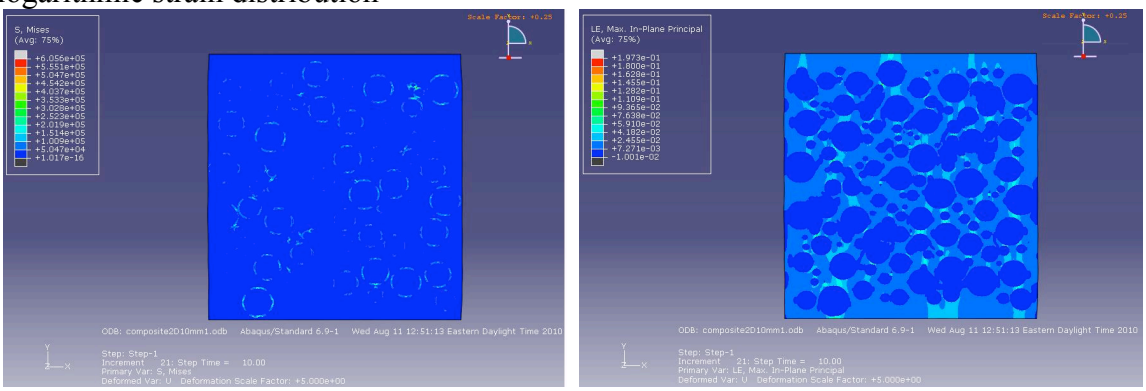

(c) von Mises stress pattern (total strain in -y direction 0.1) (d) corresponding logarithmic strain distribution

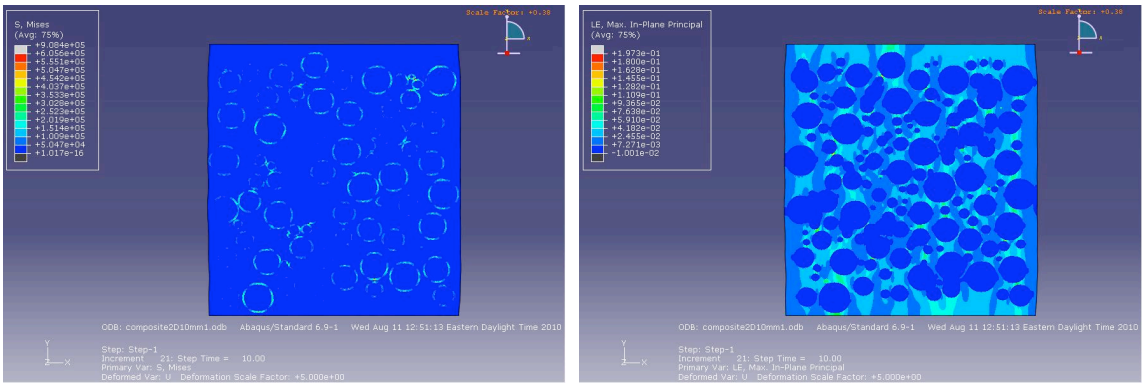

(e) von Mises stress pattern (total strain in -y direction 0.15) (f) corresponding logarithmic strain distribution

Figure 91. The von Mises stress patterns and total logarithmic strain distributions of 20 × 20 mm^2 Mg/Al/M 350 hollow sphere composite material under tensile strain in -y direction at (a) (b) 0.0075 (c) (d) 0.015 (e) (f) 0.0225 (g) (h) 0.03 (i) (j) 0.0375 (k) (l) 0.045 (m) (n) 0.0525 (o) (p) 0.06

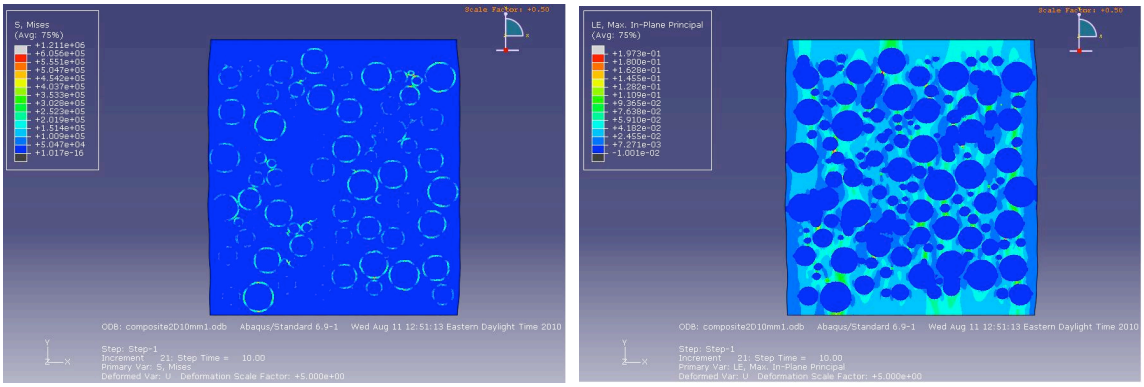

(g) von Mises stress pattern (total strain in -y direction 0.20) (h) corresponding logarithmic strain distribution

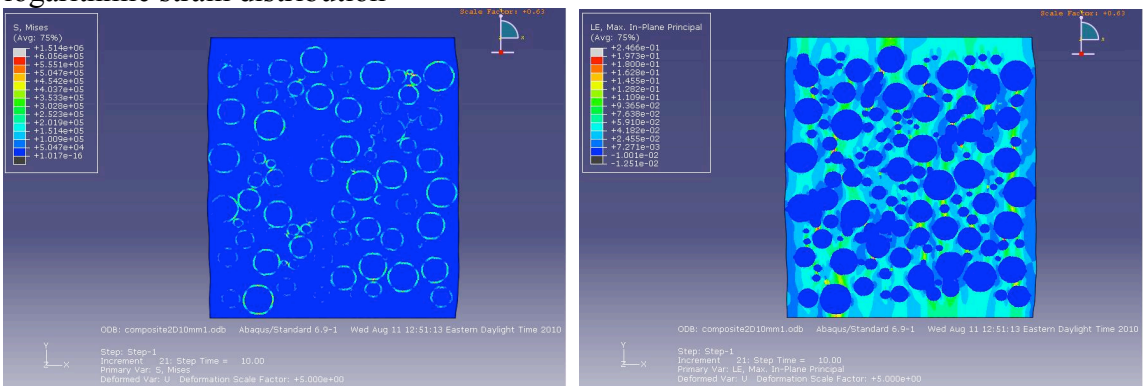

(i) von Mises stress pattern (total strain in -y direction 0.25) (j) corresponding logarithmic strain distribution

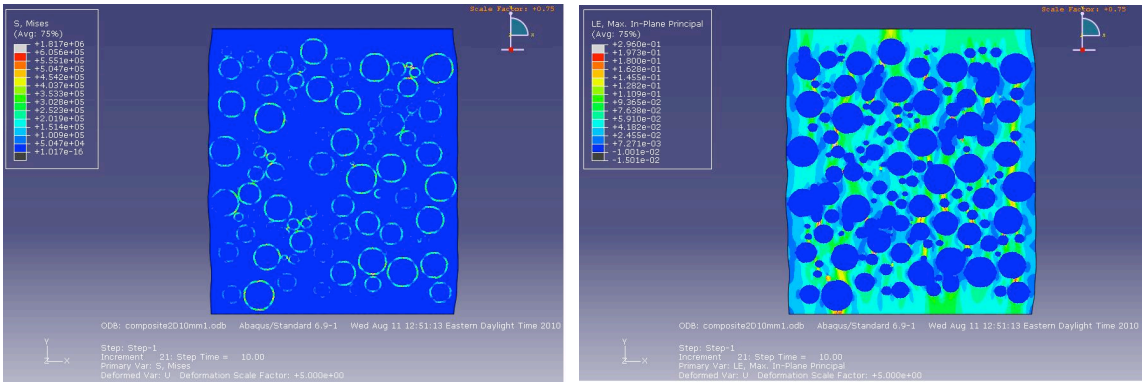

(k) von Mises stress pattern (total strain in -y direction 0.30) (l) corresponding logarithmic strain distribution

Figure 91 continued

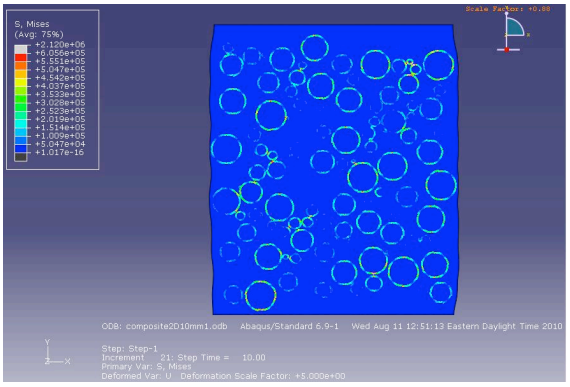

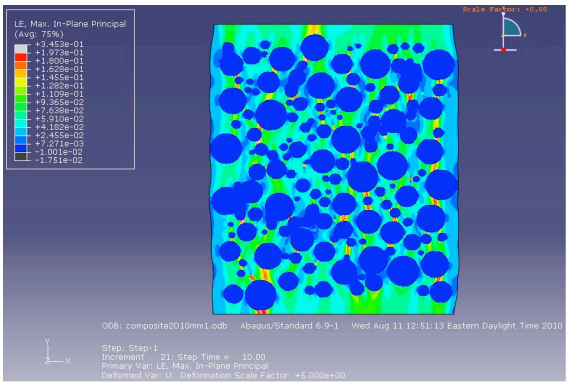

(m) von Mises stress pattern (total strain in -y direction 0.35) (n) corresponding logarithmic strain distribution

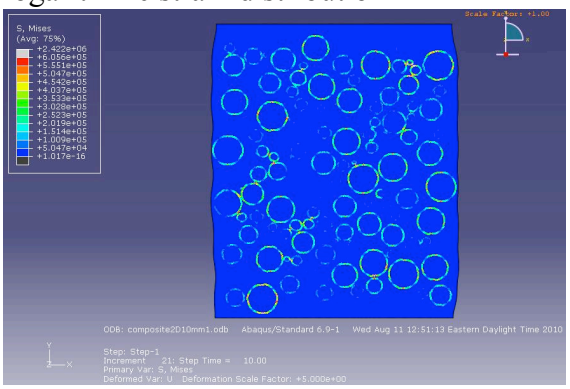

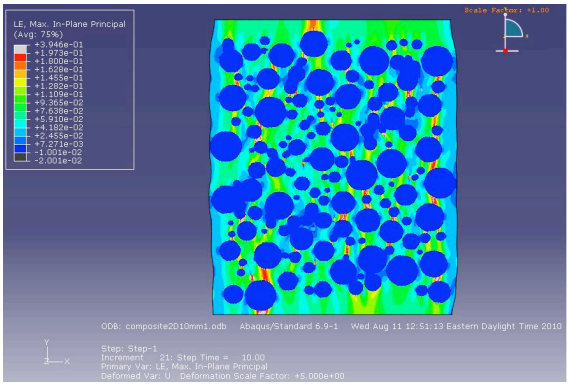

(o) von Mises stress pattern (total strain in -y direction 0.40) (p) corresponding logarithmic strain distribution

Figure 91 continued

The conclusion drawn from the simulated tension test, whose results are shown in Figure 92, is not far from that acquired from the compression test, except that the calculated Young's modulus comes a little lower than the compressive modulus (~150 MPa as opposed to 170 MPa). The reason is, we assume, the tension-induced elongation does not force the embedded spheres to collide and impinge each other as much as the shrinkage caused by compression, in which the impinging spheres exert resistance towards the external compressive force.

The accompanying experiment is yet to be conducted.

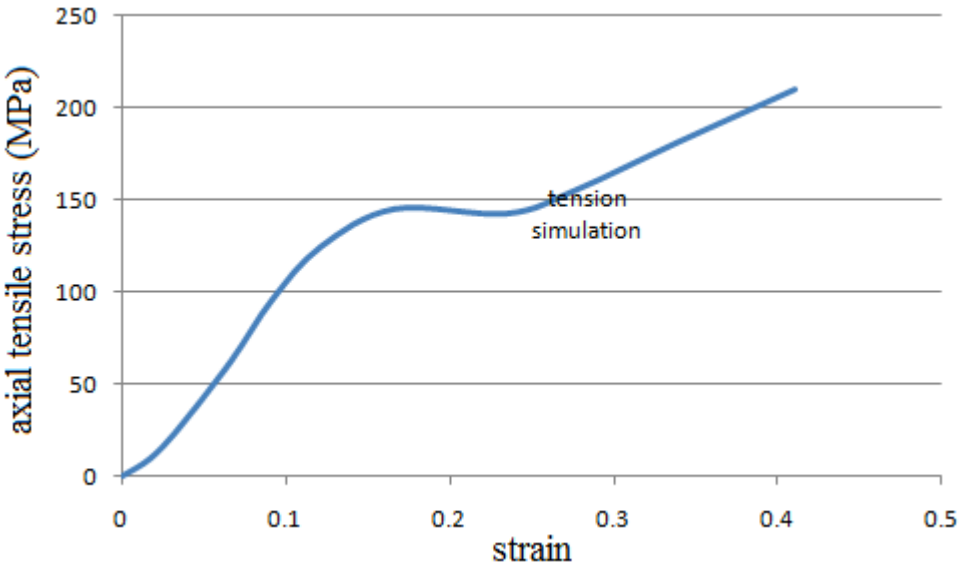

Figure 92. Tensile stress-strain curves of the Al/M350 sphere composite material

The sphere volume fraction is the subject of the following test, with the fraction varying from 10% to 40%, as exhibited in Figure 93.

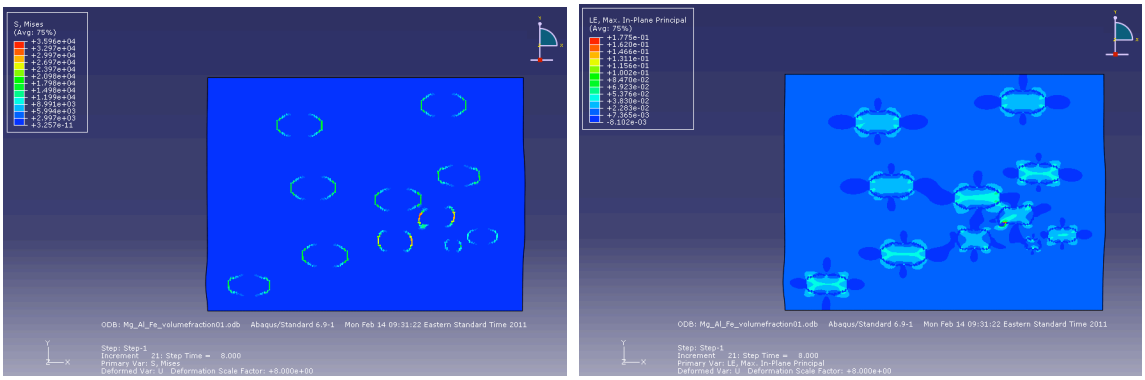

(a) von Mises stress pattern (sphere volume fraction 10%) (b) corresponding logarithmic strain distribution

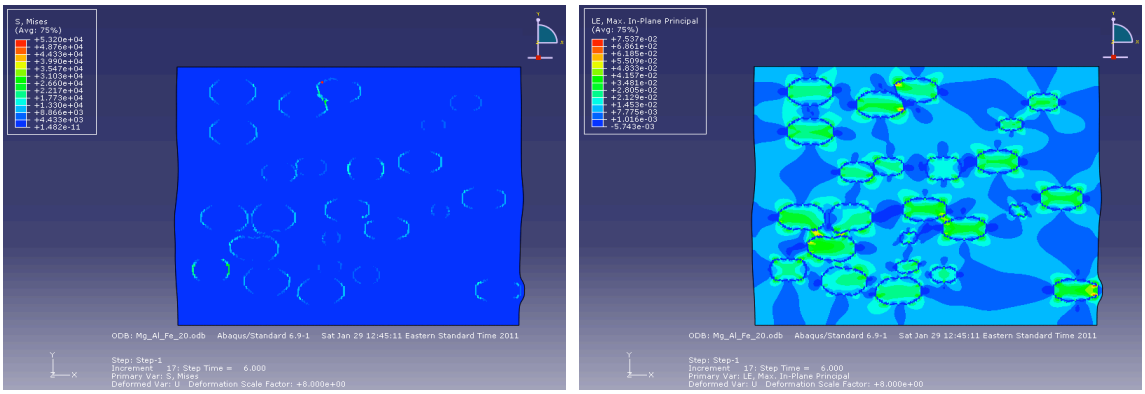

(c) von Mises stress pattern (sphere volume fraction 20%) (d) corresponding logarithmic strain distribution

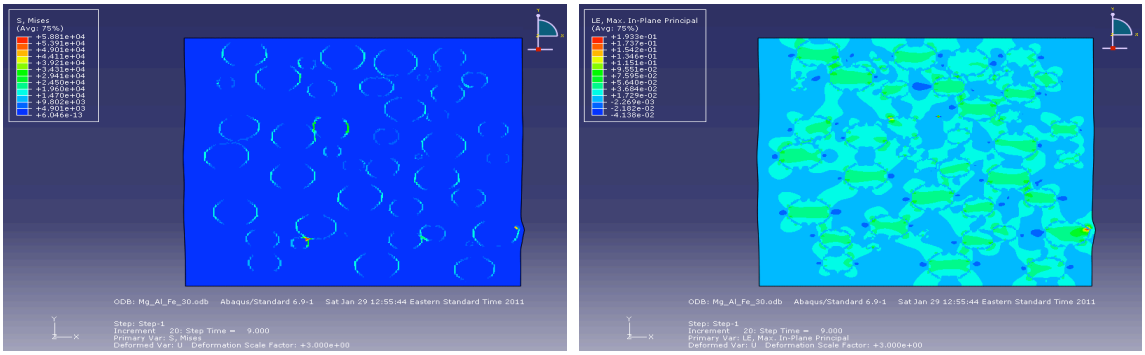

(e) von Mises stress pattern (sphere volume fraction 30%) (f) corresponding logarithmic strain distribution

Figure 93. The von Mises stress patterns and total logarithmic strain distributions of 20 × 20 mm^2 Mg/Al/M 350 hollow sphere composite material with various sphere volume fraction at (a) (b) 10% (c) (d) 20% (e) (f) 30% (g) (h) 40%

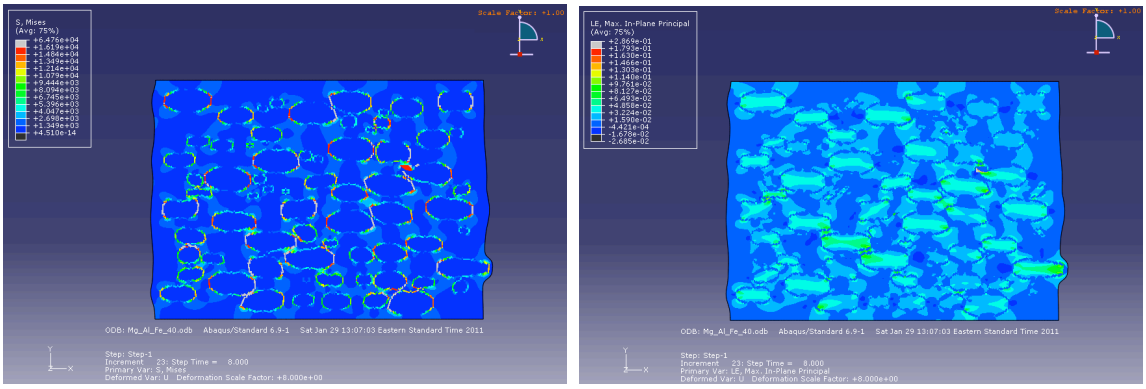

(g) von Mises stress pattern (sphere volume fraction 10%) (h) corresponding logarithmic strain distribution
Figure 93 continued

The final von Mises stress pattern, logarithmic strain pattern and stress-strain curve for 50% sphere volume fraction are shown in Figures 89 and 90. And the resulted comparison with other volume fractions are shown in Figure 94. Raising the volume fraction of spheres distinctively increases the overall strength by exhibiting higher Young's modulus and high yield strength. What is worth noting is the gradual diminishing of the bump in the stress-strain curves which occurs in the first place due to the resistance from the spheres once the compression has reached the point where the spheres start to impinge. Since the spheres are much harder than the aluminum matrix, their presence contributes greatly to the resistance to the compressive pressure, hence the enhanced modulus and bump in the stress-strain curve. Once the volume fraction starts to decrease, the overall properties of the material approaches that of aluminum alloy's.

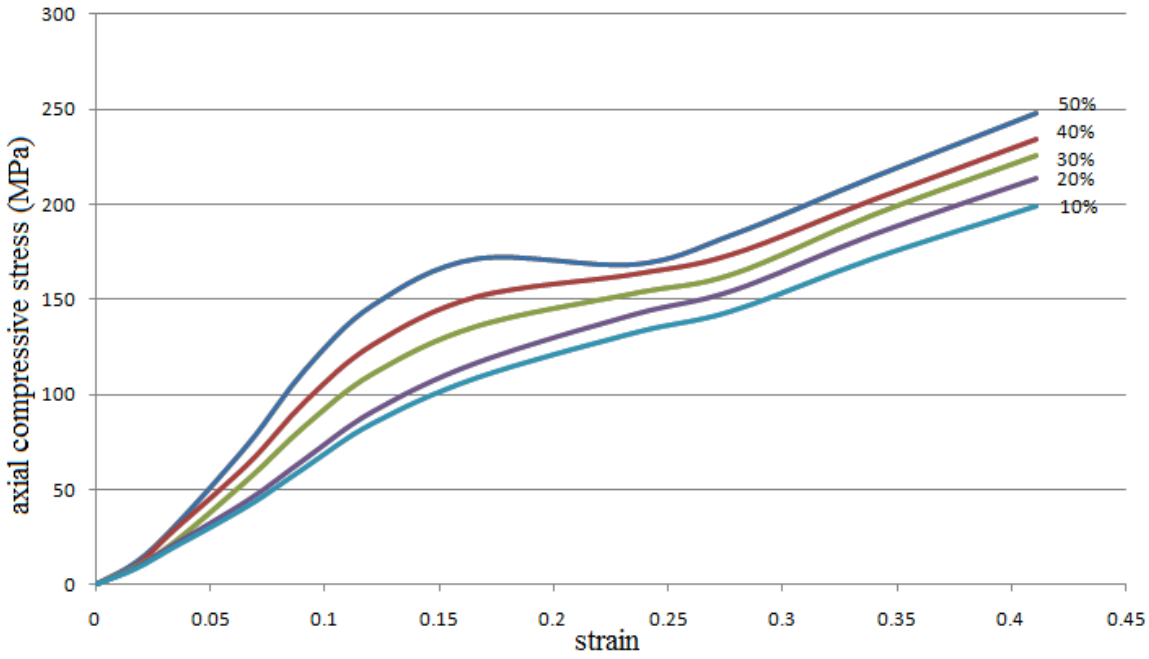

Figure 94. Compressive stress-strain curves of the Al/M350 sphere composite material with different sphere volume fractions

Following the volume fraction of spheres, various sphere wall thicknesses are tested. By rearranging Equation 30, we obtain Equation 36 that directly addresses the relationship between the relative density f_v, the average diameter d_{avg} and the wall thickness t_w.

$$f_v = \frac{6t_w}{d_{avg}} \qquad (36)$$

The f_v calculated used the current wall thickness (0.12 mm) and average sphere diameter (2.5 mm) is at 0.288. In order to examine the effects of the relative density, the diameters and the total sphere volume fraction remain unchanged while the wall thickness varies from 0.12 mm to 0.18 mm and 0.24 mm, with the relative density varying from 0.288, to 0.432 and 0.576. The accompanying geometries of the composite materials are shown in Figure 95, with the resulted final von Mises stress patterns and strain localization distributions in Figure 96.

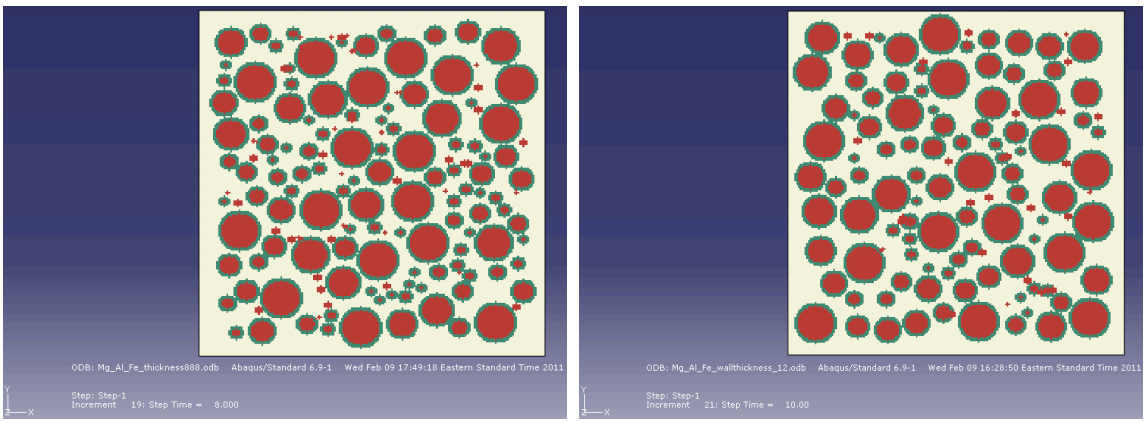

(a) sphere wall thickness 0.18 mm (b) sphere wall thickness 0.24 mm

Figure 95. 2D geometry of Mg/Al/Maraging steel hollow sphere (20 × 20 mm^2) with the sphere wall thickness at (a) 0.18 mm and (b) 0.24 mm

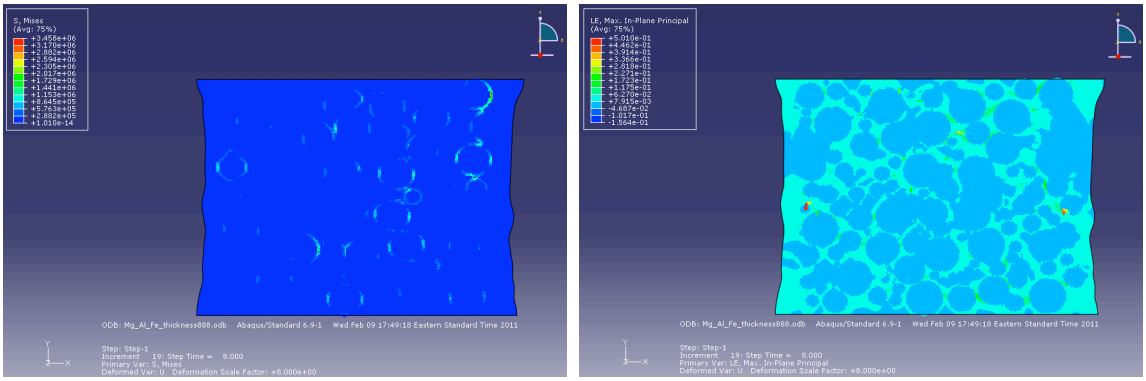

(a) von Mises stress pattern (wall thickness 0.18 mm) (b) corresponding logarithmic strain distribution

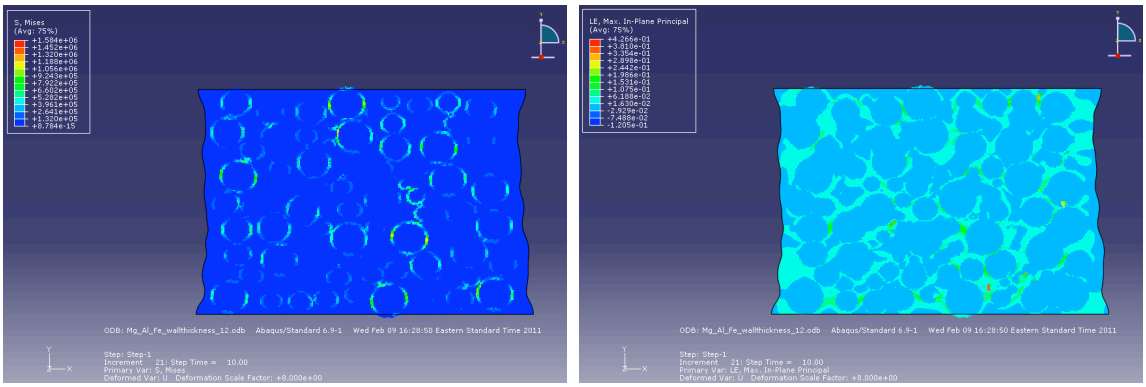

(c) von Mises stress pattern (wall thickness 0.24 mm) (d) corresponding logarithmic strain distribution

Figure 96. The von Mises stress patterns and total logarithmic strain distributions of 20 × 20 mm^2 Mg/Al/M 350 hollow sphere composite material with sphere wall thickness at (a) (b) 0.18 mm (c) (d) 0.24 mm

The resulted stress-strain curves with increasing sphere wall thickness are displayed in Figure 97.

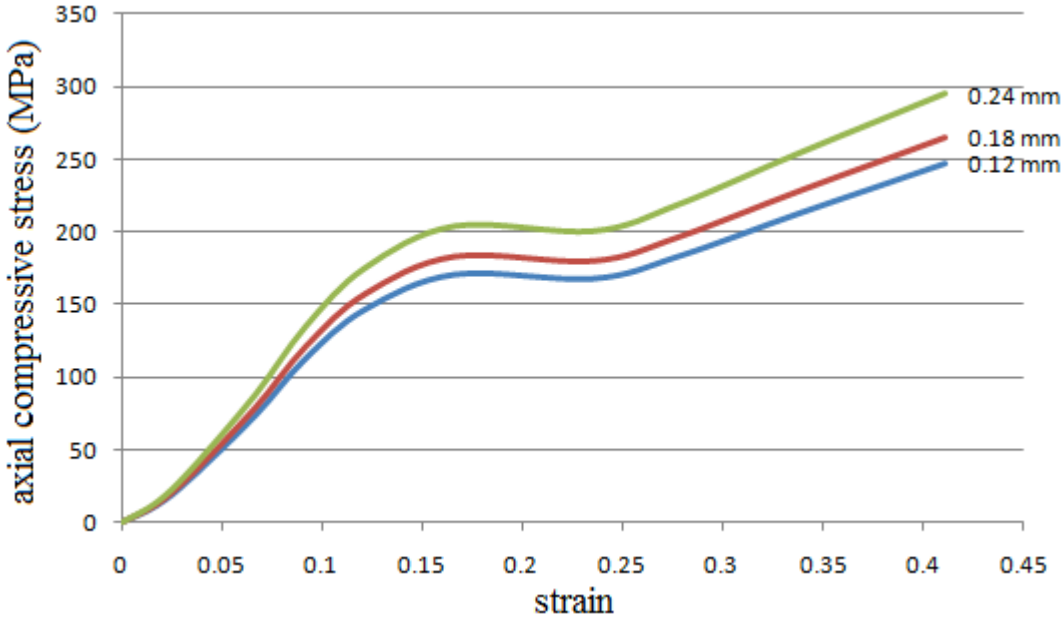

Figure 97. Compressive stress-strain curves of the Al/M350 sphere composite material with different sphere wall thicknesses

The composite material with thicker sphere walls has a higher Young's modulus and the yield strength. The 106% and 118% increase observed in the modulus and yield strength when the wall thickness increases from 0.06 mm to 0.08 mm and 0.12 mm can be explained by the fact that the thicker sphere wall provides more resistance when the spheres start to impinge each other due to the external force.

CHAPTER VI

CONCLUSIONS

In order to gain a better understanding of decarburization, a finite difference model for the decarburization that occurs in AISI 1074 low alloy steel featuring spheroidite microstructure was attempted and was validated by comparing the simulation results with experimental observations. Considering that in the actual experiments the samples are exposed to the atmosphere at both surfaces so the two-sided outward flux boundary conditions are adopted to approximate the real scenario accurately. As demonstrated by the simulation results, the two decarburization layers increase over time into the sample as the reactions proceed until the layer thickness reaches approximately 80 μm after 100 minutes, coinciding well with the experimental results well.

Then in terms of the mechanical property variations resulted from decarburization, as demonstrated in the Section 4.5, the simulation results compare favorably with the experimental observations. More importantly, the combination of the two types of models, FDM and FEM, have demonstrated the abilities to simulate many materials science-specific scenarios because the fundamental materials setting consisting of a matrix phase, second-phase particles, voids and cavities, and an altered surface is very common, as discussed in Chapter IV. By modifying the morphologies of second-phase particles and defects, more material systems and scenarios can be approximated using these models, including but not limited to gas carburization, gas nitriding, carbonitriding, case hardening among other surface treatments. In addition, many more specific features have been added to the models to bring the simulation to a different level. Such examples include the 2D-3D comparison, propagation of fracture opening and interaction between contacting surfaces, making the models approximate the reality better.

Additionally, the FEM model developed for decarburization is altered to simulate the mechanical behavior of a newly developed Mg/Al/M350 hollow sphere impact-resistant composite material, furthermore proving its exceptional ability to handle complex geometric features, which is encountered on a regular basis when dealing with such metallurgical mechanics topics.

CHAPTER VII

FUTURE WORK

The work presented in this dissertation summarizes the modeling work on the spehroidite's mechanical behaviors under the impact of decarburization layer thickness, variation of average particle size, particle volume fraction, and surface imperfection. After a series of comparisons, it is evident that the results obtained from the FEM modeling match the experimental outcomes reasonably. Many problems have been encountered over the course such as:

1) The application of periodic boundary conditions, with which the mechanical properties of bulky materials could be better calculated

2) Three-dimensional simulation has not been extensively explored due to the restriction of computing resources and time so the improvement of the algorithm and the application of parallel computing are expected to take full advantage of the prowess and flexibility of 3D modeling

3) Similar to the decarburization analysis, a lot of parametric tests can be done on the sphere-deformation model (element density, friction coefficient, sphere wall thickness, sphere diameter, distribution of different kinds of strains among others) and the composite material model (material property, 3D model, interface effects).

Two interesting issues encountered over the course of this project are both very detailed material science-related problems. The interface property is only marginally tapped into but the common understanding is that the interfacial characteristics in metals and metallic composite materials between adjacent phases are drastically different from those in ceramics and polymers, in the sense that in the former the interfacial properties are highly dependent on the lattice constant matching between the associated phases, which is termed as "coherency". Even when there is no altering in the phase materials, if

any external factors that can lead to the change of the lattice constant of either party are present, the interfacial properties will change significantly. As far as we are aware, an FEM model robust enough to embody such subtlety has yet to be constructed. Another material-science-related issue concerns the grain boundaries, which are the interfaces between two grains in polycrystalline material, to which most metals and metallic composite materials belong. The crystal orientations are different on both sides of the grain boundaries, plus grain boundaries incline to amass more second-phase particles, cavities, precipitations and defects therefore tending to exhibit vastly different behaviors than bulky materials when external force is applied. So it raises the question of how to define them since they are essentially the same material, only in a different state. It has been suggested that cohesive element could be used to represent the grain boundaries but whether this supposition is going to work or not needs more effort to find out.

APPENDIX A

SHAPE FUNCTIONS

The essence of FEM is to approximate the unknown using the previously introduced Equation $[K]\{u\} = \{F\}$, where *K*, *u* and *F* represent the stiffness matrix, a set of displacement vectors and the force. The entire domain is divided into a finite number of sub-domains or elements as we know it. Popular elements include one-dimensional linear and quadratic elements, as shown in Figure 95, two-dimensional triangular and quadratic elements, as introduced in Figures 19, 24 and 64, and those developed in three-dimension such as in Figures 53, 59 and 78.

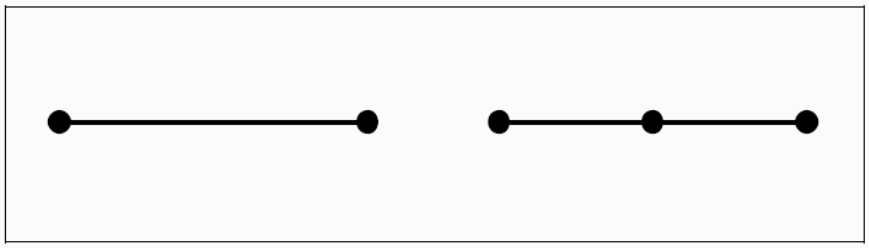

Figure 98. One-dimensional truss and beam element

Most commercial FEM software packages are equipped with but not limited to all the elements above. There is no definite answer as to which element is the "best". Eight-noded 2D (CPE8, CPS8) and twenty-noded 3D (C3D20) are often used for elasticity. In this section the truss element is selected for shape function derivation. The truss element has two nodal displacements, v_1 and v_2, at each end. For any given set of v_1 and v_2, a shape function is required to convert them into displacements along the length of the element. The selection of the functions is linear, as illustrated in Figure 96 below.

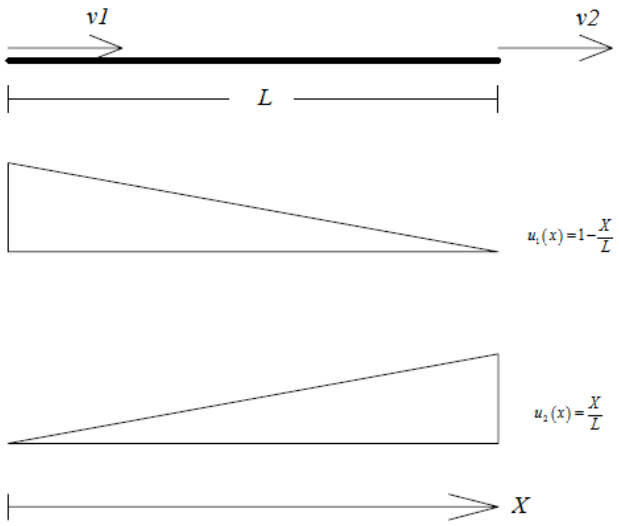

Figure 99. Truss element and its shape function

Then the shape functions need to be put into matrix form along with the end displacements to form an equation that links the displacements with the force as in Equation 37, which can be then rewritten in Equation 38.

$$u=\begin{bmatrix}1-\frac{x}{L} & \frac{x}{L}\end{bmatrix}\begin{Bmatrix}v_1\\v_2\end{Bmatrix}=\left(1-\frac{x}{L}\right)v_1+\left(\frac{x}{L}\right)v_2 \qquad (37)$$

$$\{u\}=[H(x)]\{v\} \qquad (38)$$

Now a differential equation is needed to convert the displacement into strain, as shown in Equation 39, which can be rewritten into Equation 40 if an operator matrix $D=\left\langle\frac{\partial}{\partial x}\right\rangle$ is used.

$$\varepsilon_x=\frac{\partial u(x)}{\partial x} \qquad (39)$$

$$\varepsilon_x=D[H(x)]\{v\} \qquad (40)$$

Note that the nodal displacements, *v*, are constants with respect to *x* and need not to be operated on or differentiated. Therefore, only the derivatives of the shape functions

need to be taken into consideration. In this case with truss element, the strain can then be written by substituting the shape function matrix ***H(x)***, and applying the ***D*** operator giving Equation 41:

$$\varepsilon_x = \left\langle -\frac{1}{L} \quad \frac{1}{L} \right\rangle \begin{Bmatrix} v_1 \\ v_2 \end{Bmatrix} \qquad (41)$$

Typically, the matrix resulted from the differential operator ***D*** multiplying the shape function matrix ***H(x)*** is denoted as ***B***, the strain-displacement matrix. The strain is then commonly written in the short form Equation 42:

$$\{\varepsilon_x\} = [B(x)]\{v\} \qquad (42)$$

We also need the relationship of Hook's law that converts strain into stress, in Equation 43:

$$\sigma = E * \varepsilon \qquad (43)$$

E in Equation 37 is the Young's modulus. Therefore, if we calculate the internal strain energy, which equals the integration of virtual strain over stress, the substitutions would result in Equation 44:

$$\delta W_i = \int_{volume} \overset{-T}{\varepsilon} \quad \delta\sigma = \int_{volume} \left(\overset{-T}{v} * B^T * E * B * v \right) \delta V \qquad (44)$$

Equating internal to external virtual work and remove the arbitrary virtual displacement results in Equation 45:

$$S = \int_{volume} \left(B^T * E * B \right) \delta V * v \qquad (45)$$

As a result, we can see the integral is just the element stiffness. Taking that portion out of the equation gets the stiffness matrix as in Equation 46:

$$K = \int_{volume} \left(B^T * E * B \right) \delta V \qquad (46)$$

As defined previously, ***B*** is the strain-displacement matrix and ***E*** is the familiar Young's modulus. For this case where the involved analyses are linear, ***E*** is just the 3D representation of Hook's Law. Multiplying the matrices after the partial integration for the area and removing the constants from the integral we get Equation 47:

$$K = AE * \int_{length} \begin{bmatrix} \frac{1}{L^2} & -\frac{1}{L^2} \\ -\frac{1}{L^2} & \frac{1}{L^2} \end{bmatrix} * dx \qquad (47)$$

Integrating the matrix term by term over the length of the element results in the stiffness matrix for a truss element, as in Equation 48:

$$K = \frac{AE}{L} * \begin{bmatrix} 1 & -1 \\ -1 & 1 \end{bmatrix} \qquad (48)$$

Equation 42 is just the stiffness matrix for one element, which will be assembled with the nodal displacements to solve the problem over the entire domain. The result is identical to the standard truss stiffness matrix deduced based on traditional stiffness method. However, the above derivations include the shape function process that can be extended to other types of elements where traditional stiffness by definition methods are not possible. More about shape functions is available in the following references [101-106].

REFERENCES

[1] J. K. Cochran, K. J. Lee and T. H. Sanders, Inconel hollow sphere structures for lightweight sandwich panels. *NASA final report*, Contract No. NAG-1-2245, August 1, 1999 to January 31st, 2000.

[2] C. G. Lim, SURF 2000, project report.

[3] J. K. Cochran, Deep Spring Technology Inc. proposal.

[4] A. G. Odeshi, M. N. Bassim, and S. Al-Ameeri, Effect of heat treatment on adiabatic shear bands in a high-strength low alloy steel. Materials Science and Engineering: A, 419(1-2): 69-75, 2006.

[5] G. L. Kayak, Fe-Mn-Al precipitation-hardening austenitic alloys. *Metal Science and Heat Treatment*, 11(2): 95-97, 1969.

[6] B. L. Ferguson, Z. Li and A. M. Freborg, Modeling heat treatment of steel parts. *Computational Materials Science*, 34(3): 274-281, 2005.

[7] G. Krauss, Steels: Heat treatment and processing principles. *ASM International*, pp. 497, 1990.

[8] J. C. Fulton and S. Ramachandran, Decarburizing molten steel. *US Patent* 3649246, Mar 1972.

[9] G. V. Slottman, Decarburization of steel. *US Patent* 2502284, Mar 1950.

[10] R. F. Decker, Alloy design using second phases. *Metallurgical and Materials Transactions B.,* 4(11): 2495-2518, 1973.

[11] R. P. Smith, The diffusivity and solubility of carbon in alpha-iron. *Transactions of the Metallurgical Society of Aime*, 224: 105-111, 1962.

[12] M. J. Whelan, On the kinetics of precipitate dissolution. *Metal Science Journal*, 3: 95-97, 1969.

[13] M. Nomura, H. Morimoto and M. Toyama, Calculation of Ferrite Decarburizing Depth, Considering Chemical Composition of Steel and Heating Condition. *ISIJ International*, 40(6): 619-623, 2000.

[14] Y. Iguchi, T. Kouda and T. Shibata, Kinetics of decomposition and re-oxidation resistance of θ- and x-Iron carbides at elevated temperatures and influence of their formation conditions. *ISIJ International*, 44(2): 243-249, 2004.

[15] H. B. Aaron and G. R. Kotler, The effects of curvature on the dissolution kinetics of spherical precipitates. *Metals Science Journal*, 4: 222-225, 1970.

[16] Wagner and H. Buckle, Metallforschung 1, 175(1946).

[17] L. Cerully, T. H. Sanders, Jr. and J. K. Cochran, Gas Carburization and Heat Treatment of Reduced Metal-Oxide Strip. *Materials Science and Technology Conference Proceedings*, Oct. 2008.

[18] M. C. Vincent, H. B. Miller, and D. Milton-Taylor, Erosion by proppant: a comparison of the erosivity of sand and ceramic proppants during slurry injection and flowback of proppant. *SPE Annual Conference and Exhibition*, 26-29 Sep. 2004, Houston, Texas.

[19] R. A. Weinhardt, System and method for quantitative determination of mixing efficiency at oil or gas well. *US Patent*, 5365435, Nov. 1994.

[20] R. J. Vreeburg, L. P. Roodhart, and D. R. Davies, Proppant backproduction during hydraulic fracturing - a new failure mechanism for resin-coated proppants. Journal of Petroleum Technology, 46(10): 884-889, 1994.

[21] L. Cerully, The fabrication of thin-walled steel alloys through the gas carburization of reduced metal oxide extrusions. PhD thesis, Georgia Institute of Technology, 2010.

[22] L. Cerully, T. H. Sanders, Jr. and J. K. Cochran, Gas carburization and heat treatment of reduced metal-oxide strip. *Materials Science and Technology Conference Proceedings*, Oct. 2008.

[23] H. J. Grabke and E. M. Muller-Lorenz, Effect of sulfur on the stability of cementite. *Materials Technology, Steel Research 66*, No. 6, 1995.

[24] A. Schneider, G. Inden, H. J. Grabke, Q. Wei, E. Pippel and J. Woltersdort, Effect of H_2S on formation and decomposition of Fe_3C and Fe_5C_2 under metal dusting conditions. *Steel Research* 71, No. 5, 2000.

[25] E. Pippel, J. Woltersdorf, H, J, Grabke and S. Strauss, Microprocesses of metal dusting on iron. *Steel Research* 66, No. 5, 1995.

[26] W. Jost, Diffusion in solids, liquids, gases. *Academic Press Inc.*, Publishers, New York, 1952.

[27] R. R. Judd and H. W. Paxton, Kinetics of Austenite Formation from a Spheroidized Ferrite-Carbide Aggregate. *Transactions of the Metallurgical Society of AIME*, 242: 206-215, 1968.

[28] H. B. Aaron, D. Fainstein and G. R. Kotler, Diffusion-Limited Phase Transformations: A Comparison and Critical Evaluation of the Mathematical Approximations. *Journal of Applied Physics*, 41: 4404-4410, 1970.

[29] H. B. Aaron and G. R. Kotler, Second Phase Dissolution. *Metallurgical Transactions*, 2: 393-408, 1971.

[30] Y. Prawoto, N. Sato, I. Otani, and M. Ikeda, Carbon restoration for decarburized layer in spring steel. ASM International, 13: 627-636, 2004.

[31] W. Stallard, Process of producing surface-decarburized steel sheets or plates. *US Patent*, 4007064, Feb. 0977.

[32] L. Quan, L. Cerully and T. H. Sanders, Calculation of decarburization depth in AISI 1074 steel with spheroidite microstructure at 700 ºC. AIST Steel Properties and Applications Conference Proceedings, 4: 69-79, 2009.

[33] J. E. Smith and M. L. Jordan, Mathematical and graphical interpretation of the log-normal law for particle size distribution analysis. *Journal of Colloid Science*, 19(6): 549-559, 1964.

[34] M. X. Zhang and P. M. Kelly, Crystallography of spheroidite and tempered martensite. *Acta Materialia*, 46(11): 4081-4091, 1998.

[35] A. Thom and C. J. Apelt, Field computations in engineering and physics. *London: D. Van Nostrand*, 1961.

[36] R. W. Clough, Original formulation of the finite element method. *Finite Elements in Analysis and Design* 7: 89-101, 1991.

[37] O. C. Zienkiewicz, and Y. K. Cheung, Finite element solution of field problems, The Engineer, 507-510, 1965.

[38] http://www.vinafea.com/2009/05/finite-element-analysis.html (02.11.2011)

[39] K. H. Huebner, D. L. Dewhirst and T. G. Byrom, The finite element method for engineers. *A Wiley-Interscience Publication*, John Wiley & Sons Inc. 2001.

[40] B. Swartz and B. Wendroff, The relative efficiency of finite difference and finite element methods. I: hyperbolic problems and splines. *Siam on Numerical Analysis*, 11(5): 979-984, 1974.

[41] C. A. J. Fletcher, A comparison of finite element and finite difference solutions of the one- and two-dimensional Burgers' equations. Journal of Computational Physics, 51(1): 159-188, 1983.

[42] G. M. Hulbert, Time finite element methods for structural dynamics. *International journal for numerical methods in engineering*, 33(2): 307-334, 1992.

[43] Z. Ren, Comparison of different force calculation methods in 3D finite element modeling. *Magnetics, IEEE Transactions*, 30(5): 3471-3474, 1994.

[44] T. Jerrica, IUPAC compendium of chemical terminology - the gold book. *International Union of Pure and Applied Chemistry*, 2009.

[45] www.matweb.com (01.10.2011)

[46] http://upload.wikimedia.org/wikipedia/commons/c/cc/Yield_surfaces.svg (02.02.2011)

[47] G. E. Dieter, Mechanical metallurgy. *McGraw-Hill*, 2nd edition, 1976.

[48] A. Villuendas, R. Roca and J. Jorba, Change of Young's modulus of cold-deformed aluminum AA 1050 and of AA 2024 (T65): a comparative study. *Materials Science Forum*, 539-543: 293-298, 2007.

[49] Y. Xu, M. Umemoto , and K. Tsuchiya, Comparison of the characteristics of nanocrystalline ferrite in Fe-0.89C steels with pearlite and spheroidite structure produced by ball milling. *Materials Transactions*, 43(9): 2205-2212, 2002.

[50] http://en.wikipedia.org/wiki/Yield_strength (01.31.2011)

[51] A. J. Ardell, Precipitation hardening. Metallurgical and Materials Transaction A, 16(12): 2131-2165, 1985.

[52] J. W. Martin, Precipitation hardening. *Pergamon Press, ltd*. Oxford, England, p231, 1968.

[53] R. Lagneborg, Recovery creep in materials hardened by a second phase. *Journal of Materials Science 3*, 596-602, 1968.

[54] T. Gladman, Precipitation hardening in metals. *Materials Science and Technology*, 15(1): 30-37, 1999.

[55] S. Mader and S. Herd, Formation of second phase particles in aluminum-copper alloy films. *Thin Solid Films*, 10(3): 377-389, 1972.

[56] J. R. Groza and J. C. Gilbeling, Principles of particle selection for dispersion-strengthened copper. *Materials Science and Engineering: A*, 171(1-2): 115-125, 1993.

[57] O. D. Sherby and E. M. Taleff, Influence of grain size, solute atoms and second-phase particles on creep behavior of polycrystalline solids. *Materials Science and Engineering: A*, 322(1-2): 89-99, 2002.

[58] A. Kelly, The strengthening of metals by dispersed particles. *Proceedings of the Royal Society of London. Series A, Mathematical and Physical Sciences*, 282(1388): 63-79, 1964.

[59] S. D. Cramer and B. S. Covino, Jr., ASM Handbook. Volume 13B: Corrosion: Materials, *ASM International*, 2005.

[60] J. G. Yang, Finite element analysis, 1997, (12.28.2010) http://scholar.lib.vt.edu/theses/available/etd-6197-6556/unrestricted/ch2.PDF

[61] A. A. Griffth, The phenomena of rupture and flow in solids. *Philosophical Transactions of the Royal Society of London. Series A, Containing Papers of a Mathematical or Physical Character*, 221: 163-198, 1921.

[62] D. Roylance, Introduction to fracture mechanics. *Department of Materials Science and Engineering, Massachusetts Institute of Technology*, Cambridge, MA 02139, June 14th, 2001.

[63] J. Weertman, Fracture mechanics: A unified view for Griffith-Irwin-Orowan cracks. *Acta Metallurgica*, 26(11): 1731-1738, 1978.

[64] C. K. Chao and R. C. Chang, On the energy release rate of finite cracked bodies. *Department of Mechanical Engineering, National Taiwan University of Science and Technology*, Taipei, Taiwan 10672.

[65] H. G. deLorenzi, On the energy release rate and the J-integral for 3-D crack configurations. *International Journal of Fracture*, 19(3): 183-193, 1982.

[66] H. G. deLorenzi, Energy release rate calculations by the finite element method. *Engineering Fracture Mechanics*, 21(1): 129-143, 1985.

[67] G. P. Cherepanov, The propagation of cracks in a continuous medium. *Journal of applied mathematics and mechanics*, 31(3): 503-512, 1967.

[68] J. R. Rice, A path independent integral and the approximate analysis of strain concentration by notches and cracks. *Journal of Applied Mechanics*, 35: 379-386, 1968.

[69] http://cr4.globalspec.com/thread/20315 (02.15.2011)

[70] J. A. Begley and J. D. Landes, The J integral as a fracture criterion. *The Fifth National Symposium of Fracture Mechanics*, STP 513:1-21, 1972.

[71] H. M. Westergaard, Bearing pressures and cracks: Bearing pressures through a slightly waved surface or through a nearly flat part of a cylinder, and related problems of cracks. *Journal of Applied Mechanics*, A: 49-53, 1939.

[72] J. W. Dally, W. L. Fourney and G. R. Irwin, On the uniqueness of the stress intensity factor - crack velocity relationship. *International Journal of Fracture*, 27(3-4): 159-168, 1985.

[73] C. H. Wang, Introduction to fracture mechanics. *Airframes and Engines Division, Aeronautical and Maritime Research Laboratory, Department of Defense, Commonwealth of Australia*, 1996.

[74] V. E. Saouma, Fracture mechanics lecture notes. *Department of Civil Environmental and Architectural Engineering, University of Colorado*, Boulder, CO 80309-0428.

[75] G. T. Hahn, A model for yielding with special reference to the yield-point phenomena of iron and related bcc metals. *Acta Metallurgica*, 10(8): 727-738, 1962.

[76] A. Cracknell and N. J. Petch, Frictional forces on dislocation arrays at the lower yield point in iron. *Acta Metallurgica*, 3(2): 186-189, 1955.

[77] J. M. Krafft, An interpretation of lower yield point plastic flow in the dynamic testing of mild steel. *Acta Metallurgica*, 10(2), 85-93, 1962.

[78] A. H. Cottrell and B. A. Bilby, Dislocation theory of yielding and strain ageing of iron. Proceedings of the Physical Society. Section A, 62(1): 49-62, 1949.

[79] L. J. Baker, S. R. Daniel, and J. D. Parker, Metallurgy and processing of ultralow carbon bake hardening steels. Materials Science and Technology, 18(4): 355-368, 2002.

[80] J. K. Cochran, T. H. Sanders, T. M. McCoy and L. B. Cerully, Carburization of low alloy steel hollow proppants. *Technical Performance Report 9, Contract # 106260, Deep Springs Technology*, March, 2010.

[81] http://www.steelforge.com/metaltidbits/maraging.htm (04.10.2010)

[82] J. K. Cochran, T. H. Sanders, T. M. McCoy and L. B. Cerully, Carburization of low alloy steel hollow proppants. *Technical Performance Report 11, Contract # 106260, Deep Springs Technology*, July, 2010.

[83] K. Velusamy, T. Sundararajan, and K. N. Seetharamu, Interaction Effects Between Surface Radiation and Turbulent Natural Convection in Square and Rectangular Enclosure. *Journal of Heat Transfer*, 123(6), 1062-1071, 2001.

[84] P. Wriggers, and C. Miehe, Contact constraints within coupled thermomechanical analysis - a finite element model. *Computer Methods in Applied Mechanics and Engineering*, 113(3-4): 301-319, 1994.

[85] N. Stromberg, L. Johansson, and A. Klarbring, Derivation and analysis of a generalized standard model for contact, friction and wear. *International Journal of Solids and Structures*, 33(13): 1817-1836, 1996.

[86] T. Smolnicki, E. Rusinski, and J. Karlinski, FEM modeling of fatigue loaded bolted flange joints. *Journal of Achievements in Materials and Manufacturing Engineering*, 22(1): 69-72, 2007.

[87] D. Siminiati, FEM numerical algorithm on contact problem for non-conform elastic bodies. *Proceedings of the 11th Scientific International Conference* "Achievements in Mechanical and Materials Engineering", AMME'2002, Gliwice - Zakopane, 495-498, 2002.

[88] H. Razavi, A. Abolmaali, and M. Ghassemieh, Invisible elastic bolt model concept for finite element analysis of bolted connections. *Journal of Constructional Steel Research*, 63(5): 647-657, 2007.

[89] A. R. Khoei, and M. Nikbakht, Contact friction modeling with the extended finite element method (X-FEM). *Journal of Materials Processing Technology*, 177: 58-62, 2006.

[90] N. J. Carpenter, R. L. Taylor, and M. G. Katona, Lagrange constraints for transient finite element surface contact. *International Journal for Numerical Methods in Engineering*, 32(1): 103-128, 1991.

[91] P. Wriggers, T. V. Van, and E. Stein, Finite element formulation of large deformation impact-contact problems with friction. *Computers & Structures*, 37(3): 319-331, 1990.

[92] D. P, and D. R. J. Owen, Computational model for 3-D contact problems with friction based on the penalty method. *International Journal for Numerical Methods in Engineering*, 35(6): 1289-1309, 1992.

[93] A. B. Chaudhary, and K. J. Bathe, A solution method for static and dynamic analysis of three-dimensional contact problems with friction. *Computers & Structures*, 24(6): 855-873, 1986.

[94] J. C. Simo, and T. A. Laursen, An augmented Lagrangian treatment of contact problems involving friction. *Computers & Structures*, 42(1): 97-116, 1992.

[95] http://www.mece.ualberta.ca/tutorials/ansys/at/contact/contact.html (08.28.2010)

[96] K. L. Lawrence, Ansys workbench tutorial: Structural & thermal analysis. *SDC Publications, Schroff Development Corporation*, 2010.

[97] A. K. Safina, and R. Z. Dautov, Revised quadratic subparametric triangular finite element of the second-order accuracy. *Kazan. Gos. Univ. Uchen. Zap. Ser. Fiz.-Mat. Nauki*, 149(4): 132-145, 2007.

[98] M. Vesenjak, T. Fiedler, A. Ochsner, and Z. Ren, Numerical analysis of metallic hollow sphere structures. *7. LS-DYNA Anwenderforum*, Material III - Kunststoffe: D III 1-6, 2008.

[99] T. J. Lim, B. Smith, and D. L. McDowell, Behavior of a random hollow sphere metal foam. *Acta Materialia*, 50: 2867-2879, 2002.

[100] J. Cochran, T. Sanders, and N. Thadhani, Lightweight metal alloy composite for armor. *ARL Proposal submitted to Deep Springs Technology*, Toledo, Ohio, July 2010.

[101] D. Swenson, Finite element concepts. *Prentice-Hall, Inc.* 1996.

[102] T. J. R. Hughes, The finite element method: linear static and dynamic finite element analysis, *Prentice-Hall, Inc.* 1987.

[103] J. N. Reddy, An introduction to the finite element method, third edition. *McGraw-Hill*, New York, 2005.

[104] K. H. Huebner, D. L. Dewhirst, D. E. Smith, and T. G. Byrom, The finite element method for engineers, fourth edition. *John Wiley & Sons, Inc.*, New York, 2001.

[105] C. T. F. Ross, Advanced applied finite element methods. *Horwood Series in Engineering Science*, 1998.

[106] V. Adams, and A. Askenazi, Building better products with finite element analysis. *Onword Press*, 1999.